

11

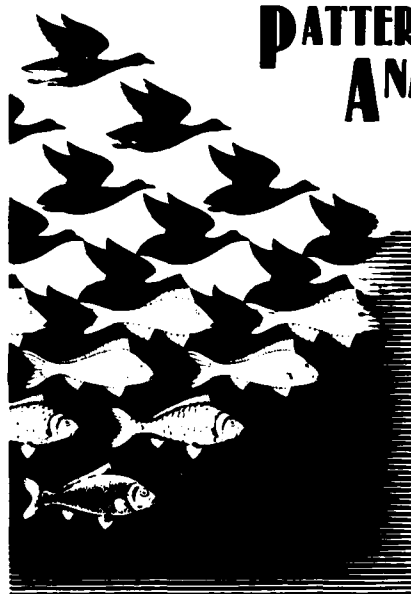
NORDA Technical Note 176

Naval Ocean Research and  
Development Activity  
NSTL, Mississippi 39529



AD A 140195

# PAME Proceedings



## PATTERN ANALYSIS in the MARINE ENVIRONMENT

an  
Ocean Science  
and Technology  
Workshop

March 24-26, 1982

DTIC  
ELECTE  
S FEB 8 1984 D  
B



Sponsored by the  
Chief of Naval Research

Robert M. Brown, Editor

Ocean Science and Technology Laboratory  
Mapping, Charting and Geodesy Division

Approved for Public Release  
Distribution Unlimited

October 1983

DTIC FILE COPY

84 02 08 003

## COMPONENT PART NOTICE

THIS PAPER IS A COMPONENT PART OF THE FOLLOWING COMPILATION REPORT:

(TITLE): PAME Proceedings, Pattern Analysis in the Marine Environment, an  
Ocean Science and Technology Workshop Held at the Naval Ocean Research  
and Development Activity, NSTL, MS. on 24-26 March 1982.

(SOURCE): Naval Ocean Research and Development Activity, NSTL, MS.

TO ORDER THE COMPLETE COMPILATION REPORT USE AD-A140 195.

THE COMPONENT PART IS PROVIDED HERE TO ALLOW USERS ACCESS TO INDIVIDUALLY AUTHORED SECTIONS OF PROCEEDINGS, ANNALS, SYMPOSIA, ETC. HOWEVER, THE COMPONENT SHOULD BE CONSIDERED WITHIN THE CONTEXT OF THE OVERALL COMPILATION REPORT AND NOT AS A STAND-ALONE TECHNICAL REPORT.

THE FOLLOWING COMPONENT PART NUMBERS COMPRISE THE COMPILATION REPORT:

AD#:	P003 117	TITLE:	Cluster Analysis Package for Image Segmentation.
	P003 118		Fourier Shape Analysis: A Multivariate Pattern Recognition.
	P003 119		Fuzzy Algorithms for Pattern Recognition.
	P003 120		The Use of Satellite Observations of the Ocean Science in Commercial Fishing Operations.
	P003 121		Digitally Controlled Sonars.
	P003 122		Application of Computer Image Processing to Underwater Surveys.
	P003 123		The Identification and Inversion of Acoustic Multipath Data at Long Range in the Ocean.
	P003 124		Principal Components as a Method for Atmospherically Correcting Coastal Zone Color Scanner Data.
	P003 125		Water Mass Classification in the North Atlantic Using IR Digital Data and Bayesian Decision Theory.
	P003 126		Spatial Image Processing Masks from Frequency Domain Specifications.

**BLANK PAGES  
IN THIS  
DOCUMENT  
WERE NOT  
FILMED**

# Abstract

The Pattern Analysis in the Marine Environment (PAME) Workshop Proceedings contains ten of the papers presented at an Ocean Science and Technology Workshop sponsored by the Chief of Naval Research and hosted by the Naval Ocean Research and Development Activity, NSTL, Mississippi, 24-26 March 1982.

PAME Workshop topics ranged from computer science, pattern analysis, and artificial intelligence to specific problem areas, applications, and requirements in ocean science. The workshop was organized in the following five sessions:

- Image Analysis Techniques I;
- Image Analysis Techniques II;
- Pattern Analysis Techniques;
- Space Technology for Ocean Applications;
- Ocean Patterns in Space-Time.

A number of presentations were informal and tutorial in nature. An abstract of all presentations is included, along with a complete list of attendees.

Accession For	
NTIS GRA&I	<input checked="checked" type="checkbox"/>
DTIC TAB	<input type="checkbox"/>
Unannounced	<input type="checkbox"/>
Justification	
By	
Distribution/	
Availability Codes	
Dist	Avail and/or Special
A-1	





## Acknowledgments

These Pattern Analysis in the Marine Environment (PAME) Workshop Proceedings are part of an overall program sponsored by the Chief of Naval Research and hosted by the Naval Ocean Research and Development Activity (NORDA). The project was funded by Program Element 61153N. The purpose of these Ocean Science and Technology Workshops is to bring together members of the government, academic, and industrial communities to focus attention on specific issues of interest to the Navy.

The PAME Workshop chairman would like to express his special appreciation to the NORDA Technical Director, Dr. James E. Andrews, for his encouragement and support of the PAME Workshop and for presenting the Keynote Address and to all the authors, presentors, and PAME participants. Administrative activities of the workshop were coordinated through the University of Southern Mississippi under the direction of Myron Webb.

# Preface

**SPONSORED** by the Chief of Naval Research and hosted by the Naval Ocean Research and Development Activity (NORDA), this workshop was one in a series of ocean science workshops held to highlight areas of significance to the Navy.

**GOAL:** The intent of the PAME Workshop was to provide a forum for expert discussions of (1) pattern analysis (PA) applications, requirements, and problems by the ocean science community, (2) tools available within the computer science and artificial intelligence (AI) areas, and (3) concrete interaction between these two fields.

**WORKSHOP PHILOSOPHY:** The marine science community was urged to present (1) examples of its work that employ PA techniques and (2) formulate ocean science problems in careful (and concrete) terms so that other participants, both AI/computer scientists and ocean scientists, could consider these PA requirements and interact with them by discussing potential solution areas, similar examples from other fields, and by absorbing these needs and formulating new areas for R&D in PA to support such ocean environmental tasks.

On the part of the PA and AI communities, efforts were made to consider the very difficult "real world" problems in PAME and to illustrate and present potential tools/techniques that could be applied to these areas in the near to intermediate term. This guideline applied especially to problem and "feature" definition and evaluation procedures but also to classification schemes. Thus an attempt was made to emphasize current state-of-the-art, as it is available to the marine community, in contrast to R&D challenges and problems in the AI or PA fields for their own sake.

With increasing performance and requirements of ocean science information systems (OSIS), the NAVY is faced with greater demands for pattern analysis and information extraction techniques to help solve its operation problems as well as advance its tech base science programs. It is hoped that interaction at the PAME Workshop contributed and fostered such technology and requirements transfer between these two communities. To this end, the participants to the workshop were invited from diverse fields of interests and an informal environment for information exchange was encouraged.

**WORKSHOP FORMAT:** There were five half-day (3 hour) sessions in the workshop. Each session had from three to five speakers and ample time for discussion both of the details of a given presentation and the themes that grew out of the talks in that session. Appendix A contains the original PAME Agenda. Approximately one hour was set aside for this type of informal interchange with the session speakers acting as catalysts/panel where appropriate. The workshop was limited in attendance to approximately 50 persons to accommodate the format described above and because of the size of the River House facility. Approximately half of the participants presented papers.

**PRESENTATIONS AND PROCEEDINGS:** The presentations varied in length from 15-45 minutes with 30 minutes being typical. They included outlines of ongoing investigations of interest to the marine scientists, current PAME problem areas, topics for new research, and tutorials on specialized AI subjects. A brief abstract of each presentation was available in the PAME Abstract Booklet before the workshop began. These original abstracts are reproduced in Appendix B. These PAME Proceedings document some of the information exchange at the workshop and point to and clarify

areas for future R&D and application of Pattern Analysis in the Marine Environment by both ocean and PA scientists.

OTHER ACTIVITIES: A long lunch hour was held on both Wednesday and Thursday outside "under the trees" at the pavillion near the River House. Again, this approach was designed to encourage continuation of informal exchange between the participants. Two evening meal functions were also included in the agenda. The workshop adjourned on noon Friday to allow participants to catch afternoon flights or to visit the Gulf Coast and New Orleans areas.

ROBERT M. BROWN, CHAIRMAN  
Ocean Science and Technology Workshop  
PATTERN ANALYSIS IN THE MARINE ENVIRONMENT

# Contents

Cluster Analysis Package For Image Segmentation M. F. Janowitz <i>AD-P003 117</i>	1
Fourier Shape Analysis: A Multivariate Pattern Recognition Approach <i>AD-P003 118</i> Robert Ehrlich and William E. Full	47
Fuzzy Algorithms for Pattern Recognition James C. Bezdek <i>AD-P003 119</i>	69
The Use of Satellite Observations of the Ocean Science in Commercial Fishing Operations R. D. Montgomery <i>AD-P003 120</i>	121
Digitally Controlled Sonars George R. Hansen <i>AD-P003 122</i>	157
Application of Computer Image Processing to Underwater Surveys Peter R. Paluzzi <i>AD-P003 122</i>	173
The Identification and Inversion of Acoustic Multipath Data at Long Range in the Ocean Michael G. Brown <i>AD-P003 123</i>	189
Principal Components as a Method for Atmospherically Correcting Coastal Zone Color Scanner Data Ronald J. Holyer <i>AD-P003 124</i>	199
Water Mass Classification in the North Atlantic Using IR Digital Data and Bayesian Decision Theory Robert E. Coulter <i>AD-P003 125</i>	225
Spatial Image Processing Masks from Frequency Domain Specifications E. R. Meyer and R. C. Gonzalez <i>AD-P003 126</i>	237
APPENDIX A: Agenda	249
APPENDIX B: Abstracts	253
APPENDIX C: List of Attendees	279

# Cluster Analysis Package for Image Segmentation

M. F. Janowitz

Department of Mathematics and Statistics  
University of Massachusetts  
Amherst, MA 01003

## ABSTRACT

A description is given of the underlying motivation and actual implementation of a number of cluster analysis algorithms that can be used for the segmentation of images collected by remote sensing devices. The outputs of the various algorithms are illustrated on both real and simulated data.

## I. INTRODUCTION

Satellites tend to spew massive data sets back to us at an alarmingly rapid rate. Because of the high initial investment both in the satellite and in the equipment needed to transmit, receive and interpret this data, there is a natural tendency to collect and store everything that comes back to us. This creates problems in database management and data retrieval that will not be addressed here; nonetheless, an indication will be given of the possible use of low resolution segmented images as efficient low cost means of summarizing large digital pictures.

The goal of this report is the description of a package of cluster analysis algorithms that seem useful for the segmentation of monochromatic digital remote sensing data. The work was done at four levels: underlying motivations, development and implementation of algorithms, simulations, and real data analysis. The present report is restricted to techniques that deal with a single feature, with multiple feature selection to be investigated at a later date. Section II presents the motivation for both the cluster techniques and the statistics they use, while Section III contains a careful description of the techniques. In Section IV some simulated data is analyzed, while Section V contains a description of the use of low resolution pictures as summaries of large digital images. The remaining section presents the results of the algorithms as applied to real data as well as to real data with additive noise. The paper is based in part on work that was reported in [4], and it will be useful to consult that reference in connection with the current paper.

## II. BASIC ASSUMPTIONS

Here is a list of the assumptions that underly all of the cluster algorithms. They are based largely on the work of Bryant [1] and Coleman and Andrews [2], p. 775.

A1. The input data consists of an  $m \times n$  matrix  $A$ , each of whose entries is a positive integer.

A2. There is an underlying function  $F$  defined on a rectangular region of a Cartesian plane. This function might represent temperature, brightness, or some

other attribute of the plane. Thus  $F$  is a real-valued function whose domain is a closed rectangle of the form  $\{(x,y): a < x < b, c < y < d\}$  for fixed real numbers  $a, b, c, d$ .

A3. There is a natural division of the domain of  $F$  into a finite number of regions  $R_1, R_2, \dots, R_t$ . Each such region is connected, has a smooth boundary, and can be characterized by the values of  $F$ . It might be that the regions  $R_i$  correspond to fixed values of  $F$ , or that they can be distinguished by some sort of texture measure applied to  $F$ , or possibly some combination of features of  $F$ .

A4. The observer has no direct knowledge of the number of regions, their location, or the values of  $F$  within a given region. There is, however, knowledge of the manner in which the regions are characterized by  $F$ . Nonetheless, the observer has no direct knowledge of any of the values of  $F$ .

A5. Each entry of the input matrix  $A$  is the result of an estimate of  $F$  by a sensing device that introduces errors in at least three ways. First of all, the device produces an average value of  $F$  over a small subregion of the plane. Thus the device produces a function with finite domain, each of whose values corresponds to the average value of  $F$  over a suitable subregion of the plane, with adjacent values of the device corresponding to adjacent subregions. Secondly, there is additive noise associated with the process by which the device reads the values of  $F$ . Thirdly, the device discretizes its output by rounding it off to the nearest integer. This can all be succinctly summarized by the mathematical assertion that the values of the input matrix  $A$  correspond to values of a random variable

$$G = \text{NINT} (\bar{F} + N)$$

where  $\bar{F}$  is the function with finite domain obtained by averaging  $F$  over suitable subregions, and  $N$  is a random noise variable whose restriction to region  $R_i$  has expected value 0 and variance  $\sigma_i^2$ , with  $\text{NINT}$  denoting the function that rounds a real number to the integer to which it is closest. No further assumptions are made about the distribution of  $N$ . It is assumed that  $G$  has spatial significance in that adjacent values of  $G$  correspond to adjacent regions of the plane.

A6. Near the boundary of a region, the sensing device will sometimes be averaging values of  $F$  from more than one region. This can produce values of  $\bar{F}$ , hence of  $G$ , that do not seem to belong to any of the regions in question. These boundary points may appear to represent a region of their own, or may even seem to belong to some other region of the plane that is not located near the boundary in question.

A7. The input data  $A$  has only ordinal significance.

Assumption A7 will not always be made, but when it is made, an appropriate model for image segmentation is provided by the notion of a partially ordered partition of the domain of  $\bar{F}$ . This is a pair  $(P, \leq)$  where  $P$  is a partition of the domain, and  $\leq$  a partial order on the equivalence classes of  $P$ . A start to the investigation of these objects appears in [4], and further work is currently in progress. In any event, the image segmentation problem within the context of the above assumptions may now be given a precise formulation:

IMAGE SEGMENTATION PROBLEM. Given the values of the input random variable  $G$ , together with whatever information is available concerning the noise variable  $N$  and the manner in which the underlying regions are determined by  $F$ , estimate the number of regions  $t$ , their location, and the value(s) of  $F$  that determine each region.

In the next section several image segmentation algorithms will be described. The underlying philosophy is quite simple, and in summary asserts two things: (1) Before attempting a complicated algorithm, one should at least investigate the simple ones. (2) When looking for a needle in a hay stack, it is reasonable to look for needle-shaped objects. When stated in the above form, the philosophy appears rather superficial. The point though is that if a simple straightforward algorithm will work, why try anything more complicated? Considerations such as computer time and relation of the input to the output data are naturally involved here.

The algorithms will all involve both the values of the input matrix  $A$  and their spatial distribution. In order to motivate the discussion of the next section, let us consider a simple statistical model. Suppose that the input data represents 2 regions,  $X$  and  $Y$ . Suppose further that the variable  $N$  is independently distributed. One can therefore assume that there is a probability  $p$  that an interior member of  $X$  will have probability  $p$  of being assigned to  $Y$ , and conversely, an interior member of  $Y$  will have probability  $p$  of being assigned to  $X$ , with these probabilities being independent. In view of A6, boundary points would naturally have a higher probability of being misclassified. In any event, if  $A$  is an  $m$  by  $n$  matrix, one would expect that at least  $pmn$  points would be misclassified. Let us see what happens, however, if the classification of a point is based in part on the classification of its neighbors. More specifically, let us consider a 3 by 3 neighborhood centered on an interior point of  $X$ . Assuming all 9 points in the neighborhood belong to  $X$ , let us base the assignment of  $X$  on that of wherever 5 out of 9 points are assigned. This rule will in the sequel be referred to as the 5/9 rule. If  $B(p;9,k)$  represents the binomial probability that  $k$  out of the 9 points have been assigned to  $Y$ , then the probability of misclassifying the given point is evidently

$$B(p;9,5)+B(p;9,6)+B(p;9,7)+B(p;9,8)+B(p;9,9).$$

For a  $k$  by  $k$  neighborhood ( $k$  an odd integer), one would use a  $j/k^2$  rule, where  $j = (k^2+1)/2$ . The only other rule that will be considered will be the 3/5 rule, and this refers to a decision based upon the point and its 4 immediate neighbors (North, South, East and West). The probabilities for these decision rules are also based upon the binomial distribution. Table 1 illustrates how the probabilities of misclassification can be improved by the use of such decision rules. Though it is clear that larger windows decrease the probability of misclassification of interior points, it should be noted that larger windows also tend to include points that are not in the given cluster, and this can tend to produce errors. An indication of this effect occurs in Table 2.

To illustrate the calculation of the probabilities in Table 2, let us consider the 5/9 rule with 1 point from another cluster. Specifically, it will be assumed that the given point and 7 of its neighbors belong to  $X$  and that a single neighbor is in  $Y$ . We want the probability that at least 5 out of the 9 points will be put in  $X$  by the input matrix  $A$ . The point in  $Y$  will have probability  $1-p$  of being

Rule	Probability of misclassification								
	.1	.2	.3	.35	.4	.45	.46	.47	.48
3/5	.009	.058	.163	.235	.317	.407	.425	.444	.463
5/9	.001	.020	.099	.172	.267	.379	.402	.427	.451
13/25	0	0	.018	.060	.154	.306	.343	.381	.420
25/49	0	0	.002	.015	.078	.280	.287	.336	.389
41/81	0	0	0	.003	.034	.183	.235	.294	.359
61/121	0	0	0	0	.013	.135	.189	.254	.330
85/169	0	0	0	0	.004	.096	.148	.217	.301

Table 1. Probability of misclassifying interior points using various spatial rules. See text for explanation of the rules. Each probability is rounded to 3 places. The top row gives the probability of misclassifying an individual pixel.

Rule	Other Cluster	Probability of misclassification								
		.1	.2	.3	.35	.4	.45	.46	.47	.48
3/5	1	.047	.150	.269	.328	.387	.444	.455	.466	.477
	2	.225	.346	.415	.440	.461	.481	.485	.489	.492
5/9	1	.005	.047	.153	.228	.313	.405	.424	.443	.462
	2	.021	.106	.228	.295	.363	.432	.445	.459	.473
	3	.087	.216	.325	.373	.417	.459	.467	.475	.484
	4	.293	.392	.439	.457	.472	.486	.489	.492	.497
13/25	1	0	.001	.025	.076	.174	.321	.355	.390	.426
	2	0	.002	.036	.095	.195	.335	.367	.399	.433
	3	0	.004	.051	.117	.218	.350	.379	.409	.439
	4	0	.008	.071	.143	.243	.365	.391	.418	.445
	5	0	.015	.096	.172	.269	.380	.404	.428	.452
	6	.001	.029	.128	.206	.296	.396	.417	.437	.458

Table 2. Probability of misclassifying boundary points using various spatial rules. See text for explanation of the rules. The "Other Cluster" column gives the number of points in the neighborhood that do not belong to the cluster under consideration.



classified in Y and probability p of being put in X. Thus the desired probability is given by

$$(1-p)[B(p;8,5) + B(p;8,6) + B(p;8,7) + B(p;8,8)] + \\ p[B(p;8,4) + B(p;8,5) + B(p;8,6) + B(p;8,7) + B(p;8,8)].$$

Hopefully, what will make the algorithms work is the fact that the number of boundary points is small relative to the number of interior points, so that the rather dramatic increase in probability of misclassification shown in Table 2 will not really have too much effect. To illustrate this, some simulations were tried based upon the data in Figs. 1 and 2. Each of these data sets involves 2 input clusters. White noise was added to each picture with the indicated signal to noise ratio shown in Table 3. Here one can define the signal to noise ratio as the difference in mean values of the data in the 2 input clusters divided by the standard deviation of the noise. For purposes of comparison, the simulations were also run on data consisting entirely of interior points. The results are fairly consistent with the earlier theoretical results of Tables 1 and 2. The effect of large windows on the classification of boundary points can be seen by examining the data for the 13/25 decision rule. Note the higher probability of misclassification for the data having a boundary as opposed to the same size data set of interior points.

### III. THE CLUSTERING ALGORITHMS

This section will contain a careful description of the algorithms that do the image segmentation. Some of them are numeric and some ordinal, but they are all variations on the same theme. They are based on the following items: (a) a procedure for removing rarely occurring clusters; (b) a determination of the "scatter" of each cluster; (c) a decision based upon scatter as to which clusters should be removed; (d) a rule for reassigning the points that belong to clusters which are removed; (e) a stopping rule. Accordingly, the discussion will break into a number of sections. In all of this, it will be assumed that the input is an m by n matrix A with integer values, and that the desired regions  $R_1, \dots, R_t$  are characterized by having constant values of A over a connected spatial domain with a smooth boundary.

#### A. PREFILTERS

A number of prefilters are available in the program.

##### 1. k by k mean ( $k = 3, 5, 7, \dots$ )

The value at each point of A is replaced by the mean of a k by k neighborhood centered at that point. This mean is either rounded to the nearest integer or to the nearest integer that happens to occur in A. For ordinal data, A is rank ordered before applying the filter.

##### 2. Special k by k mean

This is identical to the k by k mean except that in each neighborhood the j (j a parameter) highest and lowest values are first removed. This tends to reduce spot noise. A similar approach to this is described in J. S. Lee [6], and it is planned to incorporate his sigma filter into the cluster package.

Data	Noise Ratio	Decision Rule	With Boundary		All interior points	
			Mean	SD	Mean	SD
Fig. 1	1.25	None	.2697	.0203	.2820	.0182
		3/5	.1607	.0290	.1341	.0241
		5/9	.1233	.0247	.0699	.0196
		13/25	.0947	.0146	.0035	.0030
	1.00	None	.3100	.0199	.3178	.0262
		3/5	.2218	.0336	.1935	.0377
		5/9	.1784	.0271	.1256	.0276
		13/25	.1381	.0272	.0333	.0217
	0.67	None	.3810	.0306	.3857	.0228
		3/5	.3015	.0524	.2910	.0401
		5/9	.2629	.0578	.2353	.0452
		13/25	.2100	.0521	.1178	.0449
	0.50	None	.4170	.0265	.4168	.0163
		3/5	.3564	.0447	.3361	.0333
		5/9	.3276	.0611	.2902	.0340
		13/25	.2739	.0669	.1810	.0391
	0.25	None	.4501	.0282	.4544	.0225
		3/5	.4153	.0513	.4108	.0399
		5/9	.3987	.0652	.3737	.0532
		13/25	.3619	.0744	.3048	.0883
Fig. 2	1.25	None	.2751	.0194	.2979	.0118
		3/5	.1491	.0297	.1620	.0197
		5/9	.1000	.0241	.0945	.0197
		13/25	.0482	.0125	.0118	.0068
	1.00	None	.3109	.0189	.3402	.0204
		3/5	.1062	.0245	.2179	.0274
		5/9	.1389	.0265	.1481	.0265
		13/25	.0644	.0162	.0386	.0187
	0.67	None	.3633	.0186	.3788	.0096
		3/5	.2744	.0262	.2836	.0141
		5/9	.2186	.0331	.2225	.0223
		13/25	.1238	.0288	.0913	.0206
	0.50	None	.4104	.0160	.4281	.0232
		3/5	.3419	.0314	.3607	.0377
		5/9	.3003	.0296	.3172	.0530
		13/25	.2180	.0377	.2157	.0856
	0.25	None	.4527	.0188	.4599	.0182
		3/5	.4118	.0332	.4212	.0386
		5/9	.3916	.0487	.4028	.0496
		13/25	.3393	.0461	.3496	.0662

Table 3. Simulated data based upon 10 trials. Entries in the table are the probabilities of misclassification. In the absence of any other decision rule, a nearest neighbor rule is used. The probabilities under the "With Boundary" heading relate to the actual data of Figs. 1 and 2, while the other probabilities are based upon trials using the same random noise, but with all points interior to a single region. "Noise ratio" refers to the signal to noise ratio as defined in the text.

Fig. 1. Data set used for simulations shown in Table 3.



### 3. Weighted k by k mean

This allows for weighting the points in a k by k neighborhood to take into account the fact that more distant points should not have the same effect as closer ones.

### 4. k by k median

This outputs the median value of a k by k neighborhood centered around each point of A.

### 5. k by k mode

The output of this filter is the most frequently occurring value within a k by k neighborhood centered on each point. In case of a tie, the median of the tied values is used.

## B. THINOUT

The input here is the output of whatever prefilter is being used. It begins by removing a border around the picture. The width of this border depends upon the size of the window to be used in C. This function produces a preliminary assignment of clusters based upon a histogram analysis. It does a frequency count on the values occurring in the interior of A; i.e., those values that are not in the removed border. It then removes those values that either occur entirely in the border, or which do not have frequent occurrence. A parameter can be set so that THINOUT removes all but a certain number of clusters, or else all that have a frequency of occurrence that is below some fixed percentage of the total number of points. The default setting is (.02)mn. Points are reassigned to the nearest remaining value. For ordinal data one proceeds on ranks rather than on actual values.

## C. MEASURES OF DISPERSION

At this point the data has had a preliminary assignment to clusters. One wants to establish a spatial criterion for the removal of clusters. Since the goal is to produce connected subregions of the plane, the idea is to remove those clusters that are the most scattered on the basis that they are least likely to lie entirely within one of the desired regions  $R_1, \dots, R_t$ . Though no assumption is made directly as to the distribution of the values of  $F$ , the procedure is nonetheless based upon the distribution of a normal random variable. The closer a cluster is to the expected value of one of the regions, the more likely it is to have a low amount of scattering in the plane. Each of the measures of scatter looks at a k by k window centered upon a given pixel. For that reason the scatter cannot be computed for the outermost rows and columns, where j is the greatest positive integer under k/2. This is the restriction that was mentioned at the beginning of B. Here then are the various measures of scatter that relate to a fixed cluster  $C_j$ .

### 1. Nondirected dispersion

For each point in  $C_j$ , one looks at a k by k neighborhood centered on that point, and counts up the number of members of that neighborhood that are not

in  $C_i$ . One sums these numbers up over all points in  $C_i$ , and divides by the number of neighborhoods times  $k^2 - 1$  to obtain the empirical probability that a point in  $C_i$  will have a neighbor in a  $k$  by  $k$  neighborhood that does not belong to  $C_i$ . This is used as a measure of the scatter of the cluster  $C_i$ .

## 2. Rectangularly directed dispersion

The nondirected dispersion measure treats boundary points in much the same way that it does noise. Thus if the cluster  $C_i$  has a long boundary, it will tend to have a high nondirected dispersion, even though it may itself not be scattered. One can compensate partially for this by looking at directional versions of the dispersion measures. The idea is that noise should look like noise in all directions, whereas boundary points of a cluster will have a direction in which they do not appear noisy (the direction of the cluster to which they bound). This measure is identical to the nondirected dispersion except that at each point in  $C_i$ , it takes the minimum of the number of points not in  $C_i$  in each of the 4 subregions of the  $k$  by  $k$  neighborhood lying to the North, South, East and West of the given point.

## 3. Diagonally directed dispersion

This is the same as 2 except that the 4 directions chosen are the 4 diagonal directions.

## 4. Fully directed dispersion

Here the minimum is taken over all 8 directions.

Tables 4 through 7 illustrate the operation of the nondirected dispersion in locating the expected value of a region  $C_i$ , given the output of  $G$ . Tables 4, 5, 6 contain data based upon 3 by 3, 5 by 5, and 7 by 7 prefilters acting on Gaussian noise, while the data in Table 7 comes from uniform noise. Note how the values of the dispersion increase as one gets further away from the expected value of 0. The prefilters that seem especially effective are called the MM and MMM filters. These are 3 by 3 mean filters iterated twice and three times. These are examples of weighted  $k$  by  $k$  filters. A careful description of them occurs in Janowitz [4] as well as Rosenfeld and Kak [7].

## D. THE CLUSTERING CYCLE

With the given input matrix  $A$ , all of the clustering algorithms follow the same general format. There are two initial parameters CHOS and THRS that will be explained in the body of the description:

1. Apply an appropriate prefilter to  $A$ , and let  $B$  denote its output.

2. Apply THINOUT to  $B$ . Here CHOS is the parameter that determines the number of clusters that are outputted by THINOUT. At this point, we have preliminary clusters  $C_1, C_2, \dots, C_s$  that are determined by the numbers  $c_1, c_2, \dots, c_s$ . The idea is that cluster  $C_i$  consists of those points whose distance from  $c_i$  is

SD	WIDTH	FILTER	LEVEL								
			0	1	2	3	4	5	6	7	8
2	0	Mean	.386	.566	.965	1					
		Med	.066	.312	1	1					
2	1	Mean	.028	.134	.468						
		Med	.000	.007	.199						
4	0	Mean	.629	.692	.790	.873	.830	1	1		
		Med	.432	.539	.779	.927	.807	1	1		
4	1	Mean	.233	.280	.417	.605	.784	.928			
		Med	.015	.028	.137	.396	.749	.938			
4	2	Mean	.046	.090	.209	.391	.631				
		Med	.000	.002	.023	.119	.404				
6	1	Mean	.391	.420	.480	.562	.623	.734	.812	.885	.948
		Med	.072	.093	.178	.314	.380	.637	.755	.952	1
6	2	Mean	.171	.181	.266	.379	.512	.593	.697	.774	
		Med	.008	.007	.030	.098	.264	.383	.575	.728	

Table 4. Average dispersion based on 4 trials on 30 by 30 matrix with normal distribution having mean 0 and indicated SD. Mean is a 3 by 3 mean filter and Med a 3 by 3 median filter. Level i with width k merges levels i-k,...,i,...,i+k into a single cluster before computing the dispersion.

SD	WIDTH	FILTER	LEVEL								
			0	1	2	3	4	5	6	7	8
2	0	Mean	.126	.608	1	1					
		MM	.003	.362	1	1					
2	1	Mean	.000	.054	.475						
		MM	.000	.001	.233						
4	0	Mean	.401	.484	.587	1	1	1	1		
		MM	.087	.189	.328	1	1	1	1		
4	1	Mean	.047	.119	.342	.644	.969	1			
		MM	.000	.020	.122	.500	1	1			
4	2	Mean	.001	.019	.126	.374	.614				
		MM	.000	.000	.011	.129	.385				
6	0	Mean	.531	.554	.644	.751	.969	1	1	1	1
		MM	.226	.279	.445	.672	1	1	1	1	1
6	1	Mean	.139	.209	.379	.553	.714	.975	1	1	1
		MM	.007	.032	.117	.349	.584	1	1	1	1
6	2	Mean	.028	.054	.161	.319	.503	.739	.979	1	
		MM	.000	.002	.026	.113	.257	.663	1	1	

Table 5. Average dispersion based on 4 trials on 30 by 30 matrix with normal distribution having mean 0 and indicated SD. Mean is a 5 by 5 mean filter and MM a 3 by 3 mean filter applied twice. See Table 4 for further explanation of symbols.

SD	WIDTH	FILTER	LEVEL								
			0	1	2	3	4	5	6	7	8
2	0	Mean	.050	.569	1	1					
		MMM	.001	.389	1	1					
2	1	Mean	.000	.015	.537						
		MMM	.000	.000	.329						
4	0	Mean	.243	.379	.919	1	1	1	1		
		MMM	.033	.096	1	1	1	1	1		
4	1	Mean	.004	.098	.410	.979	1	1			
		MMM	.000	.116	.179	1	1	1			
4	2	Mean	.000	.002	.057	.336	.979				
		MMM	.000	.000	.006	.116	1				
6	0	Mean	.401	.408	.515	.900	1	1	1	1	1
		MMM	.099	.104	.202	.800	1	1	1	1	1
6	1	Mean	.037	.137	.360	.734	1	1	1	1	
		MMM	.002	.020	.144	.607	1	1	1	1	1
6	2	Mean	.004	.031	.126	.324	.668	.948	1	1	
		MMM	.000	.001	.014	.089	.574	.917	1	1	

Table 6. Average dispersion based on 4 trials on 30 by 30 matrix with normal distribution having mean 0 and indicated SD. Mean is a 7 by 7 mean filter and MMM a 3 by 3 mean filter applied three times. See Table 4 for further explanation of symbols.

RANGE SIZE FILTER			LEVEL								
			0	1	2	3	4	5	6	7	8
4	3	Mean	.497	.582	.747	.975	1				
	5	Mean	.227	.469	.969	1	1				
	5	MM	.020	.204	1	1	1				
	7	Mean	.090	.475	1	1	1				
	7	MMM	.005	.254	1	1	1				
6	5	Mean	.380	.501	.682	1	1	1	1		
	5	MM	.084	.207	.425	1	1	1	1		
	7	Mean	.213	.406	1	1	1	1	1		
	7	MMM	.034	.173	1	1	1	1	1		
10	5	Mean	.562	.550	.643	.880	.925	1	1	1	1
	5	MM	.272	.283	.476	.938	.800	1	1	1	1
	7	Mean	.424	.407	.597	.953	1	1	1	1	1
	7	MMM	.120	.132	.418	1	1	1	1	1	1

Table 7. Average results of 4 trials on 30 by 30 matrix with uniform distribution having range from -RANGE to +RANGE using a SIZE by SIZE filter of the indicated type. See Table 4 for further explanation of symbols.



smaller than its distance from any  $c_j$  ( $j \neq i$ ). One can use actual distance or a weighted distance based upon a Bayes decision rule.

3. Select a suitable dispersion measure and compute the dispersion of each cluster  $C_1, \dots, C_s$ . The parameter THRSH contains the stopping rule for the algorithm. If THRSH is a positive integer, one stops when the number of clusters does not exceed THRSH. If THRSH is a fraction between 0 and 1, then one stops when the maximum dispersion of the clusters falls below THRSH. Thus at this point, one either stops or goes on to step 4.

4. A decision is made as to which clusters are to be removed. This can either be the cluster with the highest dispersion, all clusters having that highest dispersion, the  $i$  clusters having the  $i$  highest dispersions, or all clusters whose dispersion exceeds some fixed parameter with the parameter dropping at each cycle of the program. Ties are disposed of by taking the first cluster one reaches, and the default setting is to remove all clusters having the highest dispersion value. Various other rules can also be used.

5. Here is where the various algorithms differ. If cluster  $C_i$  is to be removed, then a decision must be made as to how to reallocate its members. This reallocation can either be done globally (option G) or locally (option L). The global option sends all members of  $C_i$  to the same place, while the local option operates on a point by point basis. There are two basic techniques for this, leading to a total of 4 different rules.

ANEXT(G) would assign cluster  $C_i$  to the next higher or lower available cluster according to whether its label  $c_i$  is above or below the average of the labels of those two clusters. ANEXT(L) would do the same thing on a point by point basis. A member of  $C_i$  would be assigned to the next higher or lower cluster according to whether its B-value is above or below the average of the labels of these clusters. The technique can be modified by using cluster means as labels as opposed to the original labels  $c_1, \dots, c_s$ .

ANEAR(G) at each stage computes the means of all clusters that exist. It then reassigns  $C_i$  to the cluster to which it is closest. ANEAR(L) does the same thing on a point by point basis. Each point in  $C_i$  is assigned to that remaining cluster to which its B-value is closest.

Ordinal cluster techniques result when the input data is rank ordered; the ANEXT technique when it operates with cluster labels is also ordinal. The remaining techniques are essentially numeric.

#### IV. SOME SIMULATIONS

Having described the algorithms, we turn now to an examination of how well they perform on artificial data. The underlying regions are shown in Fig. 4. The function  $F$  was constructed by assigning values of 40, 55 and 60 to the three regions indicated therein.  $G$  was then constructed by adding various types of Gaussian and uniform noise to  $F$ . Table 8 contains the results of the simulations.



SD	Filter	Fraction correct		Dispersion cutoffs			
		Method 1	Method 2	Method 1		Method 2	
0	3 by 3 mean	.969	.969	.088	.440	.088	.440
	5 by 5 mean	.905	.929	.098	.347	.091	.285
	7 by 7 mean	.855	.857	.104	.210	.104	.245
	MM	.962	.965	.091	.421	.093	.501
	MMM	.922	.922	.097	.239	.097	.284
5	3 by 3 mean	.907	.922	.180	.406	.137	.610
	5 by 5 mean	.889	.901	.098	.256	.077	.372
	7 by 7 mean	.866	.866	.096	.239	.096	.282
	MM	.927	.938	.098	.270	.096	.337
	MMM	.924	.938	.097	.217	.117	.272
10	3 by 3 mean	.737	.757	.345	.477	.323	.477
	5 by 5 mean	.799	.800	.224	.314	.178	.377
	7 by 7 mean	.826	.826	.176	.294	.176	.247
	MM	.800	.806	.186	.302	.196	.302
	MMM	.800	.800	.149	.326	.149	.340
15	3 by 3 mean	.683	.463	.433	.598	.437	.433
	5 by 5 mean	.751	.821	.221	.398	.271	.319
	7 by 7 mean	.760	.868	.160	.258	.144	.321
	MM	.774	.767	.273	.480	.263	.375
	MMM	.812	.822	.194	.347	.171	.244
5*	3 by 3 mean	.959	.956	.100	.438	.103	.425
	5 by 5 mean	.918	.905	.076	.375	.097	.431
	7 by 7 mean	.851	.868	.110	.231	.110	.280
	MM	.922	.946	.092	.335	.092	.360
	MMM	.922	.919	.096	.341	.097	.368
10*	3 by 3 mean	.882	.886	.203	.419	.203	.419
	5 by 5 mean	.880	.868	.125	.280	.120	.361
	7 by 7 mean	.860	.860	.108	.237	.108	.277
	MM	.891	.903	.103	.292	.124	.326
	MMM	.891	.893	.118	.259	.109	.401
15*	3 by 3 mean	.722	.790	.354	.493	.301	.421
	5 by 5 mean	.865	.873	.192	.380	.148	.375
	7 by 7 mean	.837	.862	.122	.315	.106	.358
	MM	.854	.858	.219	.311	.185	.371
	MMM	.866	.822	.179	.304	.177	.324
20*	3 by 3 mean	.783	.753	.252	.517	.330	.471
	5 by 5 mean	.833	.793	.165	.375	.149	.458
	7 by 7 mean	.812	.802	.244	.266	.158	.293
	MM	.816	.816	.197	.420	.197	.413
	MMM	.835	.841	.195	.355	.162	.414

Table 8. Fraction correct classification for data in Fig. 4 using indicated prefilters. See text for explanation of prefilters and cluster methods. The dispersion was a nondirected 3 by 3 dispersion. The left hand figure indicates the result with 3 clusters, while the right hand figure is that for 4 clusters. The top data set is the original data, while the next three relate to Gaussian noise with the indicated standard deviation. The symbol  $k^*$  refers to a uniform distribution from  $-k$  to  $k$ .

It used 2 cluster methods: Method 1 was ANEXT(L) and Method 2 ANEAR(L). In each case CHOS was set at .02. Notice that for Gaussian noise, Method 1 seems to work consistently better than Method 2, while for uniform noise the verdict is mixed. The dispersion cutoffs are included to show the rather dramatic drop in the dispersion value once the program arrives at the correct number of clusters. Tables 9 through 11 contain step by step graphic representations of the manner in which the nondirected and rectangularly directed 3 by 3 dispersions behave as the clustering process proceeds. The cluster routines are ANEAR(L), and the data is a 20 by 20 matrix. Table 9 is for data having a normal distribution with expected value 20 and standard deviation 4, while Table 10 is normal with expected value 30 and SD = 8; the data for Table 11 is a mixture of two normal distributions, each with SD = 4; the top half of the data matrix had expected value 30, and the bottom half expected value 20. The parameters for the clustering process involve the use of a 3 by 3 special mean filter with CHOS set at .02 and THRS set so as to produce 6,5,4,3 and 2 clusters. The display labelled THINOUT shows the dispersions for the input to the THINOUT function. Notice the dramatic dropoff in dispersion in Table 11 when the proper number of clusters is reached, as opposed to the situation in Tables 9 and 10, where the values of the dispersion would quite properly tell that there is only one cluster in the data.

## V. LOW RESOLUTION SUMMARIES OF DIGITAL PICTURES

The problem of cataloging and summarizing the content of a large number of digital pictures is nontrivial. Naturally, one can simply produce the indicated pictures and store them, but this is an expensive process. Another method involves the use of low resolution line printer summaries. The use of such summaries also cuts down dramatically the cost of applying sophisticated image segmentation techniques to such data sets. This will be illustrated with some pictures in the next section, but here we will look at some line printer results, and see a possible application to target detection. The data are from the Westinghouse FLIR data base that was kindly supplied by Bruce Schachter. Each record consists of a 128 by 128 digital picture, and a 24 by 24 summary was produced using a 10 by 10 window that moves 5 units at a time. Thus the (1,1) position of the output is the mean of the 10 by 10 region in the upper left corner of the original record; the (1,2) position would come from a region being translated 5 units to its right, etc.

This type of low resolution picture followed by an image segmentation algorithm has some application as a target detector. The low resolution picture itself is probably too busy for a target selection algorithm to quickly work; however, in the segmented version, one can just write a program that will locate the center of those connected subregions that are in the highest (or lowest) level cluster of the output. The result is sometimes useful, as shown by Table 12. It should be noted though that these results are only indications of possible use. Much work needs to be done before a good working version of the algorithm can be produced. Simple outputs are shown in Fig. 5.

## VI. REAL DATA ANALYSIS

This final section deals with the segmentation algorithms applied to real data. There are two sources for the data: Bruce Schachter's Westinghouse FLIR data base, and satellite data (SMS II) showing the North Atlantic region of May 5, 1980. This latter tape was supplied by Robert Myers of the Air Force Geophysical Laboratory. Most of the plates are self-explanatory, but a few comments may still be in order.

**NORMAL DISTRIBUTION WITH EXPECTED VALUE 20.  
OUTPUT OF NONDIRECTED AND DIRECTED DISPERSIONS  
AT VARIOUS STAGES OF CLUSTER PROCESS**

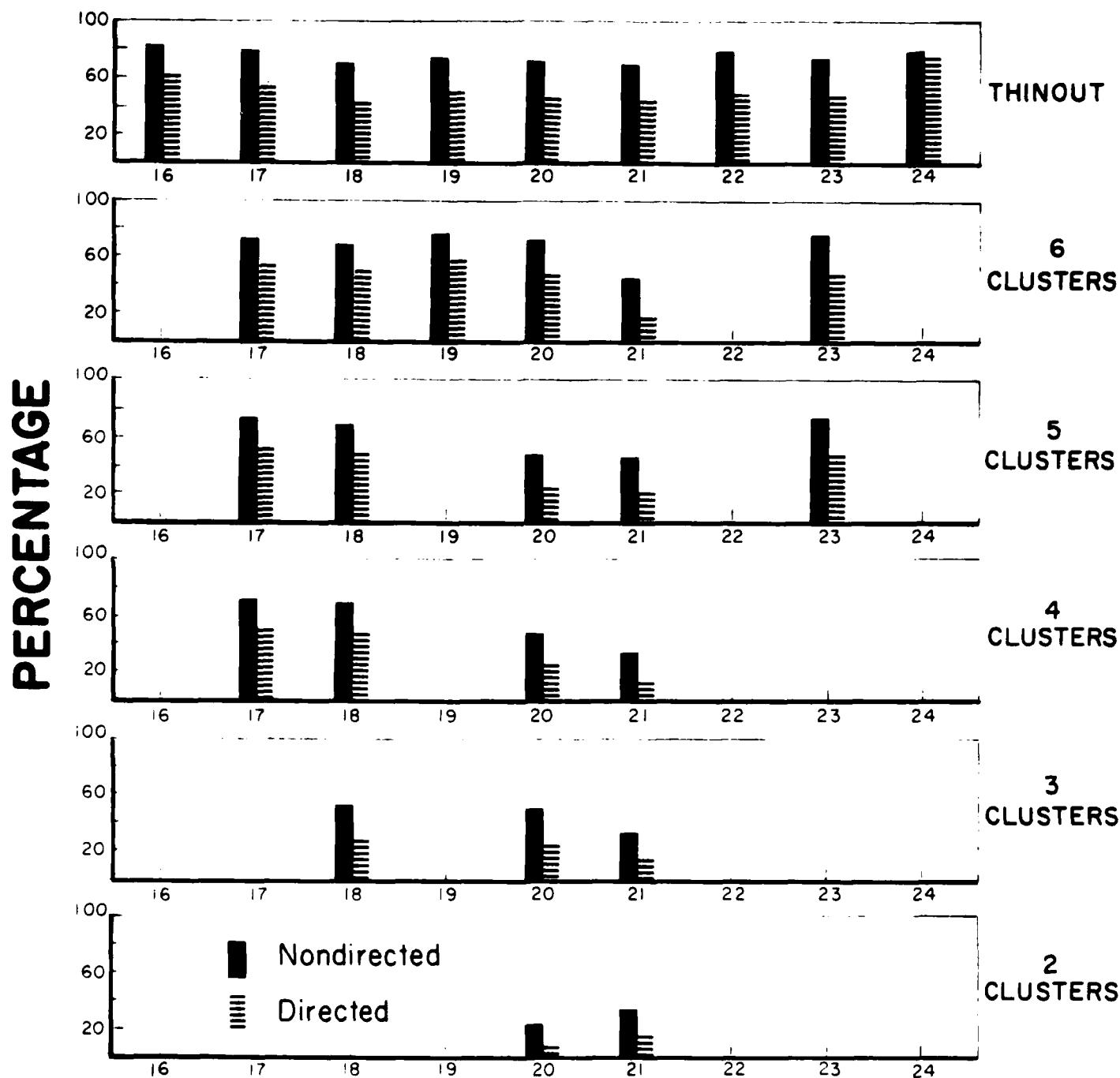


Table 9. See text for explanation.

**NORMAL DISTRIBUTION WITH EXPECTED VALUE 30.  
OUTPUT OF DIRECTED AND NONDIRECTED DISPERSIONS  
AT VARIOUS STAGES OF CLUSTER PROCESS**

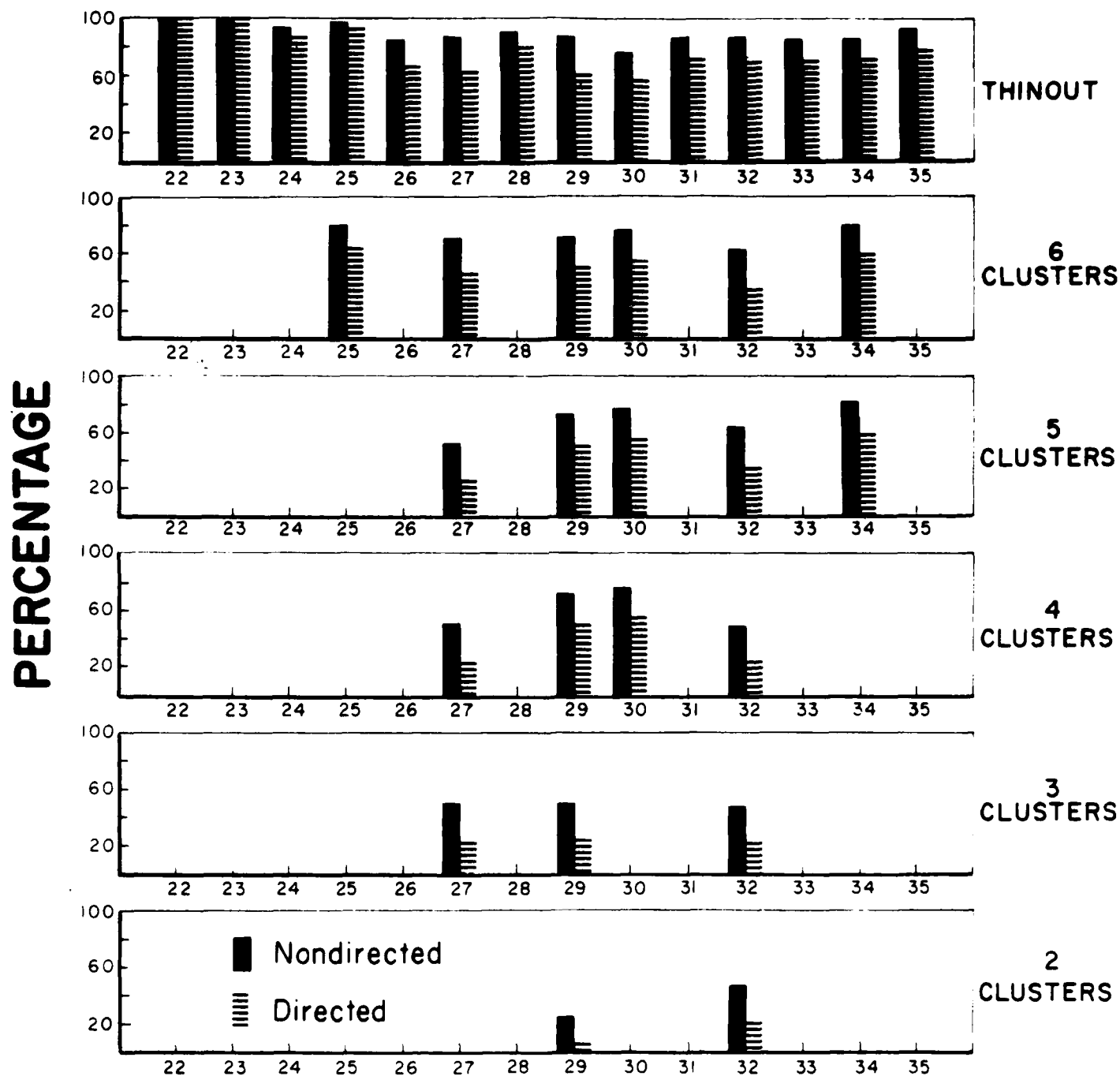


Table 10. See text for explanation.

**MIXTURE OF 2 NORMAL DISTRIBUTIONS WITH EXPECTED VALUES OF 20 AND 30. OUTPUT OF NON-DIRECTED AND DIRECTED DISPERSIONS AT VARIOUS STAGES OF THE CLUSTERING PROCESS**

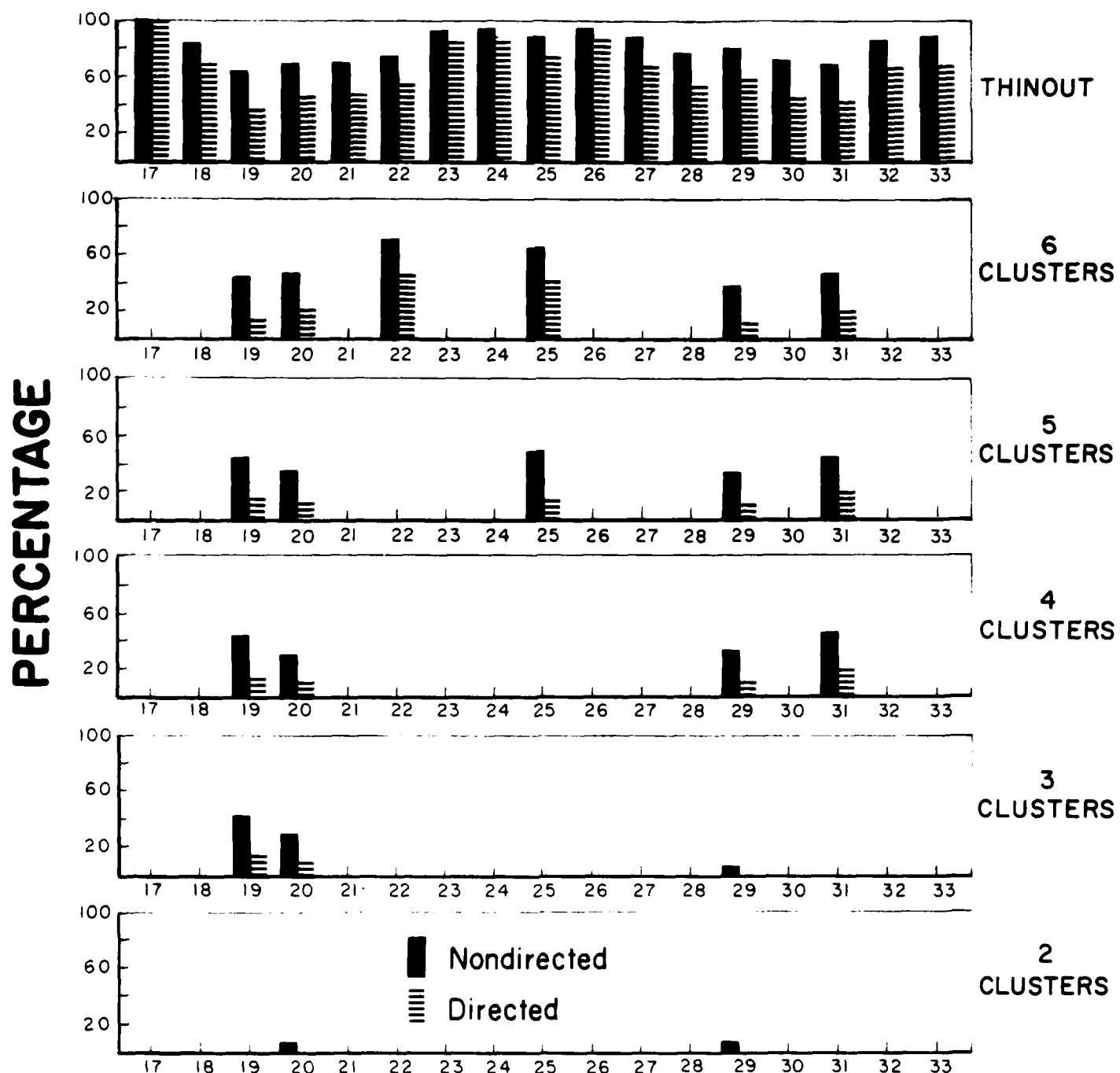


Table 11. See text for explanation.

Image	Estimated coordinates		Actual coordinates	
12	39	36	36.5	35.5
	39	93	36.5	92.5
	90	36	91.5	35.5
	90	93	91.5	92.5
13	39	39	40.5	37
	39	90	40.5	91
	87	39	87.5	37
	87	90	87.5	91
14	33	39	31	36
	33	87	31	92
	96	39	97	36
	96	87	97	92
15	30	39	28.5	40
	30	90	28.5	88
	99	39	99.5	40
	99	90	99.5	88
16	27	39	28.5	42
	30	87	28.5	86
	99	42	99.5	42
	99	87	99.5	86
17	36	30	36	31.5
	39	96	36	96.5
	93	33	92	31.5
	93	93	92	96.5
18	45	39	42	36
	45	87	42	92
	84	39	86	36
	84	90	86	92

Table 12. Estimated coordinates of targets on Westinghouse FLIR data using 12 by 12 window. Actual coordinates are as provided by Westinghouse.



[illegible][illegible]

21

Plates 1 through 6 are from the AFGL tape, and the remaining plates from the Westinghouse FLIR data. The use of low resolution summaries of data is shown in Plates 4,5,14,16,18,21 and 22. Several of the plates show the effect of adding varying amounts of Gaussian noise to the original data set. Similar work was done with uniform noise, but the results are not included here. Plates 19 through 22 are worthy of further explanation. The noise in each of them has standard deviation 5.4. Plate 19 uses white noise, but Plate 20 introduces a pattern to the noise. The pattern comes as follows: corresponding to each pixel in the original image, there is an integer randomly chosen from 1,2 and 3. If this integer is 1, then the noise at that pixel is left as is; for a value of 2, the noise is spread over a 2 by 2 region with the given point at its upper left corner; for a value of 3, the noise is spread over a 3 by 3 region. The resulting noise has a correlation of 0.67 between adjacent columns and one of 0.36 between columns separated by a single unit.

In the presence of a fair amount of noise, the segmentation programs will on occasion be influenced more by the noise than by the signal. One way to test for this is to take the cluster output for a fairly high number of regions, and subtract it from the prefilter output. One then takes the absolute value of this difference and applies a segmentation algorithm to it. What appears is a picture of what was originally suppressed. Plates 23 and 24 illustrate this technique for the data of Plates 19 and 20. Notice how clearly the central portion of the tank in the picture emerges. This technique will be more fully explored in a later paper.

#### REFERENCES

- [1] Bryant, Jack, On the clustering of multidimensional pictorial data, Pattern Recognition 11 (1979), 115-125.
- [2] Coleman, Guy B. and Andrews, Harry C., Image segmentation by clustering, Proc. IEEE 67 (1979), 773-785.
- [3] Gerson, D., Khedouri, E. and Gaborski, P., Locating ocean fronts using digital satellite temperature data and automated pattern analysis. Gulf Stream 5 (1979), 3-7.
- [4] Janowitz, M. F., Cluster analysis algorithms for image segmentation, University of Massachusetts Technical Report J8102, 1981.
- [5] \_\_\_\_\_, A model for ordinal nonhierarchical cluster methods, University of Massachusetts Technical Report J8103, 1981.
- [6] Lee, J. S., Digital image smoothing and the sigma filter, to appear.

Acknowledgement. The computer programs used for this work were designed and written by James Weigang.

The research effort was supported by ONR Contract N00014-79-C-0629.

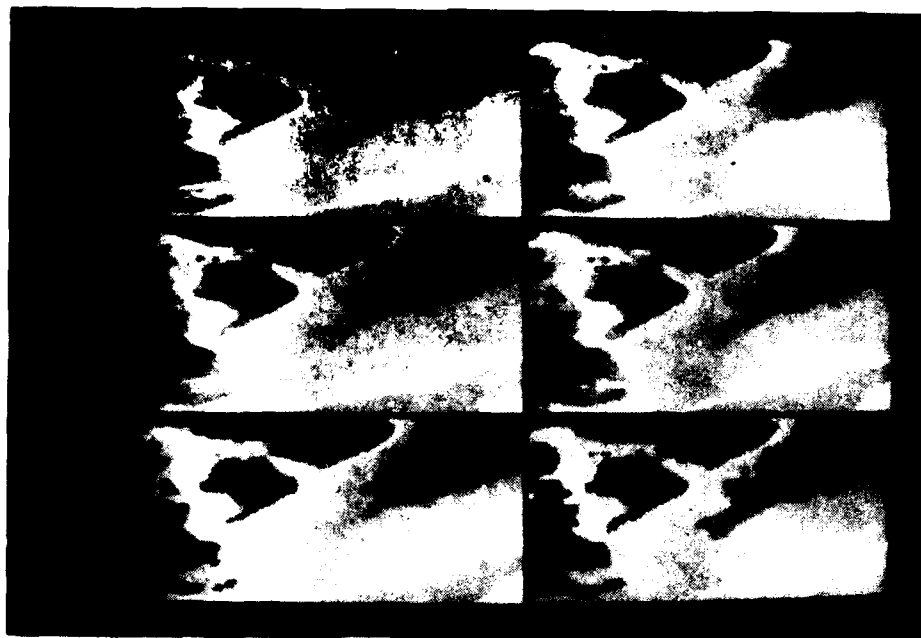


Plate 1. Chesapeake Bay Area. Pictures show original data, 3 by 3 mean filter, 17, 11, 9, and 6 regions. Cluster method is ANEAR (G).

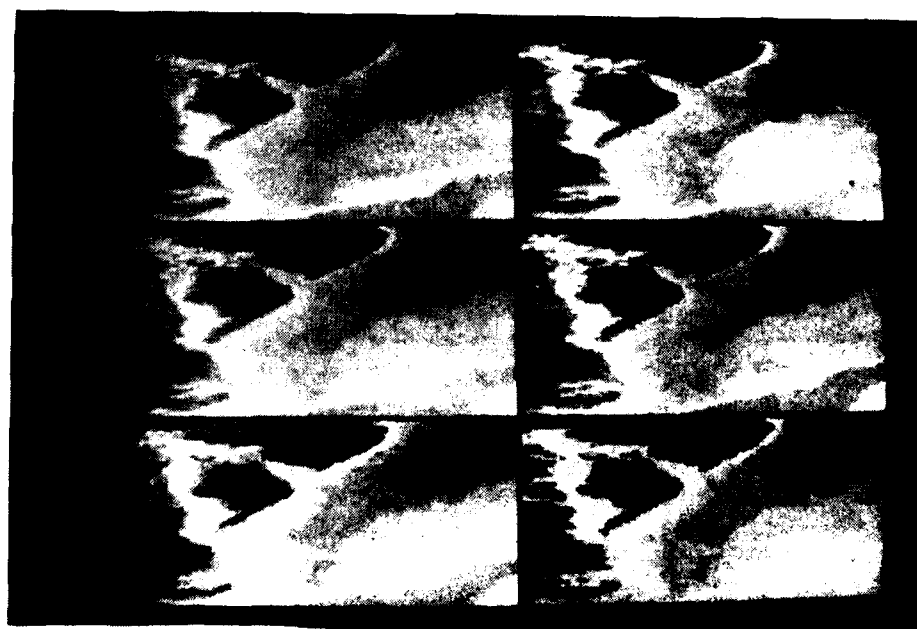


Plate 2. Chesapeake Bay Area. Pictures show original data twice followed by 17, 11, 9, and 6 regions. Cluster method is ANEAR (G) using no prefilter.

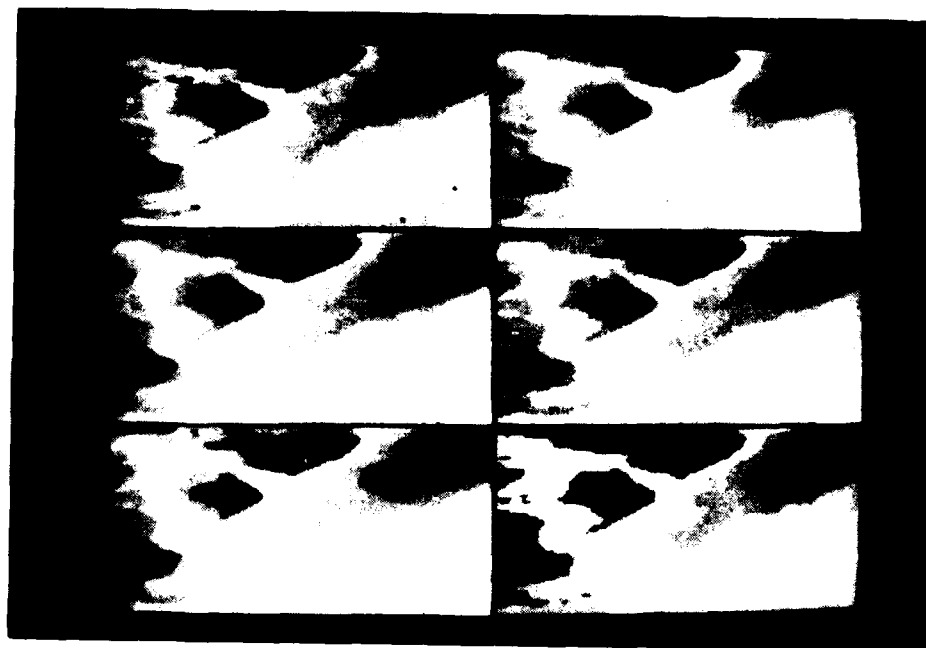


Plate 3. Chesapeake Bay Area. Pictures show original data, 3 by 3 median filter, 17, 11, 9, and 6 regions. Cluster method is ANEAR (G).

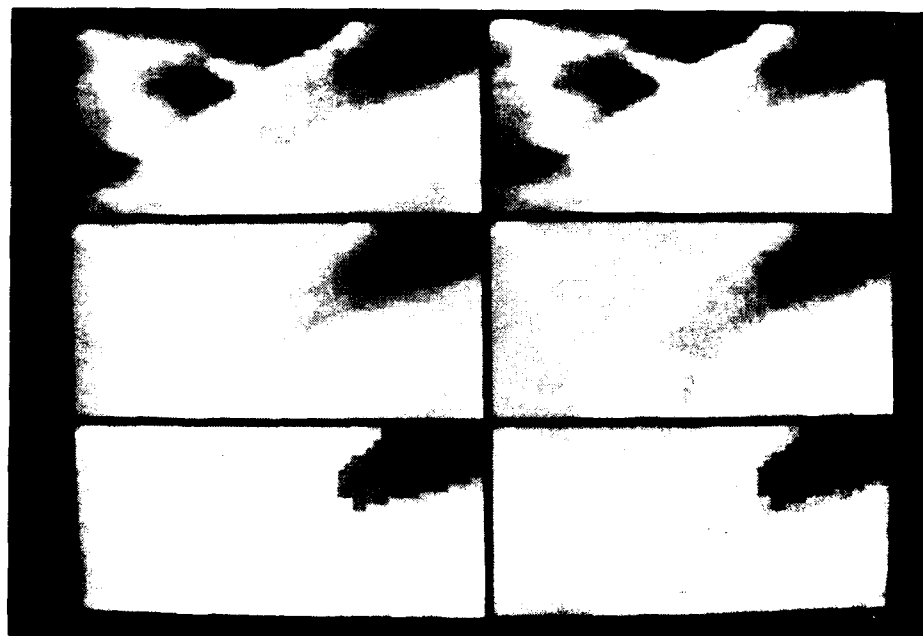


Plate 4. Data is 4 by 4 moving window applied to data of Plate 1. Pictures show original data twice, followed by 17, 11, 9, and 6 regions. Cluster method is ANEAR (L)

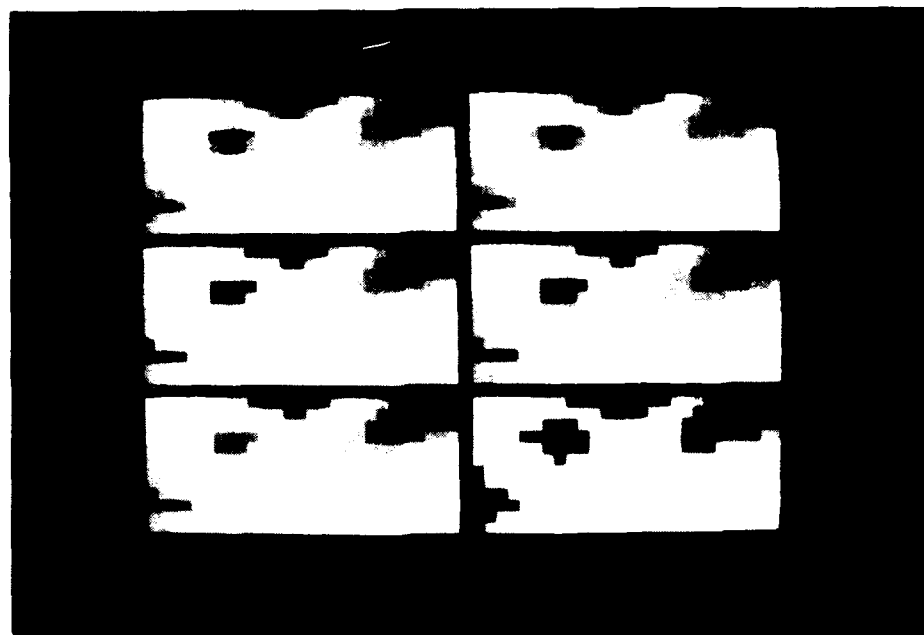


Plate 5. Data is 8 by 8 moving window applied to data of Plate 1. Pictures show original data twice, followed by 17, 11, 9, and 6 regions. Cluster method is ANEAR (L).

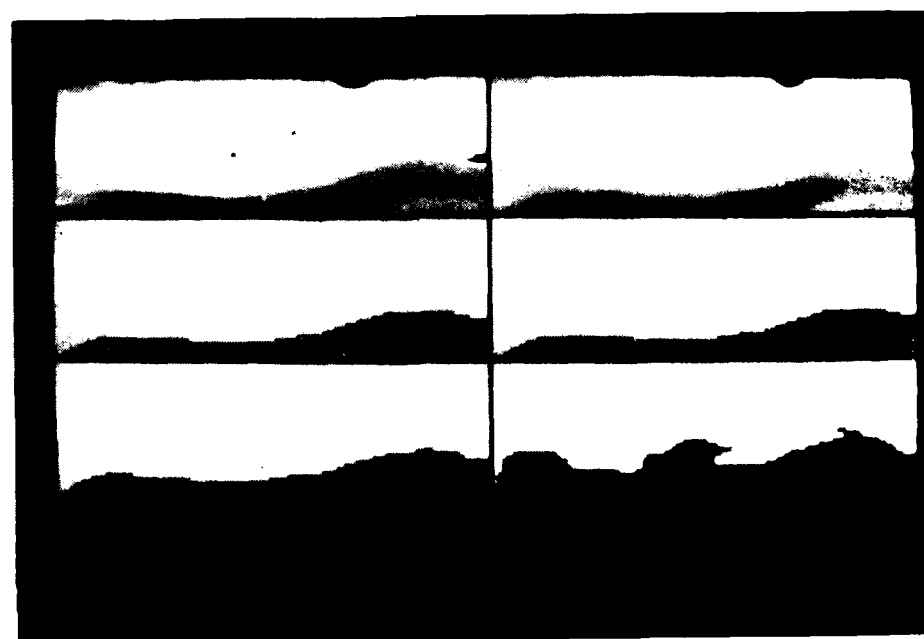


Plate 6. Edge of warm ocean front. Pictures show original data, 3 by 3 mean filter, 8, 6, 4, and 3 regions. Cluster method is ANEAR (L).

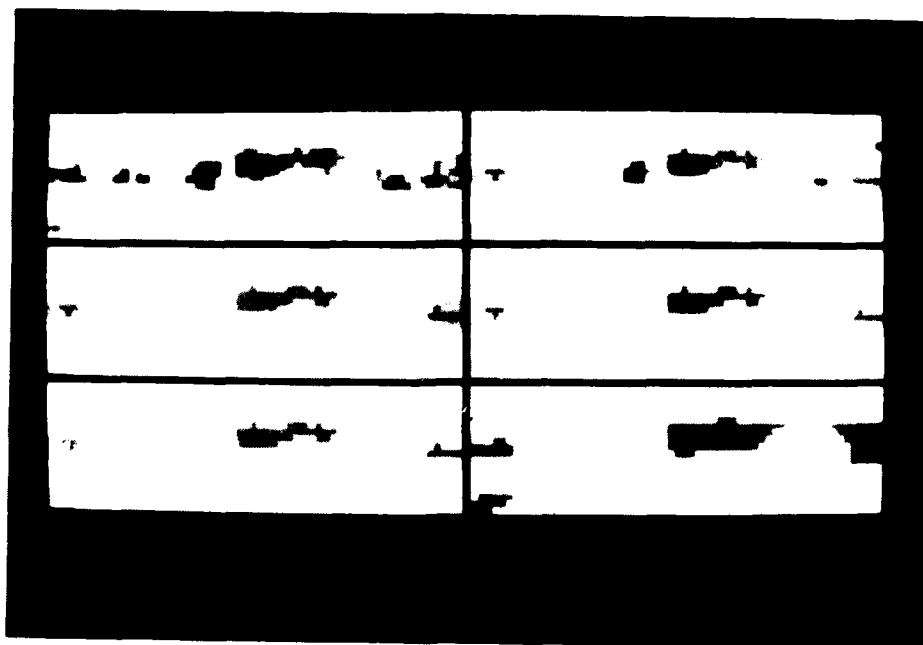


Plate 7. Portion of Record 67 of FLIR data tape. Pictures show original data, 3 by 3 mean filter, 8, 6, 4, and 3 regions. Cluster method is ANEAR (L).

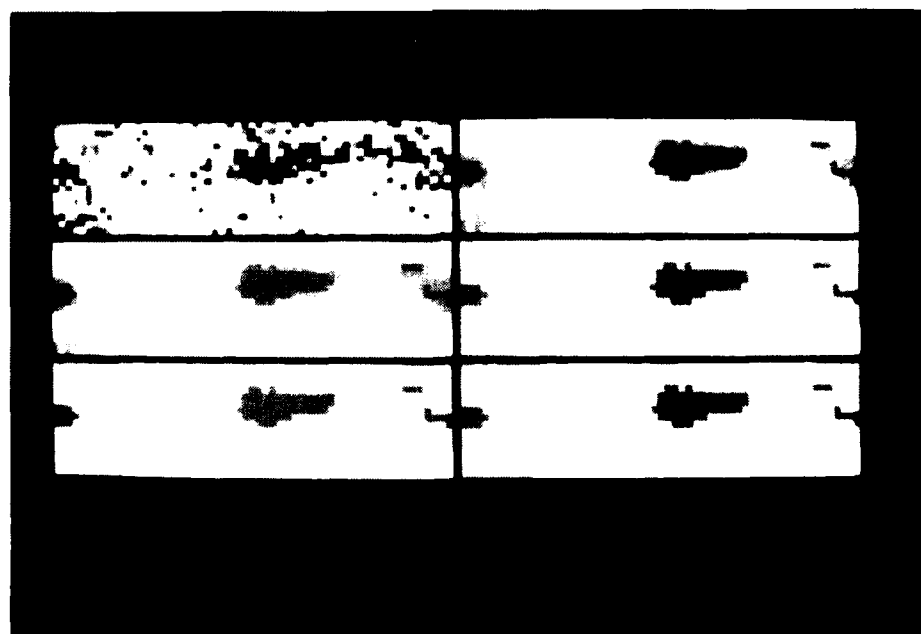


Plate 8. Data and pictures as in Plate 7, but with additive Gaussian noise having standard deviation 4.

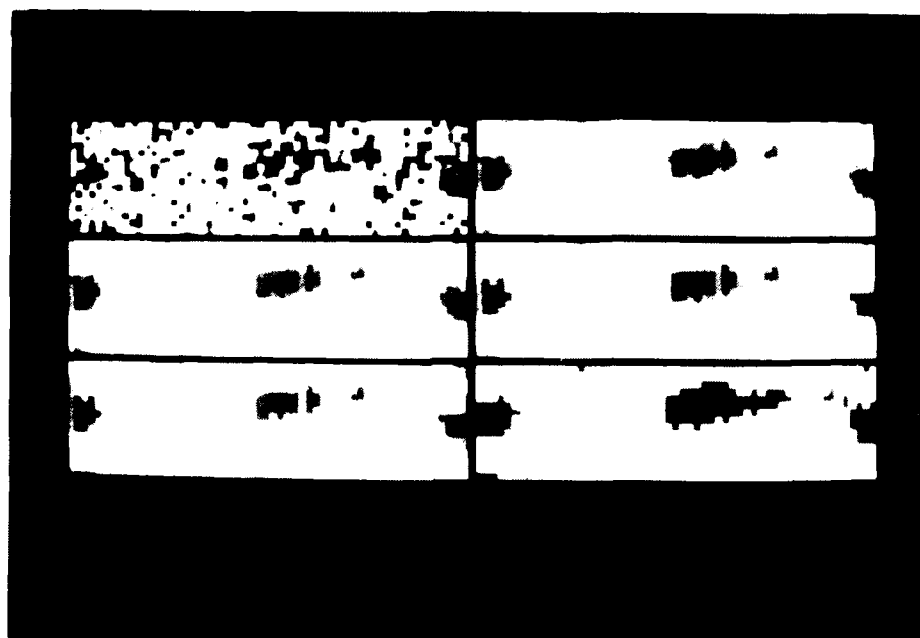


Plate 9. Data and pictures as in Plate 7, but with additive Gaussian noise having standard deviation 8.

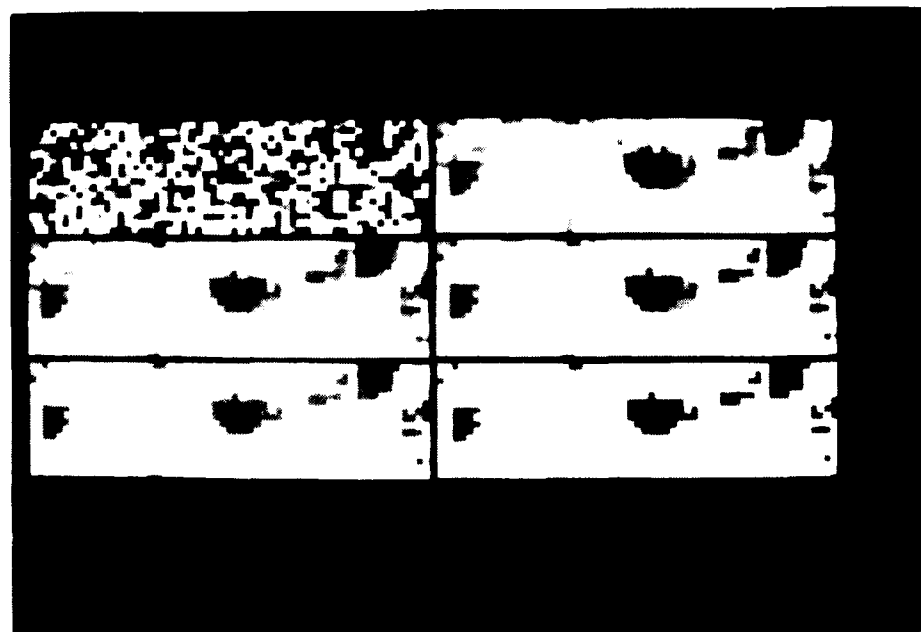


Plate 10. Data and pictures as in Plate 7, but with additive Gaussian noise having standard deviation 16.

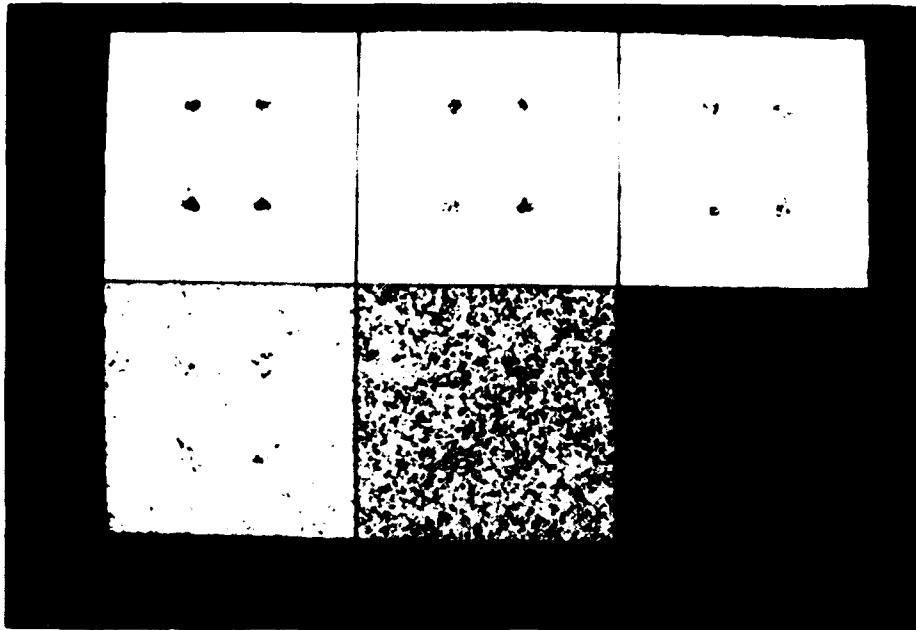


Plate 11. Record 25 of FLIR data tape. Pictures show original data, followed by addition of Gaussian noise having standard deviation of 1, 4, 8, and 16.

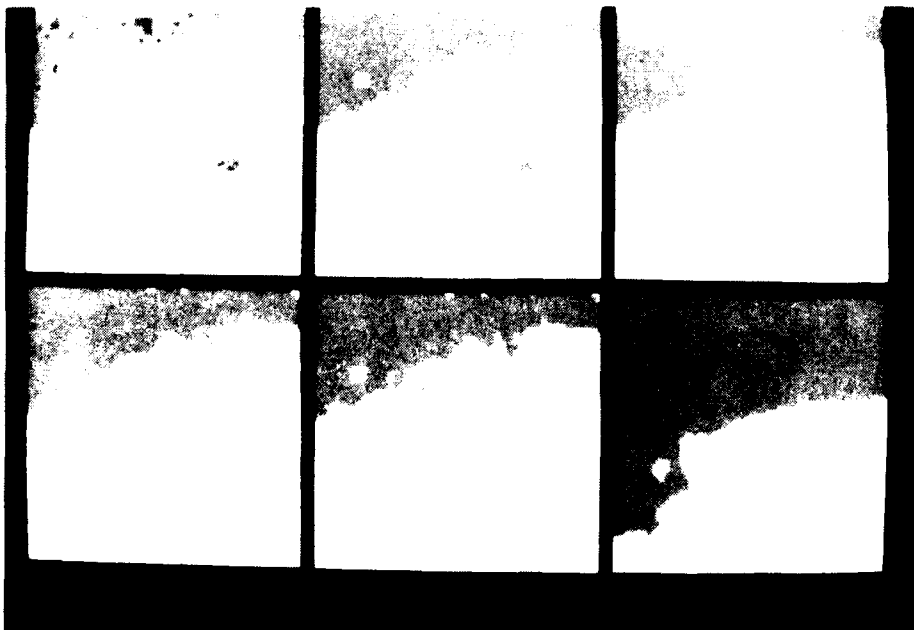


Plate 12. Upper left quarter of Record 25 of FLIR tape. Pictures show original data, 5 by 5 mean filter, 8, 6, 4, and 3 regions. Cluster method is ANEAR (L).



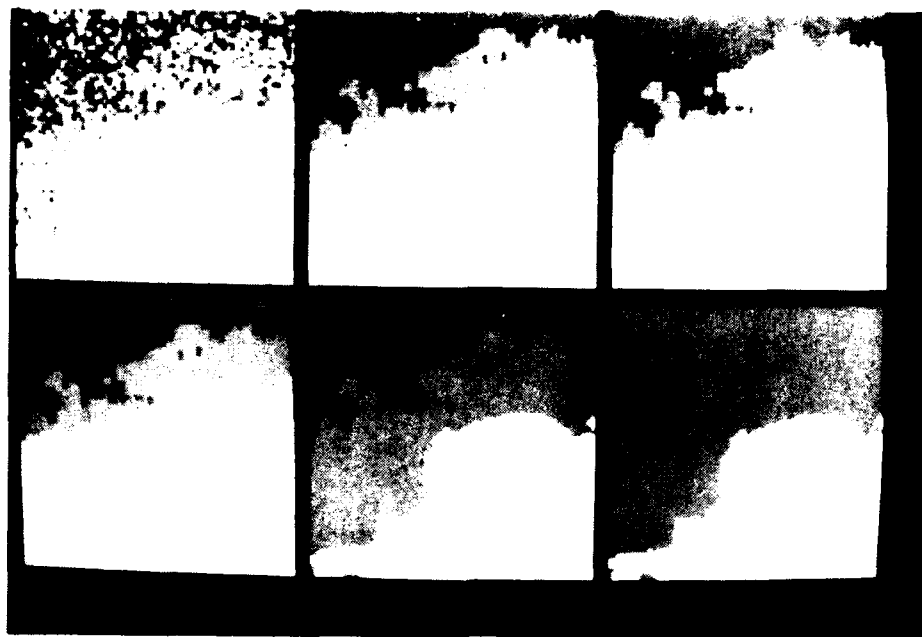


Plate 13. Same as Plate 12 except with Gaussian noise having standard deviation 4.

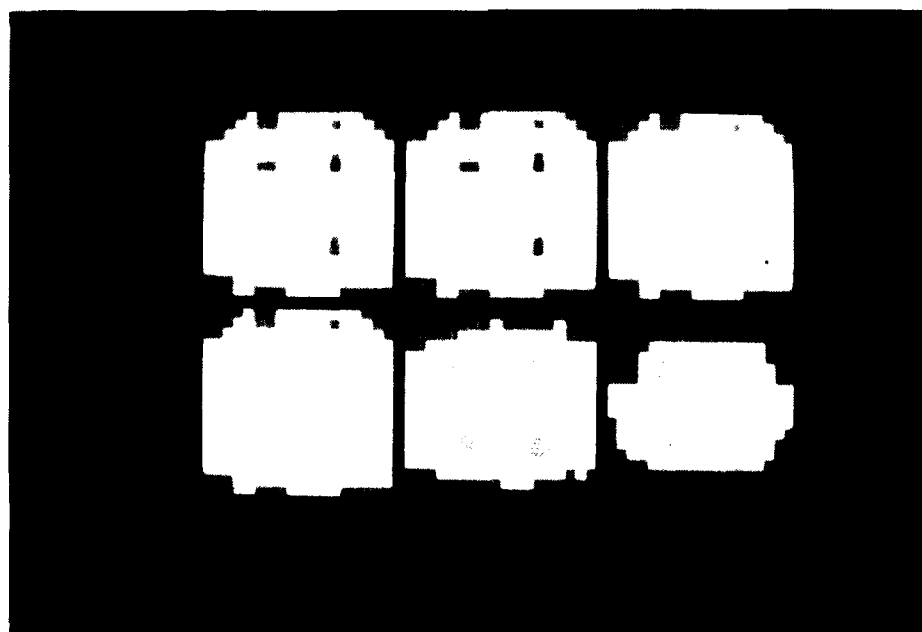


Plate 14. Record 25 with Gaussian noise having standard deviation 4. Data is 8 by 8 moving window. Pictures show original data twice, 8, 6, 4, and 3 regions. Cluster method is ANEAR (L) with no prefilter.



Plate 15. Same as Plate 12, except with Gaussian noise having standard deviation 8.

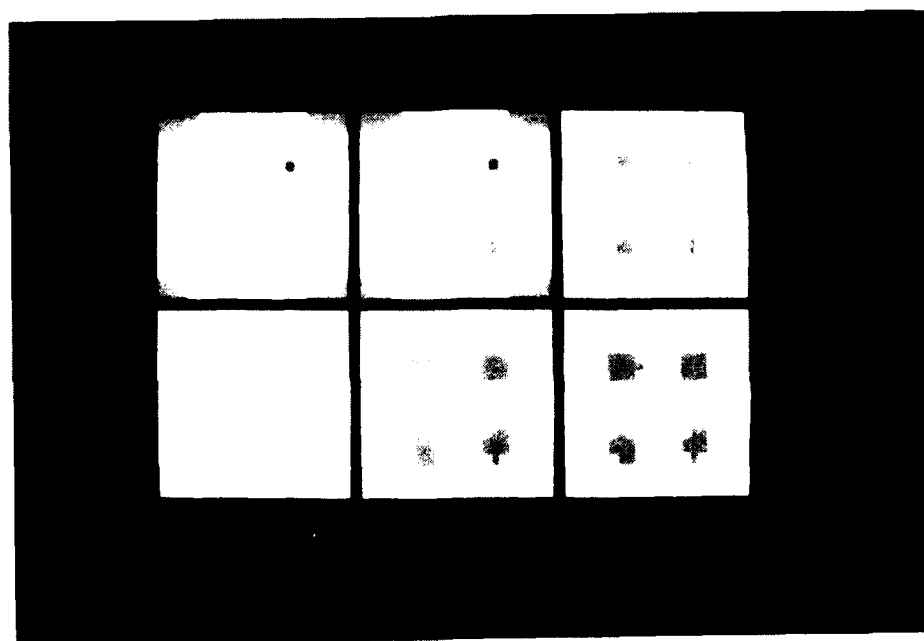


Plate 16. Same as Plate 14, except Gaussian noise has standard deviation 8.



Plate 17. Same as Plate 12, except with Gaussian noise having standard deviation 16.

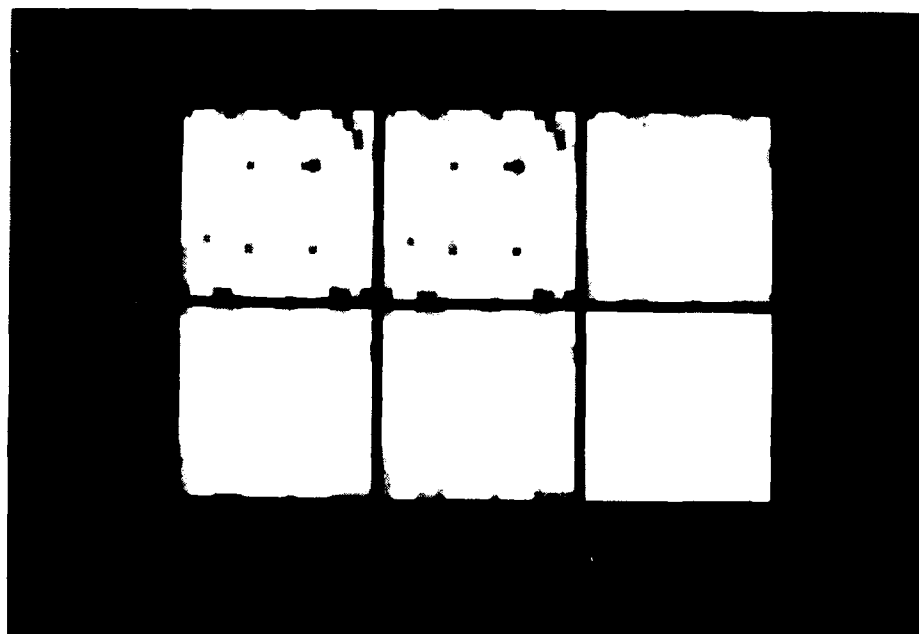


Plate 18. Same as Plate 14, except the Gaussian noise has standard deviation 16.

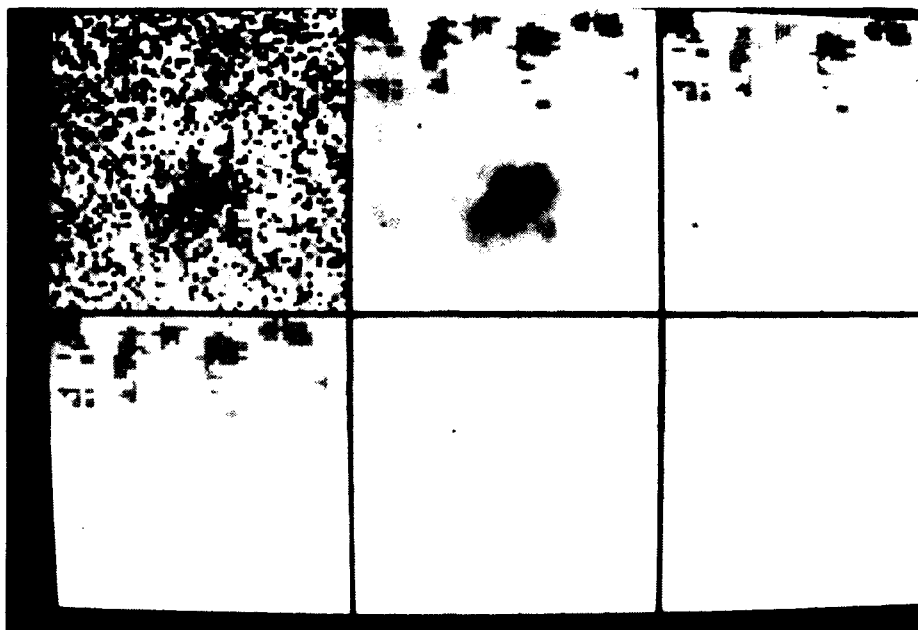


Plate 19. Same as Plate 12, except with Gaussian noise having standard deviation 5.4.

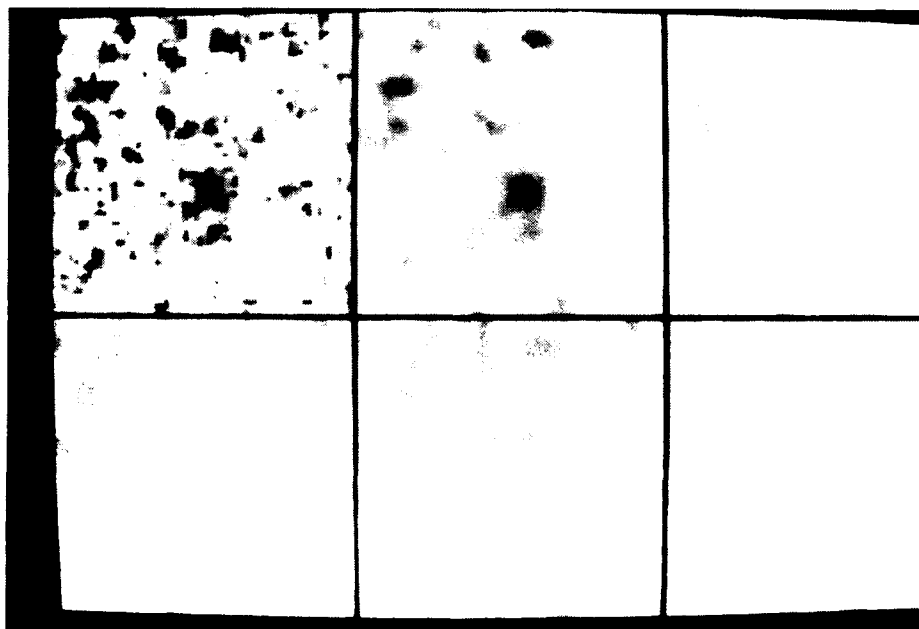


Plate 20. Same as Plate 12, but with patterned noise added. The standard deviation of the noise is 5.4.

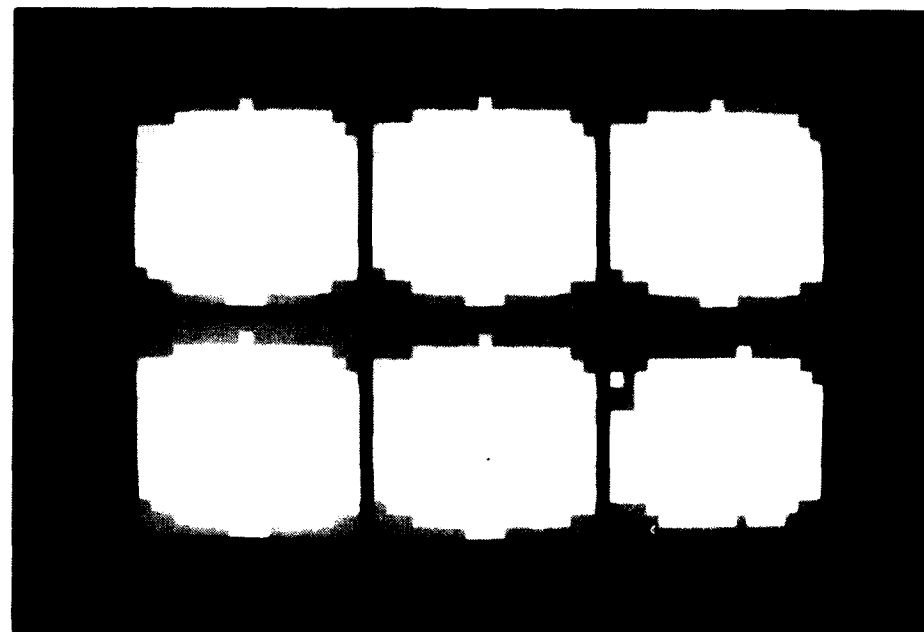


Plate 21. 8 by 8 moving window on data from Plate 19.  
Format follows Plate 14.

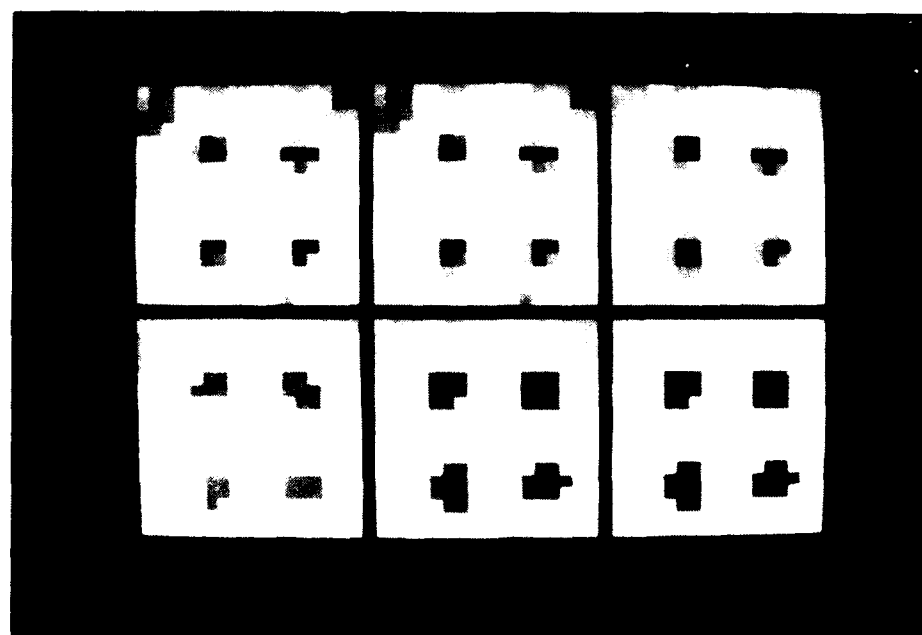


Plate 22. Same as Plate 21, except data is from Plate 20.

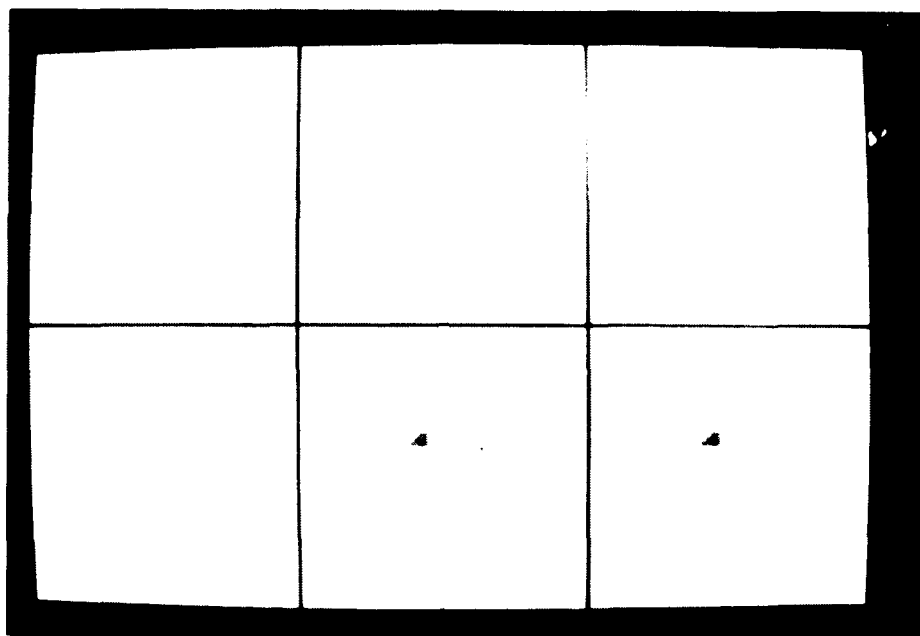


Plate 23. Data is obtained by looking at difference between prefilter output and cluster output with 8 regions of Plate 19. Pictures show this data twice, followed by output with 8, 6, 4, and 3 regions. Cluster method is ANEAR (L).

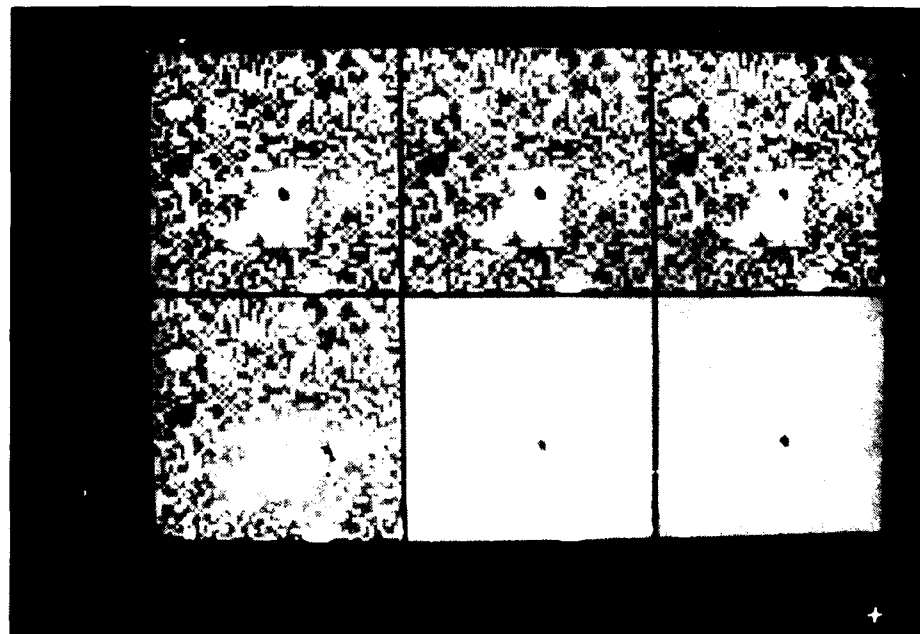


Plate 24. Same as Plate 23, except that data comes from Plate 20.

ADP003118

# **Fourier Shape Analysis: A Multivariate Pattern Recognition Approach**

Robert Ehrlich  
William E. Full

Department of Geology  
University of South Carolina  
Columbia, SC 29208

Department of Geology  
Wichita State University  
Wichita, KS 672080

## **I. INTRODUCTION**

One of the general objectives of sedimentology is to determine the origin ("provenance") of sediments. Commonly, attempts to determine provenance are predicated on the assumption that sediment sources yield a characteristic suite of minerals. Hence, once mineralogy is determined, the presence of diagnostic minerals is an unequivocal indication of the contribution of a specific sediment source. A problem arises, however, if there is little compositional contrast between sources. This may arise because either sources have common mineral assemblages or the sources in question are not primary but consist themselves of quartz-rich sediments that have lost most nonresistant minerals to dissolution or abrasion.

The most resistant common rock-forming mineral is quartz. In general, quartz abundance increases in the sand-silt size range while other less resistant minerals are selectively removed. Because of its resistance to chemical and physical attack, the shapes of quartz particles change very slowly under the influence of processes associated with transport and deposition (Kuenan, 1959; Smalley, 1966). Not surprisingly, the shapes of quartz sand and silt particles from different source terrains (or with different transport histories) are generally different (Ehrlich et al., 1980).

Most sedimentary deposits are of mixed provenance and often the number and nature of sources are not known a priori. Thus, any attempt at using quartz shape for provenance purposes must determine three things:

- 1) the number of sources,
- 2) the shape signature of each source, and
- 3) the relative contribution of each source to each sample.

*→ This article describes the design*  
 In addition, shape data must be acquired economically allowing analysis of hundreds of particles per sample and tens of hundreds of samples in any particular investigation. To this end, a simple image analysis procedure generating edge points of particles and a set of pattern recognition algorithms accomplishing end member (source) characterization and mixing proportions has been designed.

## II. IMAGE ANALYSIS

The perimeters of two-dimensional projections of quartz particles are digitized using a microprocessor controlled microscope mounted video scanning system (Fig. 1). The associated video digitizer accepts the analog signal from the video scanner and generates a spatial array of points (pixels) each of which has an associated shade of gray. Because the digitizing unit has an on-board memory acting as a buffer, it is synchronized with both the scan rate of the video scanner and the acquisition of a scene in 1/60 sec.

The microprocessor uses simple thresholding (pixel value equal to a dark shade of gray) to find the first edge point. Then, using a search pattern involving small excursions, first away from the edge and then inwards, the particle outline is traced pixel by pixel until closure is obtained (Fico, 1980). Depending on the magnification, 200-1000 points are generated for each particle. These edge points are used as raw data for the next step in the analysis.

## III. SHAPE MEASUREMENTS

Amplitude spectra of a finite Fourier series in closed form are used as shape descriptors of each particle. A Fourier series in closed form can be used to describe the outline of a grain's maximum projection silhouette to any desired precision (Ehrlich and Weinberg, 1970). Each term in this series is of the form  $R_n \cos(\theta_n - \phi_n)$  where  $R_n$  is the amplitude of the nth term or harmonic and  $\phi_n$  is the phase angle associated with this specific harmonic. Each harmonic in the series represents the contribution of a specific shape component to the total shape of the



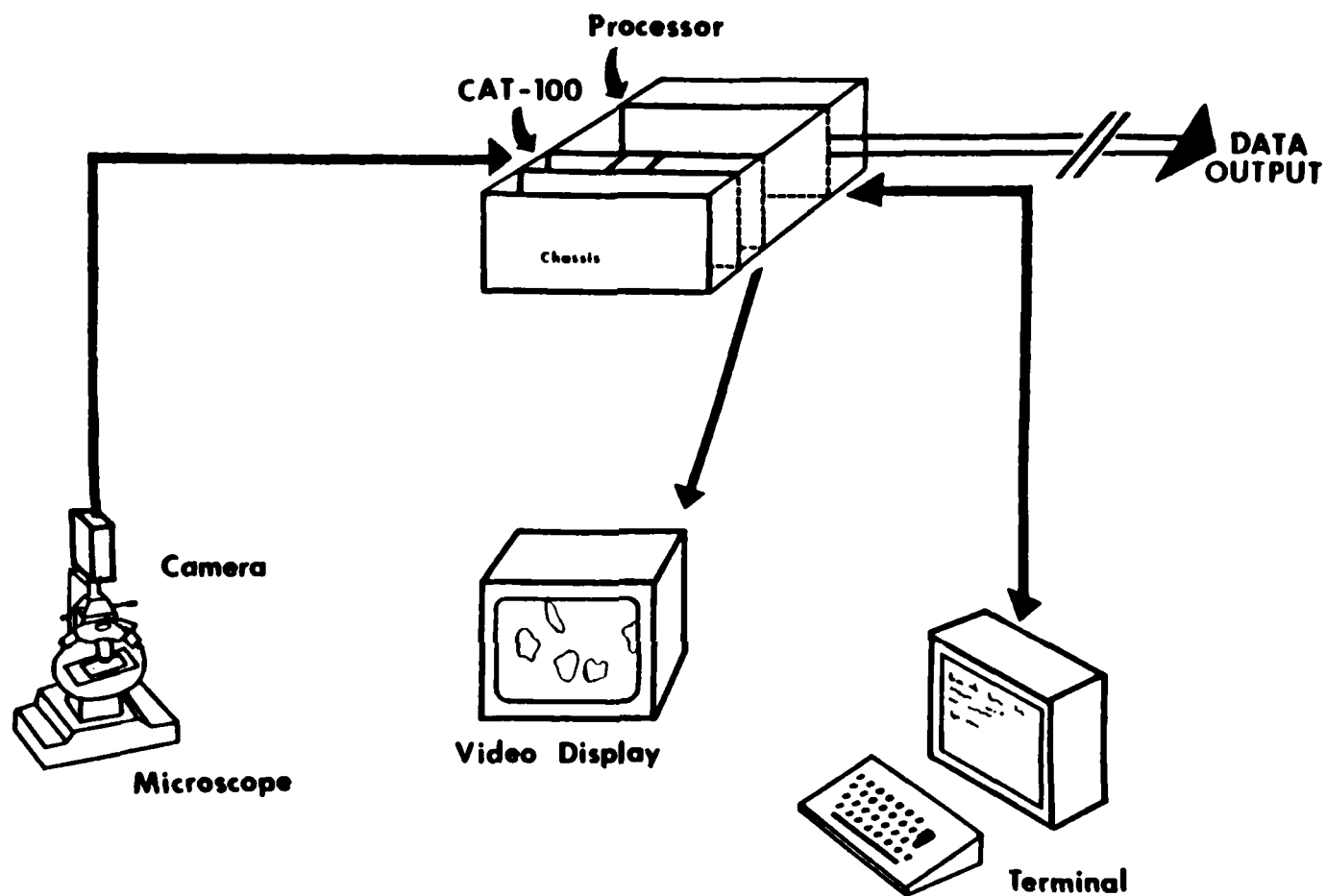


Figure 1. System hardware configuration.

grain. For example, the second harmonic represents the contribution of a "figure-eight," the third represents a trefoil, the fourth a quadrefoil, and so on. In general, the  $n$ th harmonic represents the contribution of an  $n$ -leaved clover to the empiric shape of the grain (Fig. 2). Thus, the lower harmonics are a measure of gross shape while the higher harmonics measure increasingly fine-scaled surface features. Because of the limited resolution of the measuring device, only the first 24 harmonics are calculated and used in the shape analysis.

The coordinates of the maximum projection outline derived from the video digitizing system are used to calculate the Fourier series. To produce homology between grains, the centroid of a subset of 48 points extracted from the original grain outline is always used as an origin for the Fourier series (Full and Ehrlich, 1982a). Although any origin will produce a series that converges to the same shape, the use of this centroid ensures that two grains having exactly the same shape will have the same harmonic values for their respective Fourier series. This allows the Fourier harmonic amplitudes of grains to be comparatively analyzed (Full and Ehrlich, 1982a). The amplitude of the first harmonic (an offset circle) is a measure of accuracy in finding this centroid and is not used in any shape comparisons.

For each sediment sample, 200 or more randomly selected quartz grains (generally within a narrow size range) are analyzed. Each sample is thus represented by 200 Fourier series. At any specific harmonic of those series, a sample is represented by 200 amplitude values (one for each particle). These values can be displayed in a "shape-frequency distribution" at each harmonic wherein each harmonic amplitude is plotted against frequency of occurrence (Ehrlich et al., 1980). Thus each sample is represented by 23 shape-frequency distributions--one for each harmonic 2-24.

Aspects of information theory (Shannon, 1948) can be used to cast the above harmonic amplitude distributions in an optimal configuration (Full et al., 1982c). The algorithm that produces such an optimal configuration is based on information entropy. The information entropy (as defined by Shannon, 1948) of any frequency plot is a measure of contrast between intervals. A low entropy value indicates that the amplitude value of any grain has a much greater probability of falling in certain intervals than in others. Thus a frequency plot with low entropy is a distribution with well-developed modes and anti-modes exhibiting large contrast between intervals. A high entropy value indicates relatively small contrast between intervals. "Maximum

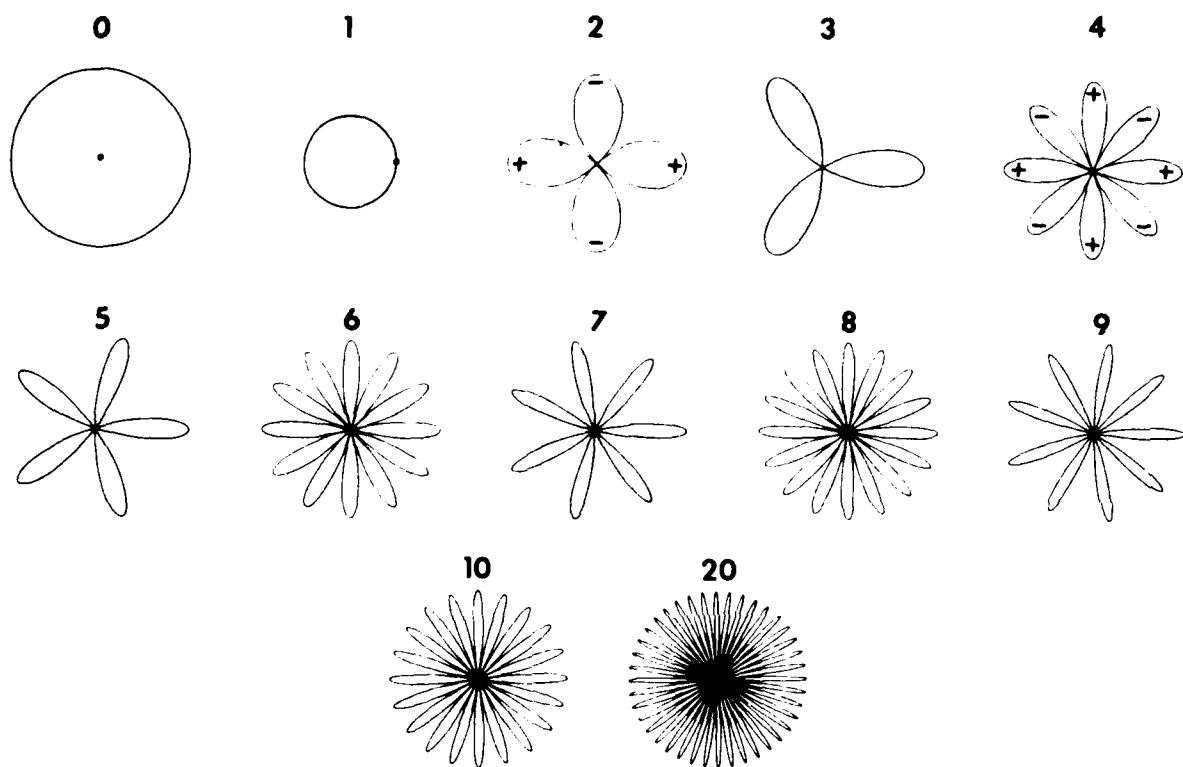


Figure 2. Plots of circular harmonics.

Amplitude = 1.00: Phase angle =  $0^\circ$

entropy" is attained when the amplitude value of any grain has equal probability of occurring in any interval (Shannon, 1948), i.e., when the frequencies in each interval are equal.

Using one given harmonic, if amplitude values from all samples are pooled together into a single shape-frequency distribution, then the widths of the intervals can be adjusted such that the frequency plot displays maximum entropy. Thus the width of the intervals can be unequal and depend on the shape of the distribution of the entire pooled data set. Individual sample frequency plots cast with these variable interval widths have been shown to provide maximum information upon any subsequent analysis (Full et al., 1982c).

The problem exists of which harmonic(s) (2-24) have the greatest potential for a clear, unambiguous solution upon subsequent shape analysis. We need to choose the harmonic(s) that exhibits the greatest contrast between individual sample frequency plots. The "relative entropy" of the entire data set can be used to measure this contrast (Full et al., 1982c). The relative entropy is the average entropy of the individual sample plots divided by the maximum possible entropy. The lower the relative entropy of a data set, the more contrast exists between samples contained in that set. Thus the relative entropy can be used as a feature extractor (Full et al., 1982c). Choosing the harmonic with the lowest relative entropy will produce optimal results from the unmixing algorithms described below.

#### IV. PATTERN RECOGNITION

##### A. CABFAC/EXTENDED CABFAC

Once each sample is cast as a frequency distribution, with class intervals defined by the maximum entropy argument, the array is in an optimal configuration for subsequent analysis. Proportions of particles in the class intervals at a given harmonic comprise a constant-sum variable set (they sum to 100% in this case). Each sample can be viewed as a vector defined on a set of orthogonal axes one for each class interval of the frequency distribution. Because the number of class intervals is generally large (say >10) this "measurement space" is of high dimensionality and so it is difficult for most normal persons to visualize. The fact that the values of each sample-vector sum to 100% immediately confines the data to a hyperplane of

dimensionality one less than the number of intervals (Full et al., 1982a). In addition, if we assume that two or more sets of intervals wax and wane together from sample to sample (maintain constant relative proportions) then the number of independent sets of intervals doing so is equal to the number of "end members." For reasons exactly analogous to the aforementioned constant-sum restriction, this further reduces the number of directions in which the data array can spread in measurement space. In fact, the data must be confined to a hyperplane of one dimension lower than the number of end members. For instance, if all samples were mixtures of only two end members (each may consist of many characteristic modes) then, in the absence of random perturbations, the vertices of the sample vectors will be arrayed along a line embedded in a measurement space of higher dimensionality. The space of lower dimension which is sufficient to contain the data array is called "mixture space" (Full et al., 1982c).

A method to determine the dimensionality of mixture space has evolved over the past decade (Imbrie, 1963; Klován and Imbrie, 1971; Klován and Miesch, 1976; Miesch, 1976a). This has resulted in the algorithm EXTENDED CABFAC (Klován and Miesch, 1976). The algorithm CABFAC (Klován and Imbrie, 1971) evolved from conventional factor analysis (Harmon, 1960). Conventional factor analysis seeks, through analysis of correlated variables (via either a correlation or a variance-covariance matrix), to produce a set of new variables (factors) that are, themselves, uncorrelated. Often most of the variance associated with the old variable set is associated with fewer variables in the new set. Imbrie and students (Imbrie and Purdy, 1962; Imbrie, 1963), utilizing the general mathematical-analytical framework of conventional factor analysis (eigenvector-eigenvalue evaluation of a scatter matrix), built an analogous analytical system for determining the relationships between multivariate sample vectors. Sample vector pairs can be related via their vector cosines (termed similarity coefficients) which are exactly analogous to correlation coefficients between variable pairs. However, when the number of samples is large, calculations of a complete similarity matrix overwhelms the capacity for many computers. To alleviate this, Klován and Imbrie (1971) derived the necessary information by diagonalizing the cross product matrix formed by pairwise comparison of variables. Klován and Imbrie (1971) thus demonstrated the functional relationship between conventional (variable-based) factor analysis (termed "R-mode" factor analysis) and sample-vector analysis (sometimes termed "Q-mode factor analysis").

Program CABFAC determines a new set of orthogonal reference axes in place of those defined by the original class-intervals. Commonly, to simplify interpretation, this new set is rotated using the varimax criterion (Imbrie, 1963).

Program EXTENDED CABFAC (Klovan and Miesch, 1976) contains as its basis program CABFAC of Klovan and Imbrie (1971). However, two important features have been added: 1) the results (scores of reference axes) are reported in the same units as the input data vectors, and 2) a new criterion is developed to determine the dimensionality of mixture space (Miesch, 1976a). Once the true dimensionality of the data is known, the ends of the sample vectors are projected into this "reduced space" within which individual points (each representing a multivariate vector) can be defined that, when connected by straight lines, will form a geometric figure (termed a "polytope") enclosing the data cloud. The minimum number of polytope vertices needed is one more than the dimensionality of this reduced space. For instance, the vertices of a triangle in a plane are sufficient to classify all enclosed samples in terms of positive linear combinations of end members (vertex compositions).

#### B. QMODEL

Program EXTENDED CABFAC does not itself identify the end members. Accordingly, Klovan and Miesch developed program QMODEL whose object is to determine end members with more realistic compositions (i.e., positive class interval proportioning in data space). Program QMODEL defines end members in one of three ways. The first way is to use the principal axes after the varimax rotation as end members. Although this method generally assures positive composition loadings (proportions of each end member in mixing space), positive composition scores (actual interval proportions in data space) are not guaranteed. The second method, optional in QMODEL, is to manually locate the end members. To aid in this, Miesch (1976b) has devised program EQSPIN. But unless the user has extremely tight control on the model being developed, he will have difficulty in finding a solution to the problem, especially when four or more end members are involved.

The third method available in QMODEL is an oblique solution which, by searching either the varimax space or data space, locates extremal points (vectors) as end members. These points, representing real samples, become reference axes. After locating these points within the varimax data set, the coordinates of points in this

space are normalized by dividing the squared varimax factor matrix loadings by the communalities as derived by program EXTENDED CABFAC (Miesch, 1976a). Relative distances of all sample points about these new reference axes can be interpreted as mixing proportions. These proportions are called oblique composition loadings and the space defined by the above reference axis is referred to as oblique space.

With this method the remaining configuration of data (i.e., the non-extreme samples) in varimax space is not involved in end members determination. Thus, the QMODEL algorithm may be said to depend on a relatively small number of "outliers" to establish a metric for the entire data set. If the data envelope has bulges or invaginations, lines connecting the QMODEL end members may penetrate that envelope. Points falling outside the mixing polytope must contain negative proportions of one or more end members. The points with negative proportions are not easily interpretable in cases where mixing is considered an additive process. The presence of such negative mixing proportions indicates that one or more true end members have not been captured in the original data array. Therefore, new reference axes (end members), external to the data, must be located such that the envelope defined by these areas contains the data.

### C. EXTENDED QMODEL

In a recent paper, Full, Ehrlich, and Klován (1981) introduced a modification of the Q-Mode unmixing algorithm QMODEL (Klován and Miesch, 1976) wherein an iterative procedure was developed to locate feasible end members not captured within a data set. This new algorithm, EXTENDED QMODEL, finds end members whose compositions are positive (or nearly so) and can be linearly proportioned to regenerate all of the data without resorting to negative proportions. Additionally, the sum of the proportions for each data point is constrained to be unity. The subroutine that locates these end members (herein called the DENEG procedure) does so by making an "edge-adjustment" of the mixing polytope if negative mixing proportions occur in QMODEL, followed by a "vertex adjustment" if the new polytope vertices (extremal end members) contain negative proportions. The DENEG end members represent vectors more extreme than any sample in the data set.

The general steps in the DENEG algorithm are as follows:

1) Each column of the oblique composition loading matrix of QMODEL is scanned for negative composition loadings. Negative loadings are divided into three categories: negligible (0.00 to  $T_1$ ), adjustable ( $T_1$  to  $T_2$ ), and nonadjusted (less than  $T_2$ ). Nonadjusted loadings are ones that correspond to "outliers" that will not affect definition of reference axes.

2) If there are no adjustable loadings, stop. Otherwise proceed to (3).

3) For each column, identify the most negative adjustable loading, say of value  $d_i$ . Add the absolute value of  $d_i$  to every entry of the column being adjusted. Geometrically, this translates the edge represented by this column "out" a distance equal to the absolute value of  $d_i$  in the initial oblique space, parallel to the original edge defined by the initial oblique end members. (Fig. 3a).

4) Change the coordinates of all sample vectors based on the amount of "outward" movement of the edge of reference polytopes. That is, if  $X_i = x_i, \dots, x_{in}$  represents the coordinates of each vector in the initial oblique space and  $d_j, \dots, d_n$  is defined as in (3) above, then

$$x_i \text{ new coordinate} = (x_{i1} + d_1) (Z) , \dots , (x_{in} + d_n) (Z);$$

where  $Z = 1/(1 + d_1 + \dots + d_n)$ .

5) Locate the new vertices of the reference polytope in QMODEL oblique space. The coordinates of the vertex will be the corresponding distance each side was translated added to the old vertex coordinate corresponding to the translated direction, which is determined by recalling that the sum of coordinates at each vertex is unity. That is, the oblique coordinates (loadings) of each new end member  $[E_i = (d_1, \dots, d_{i-1}, c, d_{i+1}, \dots, d_n)]$  where  $d_1, \dots, d_{i-1}, d_{i+1}, \dots, d_n$  is the distance in oblique space each respective side was translated, and  $c = 1 - (d_1 + \dots + d_{i-1} + d_{i+1} + \dots + d_n)$ .



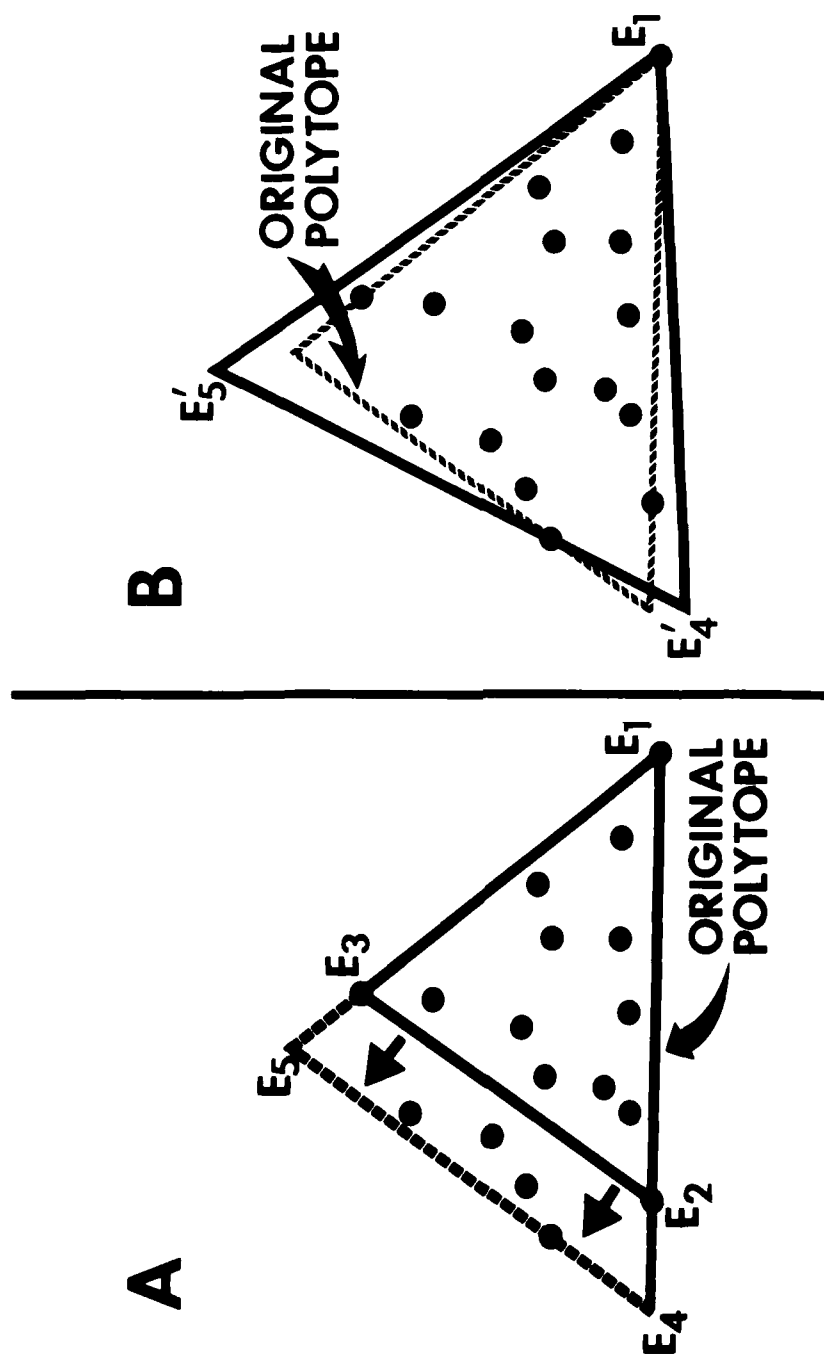


Figure 3. Pictorial representation of the edge adjustment (A) and following vertex adjustment (B) steps in the DENEG procedure.

6) Find compositions of each vertex using the QMODEL oblique transformation matrix.

7) Test the composition scores (corresponding end member composition in the original variable space) of each vertex for positivity. If all composition scores are greater than cutoff  $T_3$ , stop. Otherwise, for each unacceptable end member, zero all negative composition scores and reportion this vertex to constant sum. A result of this procedure is that edges of the new polytope need not be parallel to those of the initial QMODEL polytope (Fig. 3b).

8) Submit the new vertex compositions to QMODEL. Generate the corresponding varimax loadings.

9) If the varimax loadings of the new end members fall within a distance  $T_4$  of the previous iteration, stop. Otherwise, continue.

10) Generate a new oblique solution.

11) If the maximum number of iterations  $T_5$  have been obtained, stop. Otherwise, return to (1).

Two variable parameters in the algorithm add flexibility to the modeling process. One parameter ( $T_2$ ) defines the maximum distance a polytope side can potentially move. Points beyond this maximum specified distance are considered outliers or impurities and will not affect the overall solution. "Distance" in this sense represents the degree of movement of a side measured relative to the distance from the opposite vertex. A distance of 0.25, for instance, means that a polytope side had moved a distance equal to 25% of the distance of the opposite vertex to the original polytope side in QMODEL oblique space. Appropriate values for this parameter must be determined from the nature of the problem to be solved. In many cases where QMODEL cannot converge to a unique set of end members via the extreme normalized composition subroutine (EXNORC) or the extreme raw composition subroutine (EXRAWC), modest movement of polytope sides provides a satisfactory solution. Of course, lack of convergence of these subroutines might also indicate a wrong choice in the number of end members.

The other variable parameter ( $T_4$ ) defines the termination point of this algorithm in terms of closeness of the varimax loadings of the end members from iteration to iteration. Failure to converge may arise from either a poor end member fit, or oscillation in a narrow region between realistic varimax space and unrealistic varimax space.

Three cutoffs are used to control the amount of computer time needed to find a proper solution. One cutoff ( $T_5$ ) determines the maximum number of iterations. Another cutoff permits solutions with slightly negative composition loadings ( $T_1$ ), whereas the last cutoff permits slightly negative composition scores ( $T_3$ ). The latter two cutoffs are necessary because in some cases accepting such a factor model may better reproduce the original data set in terms of geologic modeling; the small negative values may be "close enough" to zero to be considered zero when compared to the original precision of the empirical data.

#### D. FUZZY QMODEL

In the absence of a priori knowledge, QMODEL requires the presence of vertex-extreme samples in the sample set, whereas EXTENDED QMODEL requires a set of edge-extreme samples. However, in either case, reliance on extreme data raises the possibility that a relatively few isolated data points might seriously affect the relative geometry of extreme samples with regard to a mixing polytope.

A more usual approach in conventional data analysis is not to rely on individual sample points, but to use aggregate properties of the data which tend to dissipate the effects of random variation (e.g., the greater the stability of the mean compared to an individual data value). Another reason to deduce the nature of end members from the entire data structure rather than from a few outlying points is that outliers may, in many situations, not "belong" to the rest of the data. That is, they may represent either samples not belonging to the system of interest or even incorrectly evaluated samples (i.e., errors in measurement or compilation). The alternative, "FUZZY QMODEL" (Full et al., 1982b), described herein, determines extremal end members based on the collective properties of all the data. But before the basic algorithm of FUZZY QMODEL is described, a brief overview of fuzzy clustering will be given.

In general, cluster analysis refers to a broad spectrum of methods which try to subdivide a data set  $X$  into  $c$  subsets (clusters) which are pairwise disjoint, all nonempty, and reproduce  $X$  via union. The clusters are then called a hard (i.e., nonfuzzy)  $c$ -partition of  $X$ . Many algorithms, each with its own mathematical clustering criterion for identifying "optimal" clusters, are discussed in the excellent monograph of Duda and Hart (1973). A significant fact about this kind of algorithm is the defect in the underlying axiomatic model--that each point in  $X$  is unequivocally grouped with other members of "its" cluster, and thus bears no apparent similarity to other members of  $X$ . One such way to characterize an individual point's similarity to all the clusters was introduced in 1965 by Zadeh (1965). The key to Zadeh's idea is to represent the similarity a point shares with each cluster with a function (called the membership function) whose values (called memberships) are between zero and one. Each sample will have a high degree of similarity between the sample and a cluster while memberships close to unity signify a high degree of similarity between the sample and a cluster while memberships close to zero imply little similarity between the sample and that cluster. The history, philosophy, and derivation of such mathematical systems are well documented in Bezdek (1981). The net effect of such a function for clustering is to produce fuzzy  $c$ -partitions of a given data set. A fuzzy  $c$ -partition of  $X$  is one which characterizes the membership of each sample point in all the clusters by a membership function which ranges between zero and one. Additionally, the sum of the memberships for each sample point must be unity. If the function were to define values as either zero or one, then the memberships would define a hard  $c$ -partition (i.e., conventional clustering). In this light, the proportions derived from EXTENDED CABFAC-QMODEL (Klovan and Miesch, 1976), EXTENDED QMODEL (Full et al., 1981) and FUZZY QMODEL, define fuzzy  $c$ -partitions in themselves wherein the membership functions are linear.

Bezdek (1981) discusses a number of ways to generate fuzzy  $c$ -partitions of data sets and contains many examples of data analysis drawn from a variety of applied fields, including taxonomy, medical diagnosis, and sprinkler design. The fuzzy  $c$ -means (FCM) algorithm (Bezdek, 1981) is one such fuzzy clustering technique that generates fuzzy  $c$ -partitions of a data set. The clustering criterion upon which FCM is based is the weighted sum of squared errors objective function  $J_m$  defined as

$$J_m(U, V) = \sum_{k=1}^N \sum_{i=1}^C (u_{ik})^m \|x_k - v_i\|^2 \quad (3)$$

where

1)  $U = (u_{ik})$  is a fuzzy  $c$ -partition of  $X$  (i.e.,  $U$  is a matrix whose element  $u_{ik}$  represents the membership of vector  $X_k$  in the  $i$ th fuzzy cluster). The function that defines the  $u_{ik}$  is a non-linear inverse function.

2)  $V = (v_1, \dots, v_c)$  is the set of "cluster centers" (i.e.,  $v_i$  is the "center" or core of fuzzy cluster  $i$ ). The location of the cluster centers is determined by a function which weights the contribution of each vector to a particular cluster by the memberships  $u$ .

3)  $\|\cdot\|$  = any inner product norm. In the examples given, the Euclidean norm is used.

4)  $m \in [1, \infty)$  = a weighting exponent called the fuzziness exponent.

Outlying data have virtually no effect on the locations of the centers  $v_i$  because  $(u_{ik})^m$  (the weighted membership of  $X_k$  in cluster  $i$ , raised to the  $n$ th power) approaches zero much faster than the  $(u_{ik})^m$  of the other points  $X_j$  (see eq. 3). In other words, the effects of noise can be essentially "filtered out" by adjusting  $m$ , the fuzziness weighting exponent. An example of the use of the FCM algorithm in geology can be found in Bezdek, Ehrlich et al., (1982) while a synopsis and FORTRAN listing for FCM can be found in Bezdek, Ehrlich, and Full (in preparation). Our present interest in FCM centers around three facts which are well established in both theory and practice.

1) The centers  $v_i$  generated by FCM lie well "inside" the convex hull of data set  $X$ ; this is important because the edge-adjustment DENEG procedure used in EXTENDED QMODEL always expands initial convex polytopes whose vertices are putative end members.

2) The convex hull of the  $v_i$ s is, loosely speaking, a "skeleton" of the main structure of  $X$  itself; in particular, iterative expansion of the faces of this polytope via the DENEG procedure will proceed toward the type of unmixing solution described in Full, Ehrlich, and Klován (1981).

3) Noisy points (outliers in X) will exert little effect on the spatial location of any center  $v_i$ . This is one of the primary advantages of FCM--it is relatively insensitive to the presence of outliers.

The implications of (1) - (3) for the linear unmixing problem are simple: the centers  $[v_i]$  generated by FCM always occupy spatial locations in end member space which are favorable for the initialization of the DENEG procedure. For this reason, the EXTENDED QMODEL procedure was further extended by incorporating the following algorithm:

1) Locate initial end members within normalized varimax space using the FUZZY c-MEANS algorithm.

2) Determine the varimax loadings of these initial end members and submit them as end members defining the QMODEL oblique solution.

3) As these end members are contained within the data set (as opposed to the edges of the vertices of the hull of the data), the maximum edge translation (the DENEG value) must be enlarged for the first iteration only. After these steps are performed, the DENEG procedure is continued until either a solution is found, or a cutoff value is exceeded.

In the case where the data forms a single cluster with internally uniformly distributed data, the FUZZY QMODEL algorithm is strongly influenced by the external configuration of the data. However, this influence is not derived from the outer edge of the data cluster (the convex hull) but from the geometry of an outer "zone" wherein the data density decreases. This is because of the nonlinear inverse weighting function used to define the fuzzy centers upon which outlying points have much less influence than data closer to the centers. In the case of a data cloud that is arrayed as a clearly defined geometric figure, such as a triangle, the fuzzy centers will be imbedded in the data cloud in such a manner that the vertices will define a similarly inscribed polygon. This appealing characteristic can become progressively destroyed as the data becomes more and more clustered. In such a case, the fuzzy cluster centers themselves would serve as vertices and there is no

guarantee that such vertices would bear any relationship to the "true" mixing polytope. Strong clustering can be easily detected by simple inspection of the output from the algorithm. If the data has a definite cluster structure, then the mixing model for the data must be questioned or the sampling plan carefully analyzed.

The differences between QMODEL, EXTENDED QMODEL, and FUZZY QMODEL are illustrated in Figure 4. In the following example, ternary mixing in a multivariate data set can be visualized by examining the data structure as represented in normalized varimax space (Fig 4a). It is assumed for the following illustration that any point located on this triangular plane can serve as a potential end member for the mixing systems presented below. Figure 4(b) represents a ternary mixing space. Any of the QMODEL procedures (QMODEL, EXTENDED QMODEL, FUZZY QMODEL) will identify points  $E_1$ ,  $E_2$ , and  $E_3$  (the vertices of the mixing triangle) as end members. Figure 4(c) represents a uniform data array that incompletely fills the mixing polytope depicted in Fig. 4(b). EXTENDED QMODEL could recover end members  $E_1$ ,  $E_2$ , and  $E_3$  as the proper end members of the mixing system whereas QMODEL could not. However, consider the same data configuration but with outlier  $E_4$  located external to the mixing polytope defined by  $E_1$ ,  $E_2$ , and  $E_3$  (Fig. 4d). In this example, the QMODEL procedure will define point  $E_4$  as a vertex; EXTENDED QMODEL, which uses the QMODEL solution as a starting position, would define a mixing polytope that will also contain point  $E_4$ . In both cases, the procedures cannot define triangle  $E_1E_2E_3$  as the ternary mixing system when plotted in normalized varimax space. In this instance the existence of point  $E_4$  as an "aberrant" outlier can be readily observed. However, when the number of end members are four or more, or the edges of the mixing polytope are not clearly defined by the data, it is much more difficult to detect such structure. The common occurrence of such configurations in geology motivated us to propose the alternative fuzzy means of data analysis. Whereas the initial iteration of previous methods relied heavily on the extremes of the convex hull of the data, initialization of the DENEG procedure with fuzzy clustering emphasizes the data configuration within the hull. The net effect of such a fuzzy analysis is that the effects of aberrant data is minimized.

## V. SUMMARY

The primary steps in shape analysis are the following:

- 1) Particles are digitized and the two-dimensional edge points defined.

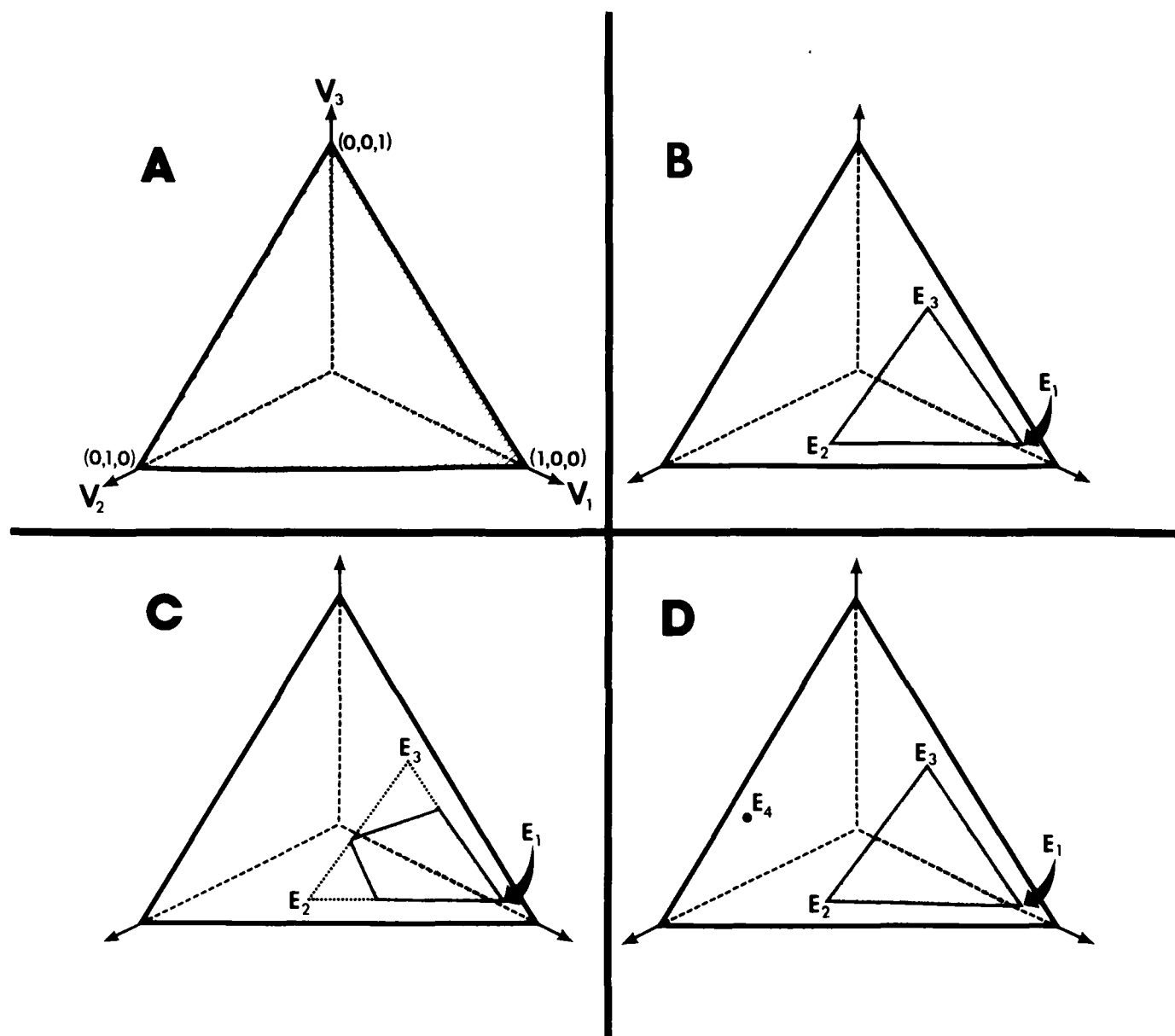


Figure 4. (A) Normalized varimax space where oblique end members can be conveniently visualized; (B) data structure (shaded) wherein end members  $E_1$ ,  $E_2$ , and  $E_3$ , contained within the data set, can be properly located by both QMODEL and EXTENDED QMODEL; (C) portion of the data (shaded) section of the triangle represented in (B) wherein end members  $E_2$  and  $E_3$ , now external to the data set, can be properly located by EXTENDED QMODEL; and (D) same data structure as (B) above except on additional point  $E_4$  is added, neither QMODEL nor EXTENDED QMODEL can recover  $E_1$ ,  $E_2$ ,  $E_3$  in this case.



2) A finite Fourier series in polar form with the particle centroid used as the origin of the polar system is calculated.

3) The multiparticle data is summarized for each sample via shape frequency plots at each harmonic using variable class interval widths based on entropy considerations.

4) The frequency diagrams in the form of sets of proportions are classified in terms of mixing proportions of end members by "unmixing" algorithms.

Our experience indicates that precise characterization of particle shape alone is not usually sufficient in itself and further "downstream" analysis is required to solve most problems. Although most problems with which we have dealt require use of the CABFACQMODEL family of unmixing algorithms, others have required other multivariate procedures such as multiple discriminate analysis.

The algorithms described in (3) and (4) above have been found useful with other types of multivariate data sets. The method of creating frequency diagrams are useful for further analysis of any complex set of frequency distributions as the defining of class intervals on the basis of maximum entropy ensures the least ambiguous results from the unmixing algorithms. The development of these unmixing algorithms (EXTENDED CABFAC, QMODEL, EXTENDED QMODEL, and FUZZY QMODEL) have allowed the interrelationships of large numbers of samples to be evaluated multivariately, using all variables simultaneously. The mixing proportions and end member compositions have proven to be of value with respect to a variety of sedimentological investigations using shape and size frequency data. Additionally, these algorithms have been used to successfully classify and analyze multichannel data from gas chromatography, gamma ray spectroscopy, major and trace element chemistry, and paleontologic assemblages.

## VI. LIST OF REFERENCES

Bezdek, J. C., 1974, Numerical taxonomy with fuzzy sets: Jour. Math. Bio., v. 1, p. 57 - 71.

Bezdek, J. C., 1981, Pattern Recognition with Fuzzy Objective Functions: Plenum Press, New York

Bezdek, J. C., R. Ehrlich, M. Trivedi, and W. E. Full, 1982, Fuzzy clustering: A new tool for geostatistical analysis: Jour. Syst., Meas. Decis., in press.

Bezdek, J. C., R. Ehrlich, and W. E. Full, in preparation, The fuzzy c-means clustering algorithms

Duda, R. O., and P. E. Hart, 1973, Pattern Classification and Scene Analysis: Wiley, New York.

Ehrlich, R., and B. Weinberg, 1970, An exact method for the characterization of grain shape: Jour. Sed. Pet., v. 40, p. 205 - 212.

Ehrlich, R., P. J. Brown, J. M. Yarus, and R. S. Przygocki, 1980, The origin of shape-frequency distributions and the relationship between size and shape: Jour. Sed. Pet., v. 50, p. 475 - 484.

Fico, C., 1980, Automated particle shape analysis -- Development of a microprocessor-controlled image analysis system: unpub. Masters thesis, Univ. of South Carolina, Columbia, SC, 60 pages.

Full, W. E., R. Ehrlich, and J. E. Klován, 1981, EXTENDED QMODEL - Objective definition of external space end members in the analysis of compositional data: Comput. Geosci., v. 1, p. 161 - 178.

Full, W. E., and R. Ehrlich, 1982a, Some approaches for location of centroids of quartz grain outlines to increase homology between Fourier amplitude spectra: Math. Geol., v. 4, p. 43 - 55.

Full, W. E., R. Ehrlich, and J. C. Bezdek, 1982b, FUZZY QMODEL: A new approach for linear unmixing; Math. Geol., v. 14, p. 257 - 268.

Full, W. E., R. Ehrlich, and S. K. Kennedy, 1982c, Information content of data displayed as histograms or frequency plots: Jour. Sed. Pet., in press.

Harmon, H. H., 1960. Modern Factor Analysis (2nd Ed.): Univ. Chicago Press, Chicago, 474 pages.

Imbrie, J. and E. G. Purdy, 1962, Classification of modern Bahamian carbonate sediments: in Mem 1, Amer. Assoc. Pet. Geol., p. 253 - 272.

Imbrie, J., 1963, Factor and Vector Analysis Programs for Analyzing Geologic Data, Tech. Report No. 6, ONR Task No. 389-135, Office of Naval Research, Geography Branch, 83 pages.

Klovan, J. E. and J. Imbrie, 1971. An algorithm and FORTRAN IV program for large scale Q-mode factor analysis and calculation of factor scores: Jour. Math. Geol., v. 3, p. 61 - 76.

Klovan, J. E., and A. T. Miesch, 1976, EXTENDED CABFAC and QMODEL computer programs for Q-mode factor analysis of compositional data: Comput. Geosci., v. 1, p. 161 - 178.

Kuenen, P. H., 1959, Experimental abrasion: 3. Fluvial action on sand: Am. Jour. Sci., v. 257, p. 172 - 190.

Miesch, A. T., 1976a, Q-mode factor analysis of geochemical and petrologic data matrices with constant row-sums: Geol. Surv. Prof. Paper 574-G, 47 pages.

Miesch, A. T., 1976b, Interactive computer programs for petrologic modeling with extended Q-mode factor analysis: Comput. Geosci., v. 2, p. 439 - 492.

Shannon, C. E., 1948, Bell System Tech. Jour., 379, 623. Reprinted in Shannon, C. E., and W. Weaver, The Mathematical Theory of Communication: Univ. of Illinois Press, Urbana, Illinois (1963).

Smalley, I. J., 1966, Formation of quartz sand: Nature, v. 211, p. 476 - 479.

Zadeh, L., 1965, Fuzzy sets: Inform. Control, v. 8, p. 338 - 353.

# Fuzzy Algorithms for Pattern Recognition\*

James C. Bezdek  
Mathematics Department  
Utah State University  
Logan, Utah 84322

## ABSTRACT

This paper contains, first, a tutorial of the basic axiomatic structure underlying many fuzzy algorithms for pattern recognition; and second, a summary of the theory and applications connected with several currently available fuzzy techniques. In particular, we consider algorithms for clustering, feature selection, classification, and shape description.

\*Supported by NSF Grant  
MCS80-02856

ADP003119

## 1. INTRODUCTION

Mathematical models of physical processes attempt to quantify hypothesized relationships between variables governing the process. Uncertainty has--and in all likelihood, always will--plague our efforts to emulate the real world with precise abstractions. In this context, there are at least three sources of imprecision that bear on the modelling of real situations:

Inexact measurements ; (1.1a)

Random occurrences ; (1.1b)

Vague descriptions . (1.1c)

These have, in turn, led to different types of mathematical models:

Deterministic ; (1.2a)

Stochastic ; (1.2b)

Fuzzy . (1.2c)

The first two sources of imprecision, and models incorporating them, have long since been part of the applied mathematician's stock in trade. The pervasive nature of vague descriptions in everyday life is so common that the human mind assimilates and uses "fuzzy data" almost instinctively. Thus, one admonishes the learning driver to put on the brakes "a bit sooner" when approaching an intersection--and the student soon learns to do so! The utilization of fuzzy information for decision making is so common that one never comes to grips with the philosophical differences between chance (flip a coin) and fuzziness (it costs about a dollar) until we want a computer to imitate our capacity to synthesize and use such information. In 1965, Zaden [1] proposed an extensive axiomatic system that attempts to

recognize, capture, and exploit non-statistical uncertainties which may arise in mathematical models. The basic structure in this system is the "fuzzy set ". The motivation for continued development of this new axiomatic structure is simple. Any physical system can be represented by various models. The "best" results are usually obtained with the most natural model; and in many situations, the physical process is best described by or generates fuzziness. In particular, fuzzy models are especially well suited for many problems arising in pattern recognition and image processing, because data substructures being sought are almost always mixed--i.e., have ill-defined boundaries (c. f. [2] for an extensive discussion).

Our objective in this paper is twofold. First, we present in tutorial fashion those elements of the fuzzy sets theory that appear crucial for the continued development of useful models in pattern recognition. Following this, we survey some current algorithms which may be useful for pattern recognition and image processing applications within the ocean science community.

## 2. HARD SETS

Sets can be represented using the object property method. If a set is well defined, its object properties provide a complete description of how to qualify for membership. Sets are customarily given capital letter names. As an example, let  $H$  be the set of real numbers greater than or equal to 6. This precise verbal description is represented as:

$$H = \{ r \in R : r \geq 6 \}, \text{ where} \tag{2.1}$$

$H$  ~ name of set

$r$  ~ name of generic set member

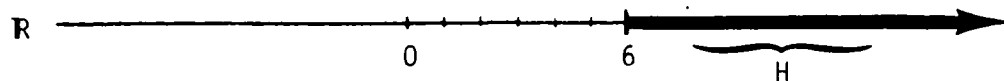
$\in$  ~ "is in"

$\mathbb{R}$  ~ name of the real numbers = source of set members

$:$  ~ "such that"

$r \geq 6$  ~ precise object property, "r is greater than or equal to 6"

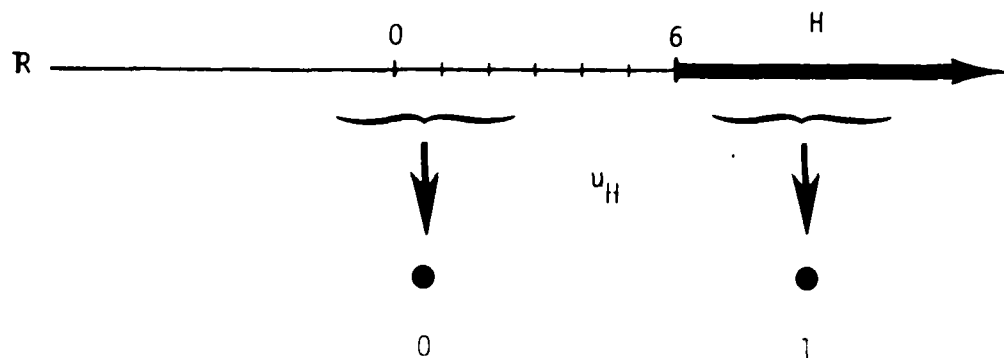
This is a "set" description of  $H$ . We often represent this description by a schematic illustrating the real number line  $\mathbb{R}$ , and  $H$ :



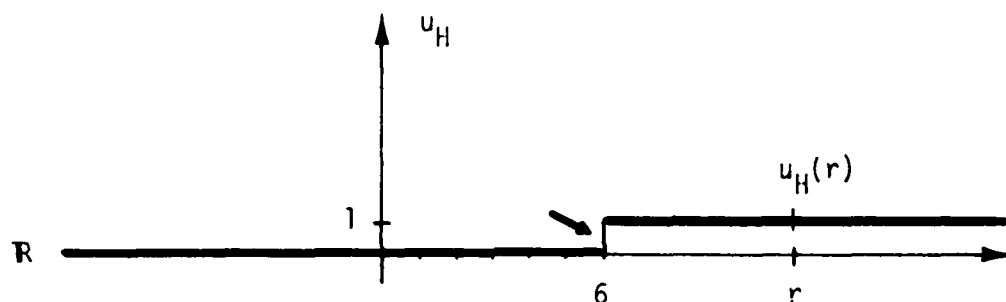
Another way to describe  $H$  is with a membership function. Since every real number  $r$  either is or is not a member of  $H$ , we can associate "belongs to  $H$ " with the number 1; and "not in  $H$ " with the number 0. We call the association a function from  $\mathbb{R}$  to the pair  $\{0,1\}$ . This association is called a "mapping" from  $\mathbb{R}$  onto  $\{0,1\}$ . This mapping is represented symbolically by giving the function a name, say  $u_H$ , and writing  $u_H: \mathbb{R} \rightarrow \{0,1\}$ , read  $u_H$  maps  $\mathbb{R}$  onto the numbers 0,1. The verbal description of  $u_H$  then assumes symbolic form:

$$u_H(r) = \begin{cases} 1 & \text{when } r \in H, \text{ i.e., } r \geq 6 \\ 0 & \text{when } r \notin H, \text{ i.e., } r < 6 \end{cases} \quad (2.2)$$

Function  $u_H$  identifies which numbers  $r$  are in  $H$ , hence is the membership function of  $H$ . Equations (2.1) and (2.2) are completely equivalent: if  $H$  is known,  $u_H$  is well defined; and conversely. Note further that  $u_H$  also specifies (as it must) the precise object property necessary to identify members of  $H$ . The equivalence of these descriptions can be illustrated graphically:



A last way to represent any hard set  $H$  is by a graph of its membership function  $u_H$ . In the present example, we simply graph the value of  $u_H$  at each  $r \in R$  directly above  $r$  itself:



Note in particular the abrupt jump from 0 to 1 in the graph of  $u_H$  at  $r = 6$ . This depicts graphically a salient feature of all hard sets: their edges (or boundaries) are always "sharp" = hence the term, "hard sets." A set of numbers which are "about 6" could not have a boundary of this type.

Finally, a note about terminology. In our example,  $H$  is a hard set, and  $u_H$  is its membership function. In general, sets and functions are different types of mathematical objects. But here,  $H$  and  $u_H$  are totally equivalent (can be constructed from each other). In this instance - although it seems peculiar - one can call  $u_H$  the hard "set" !! The point of this observation? The only mathematical characterization of a fuzzy "set" is its membership function.



### 3. HARD SUBSETS

A hard subset of a hard set is easy to define. Let  $X$  be any set, and  $A$  be any subset of  $X$ . We write

$$A \subset X \Leftrightarrow a \in A \Rightarrow a \in X, \text{ where} \quad (3.1)$$

$A \sim$  name of hard subset

$\subset \sim$  "is a subset of"

$X \sim$  name of hard set

$\Leftrightarrow \sim$  "if and only if"

$a \in A \sim$  "a is in A"

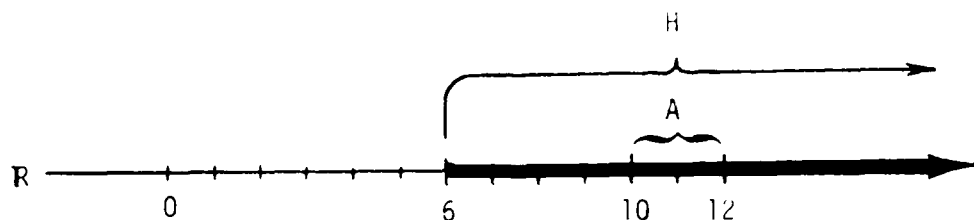
$\Rightarrow$  "implies"

$a \in X \sim$  "a is in X"

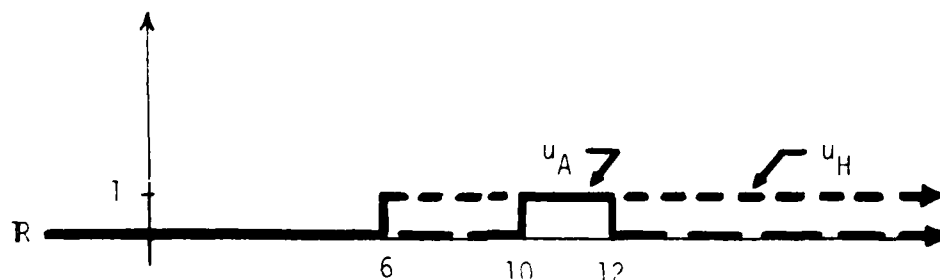
In other words,  $A$  is a subcollection of elements from  $X$ . Since  $A$  is a hard set in its own right, it is equivalent to the membership function  $u_A: X \rightarrow \{0,1\}$  defined by

$$u_A(a) = \begin{cases} 1; & a \in A \\ 0; & a \notin A \end{cases} \quad (3.2)$$

Continuing the example of S2, let  $A$  be the set of real numbers greater than 10 and less than 12, then  $A$  is a hard subset of  $H = [6, \infty)$ . Equation (3.1) becomes  $(10,12) \subset [6, \infty)$ . Schematically, we picture this as:



The graph of  $u_A$  looks like a "square wave." Note that its graph is "contained in" the graph of  $u_H$ . This always happens with hard subsets:  $u_A = u_H$  for  $r \in A$  because  $A \subset H$ . The portion of the graph of  $u_H$  which agrees with  $u_A$  simply asserts that object properties of elements of  $A$  agree with those of  $H$ : the jumps at 10 and 12 indicate the precise refinement of the property ( $\geq 6$ ) by ( $10 < r < 12$ ). Hard subsets have sharp boundaries because they are hard sets.



Consider now the set  $B$  of numbers "much greater than 6." Certainly  $B$  is a subset of  $H$  - but not in the sense of definition (3.1), because this refinement of ( $\geq 6$ ) is imprecise: it does not indicate exactly where a "membership function"  $u_B$  for  $B$  should jump up. Consequently, the framework of hard sets and subsets must be extended if one desires models in which sets such as  $B$  can be manipulated. This intuitively plausible need motivates the definition of "fuzzy" subsets.

#### 4. FUZZY SETS

Subsets of hard sets are fuzzy when they have no realization as hard subsets (equation (3.1)). To define a fuzzy subset, we extend the range of membership functions from the two point set  $\{0,1\}$  to the unit interval  $[0,1]$ . If  $X$  is any set, then  $u_B$  is a fuzzy subset of  $X$  in case  $u_B: X \rightarrow [0,1]$ :

$$\left( u_B \text{ is a fuzzy subset of } X \right) \iff \left( u_B \text{ is a function mapping } X \rightarrow [0,1] \right) \quad (4.1)$$

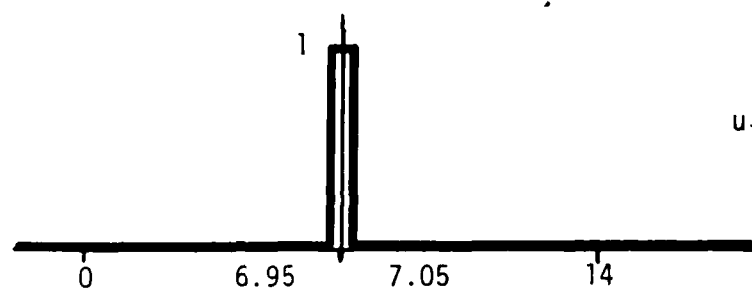
The final paragraph of S2 anticipates this definition. We may speak of the fuzzy set  $B$  of numbers "close to 9," but a function  $u_B$  which assigns memberships "in  $B$ " to numbers is the only mathematical representation we have for the vague verbal description.

For  $x \in X$ , the value  $u_B(x)$  is called the grade of membership of  $x$  in  $B$ . What does  $u_B(x)$  measure? The extent to which  $x$  possesses the imprecisely defined object properties which characterize  $B$ . This is somewhat circular, because there is no  $B$  without  $u_B$ , and yet  $u_B$  measures "degree of similarity" with things in  $B$ ! Polemics notwithstanding, we can construct useful models based on this notation. To fix the general idea, let  $\mathbb{R}$  be the hard set of real numbers, and let  $B$  be the fuzzy subset of  $\mathbb{R}$  of numbers that are "nearly 7." The graphs in Figure 4.1 depict several ways one might choose to represent  $B$ :

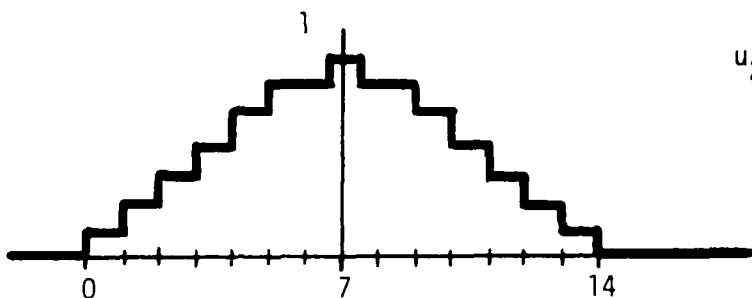
Function  $u_1$  is a hard set - one possibility for modelling the imprecise property "nearly 7" in a conventional way. Functions  $u_2$  through  $u_5$  are all fuzzy subsets of  $\mathbb{R}$ .  $u_2$  is similar to a hard set in that its graph has discrete jumps at selected base points. No jump, however, is a unit jump: in other words, no sharp edge delineates "points in  $u_2$ " from "points not in  $u_2$ ." Functions  $u_3$  and  $u_4$  are continuous:  $u_4$  is differentiable on  $[0,14]$ . Fuzzy set  $u_5$  is a subset of all of  $\mathbb{R}$ . Note that all five graphs are symmetric about  $r = 7$ : this seems plausible--it is not necessary.

The value  $u_k(r)$ ,  $k = 1,2,3,4,5$ , is  $r$ 's membership in  $B$ . Since  $u_k(7) = 1$  for every  $k$ , all five sets associate "being 7" with "as near to 7 as is possible." The situation for  $r \neq 7$ , however, is quite different. We compare memberships in  $B$  for several values of  $r$ :

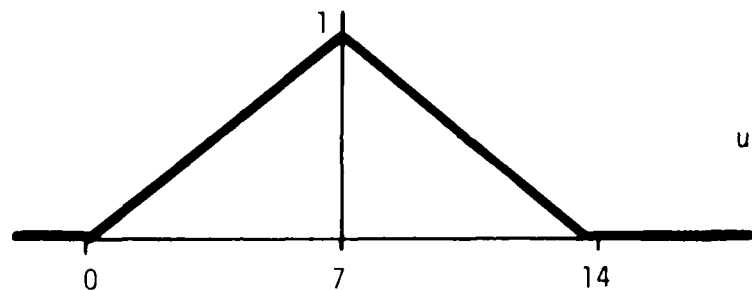
Figure 4.1 Some Fuzzy Sets for "Nearly Seven"



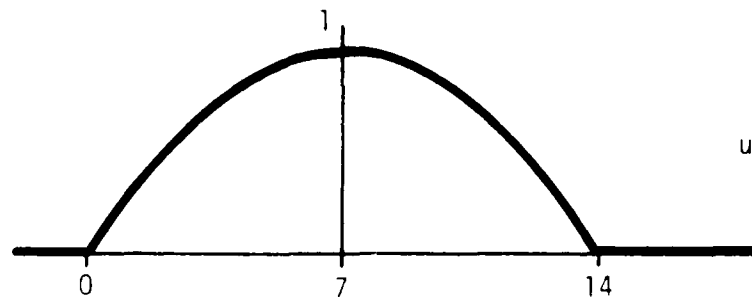
$$u_1(r) = \begin{cases} 1 & ; 6.95 \leq r \leq 7.05 \\ 0 & ; \text{otherwise} \end{cases}$$



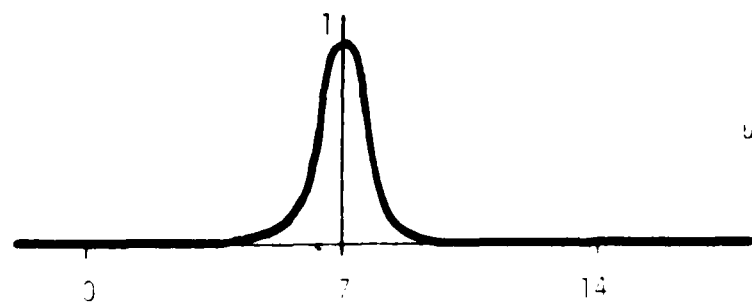
$$u_2(r) = \begin{cases} 1 & ; 6.5-7.5 \\ .86 & ; 5-6.5 \text{ or } 7.5-9 \\ .71 & ; 4-5 \text{ or } 9-10 \\ .56 & ; 3-4 \text{ or } 10-11 \\ .42 & ; 2-3 \text{ or } 11-12 \\ .28 & ; 1-2 \text{ or } 12-13 \\ .14 & ; 0-1 \text{ or } 13-14 \\ 0 & ; \text{otherwise} \end{cases}$$



$$u_3(r) = \begin{cases} (r/7) & ; 0 \leq r < 7 \\ 2-(r/7) & ; 7 \leq r \leq 14 \\ 0 & ; \text{otherwise} \end{cases}$$



$$u_4(r) = \begin{cases} r(14-r)/49 & ; 0 \leq r \leq 14 \\ 0 & ; \text{otherwise} \end{cases}$$



$$u_5(r) = e^{-(r-7)^2}$$

	$r = 6.95$	$r = 6.93$	$r = 4$
$u_1(r)$	1	0	0
$u_2(r)$	1	1	0.5600
$u_3(r)$	0.992	0.390	0.5714
$u_4(r)$	0.999	0.999	0.8163
$u_5(r)$	0.997	0.995	0.0001

These values invite several comments. Note first that fuzzy set membership increases as  $|r-7|$  decreases: the imprecise property "nearly 7" is ordered by  $u_2 - u_5$ . Thus,  $u_k(p) < u_k(q)$  implies  $|p-7| > |q-7|$  unless  $k = 1$  - i.e., the hard set  $u_1$  does not enable one to make comparisons of this kind. Suppose  $p = 1000$ ,  $q = 7.06$ . Then  $u_1(p) = u_1(q) = 0$ , but surely  $q$  is "more nearly 7" than  $p$ . Since we cannot extract this from hard set  $u_1$ , this constitutes a loss of information due to an inadequate model.

Second, we observe that the values of fuzzy membership functions not only order their arguments; but have magnitudes which allow continuous (decision) thresholding. Imagine  $B$  to be the basketball players in a certain city that are nearly 7 feet tall. You - the basketball coach at a distant college - decide to scout only those players for which  $u_k(r) > a$ ,  $0 \leq a \leq 1$ . The height brackets corresponding to several  $a$ 's are:

	$\alpha = 0.90$	$\alpha = 0.75$
$u_1$	[6.95, 7.05]	[6.95, 7.05]
$u_2$	[6.50, 7.50]	[5.00, 9.00]
$u_3$	[6.30, 7.70]	[5.25, 8.75]
$u_4$	[4.79, 9.21]	[3.50, 10.50]
$u_5$	[6.68, 7.32]	[6.47, 7.53]

Only hard set  $u_1$  has a fixed height bracket as  $\alpha$  varies. The fuzzy sets correspond to variable height brackets which depend continuously on  $\alpha$ . How would a specific model be chosen? By past experience - i.e., by observing performance on known data. Any of the four fuzzy sets might suffice for the coach's purpose once tested and fixed. Mathematical properties, e.g., continuity, differentiability, domain, may also be considered when choosing a fuzzy model. And hard set  $u_1$ ? If  $u_1(p) = 0$  with  $p = 6.949$  feet tall, you would miss this prospect completely.

Figures 4.2 and 4.3 illustrate the major differences between the hard and fuzzy models discussed in this example.

Another question that often arises concerns statistical models of this situation.

One may, of course, by experiment or otherwise, determine a probability distribution for players heights. Indeed, the normal distribution with mean  $\mu = 7$  and variance  $\sigma^2 = 1$  has for its probability density function (pdf)

$$f(r) = u_5(r) / \sqrt{2\pi} \quad (4.2)$$

Equation (4.2) suggests that  $f$  and  $u_5$  are "equivalent models". The philosophical meaning and inferences one may draw therefrom, however,

Figure 4.2 The Distinction Between Hard and Fuzzy Sets

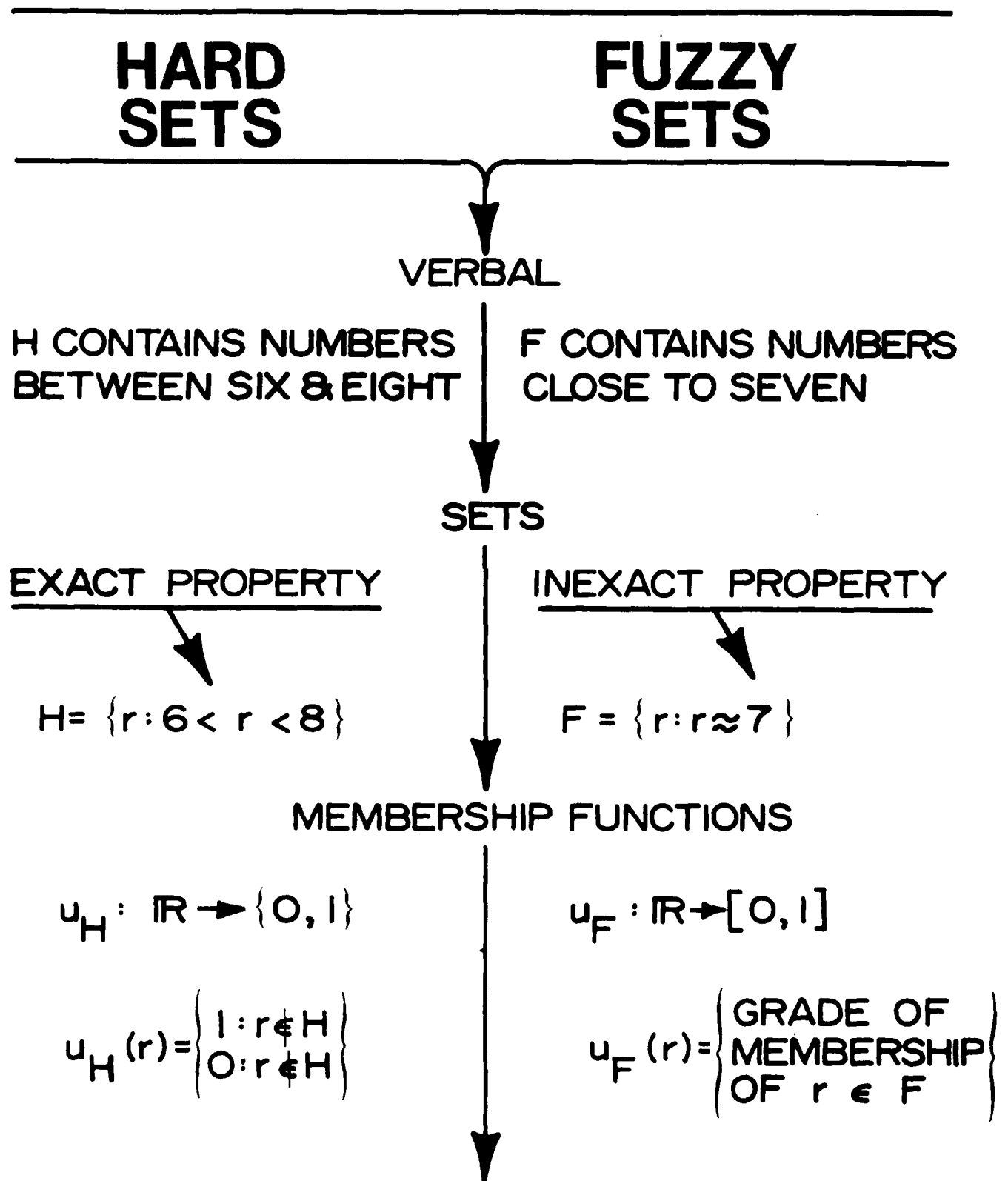
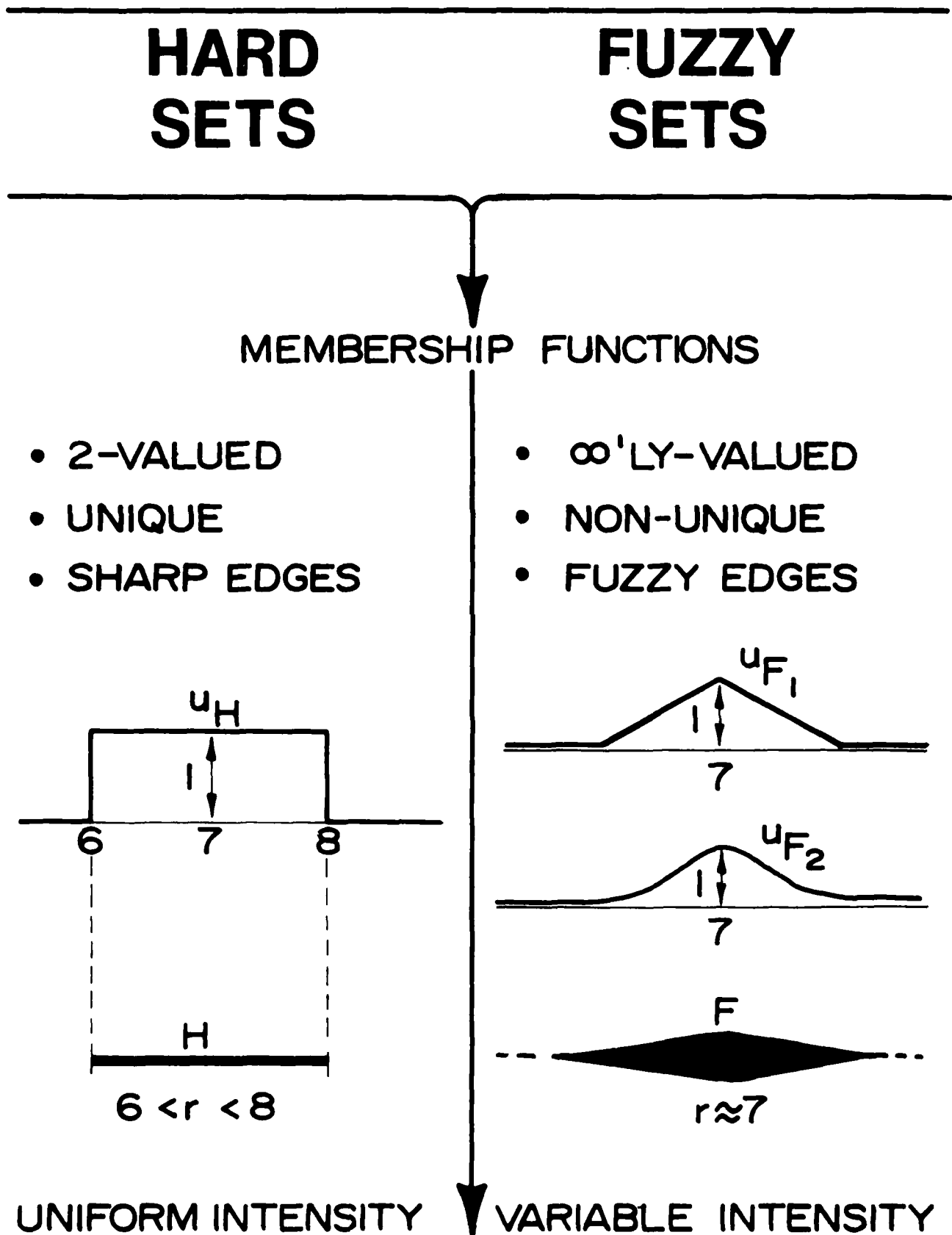


Figure 4.3 Membership Functions for Hard and Fuzzy Sets





are quite different. To see this, let  $S = [6.95, 7.05] = u_1$ , the hard set shown in Figure 4.1. In the present context,  $S = u_1$  in an event, with  $\Pr(u_1) = \Pr(S) \cong 0.04$ . What information about players heights does this convey? That, on the average, 4 players per 100 have height between 6.95 and 7.05. Suppose, for unobserved player  $p$ , you had two pieces of information:

$$\Pr(p \in S) = 0.90 \quad ; \quad \text{and} \quad (4.3a)$$

$$u_5(p) = 0.90 \quad . \quad (4.3b)$$

If you had to decide--shall I scout  $p$ ?--using (4.3a) or (4.3b), which would you use? From (4.3a), one can conclude that, with 90% certainty, the height of  $p$  is in  $[6.95, 7.05]$ : but (4.3a) also leaves a good chance that  $p$  is, say 4 feet, 6 inches tall! On the other hand, we have from (4.3b) and  $u_5(p)$  that  $p$ 's height is--with 100% certainty--in the range  $[6.68, 7.32]$ . The point? One can use either model as a basis for decisions; but surely the underlying types and amounts of information are different. As a final note, we observe that after observing  $p$ , we have:

$$\Pr(p \in S/p) = \begin{cases} 1 & ; \quad 6.95 \leq p \leq 7.05 \\ 0 & ; \quad \text{otherwise} \end{cases} = u_1(p) \quad ; \quad (4.4a)$$

$$u_5(p/p) = u_5(p) = 0.90 \quad . \quad (4.4b)$$

That is, statistical uncertainty is altered by observations; fuzzy uncertainty is not! What (4.2) really suggests is that normalized pdf's may provide, through their individual values, information which can be useful when interpreted in a non-standard way.

## 5. UNION, INTERSECTION, and COMPLEMENT

Let  $X$  be any hard set, and  $A, B$  be subsets of  $X$ . The union and intersection of  $A$  and  $B$  are:

$$A \cup B = \{ x \in X: x \in A \text{ or } x \in B \}, \quad (5.1 \text{ a})$$

$$A \cap B = \{ x \in X: x \in A \text{ and } x \in B \}. \quad (5.1 \text{ b})$$

The union symbol ( $\cup$ ) is often read "or;" the intersection symbol ( $\cap$ ) as "and." The complement of  $A$  in  $X$  is

$$\tilde{A} = \{ x \in X: x \notin A \}. \quad (5.1 \text{ c})$$

The complement symbol ( $\sim$ ) may be read as "not in."

It is both convenient and necessary to formally recognize the set with no objects as a subset of  $X$ . We call this set the empty set, and will denote it by the symbol ( $\emptyset$ ). If  $A \subset X$ ,  $\tilde{A} \subset X$  by (5.1 c). Substituting  $\tilde{A}$  for  $B$  in (5.1 a) and (5.1 b), we have

$$A \cup \tilde{A} = \{ x \in X: x \in A \text{ or } x \in \tilde{A} \} = X; \quad (5.2)$$

$$A \cap \tilde{A} = \{ x \in X: x \in A \text{ and } x \in \tilde{A} \} = \emptyset. \quad (5.3)$$

If  $A$  is itself non-empty, we have the three conditions

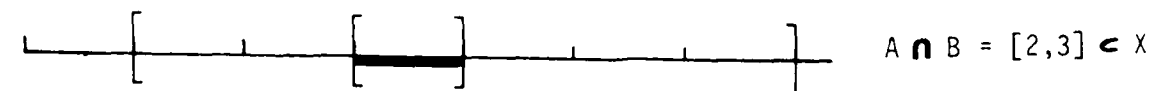
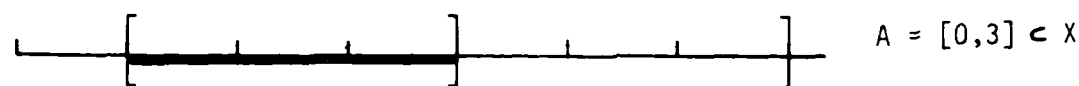
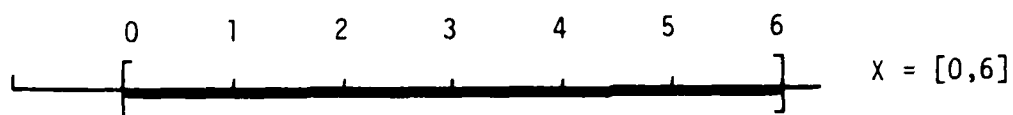
$$A \neq \emptyset; \quad (5.4 \text{ a})$$

$$A \cup \tilde{A} = X; \quad (5.4 \text{ b})$$

$$A \cap \tilde{A} = \emptyset, \quad (5.4 \text{ c})$$

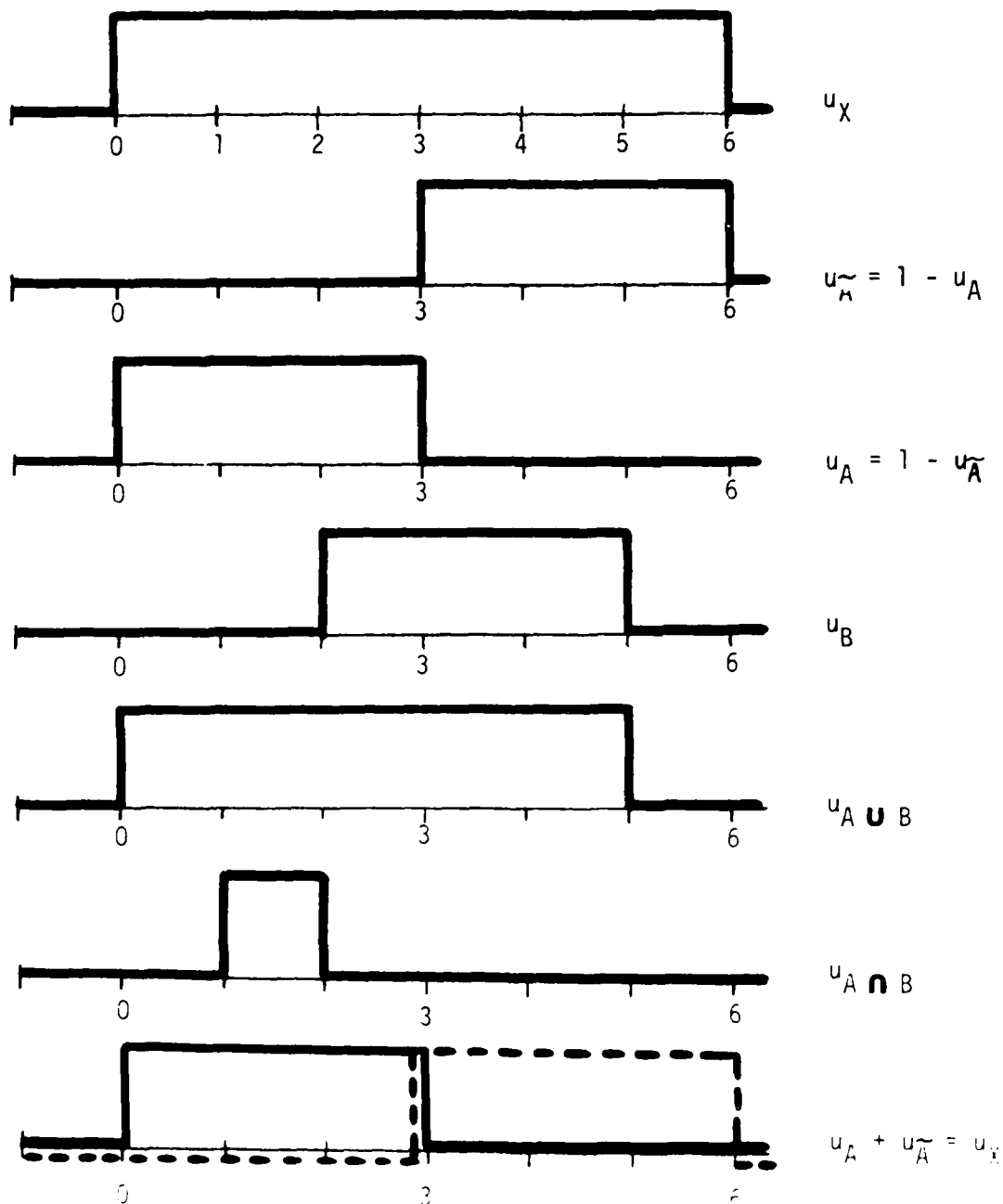
for the pair  $(A, \tilde{A})$  to be hard 2-partition of  $X$ .

Let  $X$  be the set of real numbers  $r$  for which  $0 \leq r \leq 6$ , i.e.,  $X = [0, 6]$ . Let  $A = [0, 3]$ , and  $B = [2, 5]$ : then  $\tilde{A} = (3, 6]$ , and:



A non-overlapping partition of  $X$

In this example, each of the hard sets involved has a unique membership function. The operations ( $\cup, \cap, \sim$ ) have logical equivalents in functional combinations: we can guess them by considering graphs of the membership functions:



For the union, we take the maximum of  $u_A$  and  $u_B$ ; for the intersection, the minimum: for the complement, we subtract  $u_A$  from 1:

$$u_{A \cup B}(r) = \max \{ u_A(r), u_B(r) \} ; \quad (5.5 \text{ a})$$

$$u_{A \cap B}(r) = \min \{ u_A(r), u_B(r) \} ; \quad (5.5 \text{ b})$$

$$u_{\widetilde{A}}(r) = 1 - u_A(r) . \quad (5.5 \text{ c})$$

These equations are entirely equivalent to (5.1 a - 5.1 c). They allow us to write equations (5.4) for a hard 2-partition of  $X$  as functional equations:

$$u_A \neq \mathbf{0} ; \quad (5.6 \text{ a})$$

$$u_A \cup \widetilde{A} = \mathbf{1} ; \quad (5.6 \text{ b})$$

$$u_A \cap \widetilde{A} = \mathbf{0} ; \quad (5.6 \text{ c})$$

where  $\mathbf{0}(r) = 0$ ,  $\mathbf{1}(r) = 1$ , i.e.,  $\mathbf{0} = u_{\emptyset}$ ;  $\mathbf{1} = u_X$ . Equations (5.5) and (5.6) suggest a reasonable way to define an algebra for fuzzy sets that includes hard models as a special case.

## 6. FUZZY UNION, INTERSECTION, and COMPLEMENT

The membership functions of  $A \cup B$ ,  $A \cap B$ , and  $\widetilde{A}$  are, for hard subsets  $A$  and  $B$  in  $X$ , known automatically, because the only questions concerning membership in these sets is "in or out," i.e., 0 or 1. For fuzzy subsets, however, one faces a choice: if  $u_A(x) = .62$ , and  $u_B(x) = .39$ , what values should be assigned for  $u_{A \cup B}(x)$ ,  $u_{A \cap B}(x)$ , and  $u_{\widetilde{A}}(x)$ ? These functions should map  $X \rightarrow [0,1]$ ; and, in addition, should reduce to the definitions of S5 whenever  $A$  and  $B$  are hard. Functions that satisfy both of these require-

ments are obtained by imitating equations (5.5): for fuzzy subsets A and B of X, we define

$$u_{A \cup B}(x) = \max\{u_A(x), u_B(x)\} ; \quad (6.1 \text{ a})$$

$$u_{A \cap B}(x) = \min\{u_A(x), u_B(x)\} ; \quad (6.1 \text{ b})$$

$$u_{\tilde{A}}(x) = 1 - u_A(x) \quad . \quad (6.1 \text{ c})$$

These definitions are not unique: they do, however, endow the subsequent axiomatic structure with useful properties for pattern recognition models.

To illustrate these definitions, let

$$X = \text{numbers between 6 and 10} \quad ; \quad X = [6, 10]$$

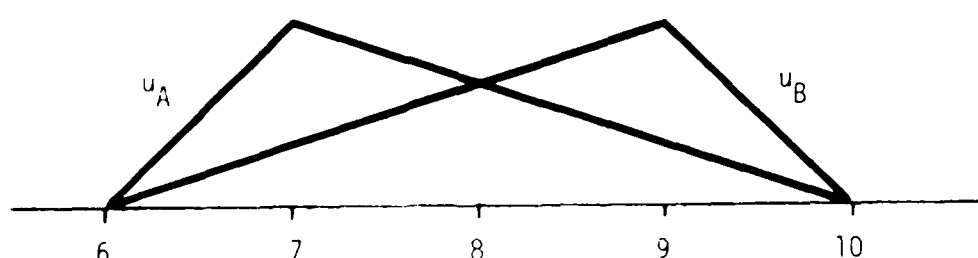
$$A = \text{numbers close to 7 in } X \quad ;$$

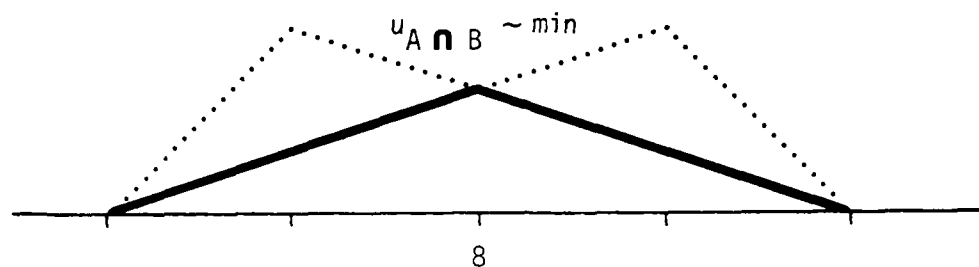
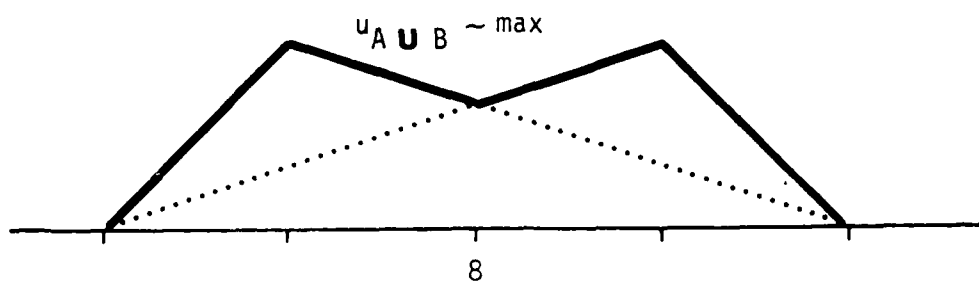
$$B = \text{numbers close to 9 in } X \quad ;$$

$$u_A(x) = \left\{ \begin{array}{ll} x - 6 & ; \quad 6 \leq x \leq 7 \\ (10-x)/3 & ; \quad 7 < x \leq 10 \end{array} \right\} ;$$

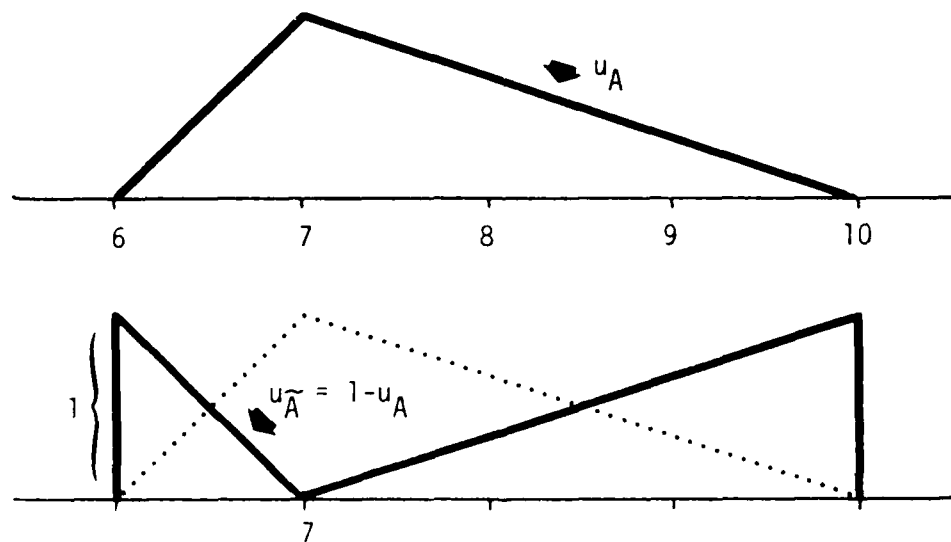
$$u_B(x) = \left\{ \begin{array}{ll} (x-6)/3 & ; \quad 6 \leq x \leq 9 \\ 10 - x & ; \quad 9 < x \leq 10 \end{array} \right\} .$$

Graphs of  $u_{A \cup B}$  and  $u_{A \cap B}$  are found by choosing the max and min of  $u_A$  and  $u_B$  at each  $x \in X$ :





The complement of  $u_A$  is the difference  $(1-u_A)$ :



Note that  $u_A(8) = u_B(8) = u_A \cup B(8) = u_A \cap B(8) = 2/3 = 0.66$ . The number 8 has the highest grade of membership in the fuzzy intersection of A and B. This is interpreted as: 8 is the number in X which is "most

nearly 7" and "most nearly 9." Now consider the fuzzy union of  $A$  and  $\tilde{A}$ . Using equations (6.1 a) and (6.1 c), we have

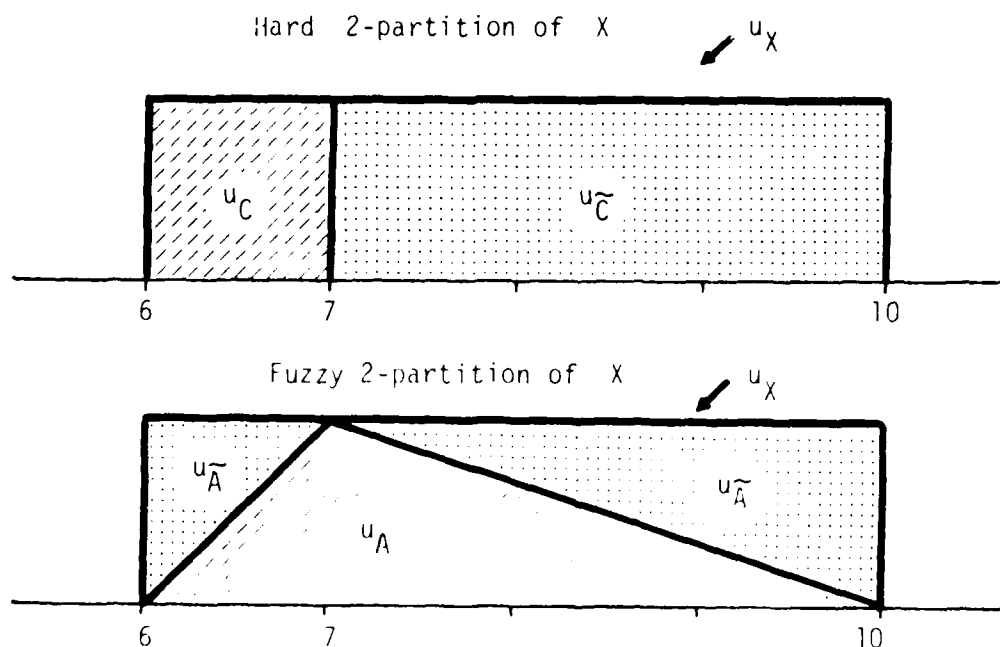
$$u_{A \cup \tilde{A}}(x) = \max \{u_A(x), 1 - u_A(x)\}.$$

For example,  $u_{A \cup \tilde{A}}(6) = \max \{0, 1\} = 1$ ;  $u_{A \cup \tilde{A}}(6.5) = \max \{0.5, 0.5\} = 0.5$ .

The latter value shows that equation (5.6 b) cannot be true for the union of an arbitrary fuzzy set  $A$  and its complement, i.e.,  $u_{A \cup \tilde{A}} \neq 1$ . The

same argument applies to the intersection:  $u_{A \cap \tilde{A}}(6) = \min \{0, 1\} = 0$ ;

$u_{A \cap \tilde{A}}(6.5) = \min \{0.5, 0.5\} = 0.5$ , so, in general,  $u_{A \cap \tilde{A}} \neq 0$ . Equations (5.6 b) and (5.6 c) do not generalize - this is, of course, exactly as we had planned! To see what has remained constant, let  $C = [6, 7]$  and  $\tilde{C} = (7, 10]$  partition  $X$ :  $C \cap \tilde{C} = \emptyset$ ;  $C \cup \tilde{C} = X$ . We compare the graphs of  $(u_C, u_{\tilde{C}})$  to  $(u_A, u_{\tilde{A}})$  in terms of the areas of  $u_C$  and  $u_A$  under  $u_X = 1$ :



Evidently hard sets  $(C, \tilde{C})$  divide the area under  $u_X$  abruptly at  $x = 7$ ; whereas  $(A, \tilde{A})$  partition it in a continuous fashion as a function of  $x$ . That



is, hard and fuzzy 2-partitions of  $X$  correspond to different kinds of hard 2-partitions of the area under the graph of  $u_v$  (different ways to allocate membership in partitioning subsets). The illustration above shows how to circumvent the apparent dilemma caused by  $u_A \cup \tilde{A} \neq \mathbf{1}$ ;  $u_A \cap \tilde{A} \neq \mathbf{0}$ . Requirement (5.6 a), that  $u_A \neq \mathbf{0}$ , is equivalent to having non-zero area under  $u_A$  (and hence  $u_{\tilde{A}}$ ): this is met by both  $(A, \tilde{A})$  and  $(C, \tilde{C})$ . And secondly, we see that, at each  $x \in X$

$$u_C(x) + u_{\tilde{C}}(x) = u_A(x) + u_{\tilde{A}}(x) = 1. \quad (6.2)$$

This equation, true by definition for two fuzzy subsets, suggests a reasonable way to define and interpret fuzzy  $c$ -partitions of  $X$  for  $c > 2$  partitioning subsets. Conditions (5.6) can be replaced by the two equations

$$u_A \neq \mathbf{0} \quad ; \quad (6.3 \text{ a})$$

$$u_A + u_{\tilde{A}} = \mathbf{1} \quad . \quad (6.3 \text{ b})$$

Equations (6.3) are equivalent to (5.6) for hard sets via (5.5), and consistent for fuzzy sets via (6.1 c). Accordingly, we shall call  $(A, \tilde{A})$  a fuzzy 2-partition of  $X$  in the sense of equations (6.3). Figures 6.1 and 6.2 summarize graphically the important distinctions between hard and fuzzy 2-partitions of  $X$ .

Figure 6.1 Hard and Fuzzy 2-Partitions of X

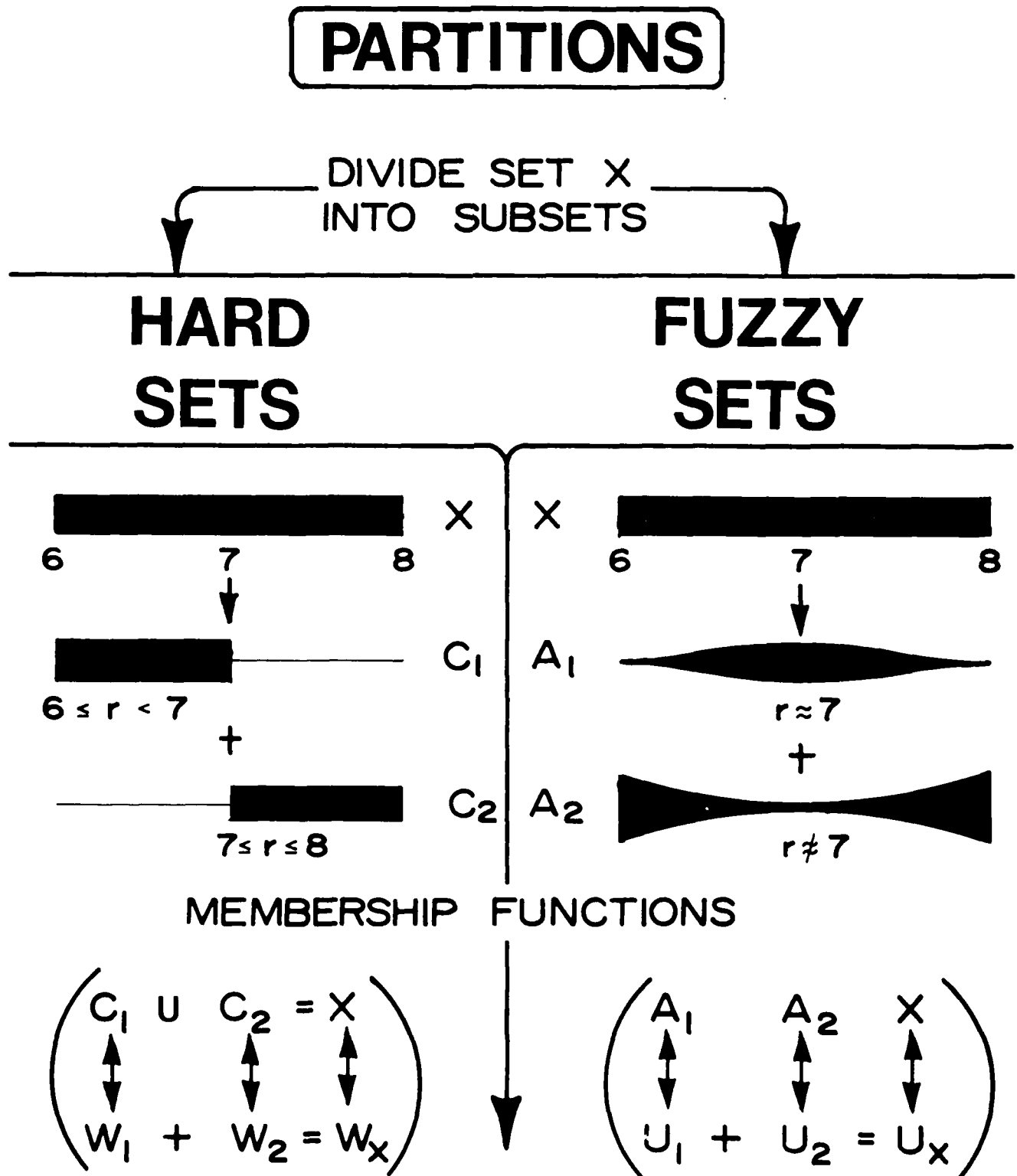
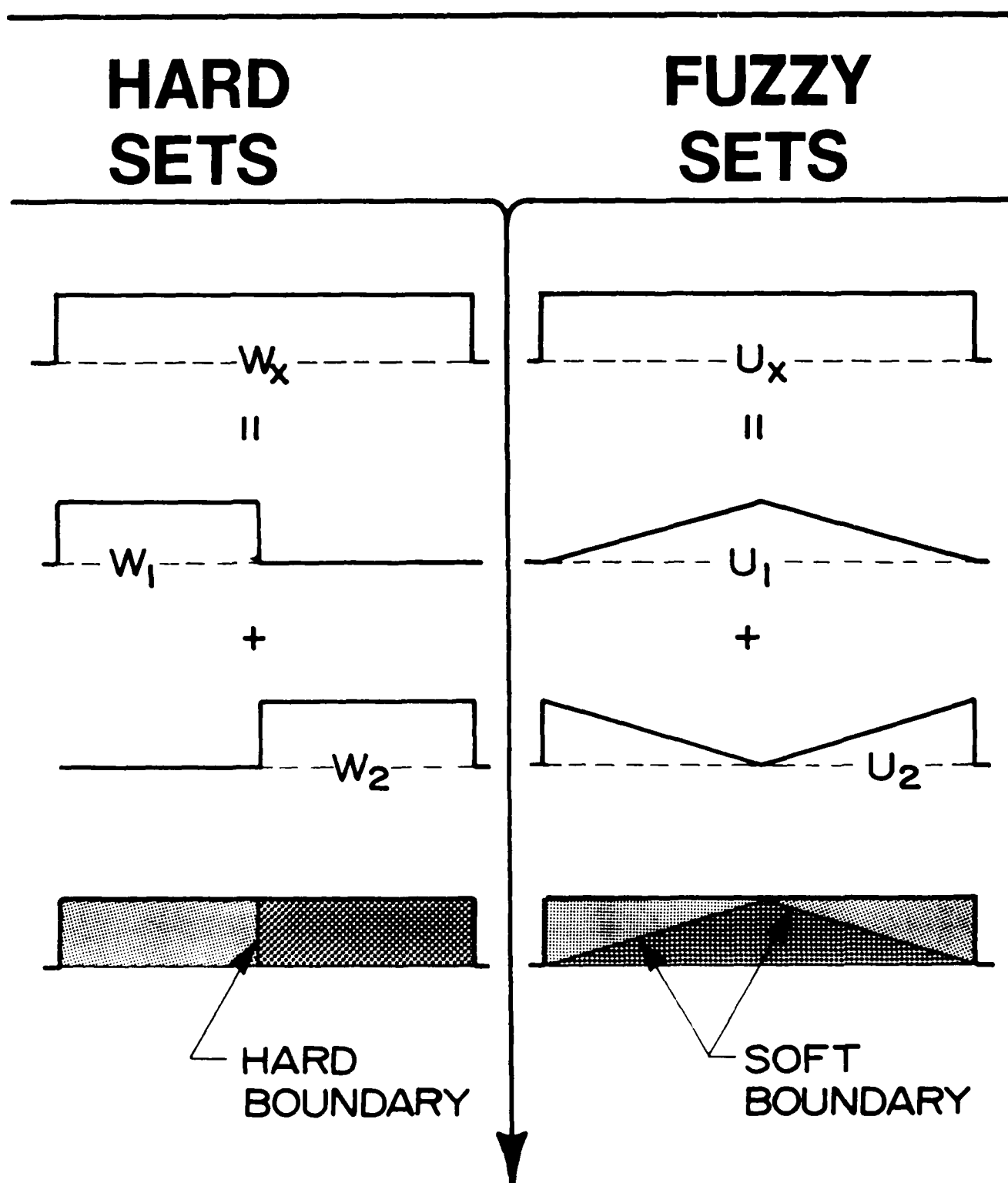


Figure 5.2 Hard and Fuzzy Partitioning Membership Functions



## 7. MATHEMATICS OF c-PARTITIONS

Let  $X$  be a set. A collection of hard subsets  $\{A_1, A_2, \dots, A_c\}$  of  $X$  is a hard  $c$ -partition of  $X$  if

$$A_k \neq \emptyset \quad \text{for all } k \quad ; \quad (7.1 \text{ a})$$

$$\bigcup_{k=1}^c A_k = X \quad ; \quad (7.1 \text{ b})$$

$$A_j \cap A_k = \emptyset \quad \text{for all } j \neq k \quad ; \quad (7.1 \text{ c})$$

These equations reduce to (5.4) when  $c = 2$ . Now let  $u_k$  be the membership function of  $A_k$ , so that, for  $k = 1, 2, \dots, c$ ,

$$u_k(x) = \begin{cases} 1; & x \in A_k \\ 0; & \text{otherwise} \end{cases} . \quad (7.2)$$

Then  $\{A_1, A_2, \dots, A_c\}$  is equivalent to  $\{u_1, u_2, \dots, u_c\}$ . In particular, equations (7.1) are equivalent to

$$u_k \neq 0 \quad \text{for all } k \quad ; \quad (7.3 \text{ a})$$

$$\sum_{k=1}^c u_k = 1 \quad . \quad (7.3 \text{ b})$$

These equations reduce to (6.3) when  $c = 2$ . Since  $A_k$  and  $u_k$  are entirely equivalent, we may call the set of functions  $\{u_1, u_2, \dots, u_c\}$  a hard  $c$ -partition of  $X$ .

Each  $u_k$  in (7.3) maps  $X$  into  $\{0, 1\}$ . Suppose now that one or more of these functions maps  $X$  into  $[0, 1]$  - i.e., is a fuzzy subset of  $X$ . In this case, equations (7.1) are meaningless; but conditions (7.3) can still be enforced. Thus, we define a fuzzy  $c$ -partition of  $X$  to be any set

of membership functions on  $X$  into  $[0,1]$  that satisfy (7.3). This definition yields a fuzzy model with the desired properties, and reduces to the hard model when all the subsets are hard; but it allows partial membership of individuals in one or more partitioning subsets when physical characteristics of objects imprecisely define their individual identities. As an example, let

$$X = [6,10] = [6,7] \cup [7,9] \cup (9,10] = \bigcup_{k=1}^3 C_k ;$$

$$A_1 = \text{numbers close to 7 in } X$$

$$A_2 = \text{numbers close to 9 in } X$$

where the membership functions of  $A_1$  and  $A_2$  are scaled down to  $(1/3)$  of their values in the previous example:

$$u_1(x) = \begin{cases} \frac{x-6}{3} & ; \quad 6 \leq x \leq 7 \\ (10-x)/9 & ; \quad 7 < x \leq 10 \end{cases} ;$$

$$u_2(x) = \begin{cases} (x-6)/9 & ; \quad 6 \leq x \leq 9 \\ (10-x)/3 & ; \quad 9 < x \leq 10 \end{cases} ;$$

Now  $u_1(x) + u_2(x) < 1$  for every  $x \in X$  - no object in the original data has full membership in  $X$ . To complete the area under  $u_X$ , we use (7.3b) to find  $u_3(x) = 1 - u_1(x) - u_2(x)$ :

$$\begin{aligned} \underline{6 \leq x \leq 7} : \quad u_3(x) &= 1 - (x-6)/3 - (x-6)/9 \\ &= (33-4x)/9 \end{aligned}$$

$$\begin{aligned} \underline{7 < x \leq 9} : \quad u_3(x) &= 1 - (10-x)/9 - (x-6)/9 \\ &= 5/9 \end{aligned}$$

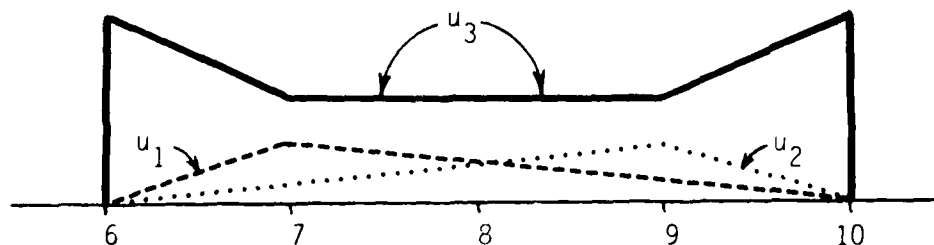
$$\underline{9 < x \leq 10}: \quad u_3(x) = 1 - (10-x)/9 - (10-x)/3 \\ = (4x-31)/9$$

$$\implies u_3(x) = \left\{ \begin{array}{ll} (33-4x)/9 & ; \quad 6 \leq x \leq 7 \\ 5/9 & ; \quad 7 < x \leq 9 \\ (4x-31)/9 & ; \quad 9 < x \leq 10 \end{array} \right\}.$$

For example, at  $x = 8$ ,  $u_1(8) = 2/9$ ,  $u_2(8) = 2/9$ ,  $u_3(8) = 5/9$ ,  $\sum u_k(8) = 1$ .  
Graphs of the membership functions  $(u_1, u_2, u_3)$  are shown below. A rough interpretation of the physical meaning of  $u_3$  can be given in terms of the functional equation  $u_3 = 1 - u_1 - u_2$ :

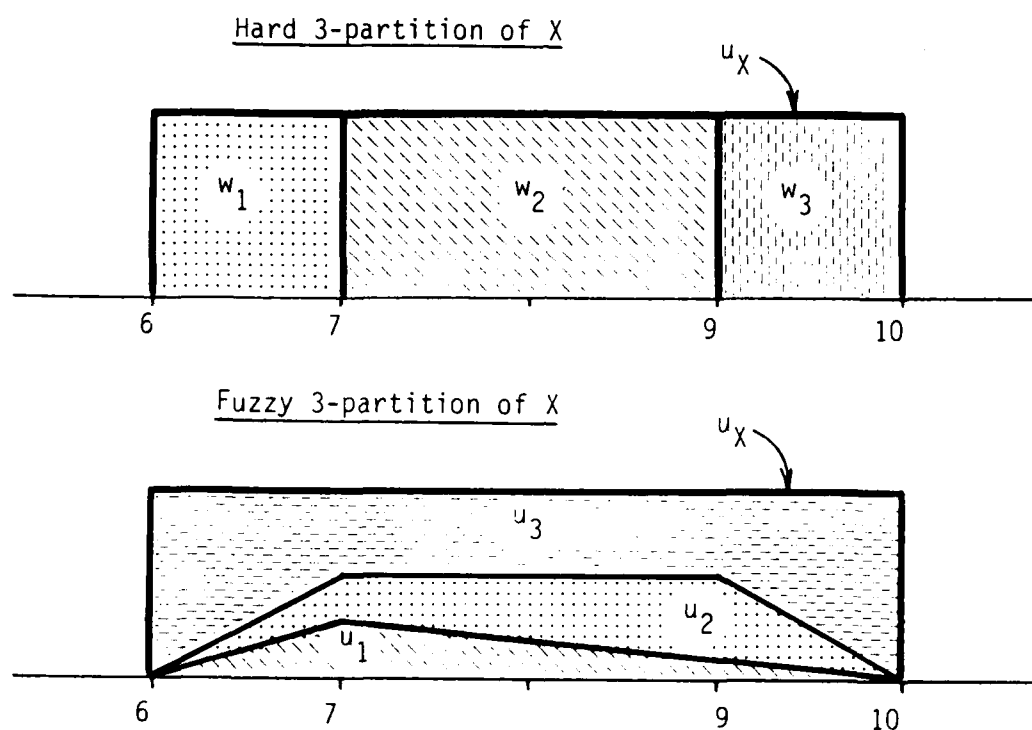
$$u_3 = \left( \begin{array}{c} \text{numbers} \\ \text{in} \\ X \end{array} \right) - \left( \begin{array}{c} \text{numbers} \\ \text{close to} \\ 7 \text{ in } X \end{array} \right) - \left( \begin{array}{c} \text{numbers} \\ \text{close to} \\ 9 \text{ in } X \end{array} \right) \\ = u_X - u_1 - u_2 \\ = (\text{numbers in } X \text{ not close to 7 and not close to 9})$$

The graph (of  $u_3$ ) shown below is compatible with this interpretation of  $u_3$ .



To exemplify the difference between this fuzzy 3-partition of  $X$  and any hard one, let  $C_1 = [6,7)$ ,  $C_2 = [7,9]$ , and  $C_3 = (9,10]$  partition  $X$ , with

hard membership functions  $w_1, w_2, w_3$ , respectively. Again comparing these partitions in terms of how they divide up the total membership in  $X$ , we depict the areas under  $u_X$  which are accounted for by each membership function as follows:



Observe that hard c-partitions again subdivide the total membership with hard boundaries (vertical unit jumps); whereas fuzzy boundaries provide a means for continuous, partial membership allocation.

## 8. PARTITION MATRICES

Let  $X = \{x_1, x_2, \dots, x_n\}$  be a finite data set. Each "point"  $x_j \in X$  might be almost any sampled feature of a physical process: a digital picture matrix, medical record, sonar signal, or polygonal shape descriptor are a few examples. Let  $(u_1, u_2, \dots, u_c)$ ,  $2 \leq c \leq n$  partition  $X$ , and denote by

$u_{kj}$  the grade of membership of  $x_j$  in class  $k$ , i.e., for all  $k, j$  define

$$u_{kj} = u_k(x_j) = \text{membership of } x_j \text{ in class } k \quad (8.1)$$

Next, array the  $(cn)$  numbers  $u_{kj}$  as the entries of a  $c \times n$  matrix

$$U = [u_{kj}]:$$

$$U = \begin{bmatrix} u_{11} & u_{12} & \dots & u_{1j} & \dots & u_{1n} \\ u_{21} & u_{22} & \dots & u_{2j} & \dots & u_{2n} \\ \vdots & \vdots & \ddots & \vdots & \ddots & \vdots \\ u_{k1} & \dots & u_{k2} & \dots & u_{kj} & \dots & u_{kn} \\ \vdots & \vdots & \vdots & \ddots & \vdots & \ddots & \vdots \\ u_{c1} & u_{c2} & \dots & u_{cj} & \dots & u_{cn} \end{bmatrix}$$

row  $k$ : (membership of every  $x_j$  in subset  $k$ )

column  $j$ : (membership of  $x_j$  in each of the  $c$  subsets)

The constraints which correspond to equations (7.3) for matrix  $U$  are easy to deduce.  $u_k \neq \mathbf{0}$  simply means that each subset has some membership, hence, each row of  $U$  has a non zero entry, or, since  $u_{kj} \geq 0$ , all  $k, j$ , that each rowsum is positive:

$$u_k \neq \mathbf{0} \iff \sum_{j=1}^n u_{kj} > 0 \quad \text{for all } k \quad (8.2a)$$

Equation (7.3b) requires the sum of the membership of each  $x_j$  to be 1: for the matrix  $U$ , each column sum is 1:

$$\sum_{k=1}^c u_k = \mathbf{1} \iff \sum_{k=1}^c u_{kj} = 1 \quad \text{for all } j \quad (8.2b)$$



Finally, we know that  $(u_1, u_2, \dots, u_c)$  is a hard  $c$ -partition of  $X$  only when every  $u_{kj} \in \{0, 1\}$ ; and is a fuzzy  $c$ -partition of  $X$  in case any  $u_{kj} \in [0, 1]$ . Adding this requirement to those of (8.2) yields definitions for partition matrices which are entirely equivalent to (7.3): The sets of all possible  $(c \times n)$  matrices corresponding to hard and fuzzy  $c$ -partitions of  $X$  we call  $M_c$  and  $M_{fc}$ , respectively:

$$M_c = \left\{ U: u_{kj} \in \{0, 1\}; \sum_j u_{kj} > 0; \sum_k u_{kj} = 1 \right\} \rightarrow \text{HARD.} \quad (8.3a)$$

$$M_{fc} = \left\{ U: u_{kj} \in [0, 1]; \sum_j u_{kj} > 0; \sum_k u_{kj} = 1 \right\} \rightarrow \text{FUZZY.} \quad (8.3b)$$

To illustrate, let  $X$  be a set of two peaches ( $x_1, x_2$ ); a nectarine ( $x_3$ ); and two plums ( $x_4, x_5$ ). For  $c = 2$ , if the peaches and plums are separated correctly, there are only 2 hard 2-partitions of  $X$ :

$$\begin{array}{l} \text{peaches} \dots\dots\dots \\ \text{plums} \dots\dots\dots \end{array} \begin{array}{c} x_3 \\ U_1 = \begin{bmatrix} 1 & 1 & \textcircled{1} & 0 & 0 \\ 0 & 0 & 0 & 1 & 1 \end{bmatrix} \end{array} ; \quad \text{and}$$

$$\begin{array}{l} \text{peaches} \dots\dots\dots \\ \text{plums} \dots\dots\dots \end{array} \begin{array}{c} x_3 \\ U_2 = \begin{bmatrix} 1 & 1 & 0 & 0 & 0 \\ 0 & 0 & \textcircled{1} & 1 & 1 \end{bmatrix} \end{array} .$$

Membership value  $u_{13} = 1$  in  $U_1$ : this assigns the nectarine to the peaches subset. In  $U_2$ , exactly the opposite occurs. In either case, this illustrates a serious deficiency of hard 2-partitions of  $X$ : they cannot portray partial relationships between individuals in the data. A much more realistic model

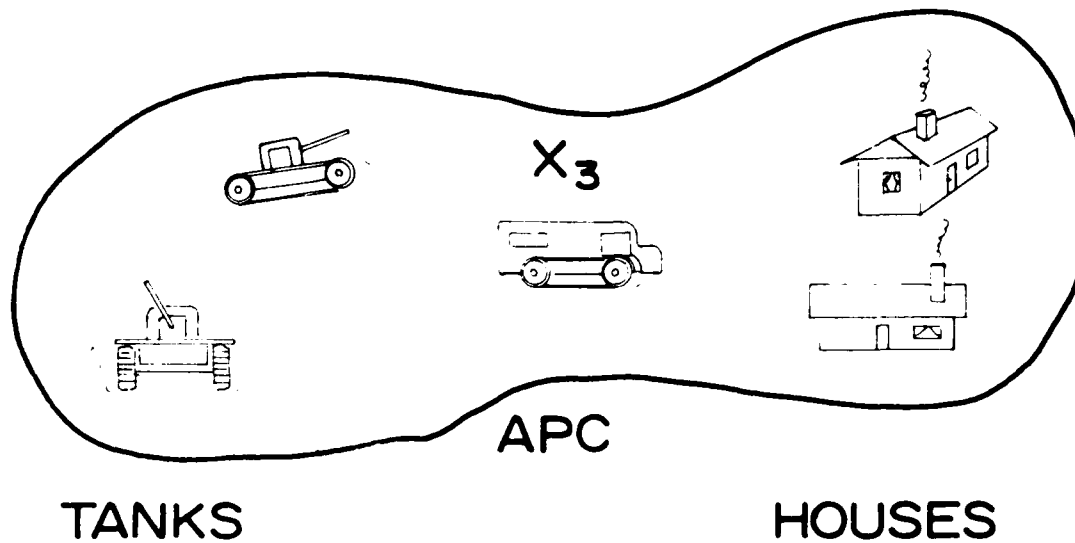
of the physical situation is given by fuzzy 2-partitions of  $X$ . One could have, in this case, a partitioning such as:

$$U_3 = \begin{matrix} & & x_3 & & \\ \begin{bmatrix} 0.96 & 1 & 0.61 & 0.05 & 0.03 \\ 0.04 & 0 & 0.39 & 0.95 & 0.97 \end{bmatrix} & & \blacktriangle \blacktriangledown & & \end{matrix}$$

Loosely speaking, about 61% of this nectarine's features are "peachlike"; and 39% are "plumlike". Is  $U_3$  more realistic than  $U_1$  or  $U_2$ ? Yes. Is it more useful? Yes. One cannot threshold decisions against 0's and 1's. Hard models present a much higher potential for classification errors, because 0's and 1's afford no means for deciding when to take a "second look". To emphasize this point, suppose the matrix  $U_3$  had for its major classes "pictures with tanks" and "pictures without tanks". Then pictures 1 and 2 almost certainly have tanks, while 4 and 5 do not. Picture 3, however, has memberships in these classes which might be -based on past experience with similar data- regarded as "suspicious". One could, e.g., decide to expend extra computing time on  $x_3$ , before rendering a decision about the contents of the picture. Figure 8.1 illustrates how this situation might arise. In the diagram,  $x_3$  is an armored personnel carrier (APC): it has some very tanklike features (round wheels, treads, profile); and some houselike features (windows, profile). Accordingly, the observed characteristics of an APC will probably contain a mixture of the dominant characteristics of tanks and houses. In this example, the advantage of fuzzy c-partitions--the ability to defer a decision based on non-distinctive membership values--is quite clear.

This concludes our tutorial exposition of the axiomatic structures underlying many fuzzy models for pattern recognition and image processing. Interested readers may consult [2] for a detailed discussion of variations,

Figure 8.1 An Example of Mixed Substructures



$$U = \begin{bmatrix} 1 & 1 & \textcircled{1} & 0 & 0 \\ 0 & 0 & 0 & 1 & 1 \end{bmatrix} \begin{matrix} \longrightarrow \text{TANKS} \\ \longrightarrow \text{HOUSES} \end{matrix}$$

$$\longrightarrow X_3 = \text{TANK}$$

$$U = \begin{bmatrix} 1 & 1 & 0 & 0 & 0 \\ 0 & 0 & \textcircled{1} & 1 & 1 \end{bmatrix}$$

$$\longrightarrow X_3 = \text{HOUSE}$$

HARD PARTITIONS CAN OBSCURE IMPORTANT PHYSICAL RELATIONSHIPS

refinements, and alternative constructions arising from this basic foundation. We again emphasize that the choice of a particular model (and algorithm to utilize it) should be made with a view towards casting the physical situation in a most natural quantitative framework. We turn now to a summary of recent work and specific examples which exemplify the utility of this new type of mathematical model.

## 9. THE FUZZY C-MEANS ALGORITHMS

In this section we discuss the fuzzy c-means (FCM) clustering algorithms. These algorithms have been utilized for clustering, classification, and feature selection in a wide variety of applications. Software for these algorithms is currently available in several high level languages, so the discussion below centers on the theoretical foundation of the methods, rather than documentation for a specific program.

A classifier is a set of  $c$  scalar fields (or discriminant functions) from feature space  $\mathbb{R}^W \rightarrow \mathbb{R}$ , say  $\{d_1, d_2, \dots, d_c\}$ , which partition  $\mathbb{R}^W$  into a  $c$  hard decision regions, say  $\{\mathbf{D}_1, \mathbf{D}_2, \dots, \mathbf{D}_c\}$ , according to the requirement that  $d_j(\underline{x}) > d_i(\underline{x})$  for all  $i \neq j$  and all  $\underline{x} \in \mathbf{D}_j$ . Any set of functions which does this equips  $\mathbb{R}^W$  with the decision rule

$$\begin{aligned} \text{decide } \underline{x} \in i & \iff \underline{x} \in \mathbf{D}_i \\ & \iff d_i(\underline{x}) > d_j(\underline{x}), \\ & \quad \text{all } j \neq i. \end{aligned} \tag{9.1}$$

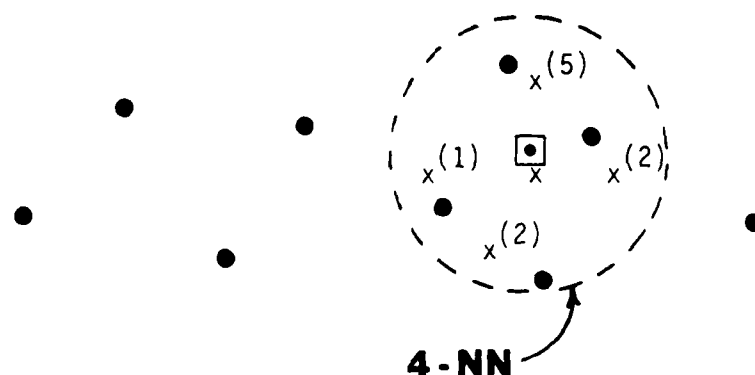
The use of (9.1) in connection with computerized classification of feature vectors  $\underline{x} \in \mathbb{R}^W$  is obvious: what is not so obvious is how

to choose the functions  $\{d_j\}$ . Usually, one secures a "training" data set  $X = \{\underline{x}_1, \underline{x}_2, \dots, \underline{x}_n\} \subset \mathbb{R}^W$  of feature vectors drawn from the physical process of interest, and tries to identify an "optimal" set of  $d_j$ 's--i.e.,  $d_j$ 's which minimize the probability of making a wrong identification. There are two kinds of probability of error: theoretical and empirical. Models based on minimizing theoretical error rates enjoy favor in academic circles, but do not necessarily outperform classifiers which are theoretically sub-optimal, because finite samples need not possess asymptotic properties. Consequently, empirical error rates--that is, observed performance on labelled test sets--are a more useful measure of expected classifier performance than are theoretically predicted probabilities of error. When using the empirical error rate, however, one should guard carefully against generalizing observed classifier performance to other samples; or worse, other physical processes. The best approach to take in classification is to study the problem at hand, and then try to choose a design which minimizes the empirical error rate for labelled samples of the process in hand.

The example to follow is condensed from reference [4]: it compares the performance of a well known deterministic classifier--the k-nearest neighbor (k-NN) design--to a fuzzy 1-nearest prototype (1-NP) model. The k-NN design is a simple classifier based on measuring the distance (Euclidean or otherwise) in feature space  $\mathbb{R}^W$  between any observed  $\underline{x}$  and its k nearest neighbors in a set of labelled data. Let  $X$  be hard c-partition, say  $X = \cup_{i=1}^c X_i$ ,  $1 \leq i \leq c$ , so that each  $\underline{x}_k \in X$  bears the label of its population class. The decision rule for the k-NN model is formulated in terms of the given hard c-partition of  $X$ :

$$\text{decide } \underline{x} \in \text{class } i \iff \left\{ \begin{array}{l} \text{among the } k\text{-nearest neighbors} \\ \text{of } \underline{x} \text{ in } X, \text{ class } i \text{ is observed} \\ \text{more often than } j, j=1, c, j \neq i. \end{array} \right\} \quad (9.2)$$

Here  $k$  is an integer,  $1 \leq k \leq n$ . As  $n \rightarrow \infty$ , (9.2) converges (in probability) to the "Bayesian classifier", which is theoretically optimal for a well defined probability of error based on the assumption that  $X$  is drawn from a mixture of  $c$  multivariate probability density functions. Accordingly, the  $k$ -NN classifier is a popular design. Two drawbacks:  $n$  never " $\rightarrow \infty$ "; and  $X$  may not be drawn from the hypothesized mixture. The geometric idea of the  $k$ -NN classifier is easy to illustrate: let  $\underline{x}_j^{(i)}$  be observation  $j$  in  $X$ , labelled as class  $i$ , and, to be concrete, let  $k=4$ :



Since class 2 occurs twice, while classes 1 and 5 occur once each in  $k=4$  tries,  $\underline{x}$  is identified as a class 2 object. The functions  $\{d_j\}_{k\text{-NN}}$  have not been identified, but are easy to define once  $X$  is labelled.

A 1-NP classifier operates by minimizing distances in  $\mathbb{R}^W$  from object  $\underline{x}$  to one of  $c$  prototypes, say  $\{\underline{v}_1, \underline{v}_2, \dots, \underline{v}_c\}$ , where  $\underline{v}_i$  is a vector of features which characterizes the "perfect" member of

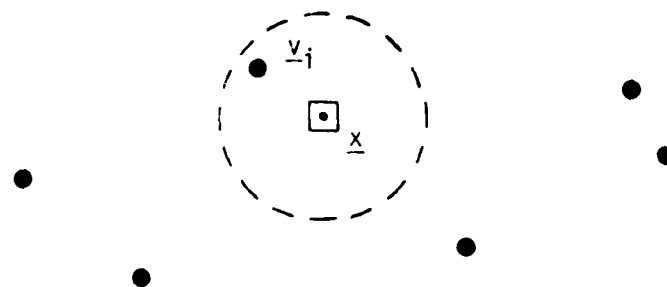
class  $i$ . If  $X$  is labelled, and  $n$  is large, the usual prototypes chosen are simply the geometric centroids of each  $X_i$ :

$$\underline{v}_i = \left( \sum_{\underline{x}_k \in X_i} \underline{x}_k \right) / n_i, \quad (9.3)$$

where  $n_i$  is the number of feature vectors in  $X_i$ ,  $1 \leq i \leq c$ . The quality of the data (amount of noise), features chosen, choice of distance measure, and reliability of observed unidentified vectors all affect the performance of the 1-NP classifier defined by the  $\underline{v}_i$ 's, which may be written as [5]:

$$d_i(x) = \langle \underline{x}, \underline{v}_i \rangle - \left( \frac{\|\underline{v}_i\|^2}{2} \right); 1 \leq i \leq c, \quad (9.4)$$

where  $\langle \cdot, \cdot \rangle$  and  $\|\cdot\|$  are, respectively, the chosen dot product and norm on  $\mathbb{R}^w$ . Implementation of (9.1) with (9.4) is illustrated as follows:



If  $X$  is unlabelled, the  $\underline{v}_i$ 's cannot be calculated with (9.3). In this case (and often, even when the  $\underline{v}_i$ 's are labelled), some other method for estimating good prototypes is needed. Many methods exist (c.f. [5]): each produce a set of  $\underline{v}_i$ 's optimal in some mathematical sense. But once the  $\underline{v}_i$ 's are fixed, equation (9.4)

always yields a 1-NP classifier. Thus, many 1-NP classifiers exist, all of which partition  $\mathbb{R}^W$  into  $c$  decision regions. The choice of a particular design (i.e., set of  $\underline{v}_j$ 's) ultimately rests with the empirical error rate--which one works best?

One way to generate  $\underline{v}_j$ 's--called fuzzy prototypes below--is by the fuzzy c-means (FCM) clustering algorithms. Let  $U$  be any fuzzy  $c$ -partition of  $X$ ; and let  $\underline{v} = (\underline{v}_1, \underline{v}_2, \dots, \underline{v}_c)$  be a set of  $c$  "cluster centers" in  $\mathbb{R}^W$ . For  $1 \leq m < \infty$ , define

$$J_m(U, \underline{v}) = \sum_{k=1}^n \sum_{i=1}^c (u_{ik})^m \|\underline{x}_k - \underline{v}_i\|^2 ; \quad (9.5)$$

$\|\bullet\|$  being here any inner product norm on  $\mathbb{R}^W$ . Local minima of  $J_m$  may identify good fuzzy  $c$ -partitionings of  $X$ , and must satisfy (c.f. [6]):

$$\underline{v}_i = \left( \sum_{k=1}^n (u_{ik})^m \underline{x}_k \right) / \left( \sum_{k=1}^n (u_{ik})^m \right) ; \quad (9.6a)$$

$$u_{ik} = \left( \sum_{j=1}^c \left( \frac{\|\underline{x}_k - \underline{v}_i\|}{\|\underline{x}_k - \underline{v}_j\|} \right)^{2/(m-1)} \right)^{-1} ; \quad m < 1 < \infty \quad (9.6b)$$

Equations (9.6) provide a way to seek local minima of  $J_m$  via iterative looping; and in particular, "good" geometric configurations in  $X$  lead to good prototypical  $\underline{v}_j$ 's with (9.6a). The advantage of (9.6a) is this: fuzzy NP's are determined algorithmically in conjunction with fuzzy  $c$ -partitions of  $X$ --and fuzzy  $c$ -partitions of  $X$  have soft



boundaries, so are relatively insensitive to noisy data and imprecisely defined subclasses. This can endow classifiers based on (9.1) and (9.4) using fuzzy prototypes (9.6a) with better error rate properties than those based on hard c-partitions of  $X$ .

EXAMPLE 1. Reference [4] discusses a data set of  $n = 300$  binary vectors, each containing 11 measured symptoms of a patient with one of  $c = 6$  stomach diseases. This data was also processed by Toussaint, who reported in [6] an estimate of the expected empirical error rate for all  $k$ -NN classifiers (as  $k, n \rightarrow \infty$ ) that use the 300 labelled samples for the neighbors. His estimate of the error rate (presumably the optimal rate of a Bayesian classifier!) was 49%. Using the same data with a fuzzy 1-NP design based on (9.1), (9.4), and (9.6a), the expected error rate reported in [4] was reduced to 39%. For this data set, then, a fuzzy 1-NP classifier yielded more accurate results than all  $k$ -NN classifiers. This implies (but cannot prove!) that data generated by this physical system are more amenable to fuzzy designs than to conventional ones. Presumably this is due to the ability of fuzzy c-partitions to accomodate imprecisely defined and/or noisy observations in this data.

A second problem considered in [4] which uses the data in a different way concerns the relative efficiency of the features measured for subclass separation. The actual values of prototypical features of the vectors  $\underline{v}_i$  calculated via (9.6a) can be used--for binary data--to rank the discriminatory power of the various measurements. The object of "feature selection" (the usual term for this undertaking) is to reduce the dimensionality of feature space with no loss in

classification power, thereby decreasing computational complexity without sacrificing classifier performance. The fuzzy feature selection method described in [4] reduced  $\mathbb{R}^{11}$  to  $\mathbb{R}^5$  with no appreciable increase in expected error rates. Further, the features selected were identical to the ones chosen by a hard method discussed by Lee in [7].

This example supports an important conclusion: when data has distinctive substructure, hard and fuzzy models can and do yield the same results (feature selection): but if substructure is imprecise or noisy, fuzzy partitions may provide better results than hard ones.

EXAMPLE 2. A different use for the FCM algorithm embodied by equations (9.5)-(9.6) has been discussed in reference [8]. This application of fuzzy partitioning also involves classifier design: in particular, Bayesian classifiers, the theoretically optimal scheme. Let data  $X$  be drawn from the mixed parametric  $w$ -variate probability density function (pdf)

$$f(\underline{x}; \underline{\theta}) = \sum_{j=1}^c p_j g(\underline{x}; \theta_j) , \quad (9.7)$$

where  $\underline{\theta} = (\theta_1, \theta_2, \dots, \theta_c)$  is a vector of parameters;  $p_j$  = prior probability of class  $j$ ; and  $g(\underline{x}; \theta_j)$  = pdf of class  $j$ . A Bayesian classifier for  $X$  is any set of  $c$  scalar fields  $\{d_j\}$  which are monotonic functions of the posterior probability of class  $j$  given  $\underline{x}$ :

$$d_j(\underline{x}; \underline{\theta}) = F(p(j|\underline{x}; \underline{\theta})) = F(p_j \cdot g(\underline{x}; \theta_j) / f(\underline{x}; \underline{\theta})) . \quad (9.8)$$

If the parameters  $[\theta_j]$  are known, (9.8) with (9.1) yields the theoretically optimal Bayesian classifier, say  $\{d_{jB}\}$ , which minimizes the error rate (volume under the "tails" outside each  $D_{jB}$  defined by  $d_{jB}$  with (9.7)). The function  $F$  in (9.8) may be, for example, the identity on  $\mathbb{R}$ ; often, the logarithmic function is used for  $F$ . If  $\theta$  is unknown, one uses  $X$ —a sample from (9.7)—to estimate  $\theta$ . Again, we call this "training" the classifier. If  $X$  is labelled, the best method for estimating each  $\theta_j$  with  $X_j$  is probably obtained by uncoupled maximum likelihood estimators (MLE). If  $X$  is not labelled, the MLE for  $(\theta_j)$  are coupled, necessitating numerical solutions. The equations for both cases appear in [8]: they are rather complex, so are omitted here. If  $g(\underline{x}; \theta_j)$  is multivariate normal with mean  $\mu_j$ , covariance matrix  $V_j$ , then  $\theta_j = (p_j, \mu_j, V_j)$  is coupled through Baye's rule to the matrix of posterior probabilities  $P = [p(\underline{x}_k | j)]$ ,  $1 \leq k \leq n$ ,  $1 \leq j \leq c$ , and MATRIX  $P$  IS A FUZZY C-PARTITION OF  $X$ ! Iteration through the ML equations, viz.,  $(p_j \triangleright \mu_j \triangleright V_j \triangleright P)$  to secure estimates for the parameters of the component pdf's is very time-consuming: e.g., each step of the MLE loop must construct  $c$  scalars;  $c$  w-vectors;  $c$  wxw matrices and their inverses; and the cxn matrix  $P$ . The results reported in [8] supported two conclusions: (i) iteration through (9.6) provides fuzzy c-partitions which are excellent initial guesses for  $P$  at a significant savings in time and expense compared to starting ML iteration from scratch; and (ii) optimal pairs  $(U, \underline{v})$  for  $J_m$  are in fact reasonable estimates of  $(P, \mu)$  without resort to ML at all!

In other words, parametrizing (9.8) via fuzzy c-means with  $X$  may be more efficient than with maximum likelihood. The resultant classifier might be called a fuzzy-1-NP Bayesian classifier: [8] shows that it is a very efficient estimate of the ML-1-NP design.

## 10. SHAPE DESCRIPTION

Let  $B = \{ \underline{b}_1, \underline{b}_2, \dots, \underline{b}_n \} \subset \mathbb{R}^2$  be a data set of ordered boundary coordinates of an arbitrary planar shape. Data of this type arise in many image processing applications: see, for example, references [9] and [10]. One way to analytically describe the boundary of a planar shape is with a set of  $c$  approximating line segments  $\{ L_i = \{ \underline{v}_i + t \underline{d}_i : a_i \leq t \leq b_i, 1 \leq i \leq c \} \}$ , where  $\underline{v}_i$  is a point on  $L_i$  (its "nucleus"), and  $\underline{d}_i$  is a unit vector parallel to  $L_i$  (its "direction"). Many approaches exist for generating an "optimal" set of  $L_i$ 's (see reference [10]). Reference [9] describes in detail a fuzzy model for generating such sets of "edge descriptors". This algorithm is based (in part) on a generalization of the FCM method discussed in S9. A weighted least-squared errors function of three sets of variables, viz., a fuzzy c-partition  $U$  of  $B$ ; a vector  $\underline{v} = (\underline{v}_1, \underline{v}_2, \dots, \underline{v}_c)$  of segment nuclei; and a vector  $\underline{d} = (\underline{d}_1, \underline{d}_2, \dots, \underline{d}_c)$  of segment directions, is iteratively minimized to generate "optimal" linear fuzzy clusters in  $B$ , together with a set of  $c$  line segments that are a good (orthogonal) least squares fit to the data. This algorithm is now fully operational, and seems to perform at least as well as the best conventional algorithms reported in [10]. A rough idea of its relative performance

can be inferred from the illustrations depicted on Figures 10.1 and 10.2, which show a data set B of 124 points drawn randomly from the continuous cell outline shown as Figure 4 in [10]. View (a) is the raw data. View (b) shows the polygonal approximations to B generated by Ramer's algorithm (c. f. [17]) with hard orthogonal least square fitting (after Fig. 5 of [10]). The solution of view (b) has  $c = 9$  segments. We observe that the solutions of views (b) and (c) taken from [10] were obtained using a different sample of 124 points from the cell outline than those shown in view (a). Since the cell has 64 vertices in a relatively short perimeter, the two samples have, in all probability, about the same visual configurations.<sup>1</sup> A comparison of Fig. 4 [10] with view (a) confirms this, as both data sets have marked "gaps" in the same places.

View (c) shows the output of the split and merge method described in [10] (after Fig. 7 of [10]). This solution has  $c = 10$  segments, and seems to be a substantial improvement over the Ramer solution. View (d) is the output of the fuzzy shapefitting algorithm when applied to data set B. Here, there are  $c = 16$  segments, so the resolution is understandably better. Reported mean squared errors in [10] are ambiguous, so do not afford a means for direct comparisons. However, it seems safe to say that the fuzzy output is, for the data set shown in view (a), a visually appealing fit that reproduces the shape of B somewhat more faithfully than the hard outputs depicted in views (b) and (c). A more direct comparison in terms of both time and accuracy will be available soon.

---

<sup>1</sup>The original data are not available. The algorithms used in [10] are currently being coded to afford a more direct comparison of accuracy and efficiency.

Figure 10.1 Shape Description

Ref [10] PAVLIDIS, T., and HOROWITZ, S. "Segmentation of Plane Curves," IEEE Trans. Comp., c-26, 1977, 236-242.

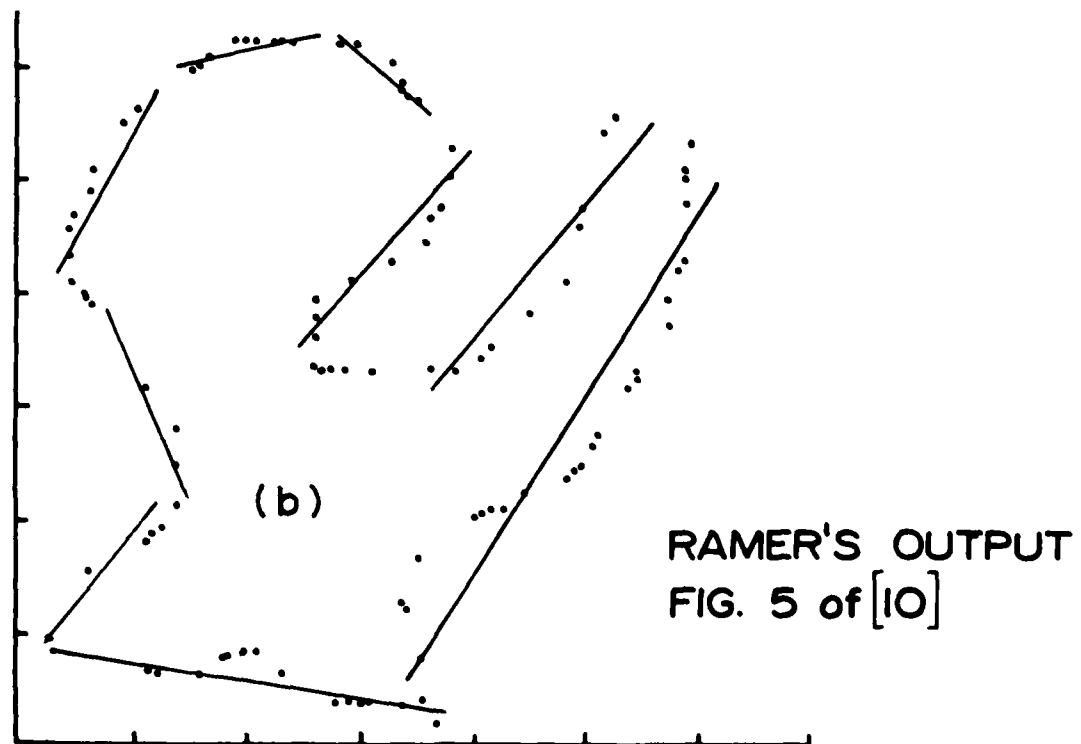
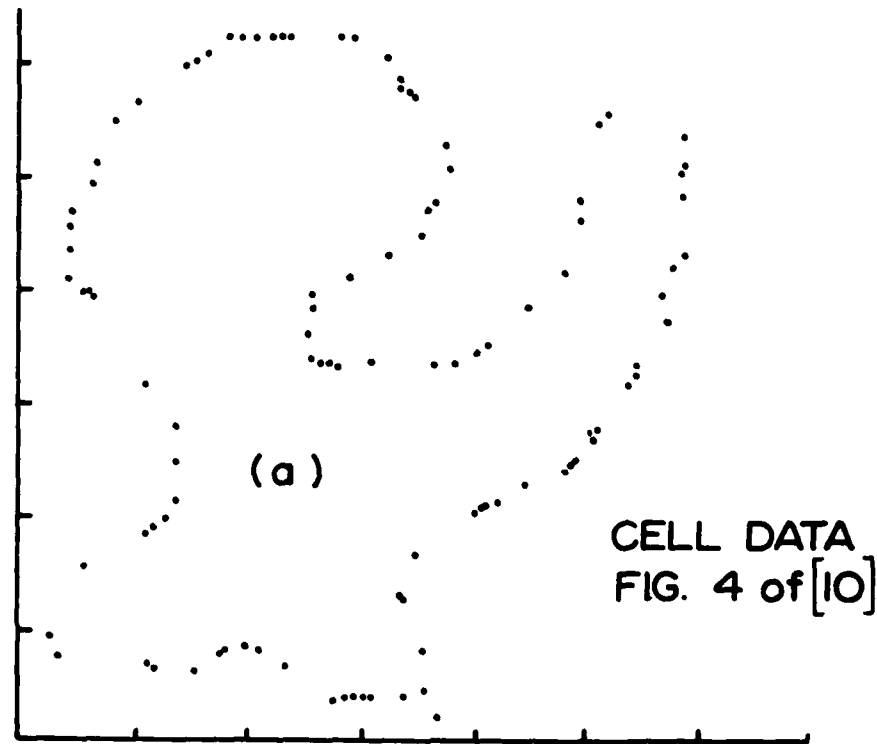
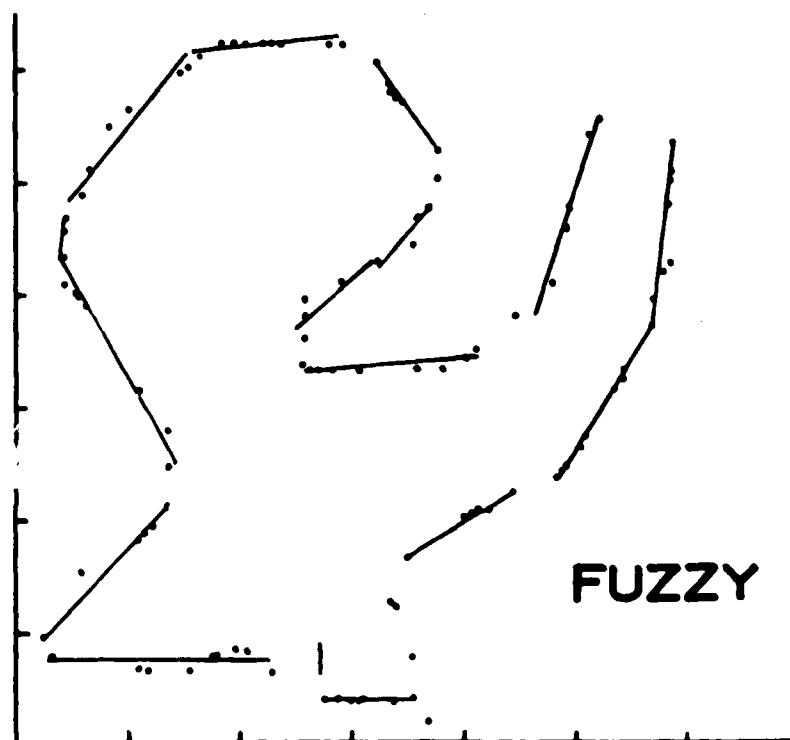
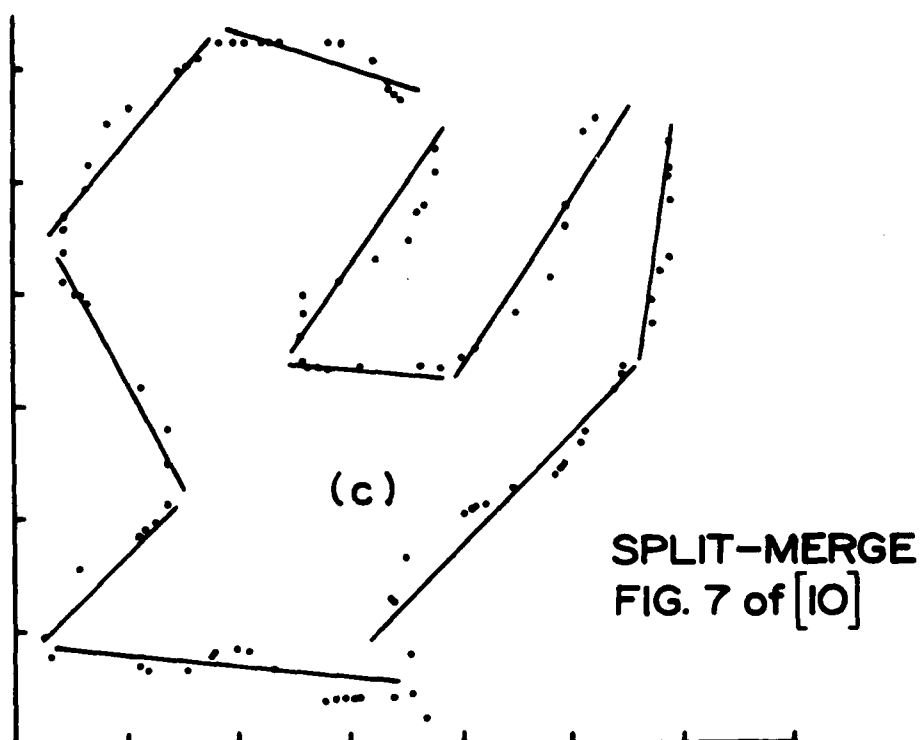


Figure 10.2 Shape Description



Another aspect of shape description algorithms is their sensitivity to noise. A slight variation of the algorithm is described at length in references [18, 19]. In order to understand the example below, we write out the functional: for  $m \in [1, \infty)$ , let

$$J_m(U, \underline{v}, \underline{d}) = \sum_{k=1}^n \sum_{i=1}^c (u_{ik})^m (a D_{ik}^2 + (1-a) d_{ik}^2), \quad (10.1)$$

where  $a \in [0, 1]$  is a mixing coefficient, and

$D_{ik}$  = the orthogonal distance from  $\underline{b}_k$  to  $L_i$  ;

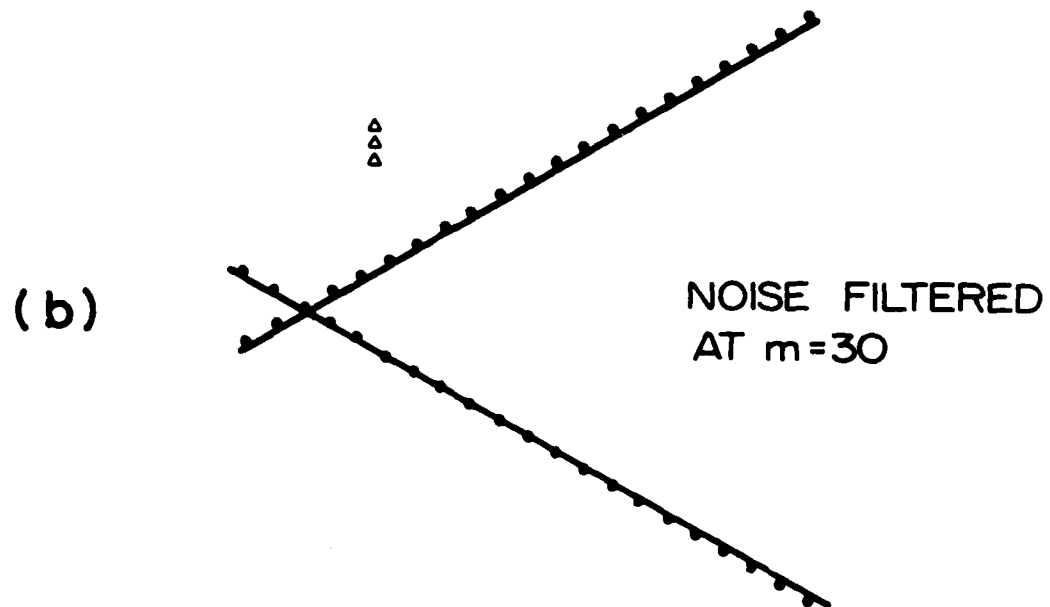
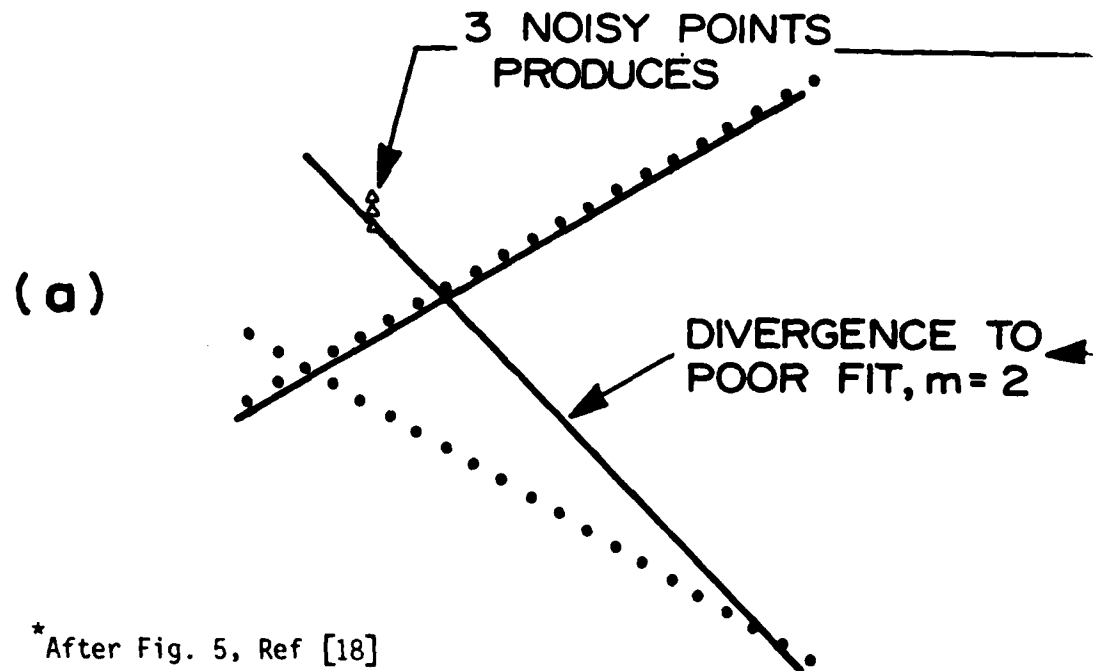
$d_{ik}$  = the Euclidean distance from  $\underline{b}_k$  to  $\underline{v}_i$  on  $L_i$  .

The algorithm finds good shape-approximating segments by minimizing the function in (10.1). Figure 5 of [18] is replicated as Figure 10.3. In view (a) are 43 points who clearly made up a set of two straight lines (the "jaws")--but with 3 noisy points. The effects of the 3 noisy points are quite severe: the lines shown in view (a) are the terminal lines from BH with initialization at the correct answer! In other words, the squared errors due to the 3 noisy points are sufficient to draw one "optimal" line away from the main linear substructure in the data. Here, the weighting exponent  $m$  in (10.1) was  $m = 2$ .

View (b) of AII.3 shows the terminal lines associated with BH output for the same data set at  $m = 30$ . The fit to the main substructure is nearly exact--i.e., the effects due to noise shown in (a) have been almost entirely eliminated. How do fuzzy memberships achieve this filtration? Consider the effect of increasing the weighting exponent  $m$  on columns of  $U$ . Because noise is not "close" to the linear structures



Figure 10.3 Shape Description



FUZZY MEMBERSHIPS CAN FILTER  
NOISY DATA

in the data, noisy points will have higher partial membership in several lines, rather than dominant membership in one. For example:

$$\begin{array}{ccc}
 \underline{b}_j \text{ on jaw} & & \underline{b}_k \text{ in noise} \\
 \begin{pmatrix} .91 \\ .09 \end{pmatrix} & & \begin{pmatrix} .63 \\ .37 \end{pmatrix} \\
 \downarrow & (u_{ik}) \longrightarrow (u_{ik})^{10} & \downarrow \\
 \begin{pmatrix} .3894 \\ 3E - 11 \end{pmatrix} & & \begin{pmatrix} .00984 \\ .00004 \end{pmatrix}
 \end{array}$$

The point? If  $\underline{b}_j$  has a strong affinity for membership in  $u_i$  (and  $L_i$ ), then  $u_{ik}$  dominates the values in column  $k$  of  $U$ . Raising these values to a higher power of  $m$  will drive the  $u_{jk}$ 's,  $j \neq i$ , to zero, leaving only  $u_{ik}$  to affect  $J_m$ . On the other hand, noisy memberships will all go to zero, because one entry is not dominant. In this way, membership itself can be used to filter noise. There is, to our knowledge, NO analogous hard method which possesses this potential: accordingly, the ability of fuzzy models to accomodate noise seems to be a decided advantage when processing noisy data.

## 11. SUMMARY

Sections 9 and 10 document several recent uses of emerging models based on fuzzy sets. From the point of view of PAME users, the fuzzy algorithms of sections 9 and 10 are perhaps most widely tested, and are currently available in useable form. These algorithms have a lot of flexibility, and can be adapted to a wide

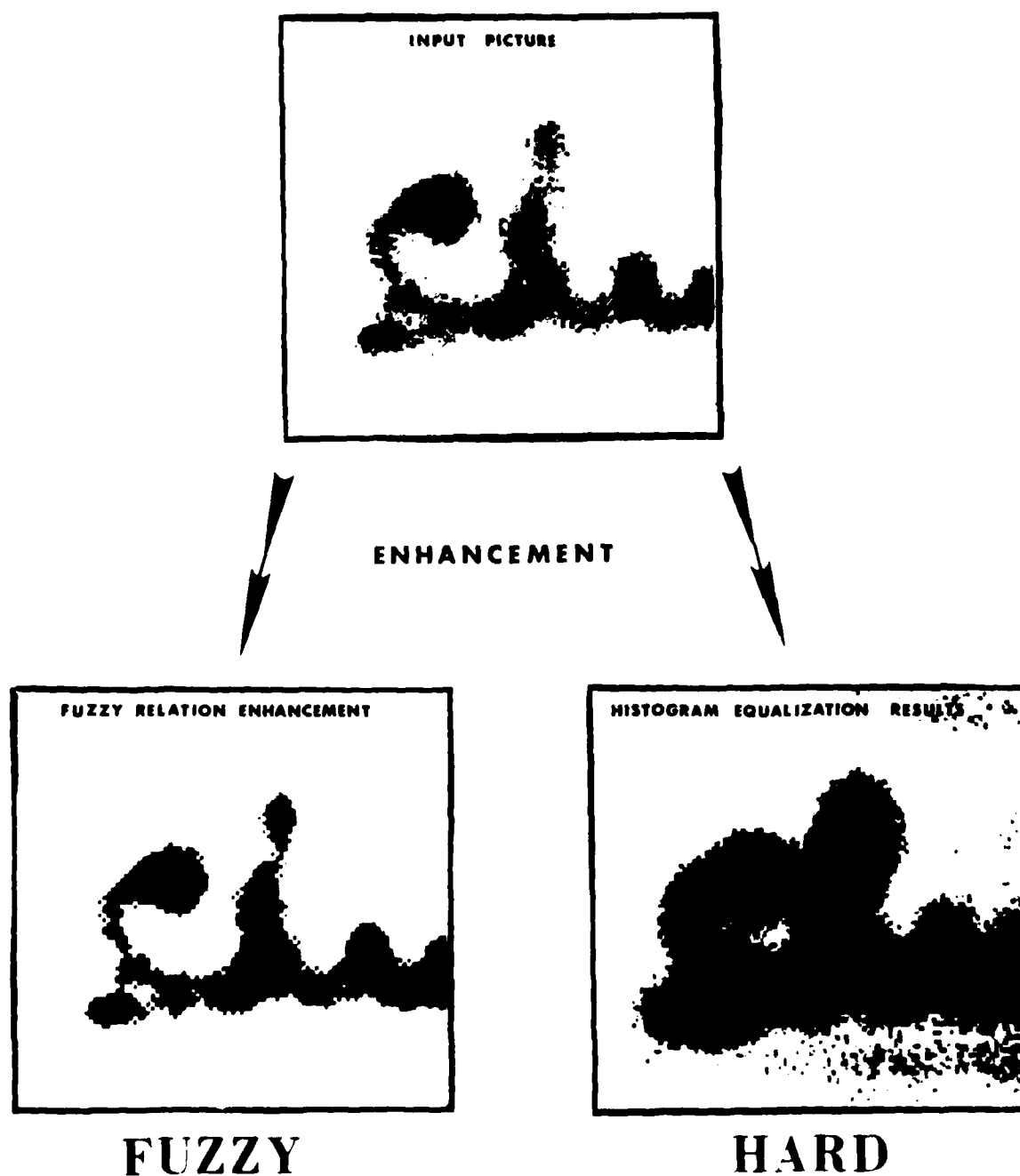
variety of applications, many of which were discussed by speakers from the Ocean Science community.

Many other applications of fuzzy algorithms are now appearing in the pattern recognition literature. One of great utility to several workshop attendees concerns (image) enhancement of ocean scenes based on sonar data. There are, of course, many conventional enhancement techniques. Reference [11] contains a nice comparison of a fuzzy method based on relational iteration that seems to work very well. Figure 11.1 illustrates this graphically (hard copy reproduction degrades all of the photographic results). It would be premature to say that fuzzy enhancement schemes will be consistently more reliable than those now in use. On the other hand, the nature of enhancement suggests that fuzzy models are a natural vehicle for this application, so this area seems ripe for accelerated development. Another area that will see rapid strides is segmentation of digital images.

In retrospect, the success of the workshop will hinge on initiation of specific contact between members of the ocean science and pattern recognition communities. The potential for fruitful interaction is enormous: the realization of this potential is our responsibility.

Figure 11.3 Fuzzy Image Enhancement

Ref. PAL,S. and KING,R. "Image Enhancement Using Smoothing with Fuzzy Sets", IEEE Trans. SMC-11(7), 1981, 494-501.



## REFERENCES

- [1] Zadeh, L. "Fuzzy Sets", *Inf. and Cont.*, 8, 1965, 338-353.
- [2] Bezdek, J. C., Pattern Recognition with Fuzzy Objective Function Algorithms, Plenum, New York, 1981.
- [3] Bezdek, J. C., and Harris, J. D., "Fuzzy Partitions and Relations: An Axiomatic Basis for Clustering", *Fuzzy Sets/Systems*, 1, 1978, 111-127.
- [4] Bezdek, J. C., and Castelaz, P., "Prototype Classification and Feature Selection with Fuzzy Sets", *IEEE Trans. SMC-7*(2), 1977, 87-92.
- [5] Duda, R., and Hart, P., Pattern Classification and Scene Analysis, Wiley, New York, 1974.
- [6] Toussaint, G., and Sharpe, P., "An Efficient Method for Estimating the Probability of Misclassification Applied to a Problem in Medical Diagnosis", *Comp. Bio. Med.*, 4, 1975, 269-278.
- [7] Lee, R. C. T., "Application of Information Theory to Select Relevant Variables", *Math. Biosci.*, 11, 1971, 153-161.
- [8] Bezdek, J. C., and Dunn, J. C., "Optimal Fuzzy Partitions: A Heuristic for Estimating the Parameters in a Mixture of Normal Distributions", *IEEE Trans. Comp.*, 1975, 835-838.
- [9] Bezdek, J. C., and Anderson, I., "Fuzzy Image Processing", Technical Report K35001, BAC, October 15, 1981.
- [10] Pavlidis, T., and Horowitz, R. "Segmentation of Plane Curves", *IEEE Trans. Comp. C-26*, 1977, 236-242.
- [11] Pal, S., and King, R., "Image Enhancement Using Smoothing with Fuzzy Sets", *IEEE Trans. SMC-11*(7), 1981, 494-501.
- [12] Gonzalez, R., and Wintz, P., Digital Image Processing, Addison-Wesley, Reading, 1977.
- [13] Rosenfeld, A., "Fuzzy Graphs", in Fuzzy Sets and their Applications to Cognitive and Decision Processes, L. A. Zadeh, et. al., eds., Academic Press, New York, 1975.
- [14] Zadeh, L.A., "Similarity Relations and Fuzzy Orderings," *Inf. Sci.*, 3, 1971, 177-200.

- [15] Kandel, A., and Yelowitz, L., " Fuzzy Chains", IEEE Trans. SMC, 1971, 61-66.
- [16] Bezdek, J. C., Spillman, R., and Spillman, R., "A Fuzzy Relation Space for Group Decision Theory", Fuzzy Sets/Systems, 1, 1978, 255-268.
- [17] Ramer, U., "An Iterative Procedure for the Polygonal Approximation of Plane Curves", Jo. Comp. Graphics and Image Processing, 1, 1972, 244-256.
- [18] Bezdek, J. C., Coray, C., Gunderson, R., and Watson, J., "Detection and Characterization of Cluster Substructure I. Linear Structure: Fuzzy c-Lines", SIAM Jo. Appl. Math., 40(2), 1981, 339-357.
- [19] \_\_\_\_\_, "Detection and Characterization of Cluster Substructure II. Fuzzy c-Varieties and Convex Combinations Thereof", SIAM Jo. Appl. Math., 40(2), 358-372.

# The Use of Satellite Observations of the Ocean Surface in Commercial Fishing Operations

D. R. Montgomery

Jet Propulsion Laboratory  
California Institute of Technology  
4800 Oak Grove Drive  
Pasadena, California 91109

## ABSTRACT

Commerical fishermen are interested in the safety of their crews, boats and gear, and in making the best catch for their time and money. Rising fuel costs, increased competition from foreign fisheries, improved knowledge about fish habits and the new 200-mile economic zone have all had an impact on the U.S. fishing industry. As a consequence, the modern fisherman, more than ever, requires reliable and timely information about the marine environment.

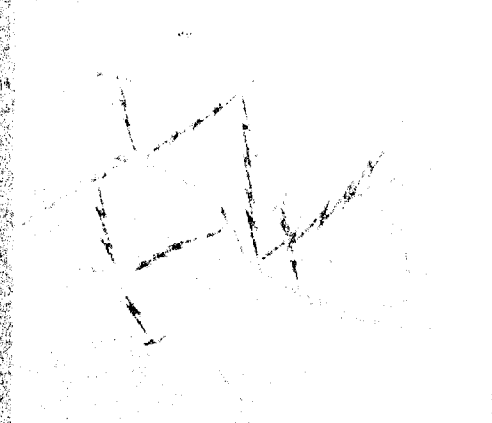
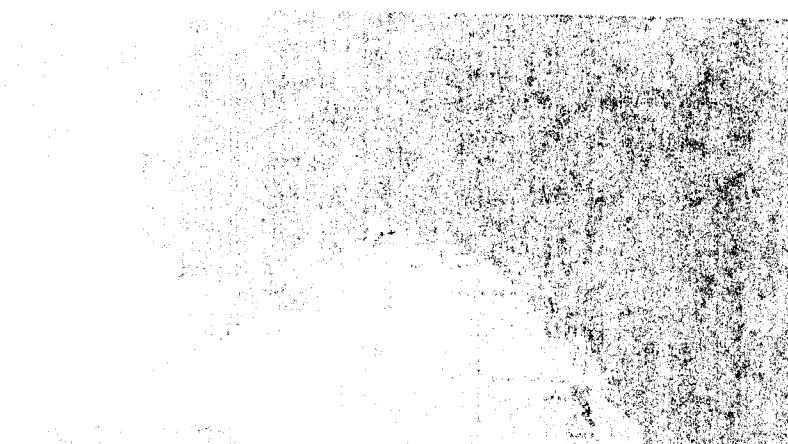
This paper describes an experimental program to utilize satellite observations of the ocean surface, in conjunction with conventional observations and products, to prepare special "Fisheries-Aids" charts for daily radio-facsimile broadcasts to commercial fishermen. These special fisheries products aggregate a broad set of ocean observations, including ocean color structure, to depict oceanographic conditions of importance to commercial fishing tactics.

Results to date have shown that improved safety at sea and decreased fuel costs can be achieved through the applied use of these special fisheries charts.

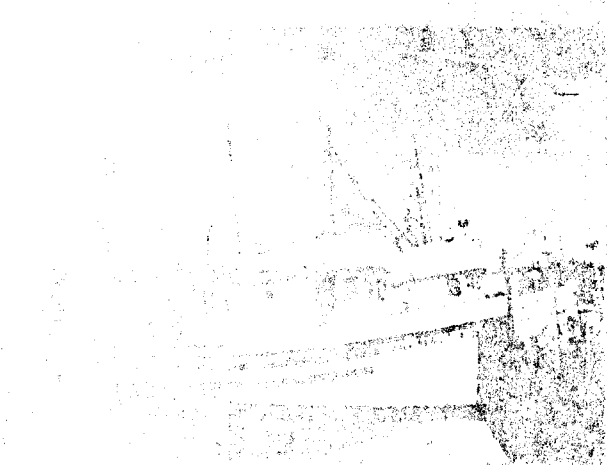
## INTRODUCTION

Commercial fishing on the high seas continues to be economically risky and physically dangerous. While fishermen are interested in safety at sea and in catching the most fish possible for their time and financial investment, escalating operating costs, especially those associated with fuel, labor and insurance continue to erode the economic viability of the industry. Successful fishermen continue to be those individuals that look for and incorporate the latest and best technology and information to enable their operations to be more efficient. This includes the increasing use of analyses and forecast of oceanographic and meteorological conditions that affect their operations at sea, and application of fisheries research findings to search and fishing efforts. Accordingly, the modern fisherman, more than ever, requires reliable environmental information.

To meet this need, the Jet Propulsion Laboratory, with the cooperation of the Ocean Services Division of the National Weather Service, has sponsored an experimental program involving the preparation and distribution of fisheries-aid products for the U.S. West Coast fishing industry, prepared with the aid of satellite observations of the ocean surface, including ocean color structure.



Electronic remote recorder  
transmission on a  
radio channel (fishing vessel).



THE WEST COAST COAST GUARDIAN PROGRAM is a  
cooperative effort by NASA/JPL  
with the participation and  
support of NOAA (and NEER), Navy/FNOC,  
and the Institute of Oceanography's  
remote sensing facility.

NASA

... demonstration program for U.S. West Coast commercial fisheries.

BEST AVAILABLE COPY



## BACKGROUND

In June 1978 the Seasat satellite was launched by the United States as a "proof-of-concept" mission to obtain measurements of ocean-surface conditions from satellite altitude. This mission proved conclusively that wave heights, surface-wind velocity, and sea-surface temperature measurements can be obtained from space under all-weather, day-night conditions. (1)

Scientific and commercial studies (2) of Seasat data, along with recent fisheries-oriented studies of a Coastal Zone Color Scanner (CZCS) currently in orbit on the Nimbus-7 satellite, have identified promising techniques that may be used to improve the analyses and forecasts of ocean-surface features (i.e., winds, waves, sea-surface temperatures, and color boundaries). These studies have shown that such techniques may well be operationally applicable to commercial fishing activities.

## FISHERIES DEMONSTRATION PROGRAM

With support from both the National Aeronautics and Space Administration and the NOAA-National Weather Service, an experimental demonstration program (Figure 1) is being conducted on the U.S. West Coast to assess the utility and benefit of specially prepared environmental charts, tailored for commercial fishing operations. These experimental charts, supplemental to the operational charts provided by the National Weather Service, are prepared on a daily basis, utilizing operational products prepared by the Navy-Fleet Numerical Oceanography Center (FNOC), Monterey, CA, and experimental ocean color charts generated by the Scripps Institution of Oceanography - Visibility Laboratory, La Jolla, CA. The products prepared by the FNOC utilize both conventional as well as satellite-derived observations, while the ocean color charts are derived from the Nimbus-7 satellite CZCS. Data from the CZCS are received by the Scripps Institution of Oceanography Remote Sensing Facility whose facilities and personnel have a unique capability to make the color data available on a near real time basis to preserve its time-critical quality.

A unique data system, developed for use with the data obtained from the Seasat satellite, provides a near real time access to the operational products of the FNOC by commercial users. This Satellite Data Distribution System (SDDS) (3) provides both operational products and selected observations, including observations from the Nimbus-7 Scanning Multichannel Microwave Radiometer (SMMR).

Figure 2 illustrates the configuration of data sources involved in preparing the experimental fisheries charts. Data from each of these sources is provided each day to a marine forecaster skilled in the preparation of marine analysis and forecast products. From this aggregated set of environmental data, the forecaster prepares a suite of fisheries-oriented charts for distribution to fishing vessels by means of daily radio-facsimile broadcasts supported by both U.S. Coast Guard Stations and radio station WWD operated by the Scripps Institution of Oceanography. Figure 3 depicts the product distribution scheme whereby the charts are made available to fishing vessels operating off the U.S. West Coast from the Bering Sea southward to the Eastern Tropical Pacific.

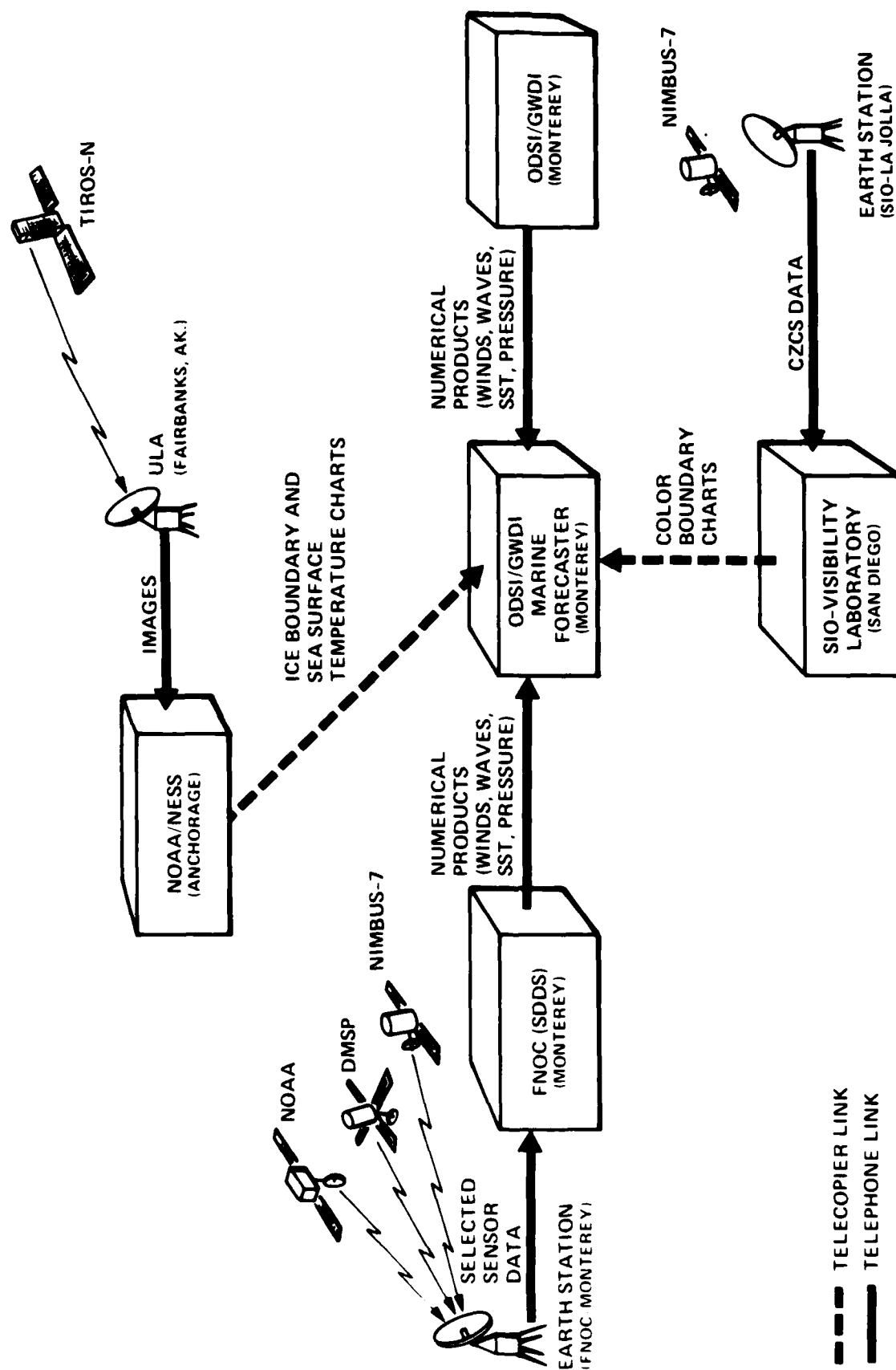


Figure 2. Sources of data for the fisheries demonstration program.

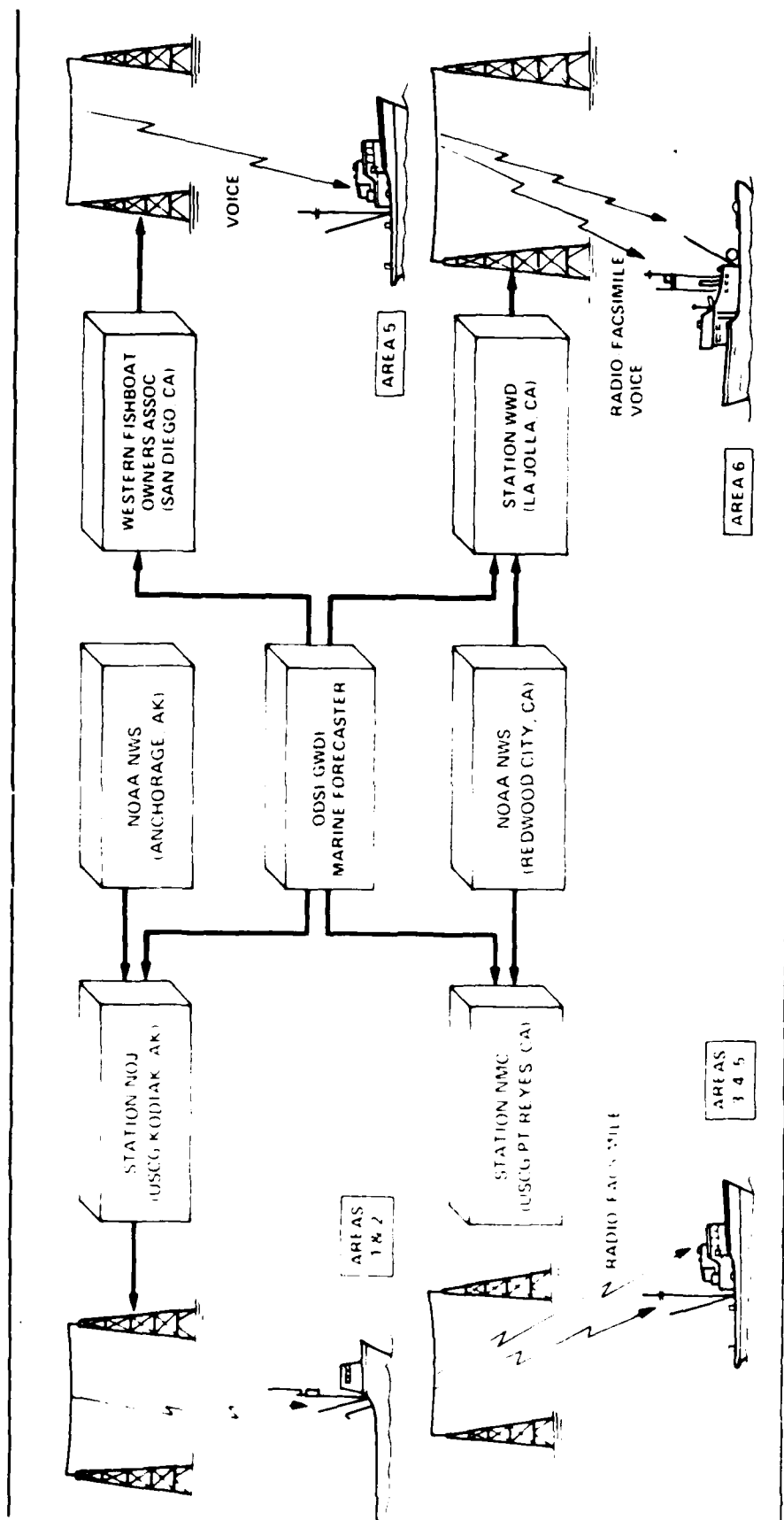


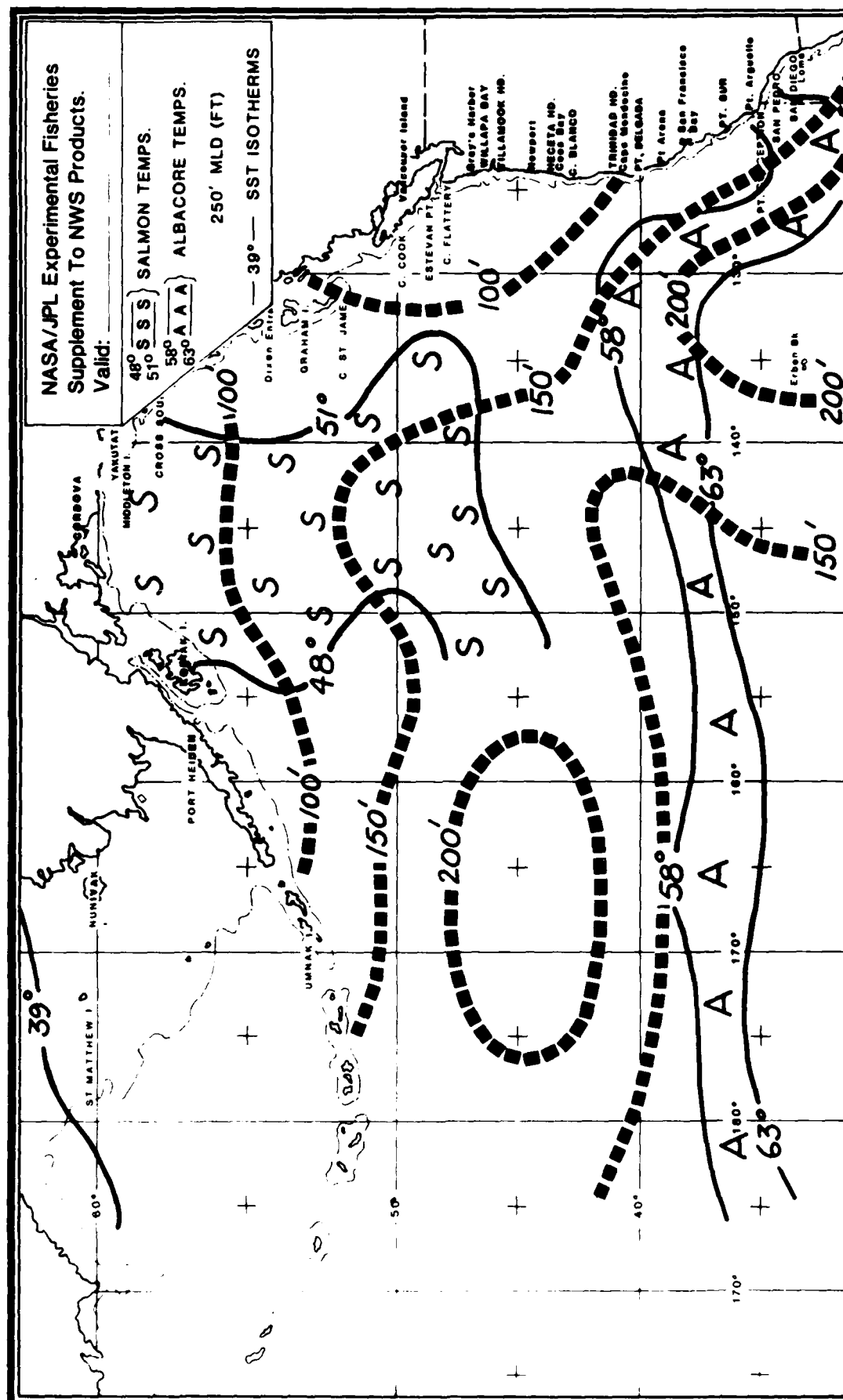
Figure 3. Data Distribution scheme for the fisheries demonstration program.

The experimental fisheries-aid charts depict atmospheric and oceanographic properties of particular use by fishermen in selecting fishing areas and fishing tactics. Figures 4, 5 and 6 illustrate three charts representative of the several charts generated as part of the demonstration effort. The chart shown in Figure 4 depicts sea surface temperatures (SST) as well as wave conditions which are noted at the latitude/longitude intersections, or at locations of special interest. Arrows denote wave direction while the number indicates the significant wave-height ( $H_{1/3}$ ) in feet. Wave conditions are derived from the FNOC Spectral Ocean Wave Model (SOWM). New SST analyses are made by computer every twelve hours using reports from ships (engine-room injection or bucket temperatures), satellites (infrared) and bathythermograph systems.

The fishing success rate for many species of fish is highest within a relatively narrow range of ocean temperatures. For example, salmon are usually caught at temperatures below 50° F, with the greatest catches occurring between 49° and 51° F. Most albacore are caught at temperatures between 60° and 64° F, while the largest percentage of tropical tuna species are caught in water temperatures between 79° and 81° F. The experimental fisheries charts depict these species-related SST bands. Figure 4 illustrates regions of preferred SST-bands for both albacore (band indicated with A) and tropical tuna (bands indicated with T). The coastal SST values (shown as NUMBER in Figure 5) are derived from the SST analysis and are based on ship reports from vessels operating in coastal waters.

The experimental charts depict key subsurface thermal characteristics. This subsurface thermal information is generated operationally by FNOC utilizing both bathythermograph soundings and climatology, and is selectively available to commercial users through the SDDS. Figures 4 and 5 illustrate, through the use of dashed lines, the depth of the mixed layer (MLD) which can be a significant parameter for several fish species, including salmon and albacore. Research conducted by Laurs has shown that albacore often tend to experience the MLD as a thermal "ceiling" in their vertical feeding excursions. Knowledge of the MLD can aid fisherman in selecting both gear and tactics while fishing for those fish species which exhibit thermal preferences.

On the experimental fisheries-aid charts, surface winds are not indicated by wind barbs as is the case on National Weather Service charts, but rather by alphanumeric characters at selected latitude/longitude intersections (see Figures 4 and 5). Selected wind derivatives from basic wind field analyses are of interest to fisherman because they are related to both significant weather and areas where nutrients tend to congregate. Wind derivatives shown on the experimental charts (see Figure 6) include the Intertropical Convergence Zone (ITCZ) and lines of convergence. The ITCZ is the region where tradewinds from the southern hemisphere converge with tradewinds from the northern hemisphere. Typically, a more-or-less continuous zone of wind convergence can be analyzed across the entire Pacific. However, parts of ITCZ are characterized by intense weather - heavy showers and/or thundershowers - while other parts exhibit weaker wind convergence and produce little more than a few cumulus clouds. Since the ITCZ normally lies within the tropical tuna-fishing area, it is shown on the fisheries charts as illustrated in Figure 6. Areas where there are numerous "C's" are the most active and are apt to have heavy showers and wind squalls. The ITCZ is located through numerical wind analyses and satellite derived visible and infrared photographs of clouds.



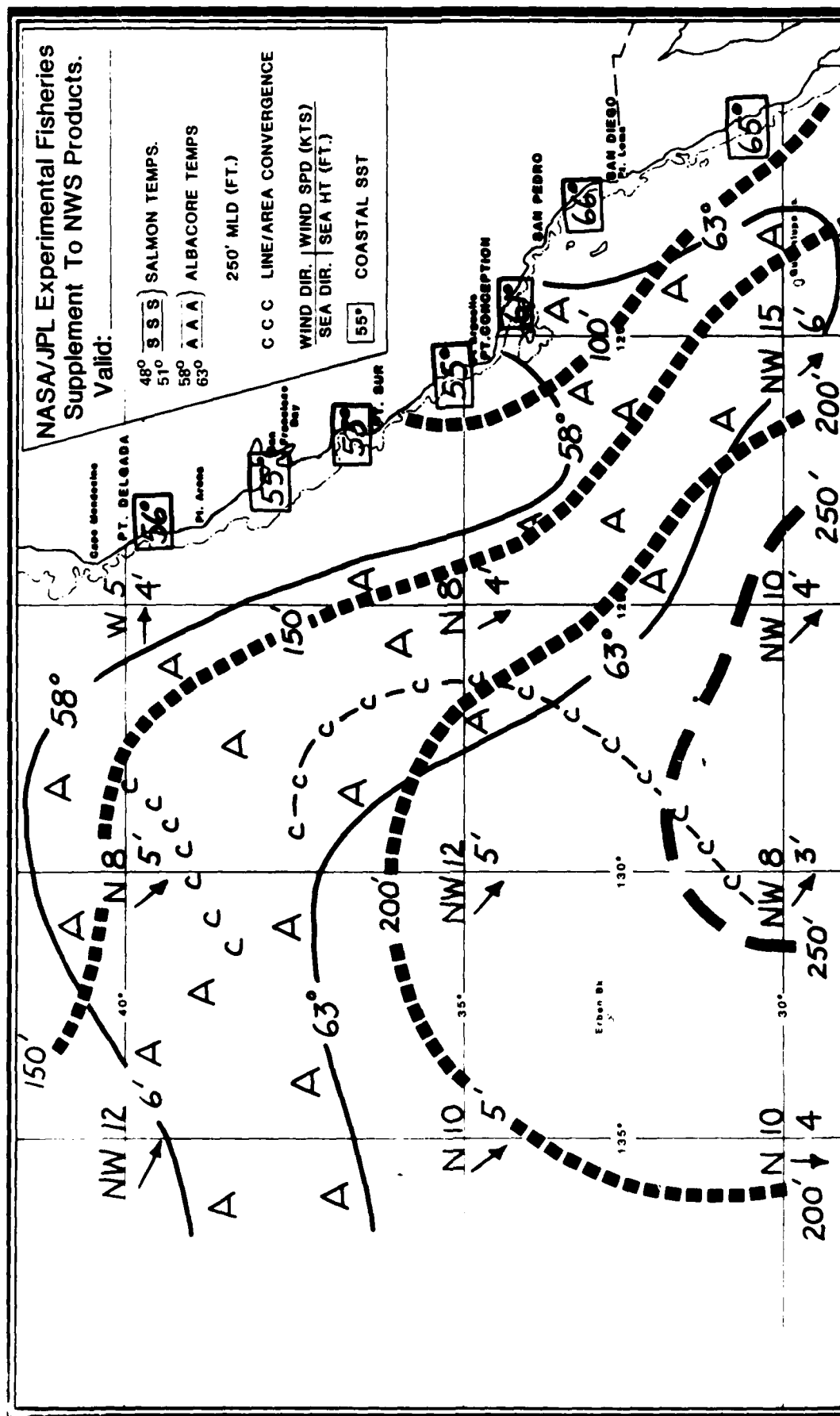


Figure 5. Sample fisheries aid chart.



Local areas and/or lines of wind convergence also represent regions of squalls and wind shifts and possible areas of local nutrient (fish-food) concentration. These areas/lines are also located by means of satellite photographs and are depicted on the experimental charts as illustrated in Figure 5.

It is a well known fact that certain characteristics of the surface wind field are favorable for concentrating nutrients at the ocean surface via upwelling. Computation of wind "curl" and wind "shear" is utilized by the marine forecaster to highlight regions where fish foods may be more concentrated. These are typically regions where horizontal variability in wind speed or wind curvature (directional change) is greatest. Areas of favorable "curl" or "shear" are shown on the fisheries-aid charts as areas or lines of convergence.

For completeness, and as a supplement to the operational National Weather Service charts, the experimental charts show wave heights and directions as characters at latitude/longitude intersections or at locations of special interest to fishermen.

The tracking and near real time data processing capability afforded by the Scripps Remote Sensing Facility and Visibility Laboratory, coupled with the fisheries research of Laurs and Lasker, have provided the opportunity to test the utility of satellite-derived ocean surface color observations in commercial fishing operations. With a near real time capability to handle the Nimbus-7 CZCS data, it is possible to provide perishable ocean color information to fishermen by radio-facsimile in sufficient time to yield a product which has a useful life of two to three days. The work of Austin (4,5), Smith (6), Gordon (7) and Laurs has provided a basis by which these data can be interpreted and correlated with water mass type and aggregation of fish species, especially albacore.

Processing of the CZCS data for fisheries applications involves the use of two CZCS channels, band 1 (443 nm) and band 3 (550 nm). Images showing chlorophyll concentration and water clarity (diffuse attenuation coefficient) can be generated by the use of processing techniques which ratio band 1 and band 3. Atmospheric scattering mechanisms contribute a significant proportion (up to approximately 90 percent) of the signal as detected by the CZCS. To create a useful set of images of the ocean surface, it is necessary to remove that portion of the detected signal which is contributed by the atmosphere. Processing algorithms used by the Scripps Visibility Laboratory (8) have proven to be particularly successful in removing the atmospheric contributions. Figure 7 shows an ocean color image from band 1 data prior to atmospheric correction. Figure 8 shows the same image following atmospheric correction, while Figure 9 illustrates a band 3 image, also after atmospheric correction. Finally, Figure 10 shows an image proportional to chlorophyll concentration generated from the ratio of the band 1 and band 3 images.





Figure 7. A Band 1 (443 nm) image from Nimbus 7 CZCS prior to atmospheric correction.



Figure 8. A Band 1 CZCS after atmospheric correction.



Figure 9. A Band 3 (550 nm) CZCS image after atmospheric correction.

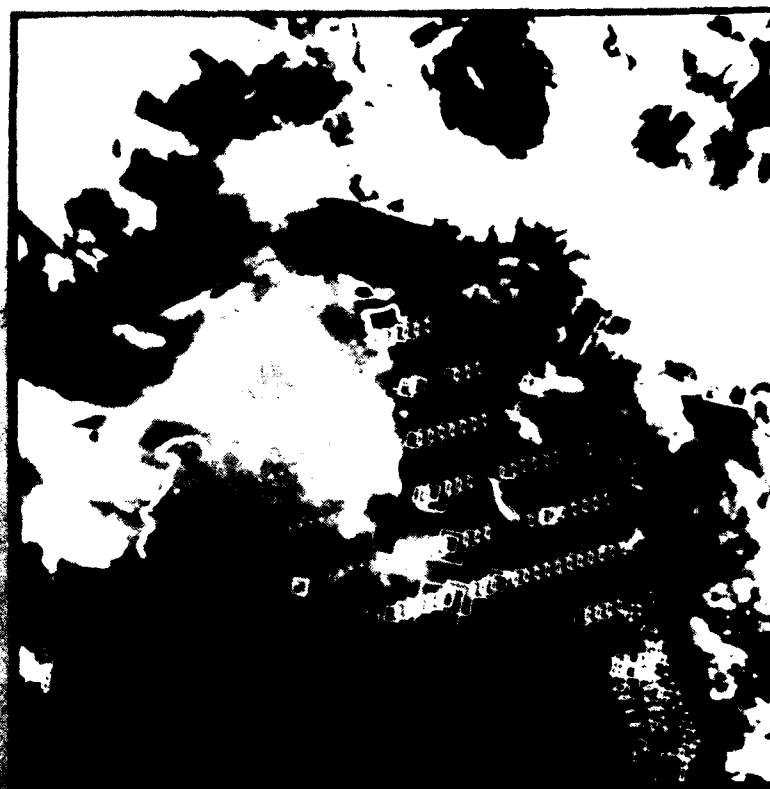
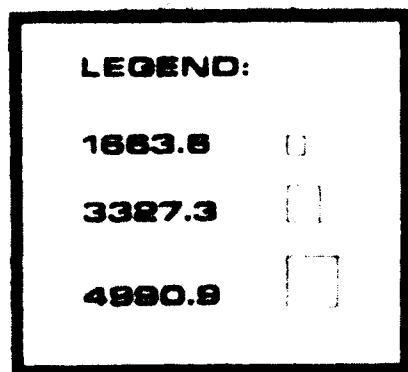


Figure 10. An atmospherically corrected CZCS image depicting the ratio of Band 1 to Band 3, which provides chlorophyll concentrations.

It has been shown by Lasker, et al. (9) that satellite derived observations of infrared sea surface temperature and ocean color (from the CZCS) can be used to describe ocean processes in relation to the Northern Anchovy and the survival of its early life stages. Figure 11 shows the distribution of anchovy eggs superimposed on the NOAA-G AVHRR thermal image of the Southern California Bight taken April 6, 1980. The 14° C isotherm, plotted from the gray-scale calibration of the AVHRR, has been drawn in as a heavy line. The feathery white objects are clouds. The squares indicate the number of anchovy eggs under one square meter of sea surface. A companion image of ocean color taken April 8, 1980, is shown in Figure 12. In this image, the distribution of anchovy eggs is superimposed on the diffuse attenuation coefficient, a factor which is proportional to both water clarity and chlorophyll concentration. These image data show that the fish have avoided freshly upwelled waters (cooler than 14° C) and have been excluded from the more warm saline water from the south. It is clear from these preliminary results that the distribution of anchovy spawning is related to ocean color boundary patterns and the distribution of chlorophyll. These satellite-derived measurements can uniquely be used to synoptically survey the 85,000 square-mile anchovy habitat and pin-point oceanographic areas where spawning can be successful, thus providing a management tool which permits a more accurate prediction of anchovy distribution and migration.

Ocean color has historically been a cue by which fishermen have identified potentially productive fishing areas. Albacore fishermen operating in U.S. West Coast waters key their fishing operations to the "blue" color of the ocean water. Laurs, et al. (10,11) using both satellite-derived sea surface temperature and ocean color observations coupled with acoustic tracking data, have begun to correlate the small-scale migration patterns of albacore tuna with ocean color structure and water temperature. Figure 13 shows a CZCS image of the U.S. West Coast in the region of Point Conception, processed to identify color structure proportional to chlorophyll concentration. Computer generated false color has been used to enhance the surface color structure. Warm, clear, oceanic water is shown in blue, while the more cool, turbid coastal water is shown in the yellow to brown color ranges. Black areas are clouds. Points marked A and B denote the area wherein acoustic tracking of several fish was conducted. Figure 14 is an infrared image of the same region (different scale) illustrating the surface thermal structure. The lighter regions are the cooler inshore waters. Preliminary results which involved correlating both the color and thermal images together with the acoustic tracking data, appear to indicate that albacore aggregate on the warm side of ocean surface temperature fronts and remain in water that has higher water clarity than the adjacent waters. While additional analysis is required to explain the role of water clarity and temperature in the mechanisms underlying the preferential aggregation of albacore in certain water masses, it is clear that these satellite derived observations of ocean color and IR temperatures can aid scientific research directed towards fisheries forecasting of the distribution, migration, and availability of the fish stock.

While further investigations are necessary to attempt to correlate albacore fish catch with water color structure, there is sufficient evidence to suggest that an ocean color structure product would be a useful tool to commercial fishermen to aid in the identification of ocean areas with the potential of aggregating quantities of albacore. Based on this knowledge, a color chart is



**Distribution of anchovy eggs superimposed on the NOAA-6 AVHRR thermal image of the Southern California Bight taken 6 April 1980. The 14°C isotherm plotted from satellite gray-scale calibration has been drawn in. Feathery white objects are clouds. Squares indicate number of anchovy eggs under one square meter of sea surface.**

Figure 11. An AVHRR image depicting the distribution of anchovy eggs in the Southern California Bight.

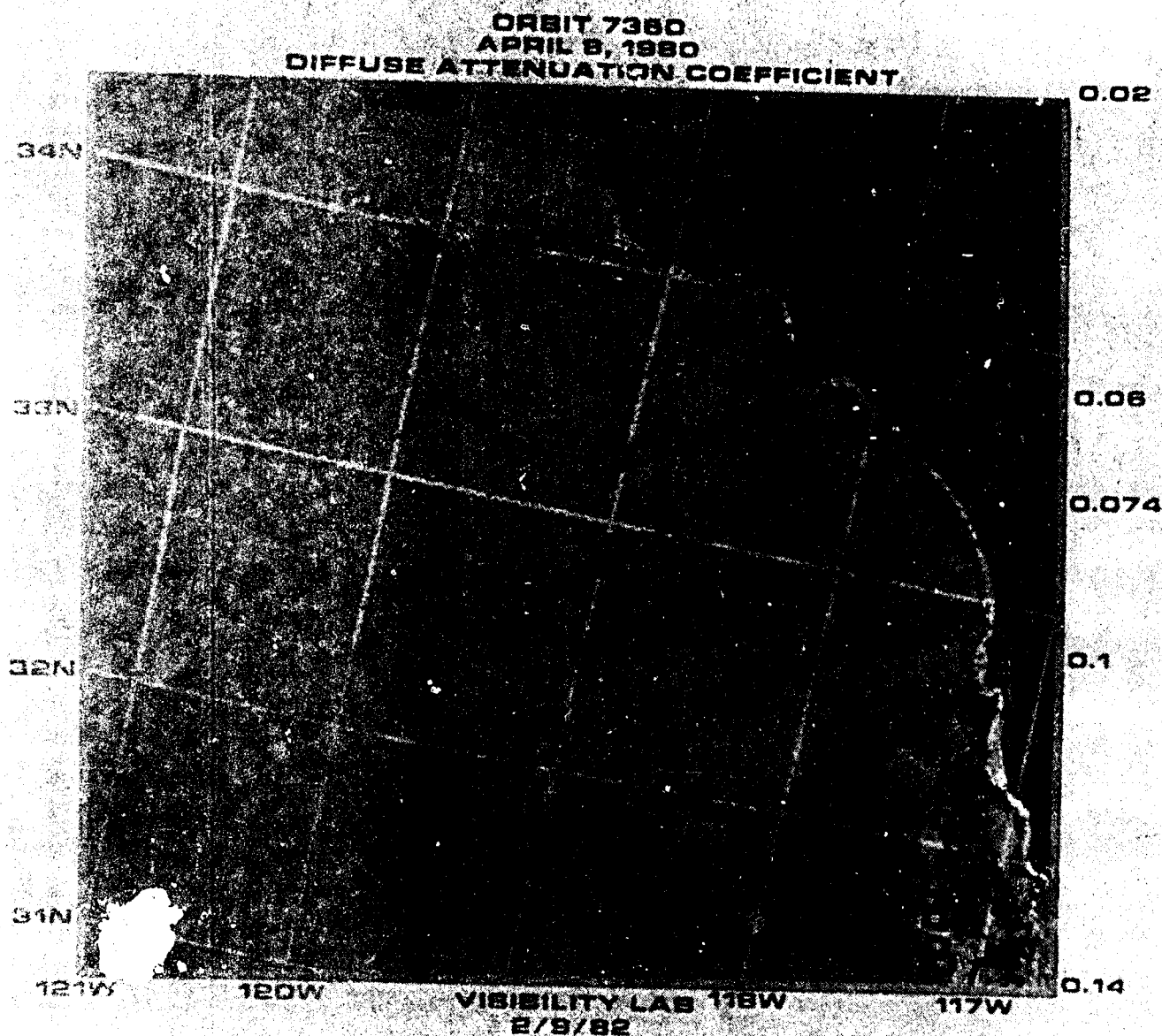


Figure 12. A CZCS image showing the distribution of anchovy eggs in the Southern California Bight.



Figure 13. A CZCS image processed using computer enhanced false color to identify water color structure showing chlorophyll concentrations. Points A and B identify regions where acoustic tracking of albacore was performed





Figure 14. A NOAA-AVHRR image corresponding to the CZCS image shown in Figure 13. Lighter portions are the cooler inshore waters.

produced as part of the Fisheries Demonstration Program and transmitted to fishermen by radio-facsimile. The radio-facsimile chart, shown in Figure 15, is derived from a computer-generated, false color image processed to highlight ocean regions of high chlorophyll concentrations and water clarity. Based on the false color image, as shown in Figure 16, a chart is drawn to identify the boundaries separating key water masses, based on chlorophyll concentration. Each water mass is identified in terms of its relative color, with the most green water labeled as "number 1 water" and the most blue water labeled as "number 4 water". Water masses of intermediate colors are noted with 2 and 3 labels.

To make maximum use of the environmental information available through both the National Weather Service and the experimental fisheries program, fishermen must correlate key meteorological and oceanographic features in order to identify ocean regions most likely to support selected fish species and which permit fishing gear to be deployed. Figure 17 has been developed as a training aid to illustrate the correlation process that will tend to highlight favorable albacore fishing areas. Figure 17 is a composite chart depicting those oceanographic and meteorological parameters shown on NWS and fisheries-aids facsimile charts. Wind and sea conditions denoted above the hash-mark line tend to exceed those limits where troll gear can be effectively deployed, while below this line wind and wave conditions are reasonable. Sea surface temperature conditions are favorable for albacore within the "A" bands and the mixed layer depth levels in the range of 50 to 150 feet are preferred for troll fishing methods. Ocean color boundaries separating warm, clear oceanic water from the colder, more turbid coastal water are highly preferred by albacore and are shown in Figure 17 as boundaries between number 2 water and number 4 water. Significant, but less preferred boundaries exist between number 2 water and number 4 water. Giving consideration to each of these parameters, including the preferred color boundaries, it is apparent from the composite training-aid chart that key ocean areas for albacore exist in the regions of 122° and 123° west longitude and 32° to 34° north latitude.

While this correlation of environmental parameters may not conclusively identify productive fishing areas since non-environmental factors also effect the feeding and migration patterns of fish, it will aid the commercial fishermen in separating those fishing areas with a higher probability of supporting fish concentrations from those with lower probabilities. And, maybe more importantly, the fishermen will be able to identify areas which are most likely not to support fish concentrations, thus allowing the fishermen to avoid selected areas and make more efficient their search operations.

The Experimental Fisheries Program has begun to illustrate to the commercial fishing industry the utility and economic viability of satellite observations of the ocean surface in their fishing operations. Assimilation of this NASA-developed satellite technology by the fishing community will be slow, but with continued demonstrations under balanced partnership arrangements between government and industry, the technology will come to play a key role in making the U.S. fishing industry more efficient, safe, cost effective and competitive on the every widening world market.

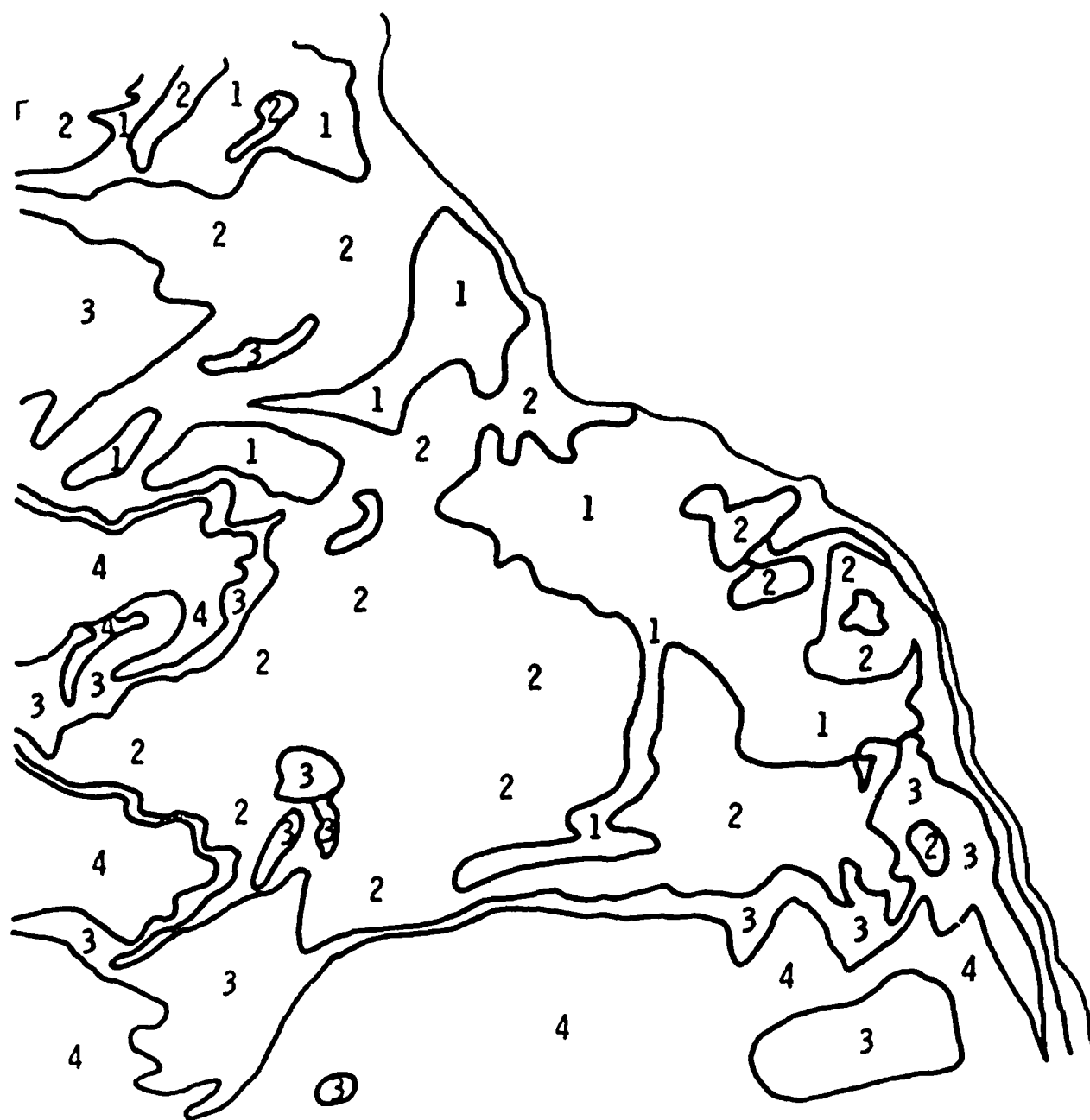


Figure 15. A color boundary chart constructed from a false-color enhanced CZCS image. Key water masses are identified by numbers. Geographic landmarks are added to chart before transmission by radio-facsimile.

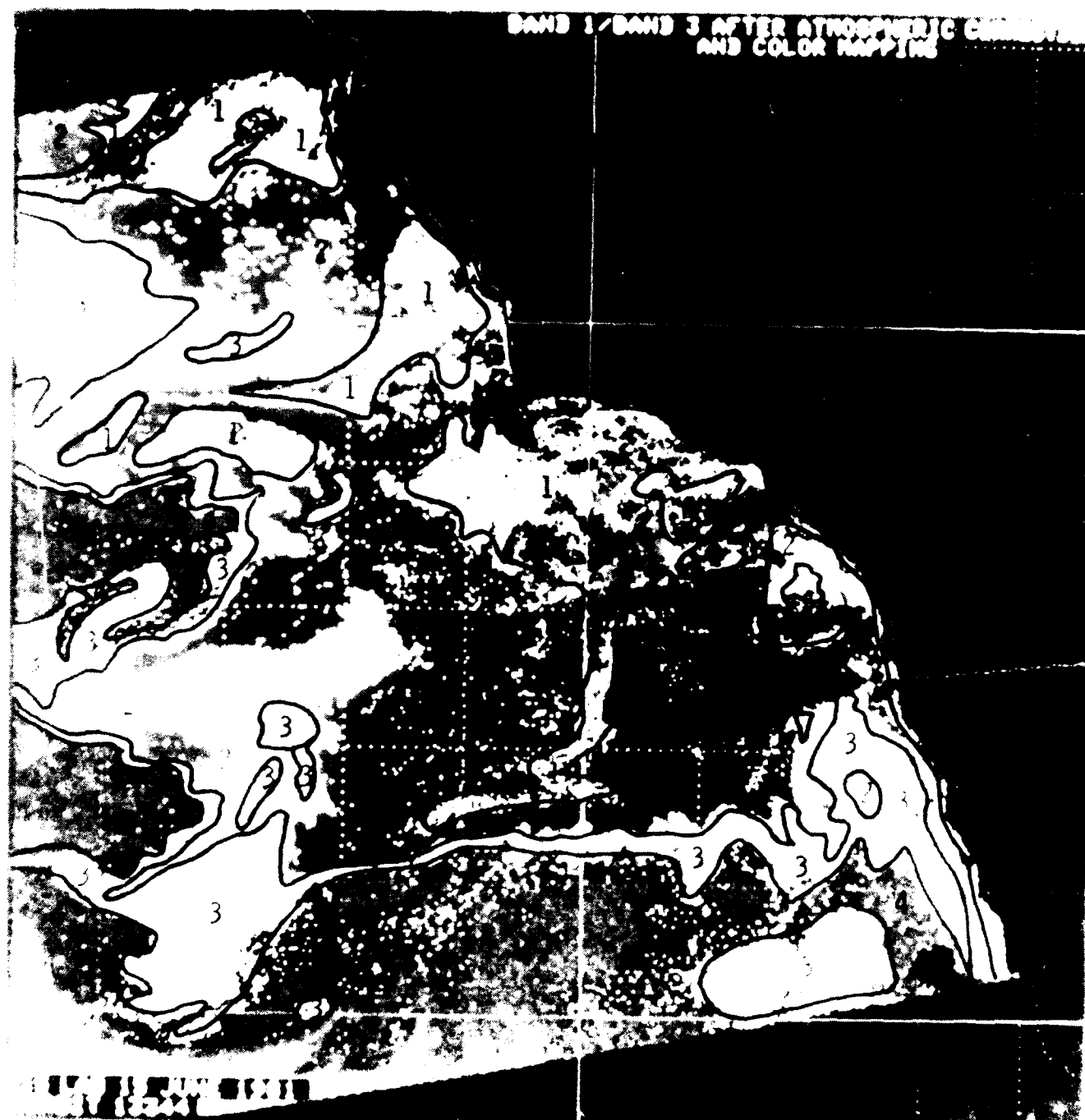


Figure 16. A false color enhanced CZCS image used to construct color boundaries as shown in Figure 15.

## OCEAN COLOR BOUNDARIES FROM NIMBUS-7

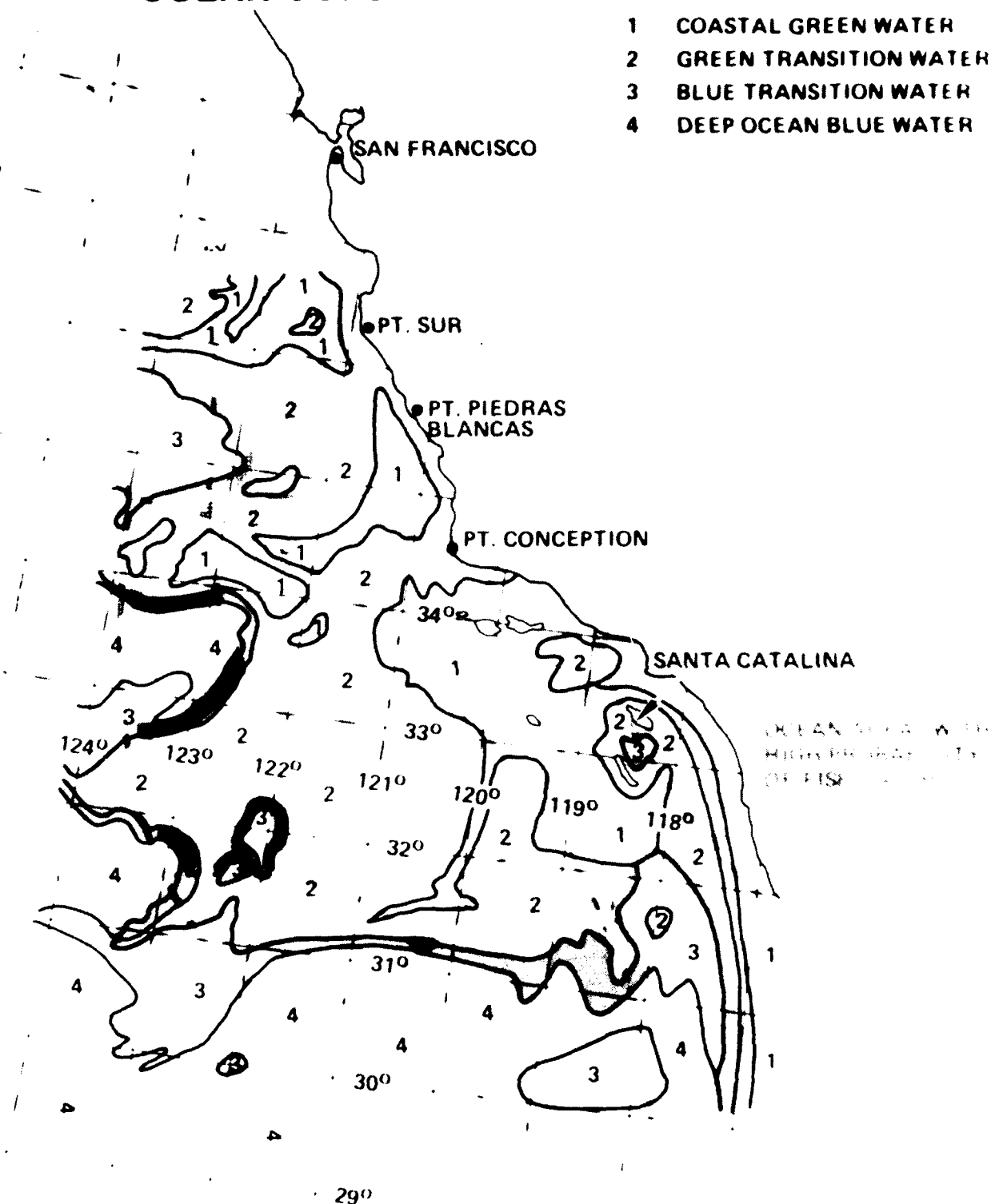


Figure 17. A composite chart showing oceanographic and meteorological features available on various operational and experimental charts transmitted by radio facsimile. The composite shows the use of environmental data in locating productive ocean areas.

## REFERENCES

1. Borne, G. H., Dunne, J. A. and Lane, D. B., "Seasat Mission Overview" Science 204: 1405-1406 (1979).
2. Hubert, H., Miller, B. P. and Montgomery, D. R., "An Evaluation of the Utility of Seasat Data to Ocean Industries", Jet Propulsion Laboratory Report No. 622-225 (1981).
3. Renfrow, T., Malewicz, K., "Seasat Satellite Data Distribution System Evaluation Report", Jet Propulsion Laboratory Report 622-219B, (1981).
4. Austin, R. W., "Remote Sensing of the Diffuse Attenuation Coefficient of Ocean Water", The 29th Symposium of the AGARD Electromagnetic Wave Propagation Panel on Special Topics in Optical Propagation, April 1981.
5. Austin, R. W. and McGlamery, B. L., "Spatial Characteristics of the Diffuse Attenuation Coefficient of Ocean Surface Water as Derived From Coastal Zone Color Scanner Data", Symposium on Radiation Transfer in the Oceans and Remote Sensing of Ocean Properties, IAMAP Third Scientific Assembly (1981).
6. Smith, R. C., and Baker, K. S., "Optical Classification of Natural Waters" Limnology and Oceanography, 23 260-267 (1978).
7. Gordon, H. R., Clark, D. K., Mueller, J. L. and Hovis, W. A. "Phytoplankton Pigments from the Nimbus-7 Coastal Zone Color Scanner: Comparisons with Surface Measurements" Science 210 63-66 (3 October 1980).
8. Gordon, H. R., "Removal of Atmospheric Effects from Satellite Imagery of the Oceans", Applied Optics, Vol. 17, No. 10, pp 1631-1636, (1978).
9. Lasker, R., Pelaez, J. and Laurs, R. M., "The Use of Satellite Infrared Imagery for Describing Ocean Processes in Relation to Spawning of the Northern Anchovy (*Engraulis mordax*)", Remote Sensing of Environment, 11: 439-453 (1981).
10. Laurs, R. M. and Lynn, R. J., "Seasonal Migration of North Pacific Albacore, (*Thunnus Alalunga*), Into North American Coastal Waters: Distribution, Relative Abundance, and Association With Transition Zone Waters" Fishery Bulletin: Vol. 75, No. 4. (1977).
11. Laurs, R. M., Yuen, H. S., and Johnson, J. H., "Small-Scale Movements of Albacore, (*Thunnus Alalunga*), In Relation To Ocean Features As Indicated By Ultrasonic Tracking and Oceanographic Sampling" Fishery Bulletin: Vol. 75, No. 2. (1977).

# Digitally Controlled Sonars

George R. Hansen  
Information Systems Division  
Jet Propulsion Laboratory  
California Institute of Technology  
Pasadena, California 91109

## I INTRODUCTION

Sonars are usually designed and constructed as "stand-alone" instruments. That is, all elements or subsystems of the sonar are provided: power conditioning, displays, intercommunications, control, receiver, transmitter, and transducer. The sonars which are a part of the Advanced Ocean Test Development Platform (AOTDP) represent a departure from this manner of implementation and are configured more like an instrumentation system. Only the transducer, transmitter, and receiver which are unique to a particular sonar function; Up, Down, Side Scan, exist as separable subsystems. The remaining functions are reserved to the AOTDP and serve all sonars and other instrumentation in a shared manner.

The organization and functions of the common AOTDP elements ~~will be~~ described and then the interface with the sonars discussed. The techniques for software control of the sonar parameters ~~will be~~ explained followed by the details of the realization of the sonar functions and some discussion of the performance of the side scan sonars.

## II AOTDP

The Advanced Ocean Test Development Platform is a deep ocean instrument system patterned very much in performance goals after the Scripps Institution of Oceanography DEEPTOW. The AOTDP consists of a submersible instrumented FISH which is connected electrically and mechanically through a tow cable with a surface towing ship. At the other electrical terminus of the cable is the AOTDP control van which houses the displays and controls for the FISH instruments as well as position determining (LORAN) and VHF and intercom communication equipments. Figure 1 is a block pictorial representation of the AOTDP system.

Both the FISH and VAN portions of the AOTDP are distributed processor systems. Figure 2 is a functional block diagram of the FISH and Figure 3 is a similar diagram of the VAN system. The FISH utilizes microprocessors while the VAN system is based on minicomputers. Three types of subsystems are common to both FISH and VAN. These are power, data, and communication. The data subsystem performs the functions of command, control, and data gathering.

The command and control computer (front end processor) in the VAN has the capability to program the microprocessors in the FISH, to command the FISH state, to accept and store data from the FISH, and to recall previously stored data. Real time processing of data from the FISH or recalled from the archive store is possible by the side scan processor. Real time processing can improve the guiding of the data taking process. The data can be displayed; on the computer console, as a

# AOTDP

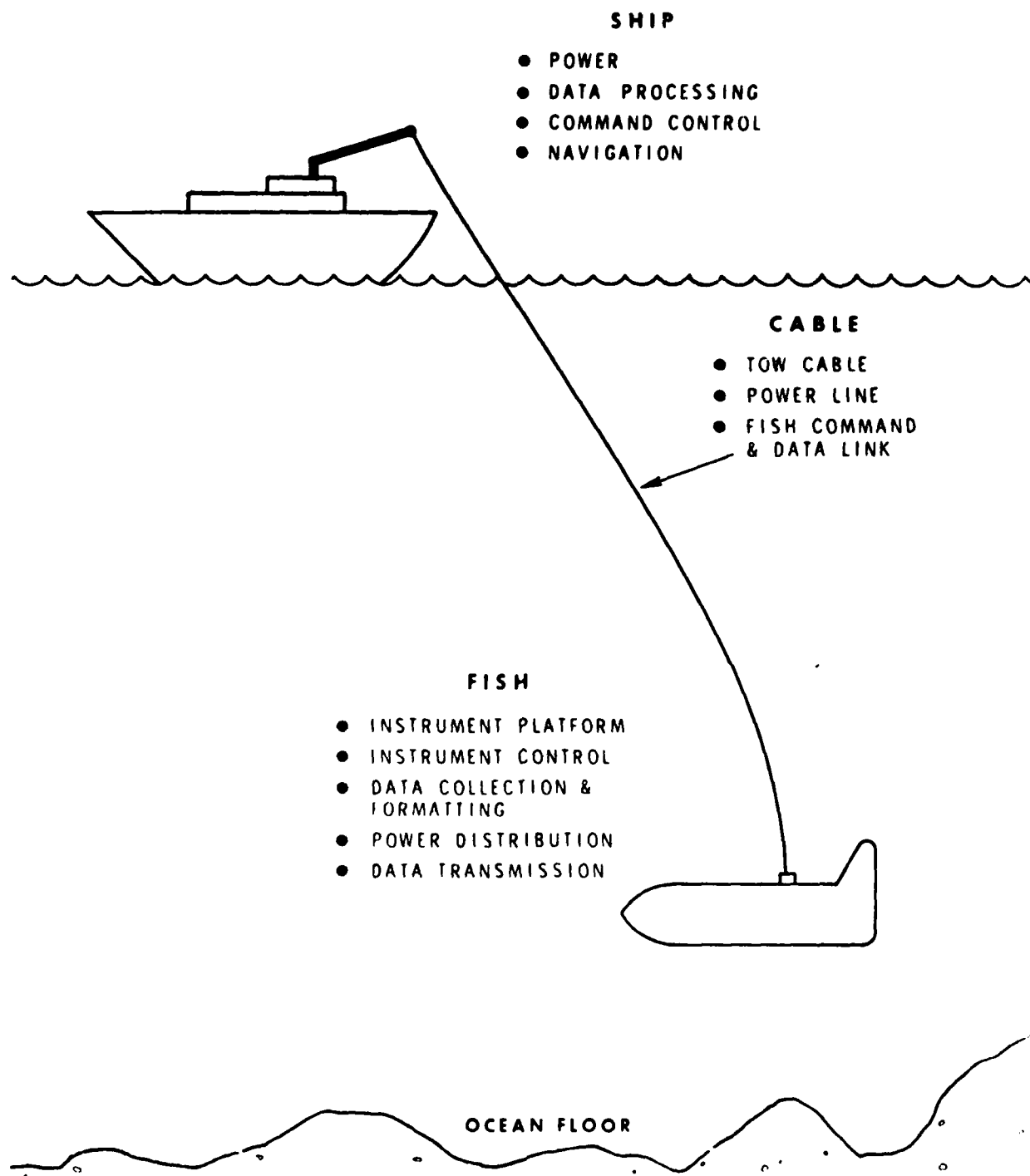


Figure 1. AOTDP system schematic of functional elements.



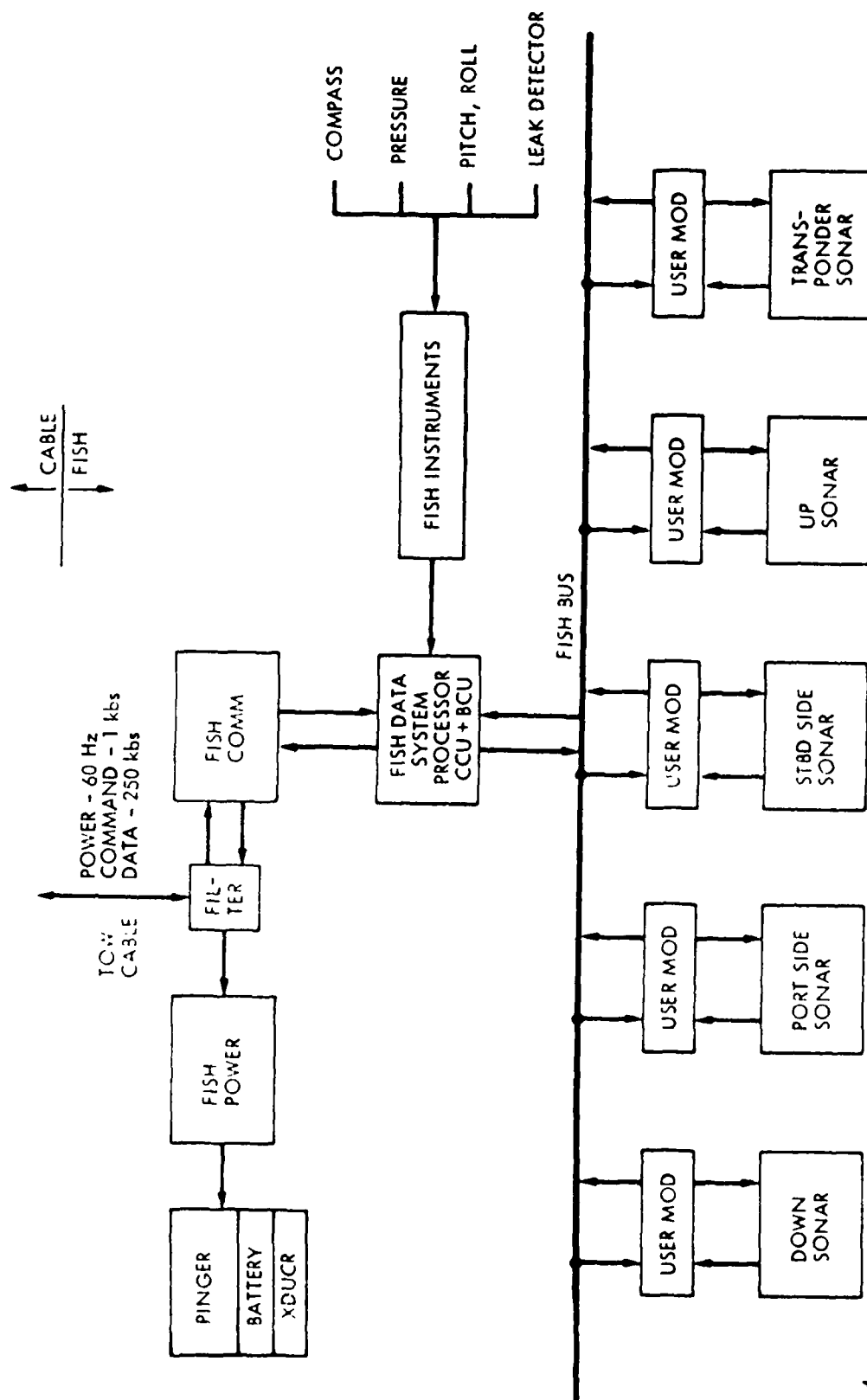


Figure 2. AOTDP FISH functional block diagram.



printed record, or graphically on a hard copy grey scale recorder or color video CRT.

The AUTDP command, control, and telemetry is almost entirely digital. That is, all information interfaces between the communication, computing, and instruments(sonars) is digital. The exceptions are engineering telemetry measurements which necessarily are analog at the measuring point but these data too are converted to digital data in the FISH data system.

The cable connecting the VAN and FISH is a conventional deep ocean cable with a single coaxial conductor sheathed with two contralaid multistrand strength members. The coaxial cable is used to convey 60 Hz power to the FISH as well as a digital command link. The command link rate is 1000 bits/s which psk modulates a 16 kHz carrier. The up telemetry link from FISH to VAN operates in full duplex with the command link and is at 250,000 bits/s Manchester coded. That is, the carrier and bit rate are at the same frequency with the carrier phase at 0 or 180 degrees depending on the data bit.

The power subsystem in the VAN which furnishes 60 Hz energy to the FISH cable is isolated from the command transmitter and telemetry receiver by a simple low pass filter. The transmitter and receiver in turn are connected to the cable through a multiple pole high pass filter.

The distributed system in the FISH is a bus connected array of microprocessors (KCA 1802 CMOS) with one high level processor controlling the bus and the remaining five each associated with a particular sonar. This organization and the interface between the sonar and the microprocessed are outgrowths of a Unified Data System research program at JPL which led to equipment realizations in the FISH and the Galileo spacecraft.

Each sonar is connected to a User Module (cf Figure 4) which relays parameter changes to the sonar and collects data from it. The User Module is a single board microprocessor with 2K bytes of RAM. The User Module is connected to the sonar through an 8 bit parallel data transfer and up to 32 discrete signal lines. The parameters which are destined for a particular sonar are sent on the FISH bus to the proper User Module and stored in the parameter table part of the RAM. These parameters are then transferred into appropriate registers which form part of the sonar by the discrete signal lines. The actual timing of these transfers depends upon the nature of the parameter. Frequency change parameters are transferred to the sonar immediately upon receipt in the User Module and new Time Varying Gain values from the TVG table are sent over each 5 msec at the real time interrupt rate. The echoes received by the sonars during the listening time are digitized in the sonar receiver and sent to the User Module. The echo amplitudes are sampled at a rate determined by a sonar command (nominally once each millisec) and transferred over the parallel data transfer to a double buffer in the User Module RAM.

Each of the lower level microprocessors is connected through a bus adaptor to the FISH bus. This is a serial 4 wire bus which controls and enables data and command transfers to and from the high level processor by each of the lower level units or between the lower level units. The bus lines operate at a 1 mHz clock rate and transfer data and commands at 80,000 bytes/s (640,000 bits/s) in a serial mode. Two lines of the bus are word and bit synch lines and the other two are for addressing and data. Owing to the nature of the organization and connections, no lower level unit can "volunteer" information to the bus or otherwise interfere with valid transfers.

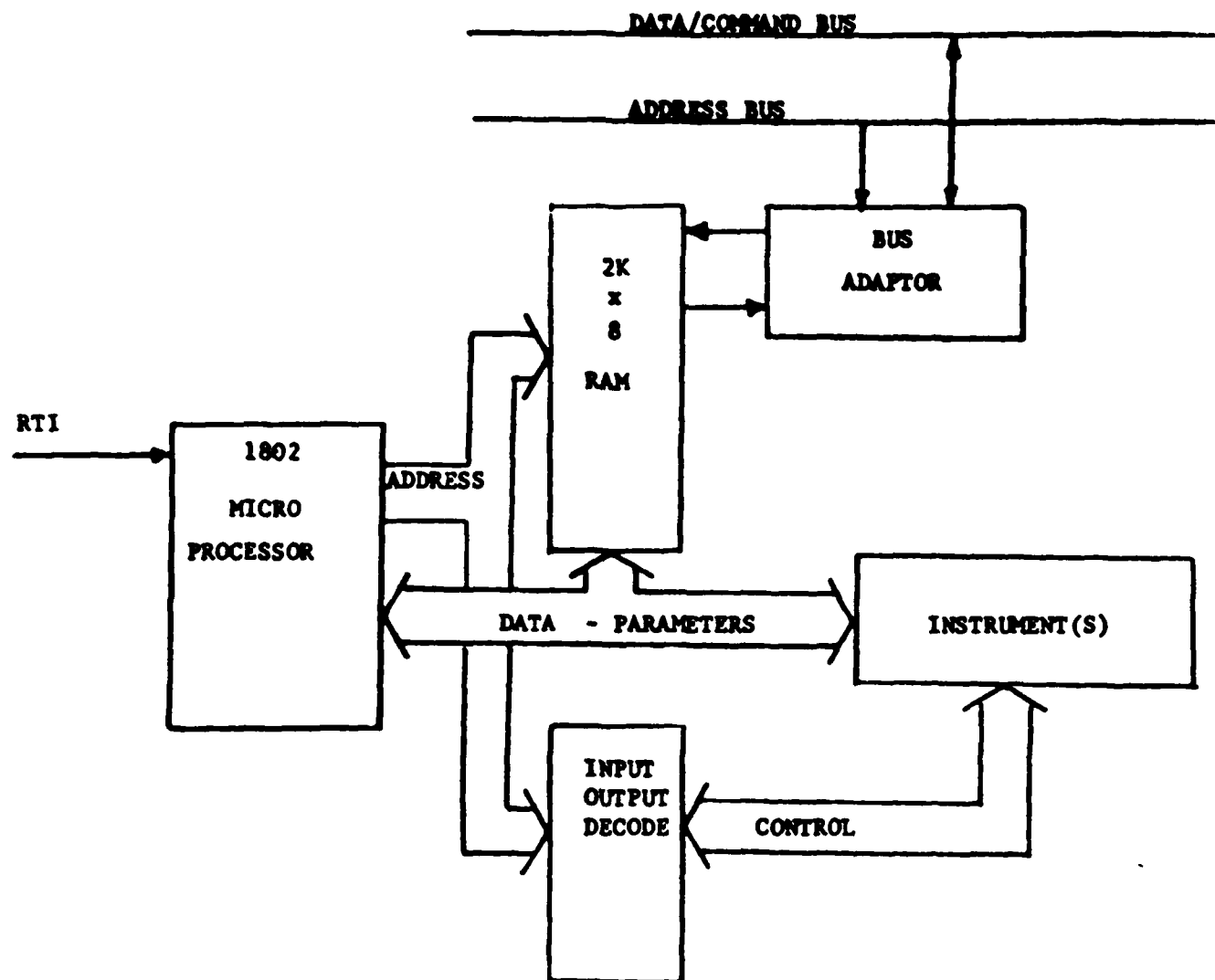


Figure 4. User module block diagram.

### III SONAR COMMANDING

The sonar transmitter and receiver parameters are determined by commands sent to the FISH from the VAN command processor. The selection of parameters is done by the operator by means of a cathode ray tube terminal keyboard. The operator makes selections from a hierarchy of menus. Four levels of menus are specifically utilized for commanding the state of the sonars. Examples of these are shown in Figures 5a, 5b, 5c, and 5d. The highest level menu (Fig 5a) shows the sonar software option as a choice. Selection of this evokes the next level menu shown in Fig. 5b, which asks which sonar is to be changed. At the third level menu depicted in Fig. 5c specific parameters of the sonars are displayed for selection. Option selections from this menu cause a request for a specific value or evoke a fourth level menu. Values are requested for parameters needing only a single byte of 8-bits to change the parameter but where several bytes would need to be changed a menu is provided. An example of the latter is frequency where a three byte command is needed. The frequency option menu is shown in Fig. 5d. The values for the frequencies range from above to below the nominal and depend upon which sonar was selected at the second level.

As each parameter is selected it is transmitted over the command channel to the higher level microprocessor in the FISH and stored in a table dedicated to parameters for the sonar being changed. An auxiliary routine provides a display of the parameters stored in the FISH. When the operator is satisfied with the changes that have been sent an initiate parameter option from the sonar menu causes this table to be sent to the sonar User Module. The parameter changes are then made to the sonar receiver and transmitter under control of the User Module program prior to the next transmitted pulse.

During the initial loading of the FISH processors the command processor loads a set of nominal parameters into the tables in the higher level FISH processor. These parameters set all sonars to the nominal frequency for each and set the transmitted power level to be zero. As a further protection the individual User Modules must be started by the operator. The intent of this procedure is to avoid incompatible transmitted power levels and pulse lengths which might damage the sonar power amplifiers.

The time varying gain (TVG) curve for each sonar is developed by a separate set of menus. These allow choices from a repertoire of functional curves and also provide for the creation and editing of TVG curves for testing purposes and actual use.

### IV SONAR RECEIVERS

All of the sonar receivers use the direct conversion technique wherein the received echoes are mixed with the carrier frequency of the transmitted pulse. This has the effect of creating an intermediate frequency centered at zero hertz. All post mixing amplification and signal handling is therefore at low audio frequencies. A common mechanization for all sonar receivers after mixing is a result of this design approach which also facilitates the logistics of spares and servicing. The functional block diagram of the receivers is shown in Figure 6.

Pre-mixing amplification takes place in two stage gain controlled amplifiers

- 0) HARDWARE COMMAND
- 1) CCU SOFTWARE COMMAND
- 2) SONAR SOFTWARE COMMAND

OPTION?

(a)

- 0) SET RECEIVER PREAMP GAIN
- 1) SET RECEIVER FREQUENCY
- 2) SET 1ST TRANSMITTER FREQUENCY
- 3) SET 2ND TRANSMITTER FREQUENCY
- 4) SET 3RD TRANSMITTER FREQUENCY
- 5) SET TRANSMITTER PULSE SHAPE
- 6) SET PULSE ORDINATE
- 7) SET PULSE DURATION
- 8) SET PULSE AMPLITUDE
- 9) INITIATE PARAMETERS
- 10) DISPLAY SONAR RETURNS

OPTION?

(c)

- 1 PORT SIDESCAN
- 2 STARBOARD SIDESCAN
- 3 DOWN SONAR
- 4 UP SONAR
- 5 TRANSPONDER SONAR

OPTION?

(b)

FREQUENCY

- 0) XXX.XXX
- 1) XXX.XXX
- 2) XXX.XXX
- 3) XXX.XXX
- 4) XXX.XXX
- 5) XXX.XXX
- 6) XXX.XXX
- 7) XXX.XXX

OPTION?

(d)

Figure 5. FISH sonar command menus

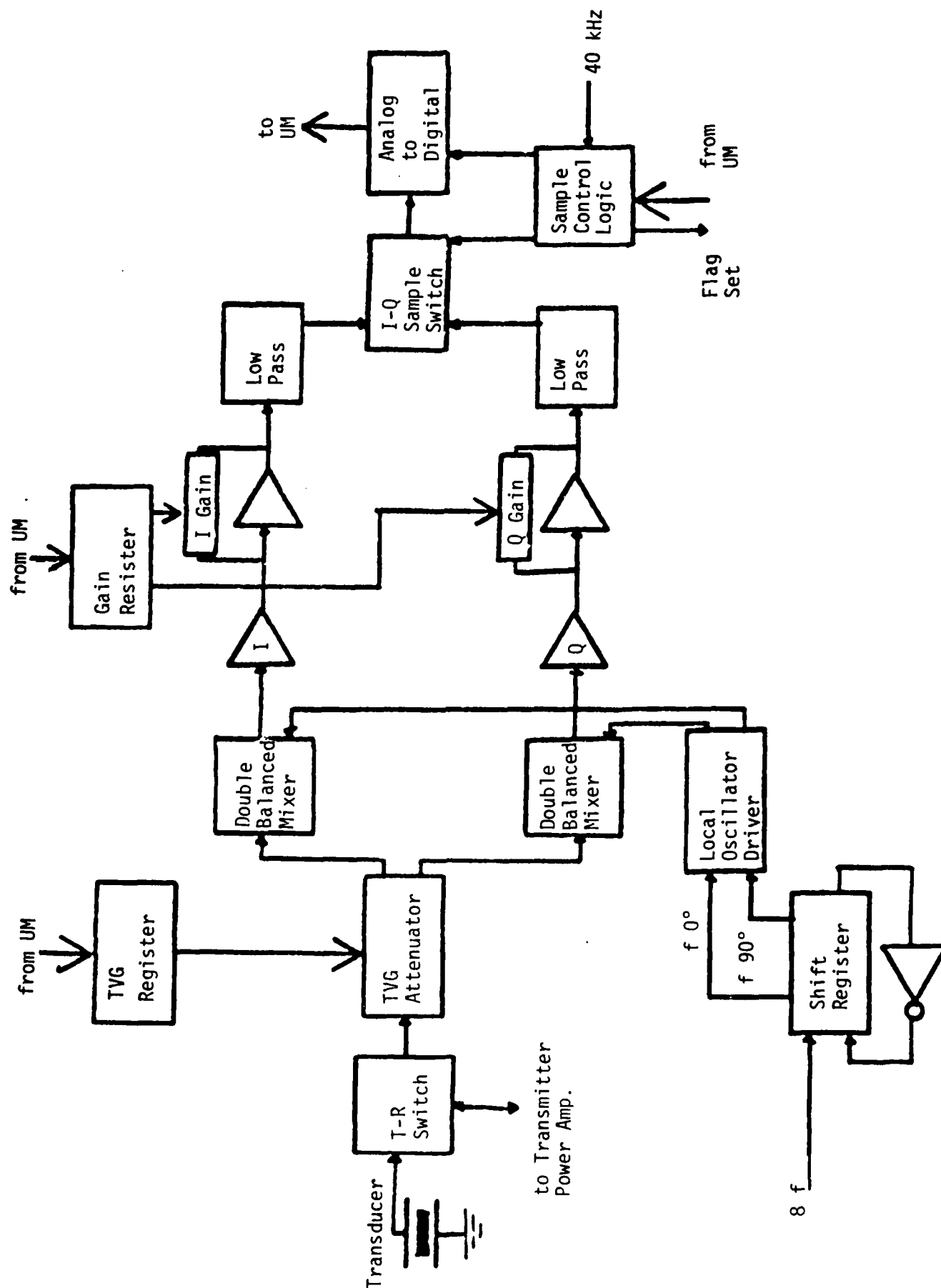


Figure 6. Sonar receiver block diagram.

tuned to the particular sonar frequency. Two stages are employed; more to achieve the desired time varying gain attenuation (TVG) rather than the amplification possible. The TVG attenuation is developed by a lossy variable resistor across a third winding on each of the tuned coupling transformers in the pre-amplifiers. The resistor used is the source-gain path of junction FET's. More than 50 db of attenuation is available through control of the DC voltage to the gates of the FET's with this circuitry.

The TVG function in these sonars is a stepped curve with a new value of attenuation available every 5 msec during listening. Every 5 msec an 8-bit value is transferred from the User Module to a register in the sonar. This value is converted to a negative DC voltage which is applied directly to the FET gates. The FET's are not identical, therefore the TVG attenuation versus the 8-bit value must be calibrated for each sonar.

The direct conversion technique requires two mixers with the local oscillators for each in quadrature in order to recover the true amplitude of the returning echoes. Two identical post mixing amplifiers are employed, mechanized with IC operational amplifiers. Overall gain control of each channel of amplifiers is obtained by using the ladder network of a digital to analog converter (DAC) to control the feedback current around one stage. Again, an 8-bit value stored in a register can control this current over a 1 to 256 range providing a gain adjustment totalling 48 db in each channel. Only one register is provided to operate the DAC in each channel to avoid inadvertent gain unbalance.

The sonar signals in each channel are filtered with a three pole low pass filter and applied to sample and hold circuitry. The two channel signals are sampled at regular intervals by a strobe derived from a programmable divider with a 40 kHz input. Normally 5 samples are taken between each 5 msec real time interrupt, but the divider can be programmed for other integral numbers of samples in this interval. The divider ratio is held in a User Module loaded register in the sonar and reloaded into the divider at each underflow.

The sampled analog values are digitized in a two-quadrant analog to digital converter and the resulting 8-bit value placed in a holding register. The byte is transferred to the User Module under microprocessor control and the interval between samples of the two channels is as small as the successive digitization and transfer will allow (about 40-50 microsec).

## V SONAR TRANSMITTERS

As in the receivers, the sonar transmitters share a common design for logistic reasons. Linear Class B amplifiers are employed to preserve the modulation envelope for the sonar pulse to the transducer. These amplifiers are conventional transformer coupled. Push-pull parallel output stages are also transformer coupled to impedance networks to match the transducer for maximum power transfer. The energy for each transmitted pulse from the sonars is stored in capacitors which are charged during the interpulse period. The capacitors are disconnected from the charging circuitry to the power supply just prior to the sonar pulse to avoid large surge loads being placed on the power supply. All sonars are pulsed simultaneously to avoid interference during listening. Figure 7 is a block diagram of the sonar transmitters and pulse forming logic.



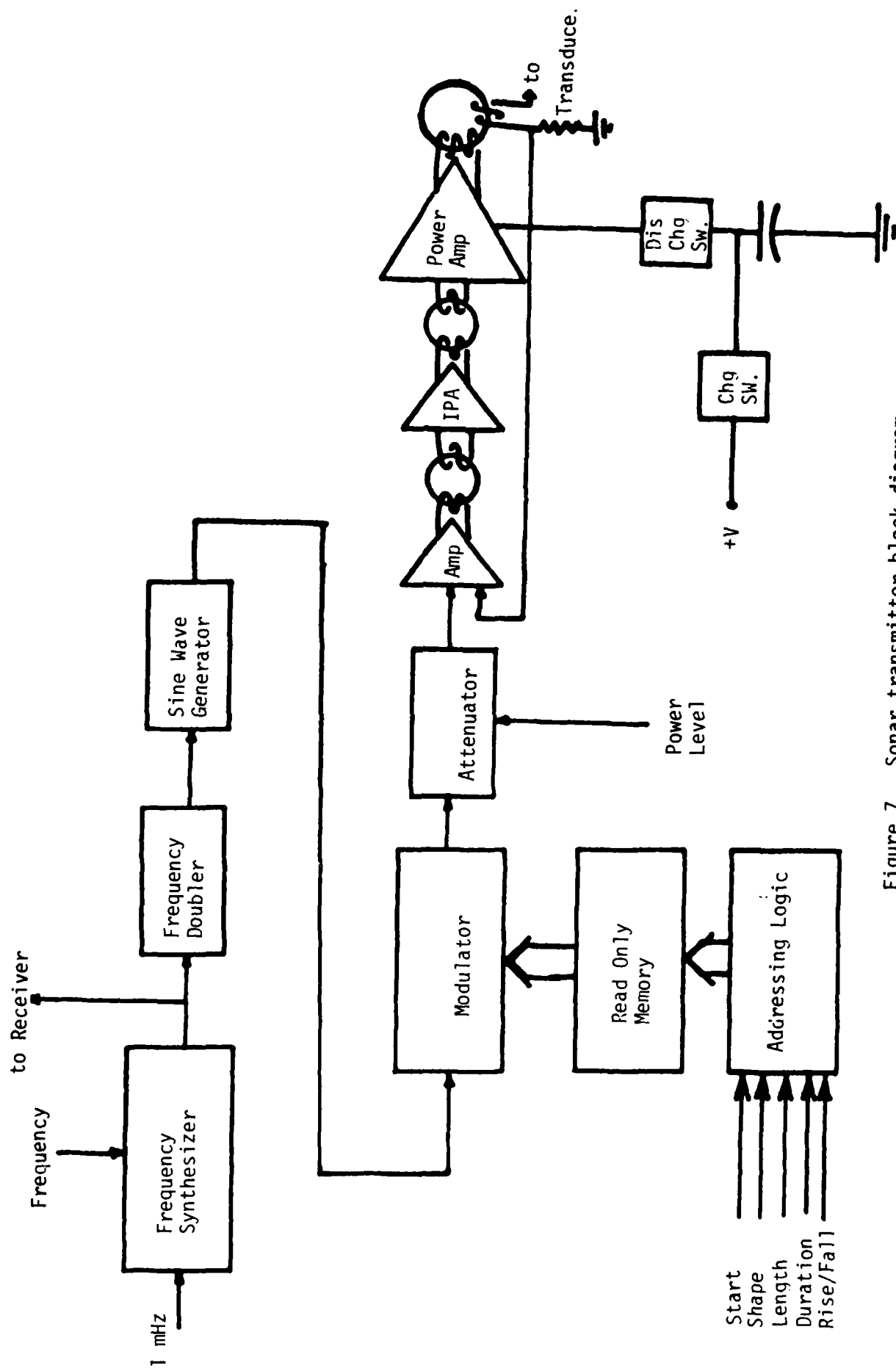


Figure 7. Sonar transmitter block diagram.

The modulated carrier pulse for each sonar is developed with pulse forming circuitry located on the same board as the sonar receiver. No gain control is provided for the power amplifiers as the amplitude of the input pulse supplied determines the output power.

The carrier frequency for each sonar is derived from a common 1 MHz reference frequency available from the FISH data system. Phase locked loop frequency synthesizers with the output frequency an algebraic fraction of the reference are used for carrier generation. The reference and the oscillator in the PLL are divided by different integers before being compared in the phase detector of the PLL. The PLL oscillator frequency then becomes a rational fraction of the reference frequency. The actual frequency developed in each sonar is eight times the carrier frequency. The carrier frequency range that is developed by this technique may be less than 10 to more than 125 kHz.

The integer division ratios for a particular frequency are furnished by the User Module to the sonar as three 8-bit values which are stored in registers in each sonar. The values are calculated by the surface command processor and sent as immediate commands whenever a new frequency is selected from the menu for a sonar.

The eight times sonar frequency is doubled digitally and used to clock a shift register which generates the carrier "sine wave." This waveform is a sixteen step approximation to a full cycle of a sine wave and is generated by a weighted resistor array driven from data in the shift register. Currents are added to or taken from a junction in accordance with the value of the resistor and data state of the register and a wave results as shown in Figure 8.

In addition to the synthesized carrier and frequency being generated by digital means, the modulation envelope and pulse characteristics are also digitally realized. Five waveforms and a phase shift keyed code are available for modulating the sonar carrier pulse. The waveforms are half cycle sine, full cycle cosine, sine X/X, rectangular pulse with linear rise and fall, and rectangular pulse with exponential rise and fall. Figure 9 is six oscilloscope photographs of the wave forms. The brighter traces are due to the stepwise nature of the individual carrier cycles. The carrier is smoothed by the tuned nature of the power amplifier and the higher frequencies do not affect the output waveform. The phase code used is a seven bit Barker code. The ordinates for a stepwise approximation for each of the various waveforms are stored in a different portion of a 256 X 8 ROM (read only memory).

Pulse selection is obtained by indicating the starting address of the shape and the number of ordinates (successive addresses) required. These two parameters are determined by the command processor when a pulse is selected from that menu and the values stored in the sonar. The total length of the pulse is also a selectable parameter and is determined by a programmable divider which times the rate at which addresses of the ROM are incremented. In actuality only the ordinates for half the pulse envelopes are stored as all pulses developed are symmetric. The ROM addresses are therefore counted up for the first half of the pulse and back down for the second half so that the address counter is returned to the initial point each time a pulse is developed. Another parameter useful for determining the duration of the flat top of rectangular pulses is also available and determines the interval of time that should elapse between the counting up and down of the ROM address counter. This parameter is also selectable from a sonar command menu.

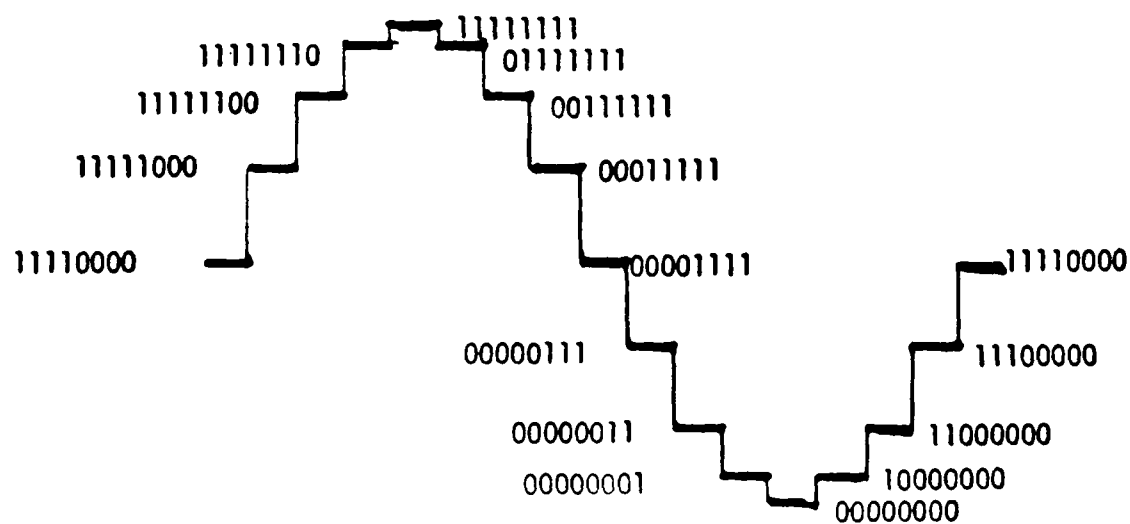
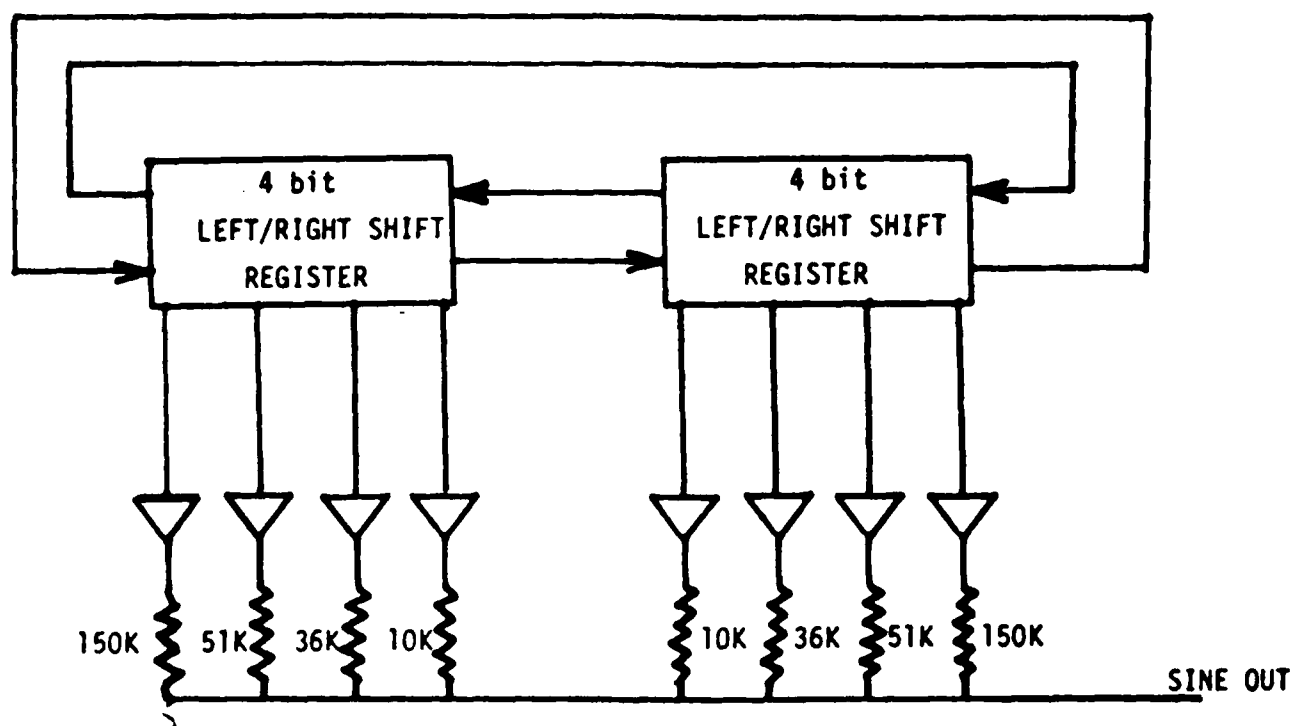
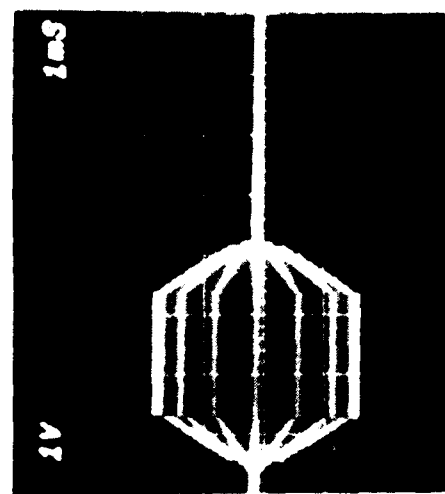
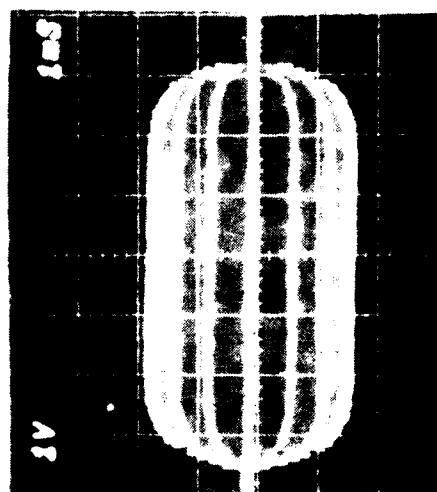


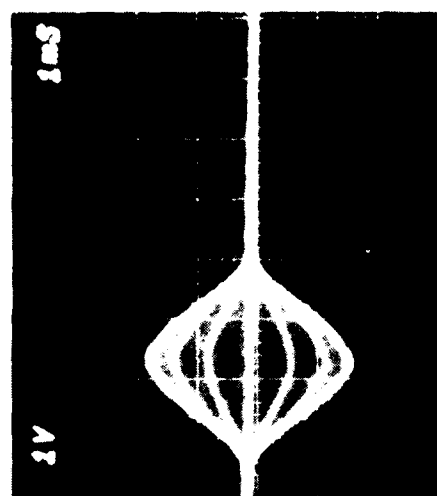
Figure 8. Sine wave generator.



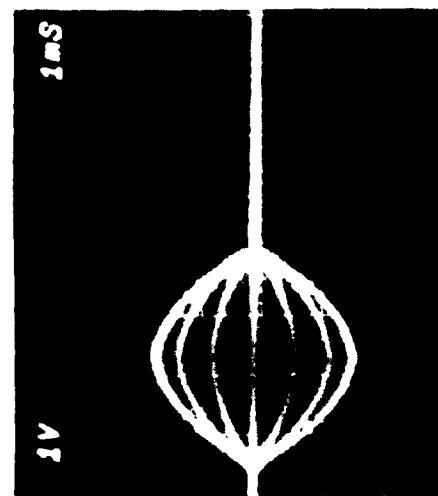
LINEAR



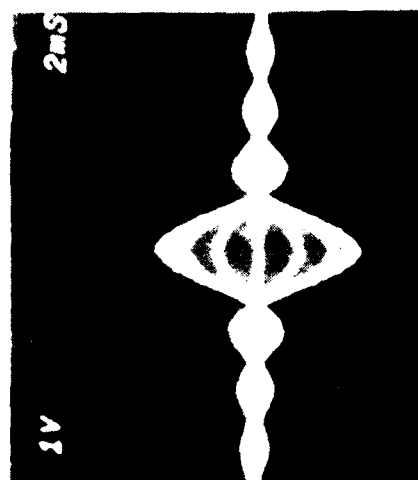
EXPONENTIAL



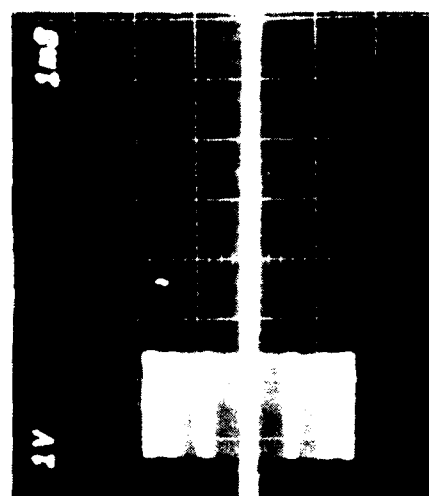
COSINE



HALF SINE



SIN X/X



BARKER

Figure 9. Pulse waveforms.

The ROM ordinates so selected by the address counter control a digital to analog converter (DAC). The "sinewave" carrier is provided to the DAC as a reference which is then multiplied by the ordinate value and thereby amplitude modulated. The modulated pulse that results is in turn used as the reference to a second DAC which uniformly multiplies the pulse by another parameter. Since the overall amplitude of the pulse determines the power output of the transducer driven by the power amplifier, this parameter determines the output power.

## VI PERFORMANCE AND STATUS

The AOTDP system has undergone three sets of sea trials. These have been conducted in the channel waters between Long Beach, CA and Catalina Island. The sonar subsystems described are employed on five sonars: port side looking, starboard side looking, down or altitude, up or depth, and the transponder interrogator. Echoes from the side scan sonars were received at ranges exceeding 400 meters when towed at a height of 75 meters midway in the water column.

Most of the development efforts have been focused on the side sonars, but every improvement tested there has been incorporated easily into the others owing to the common design. A change to the side sonars not yet included in the up, down, or transponder is a change in power amplifier design from a linear to a switching amplifier for increased power output (from 280 to 550 watts rms). This change will necessitate using pulse width rather than amplitude modulation to realize the different "waveshapes" and control maximum power out. This change has been designed but not implemented.

In May of 1982 the AOTDP system was transferred on loan to the Woods Hole Oceanographic Institution for possible inclusion into the ARGO/JASON program.

The work described in this report was carried out by the Jet Propulsion Laboratory, California Institute of Technology, under contract NAS 7-100 with the National Aeronautics and Space Administration.

# Application of Computer Image Processing to Underwater Surveys

Peter R. Paluzzi

McQuest Marine Research & Development Co. Ltd.  
489 Enfield Road  
Burlington, Ontario, Canada  
L7T 2X5

## ABSTRACT

Computer image processing has often come to be equated with automated pattern analysis, particularly within the context of spacecraft remote-sensing. Automated pattern analysis in the form of multispectral classification has been widely used for crop and lithologic mapping from Landsat images. Conversely, bottom photographs and side-scan sonar images collected during underwater surveys have rarely been subjected to automated pattern analysis. Among the reasons for this are limitations of the imaging techniques and complexity in terms of scene and pattern descriptions. It is therefore worthwhile to consider alternatives to pattern analysis for helping interpreters to work with images from underwater surveys. Computer dc notch filtering and geometric rectification by resampling are two key image processing techniques which have proved to be successful in achieving this goal. In addition, since image interpreters often compare bottom photographs and side-scan sonar records to other map based data, namely depth soundings or bathymetry, it is advantageous to also display these data as an image. Finally, while the alternative computer image processing techniques are, by themselves, powerful tools for improving image display, they also show promise for alleviating some of the problems facing automated pattern analysis as applied to underwater survey images.

## I. INTRODUCTION

In the context of spacecraft remote sensing, computer image processing has become synonymous with automated pattern analysis. Pattern analysis in the form of multispectral classification has been applied to Landsat images for crop identification and lithologic mapping. However, computer pattern analysis has not been used to the same extent for images returned by underwater surveys. Reasons for this arise from limitations of the imaging techniques and complexity in terms of the scene content and pattern descriptions. To make matters worse, the seafloor or lakebeds surveyed are areas of exploration; that is, their surfaces can be as unfamiliar to interpreters as was the backside of the moon before the age of space flight. Situations may even occur where an interpreter must identify patterns made by objects no one has seen before let alone described.

While the science and art of pattern analysis advances towards the goal of someday overcoming these problems, other approaches are available to augment the power of the image interpreter. One alternative is to use different computer image processing techniques to improve the way the images are displayed. Foremost among these techniques are image enhancement and geometric rectification. Both have been routinely used in terrestrial and planetary remote-sensing projects. The value of this aspect of computer image processing has been demonstrated by applying these techniques to two types of underwater images: bottom photographs and side-scan sonar. Since image interpretation often requires comparisons with other data, such

ADP003122

as submarine topography or bathymetry, it is also useful to display these data as an image too. Digital terrain models of the seafloor have been created from point-value data and displayed as a shaded relief image. This bathymetric imaging technique portrays the bottom morphology in a way that is similar to images from underwater surveys. Examples provided in this report graphically show how the computer processing can overcome drawbacks of the imaging systems and make the task of image interpretation easier and more productive.

## II. BOTTOM PHOTOGRAPHS

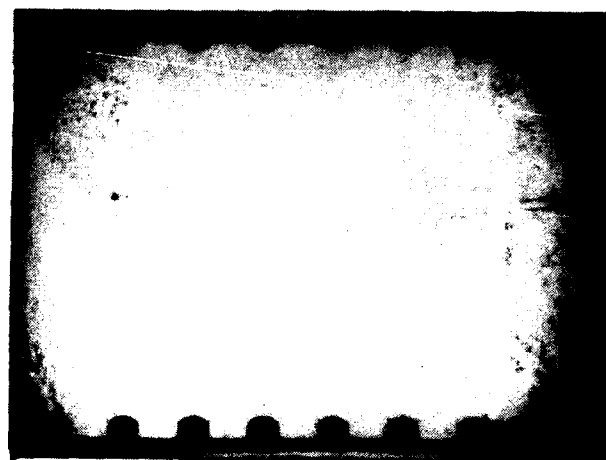
The predominant sort of image returned from underwater surveys is the photograph. Cameras which are, in principle, much like those used by casual photographers have been used in underwater surveys for years (Heezen and Hollister, 1971). Because of the optical properties of water, color film is only occasionally used in these cameras. Water filters out almost all colors except blue-green. Hence underwater photographs are essentially monochromatic except for pictures taken at ranges closer than a meter or two. Furthermore, as the distance from the camera to the object increases, water increasingly scatters light in all directions and reduces image contrast. Underwater photographs are literally useless for surveys performed at ranges greater than 20 meters or so depending on water clarity.

Normally the cameras used in surveys hang from a long line held by a ship. As the ship moves forward, the camera takes pictures of the bottom in plan-view. Unfortunately, there is little control over the camera pointing angle and very often the images possess perspective distortion. This distortion presents problems to the interpreter when the task at hand requires reliable measurements of sizes and shapes from the image.

Among the most severe of problems encountered in underwater photography is that of illumination gradients. Essentially no sunlight reaches water depths below 30 meters. When photographic surveys are conducted below this point a light must be carried with the camera. It is hardly practical to attempt to duplicate the relatively even illumination of the sun underwater; instead, a single small strobe light is used with the bottom cameras. Pictures taken with this type of lighting may have one part of the scene brighter than elsewhere. In cases where the light source is in front or in back of the camera, the resulting illumination gradient creates a dark border surrounding the scene; this is called vignetting (figure 1a).

In order to suppress such gradients an image processing technique known as "dc notch" or "high-pass" filtering has been used (Paluzzi and others, 1976). The operation of the filter is simply to blur the image with a low-pass convolutional filter and then to subtract the blurred image from the original (Castleman, 1979). After applying a brightness correction, the resulting image can be contrast enhanced to show maximum detail throughout the scene without saturating the highlighted or shaded areas. Figure 1b shows the image in figure 1a after being subjected to this processing.

One drawback to the convolutional dc notch filter is a side effect known as ringing (Castleman, 1979). The resulting visual effect of ringing is that light or dark halos surround scene objects having greatly different gray levels from that of the background. Figure 2a is a bottom photograph much like that of figure 1a with the exception that the camera that took the photograph had a lens with a wider viewing angle. Consequently, the greater coverage allows the shadows created by a protective cage surrounding the strobe light to appear prominently. When the same dc notch filter is used on the image, ringing occurs owing to the radial and annular shadows (Paluzzi and others, 1976).



A



5 Metres



B

Figure 1. Bottom photographs showing the removal of illumination gradients. Figure 1a shows a bottom photograph that has been digitized and displayed with no dc notch filtering. Objects in both the light and dark portions of the dc notch filtered image (figure 1b) are portrayed with equal clarity because the subsequent contrast enhancement operates only on the features and not the illumination gradient (after Paluzzi and others, 1976).



To overcome this problem, the image was geometrically resectioned into a polar coordinate representation centered on the strobe light (see figure 2b). The radial shadows thus became horizontal lines and the annular rings were vertical lines (Paluzzi and others, 1976). One dimensional horizontal and vertical dc notch filters were then used to effectively suppress the offending shadows (figure 2c). This image was then retransformed to its original configuration (figure 2d). Survey images processed in this way can be combined into a mosaic that is less confusing to the eye because the striking shadows are gone.

### III. SIDE-SCAN SONAR

Side-scan sonar has been used as a geological survey tool since the early to middle 1950's (Chesterman and others, 1958). It is essentially the same in operation as the familiar profiler or chart recording fathometer except for the transducer deployment and associated electronics. Side-scan sonar paints an "aerial photograph like" image of the bottom on the chart paper record by scanning a narrow line footprint with an acoustic pulse. The pulse is projected to the port and starboard sides of towfish mounted transducers in a fan shaped beam. The plane of this beam is perpendicular to the trackline as shown in figure 3. Rather than measuring the immediate depth below the towfish, side-scan sonar registers the intensity of echoes cast from objects lying on the bottom to either side. The variations in echo intensity arise from the orientation of the bottom, its acoustic reflectivity and its surface roughness. The resulting shading effect creates an image which depicts the morphology of the area. Although side-scan sonar is immensely important for revealing underwater terrain at scales which could never be seen by man, its presentation is marred by distortions inherent in the imaging technique.

Descriptions of these distortions abound in the marine literature (Belderson and others, 1972; Berkson and Clay, 1973; Clay and Medwin, 1977; Cole, 1968; Urick, 1975). The most notable forms are slant-range, ship speed and trackline distortion. Slant-range distortion is introduced by the imaging geometry. The effect is to squeeze the image away from the center (nadir). Thus, a long linear object lying on the bottom (for example a straight pipeline) which crosses the image diagonally will appear curved near the image nadir (Belderson and others, 1972). Since a side-scan sonar image is built up a line at a time by the forward motion of the towship, any miscoupling of the ship speed with the chart paper advance will expand or compress the record along the trackline. Finally, despite the best intentions of marine scientists and ships captains, the towship very rarely follows a path that is an absolutely straight line. Most side-scan chart recorders were designed with the assumption that a survey will always adhere to straight line traverses. If the heading changes while underway, for whatever reason, the recorder will not register the change and the image will be distorted.

In the end, the cumulative effect of these distortions is to warp the image of the bottom, in some cases much like a fun house mirror. Just as the reflections of familiar people and things seem strange and unrecognizable when viewed through these mirrors, so seem the bedforms and landmarks in side-scan sonar images as viewed by the interpreters. Several methods have been devised to alleviate this problem. They range from mechanically changing the way the images are set down upon the chart paper to complex flow cameras with anamorphic lenses (Berkson and Clay, 1973 and Belderson and others, 1972). A computer image processing technique known as geometric rectification by re-sampling has been effective in removing similar distortions in remote-sensing images (Castleman, 1979).

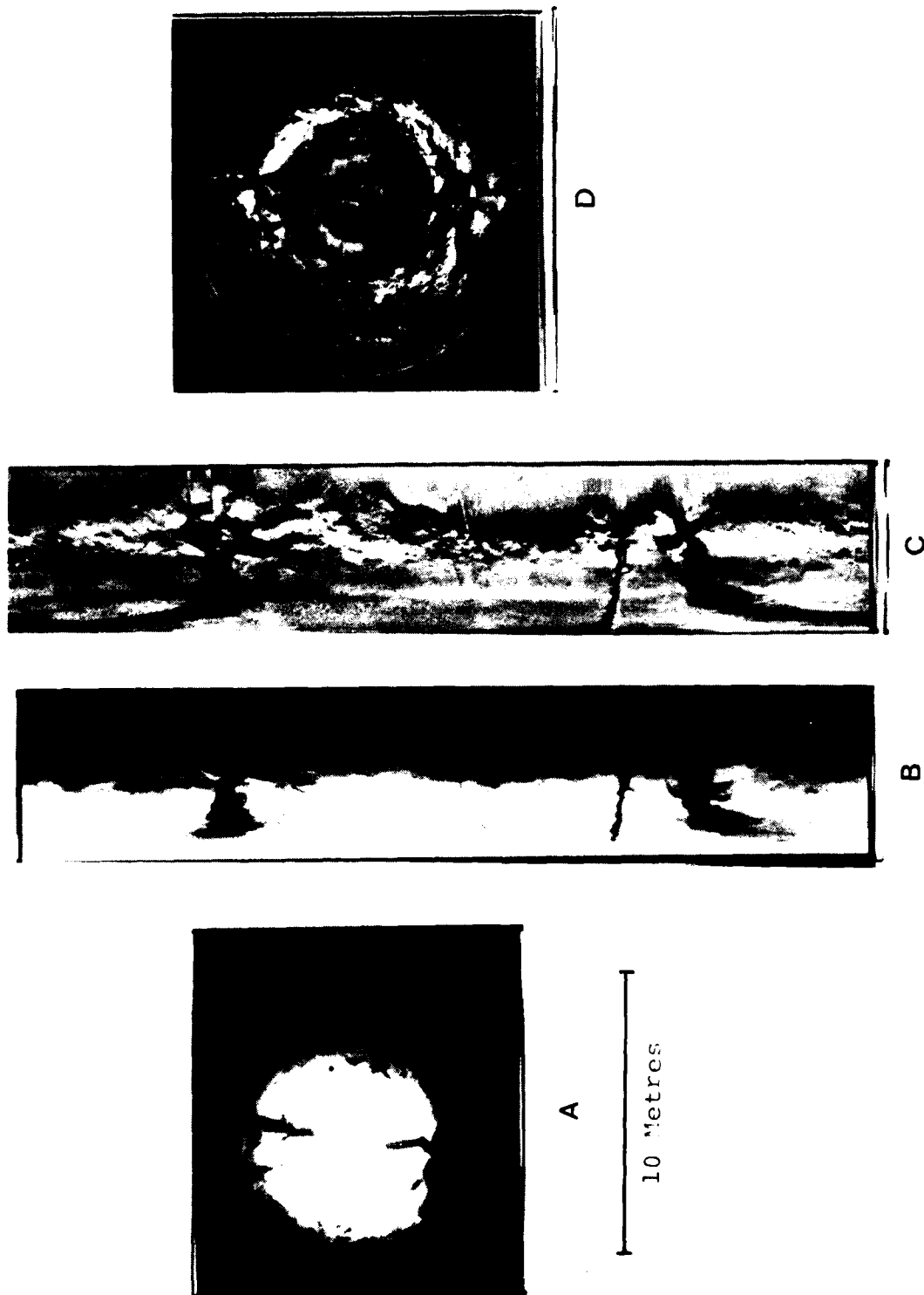


Figure 2. Bottom photographs with strobe grid shadows: before enhancement (a), transformed to polar coordinates (b), dc notch filtered (c), and retransformed to Cartesian coordinates (d) (after Paluzzi and others, 1976).

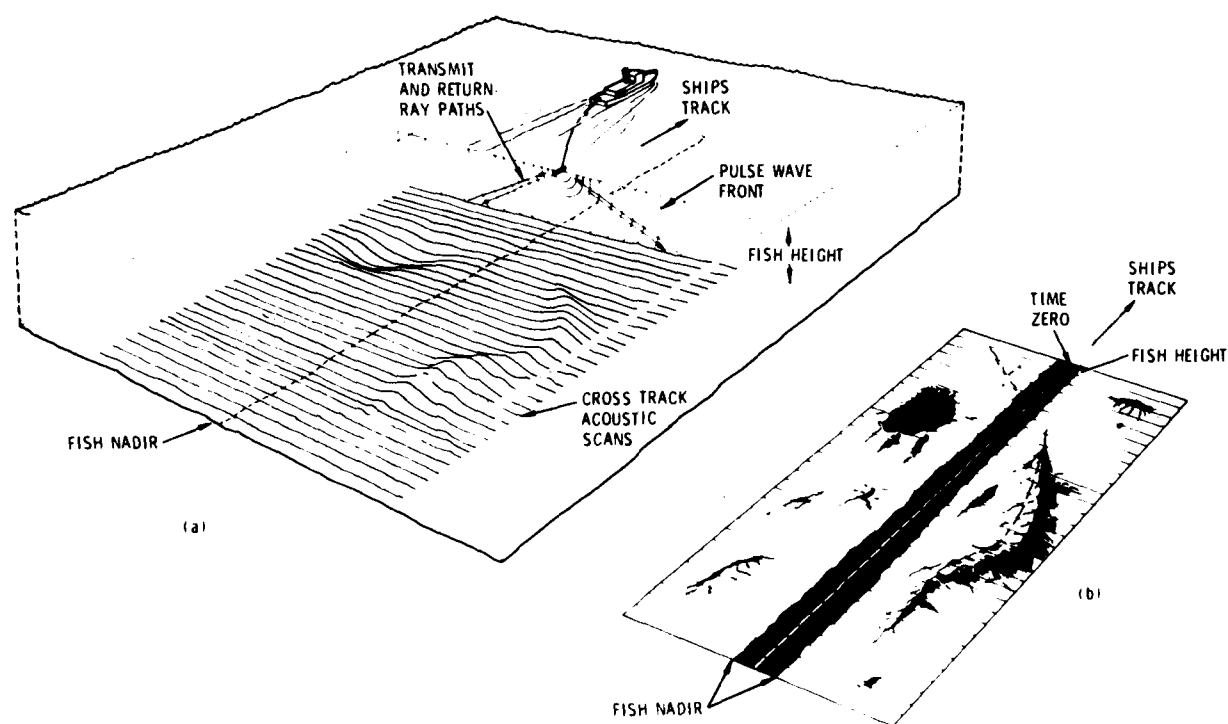


Figure 3. Schematic view of side-looking sonar, imaging technique. A sonar transceiver is towed by a survey vessel and cross-track acoustic scans are made (a). These scans are recorded aboard the vessel and displayed as a chart (b) (after Paluzzi, 1976).

Paluzzi and others (1981) have successfully used this technique to correct side-scan sonar images given certain assumptions about the imaging geometry and topography. Their work involved side-scan sonar images from the British Institute of Oceanographic Sciences long-range GLORIA system. Sonar images covering 30 km to the port and starboard were corrected for geometric distortions and shading gradients. Once corrected, the images were digitally mosaicked and transformed to a Mercator Projection. Figure 4a shows the unprocessed images and figure 5 is the final mosaic. The advantage of the computer processing in this case is that the images are presented in terms of a cartographic base and can be directly and conveniently compared to other map based data.

#### IV. BATHYMETRIC IMAGING

Comparisons of bottom photographs and side-scan sonar images to other data are important aspects of interpreting images collected during underwater surveys. Although the associated data can be almost any physical or environmental parameter, depth or bathymetric data are most frequently used. This is because bathymetric data show the topography of the survey area which greatly influences bottom currents, slope stability, sediment transport and physical chemistry of the survey site. These parameters in turn affect the bedforms, sedimentology and benthic life as they appear in bottom photographs and side-scan sonar images. The comparisons are usually made by the interpreter while he or she examines images and contour charts of the area. The charts are made by plotting iso-depth contours amongst depth data points known as soundings. Such charts show the quantitative depth data as well as a representation of terrain. A shortcoming of this type of terrain display is that it does not have the visual impact of portraying the bottom as continuous surface with relief visible by virtue of shadows and shading.

Paluzzi and Malin (1981) used bathymetric data collected during a NOAA survey of the continental margin off California to create a shaded relief image of the seafloor. To do this they placed the sounding data into an image array such that each point corresponded to a single picture element or pixel. The gray value of this pixel was a function of the depth. Since the data were not collected in a regular grid their spacing was uneven and large holidays existed between them (see figure 6). A digital terrain model based on a rectilinear latitude-longitude grid was created from the data using an interpolation technique. The result was a picture having gray scale registered depths rather than scene brightness (see figure 7). A shaded relief image was derived from the digital terrain model image by computing the surface slope in the direction of the source of illumination (figure 8a). Areas with larger gradients in the direction of the light source are given lighter gray tones and areas with shallow slopes appear mid gray. Those parts of the terrain that dip away from the light source are represented as black.

The key advantage of this technique is that it immediately conveys the visual appearance of the terrain to the viewer. This means that the interpreter is relieved of the burden of mentally transforming the contour representations of the topography into a 3-dimensional surface. The continents appear this way in conventional remote-sensing images since a camera or scanner can directly see shading effect of the sunlight falling on the landscape. Submarine topography cannot be seen at small scales because the water of the ocean or lake covers it like an opaque blanket. The bathymetric imaging display technique is consequently a way to portray the underwater terrain as if the water weren't there at all. Furthermore, because the shading is sensitive to subtle changes in gradient, it can

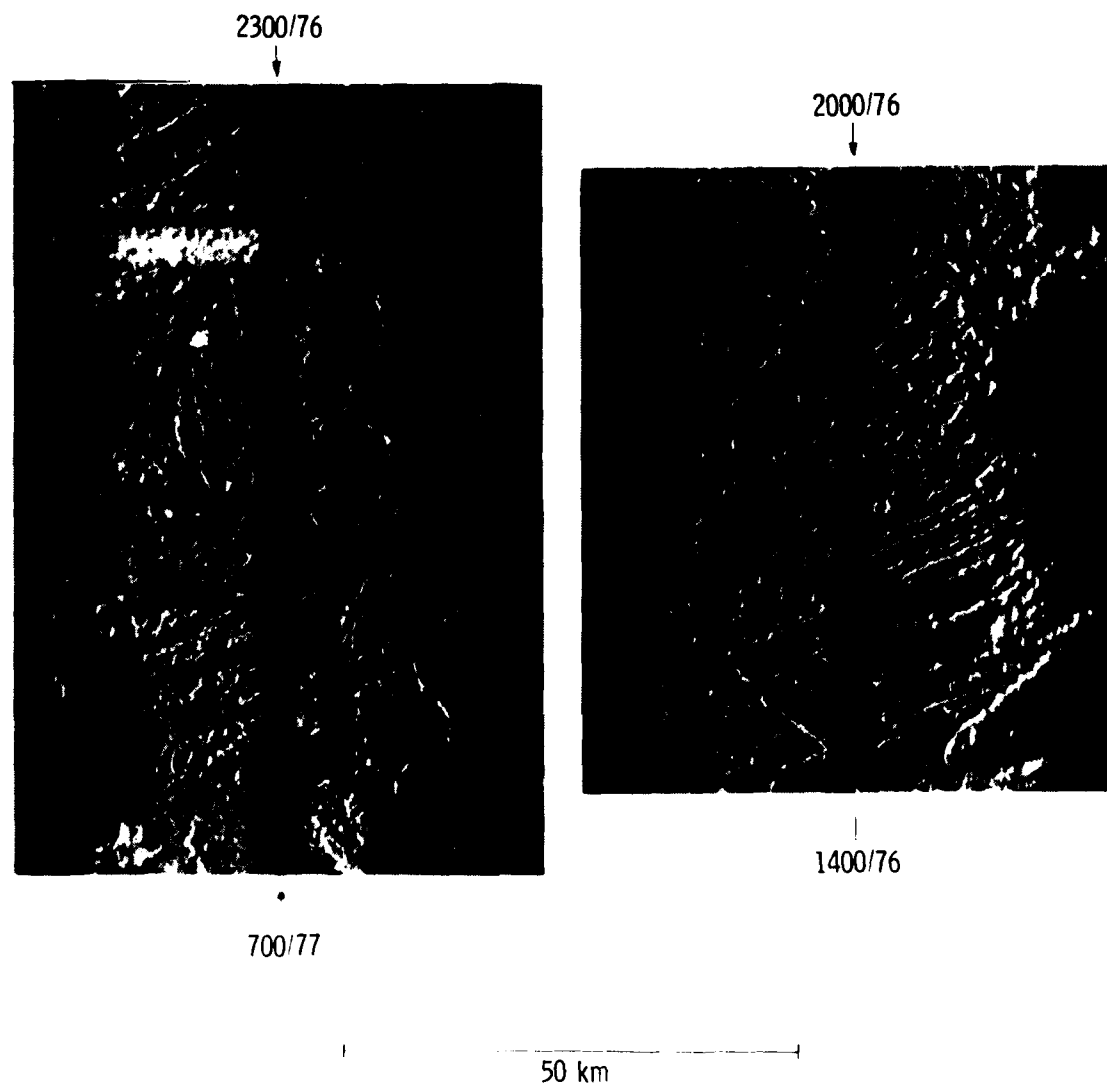


Figure 4. GLORIA side scan sonar images from the mid-Atlantic ridge. These images have not been computer processed (after Paluzzi and others, 1981).

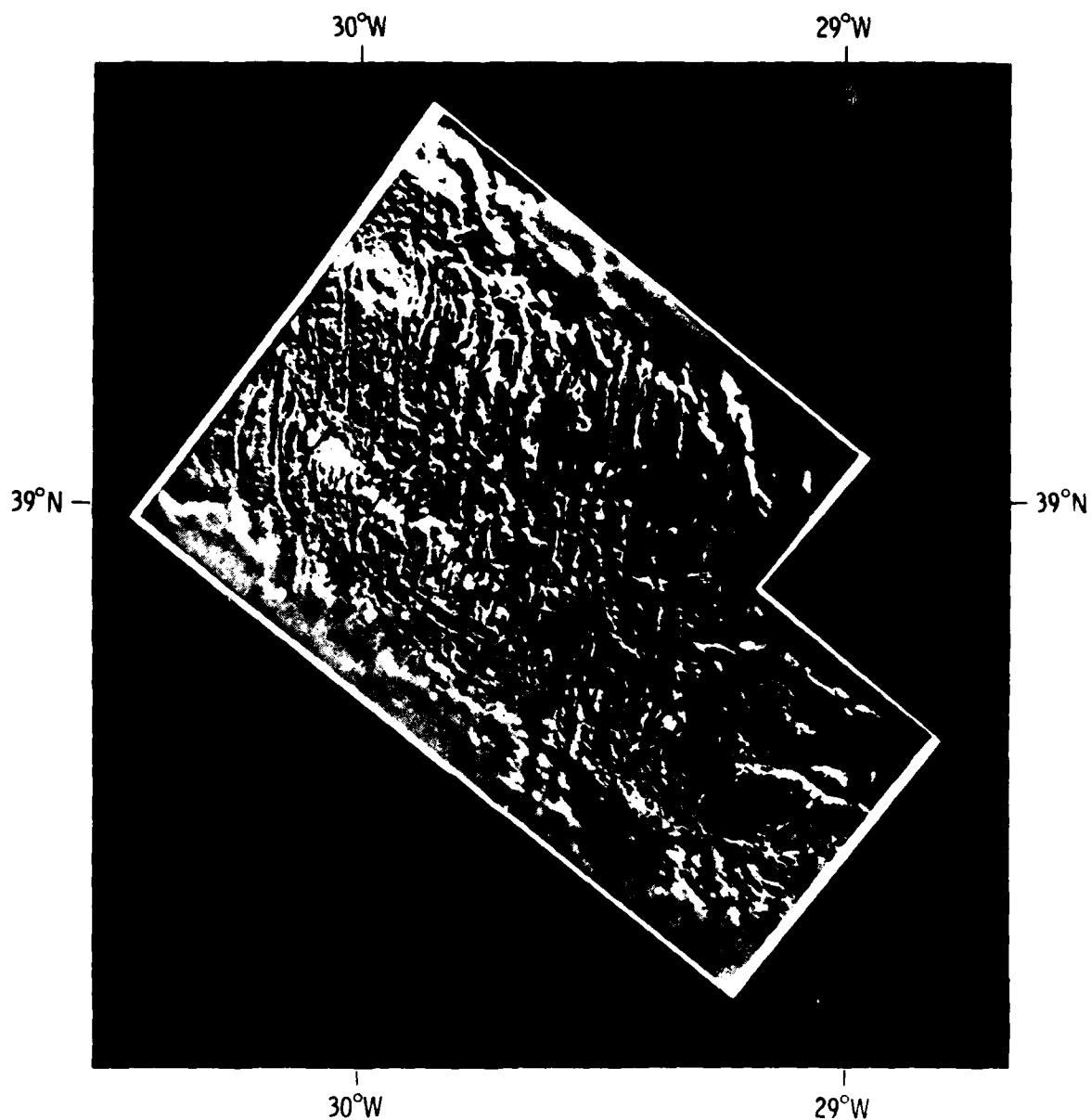


Figure 5. Computer rectified mosaic of the images in figure 4 (after Paluzzi and others, 1981).

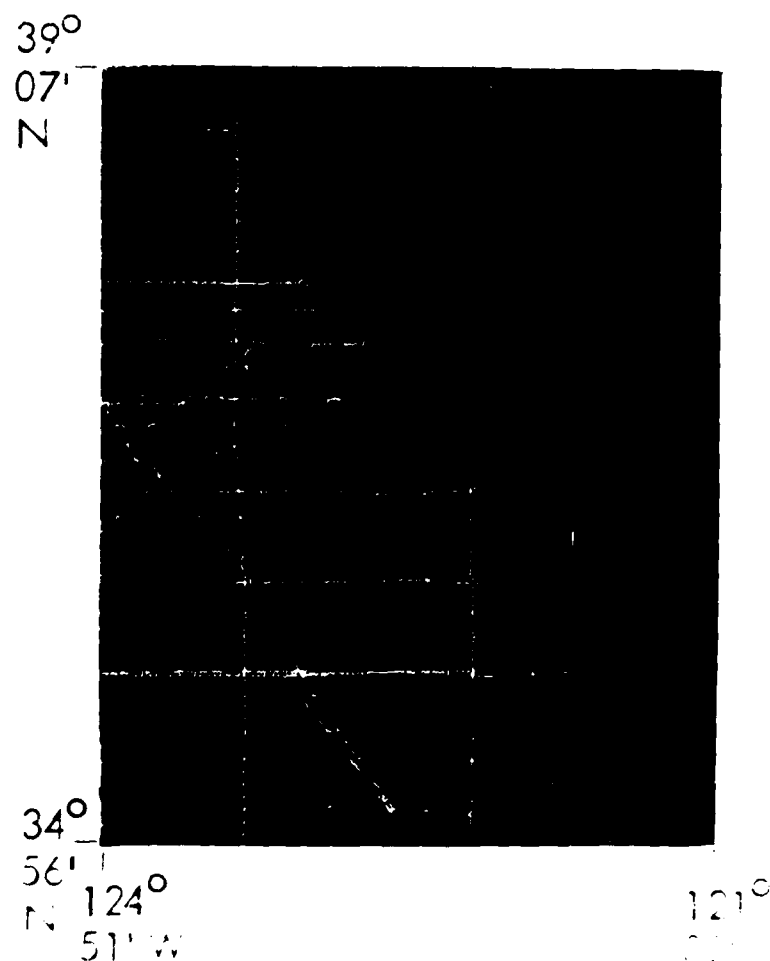


Figure 6. Bathymetric data taken off the central coast of California. The data have been placed into an image array. Each data point has a gray level representation of the depth. Darker tones mean shallow depths, lighter tones mean greater depths (after Paluzzi and Malin, 1981).

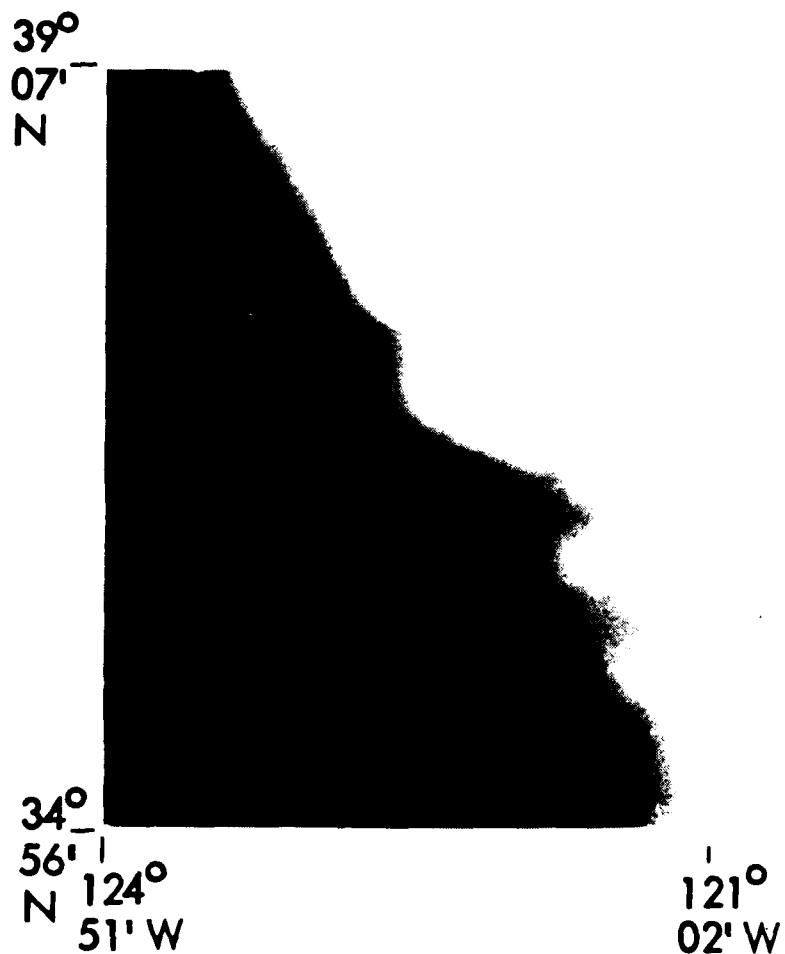


Figure 7. Depth image created by interpolating the data between the actual measured points and smoothing the resulting image. Here, lighter tones correspond to shallow areas and darker tones represent the deeper regions (after Paluzzi and Malin, 1981).



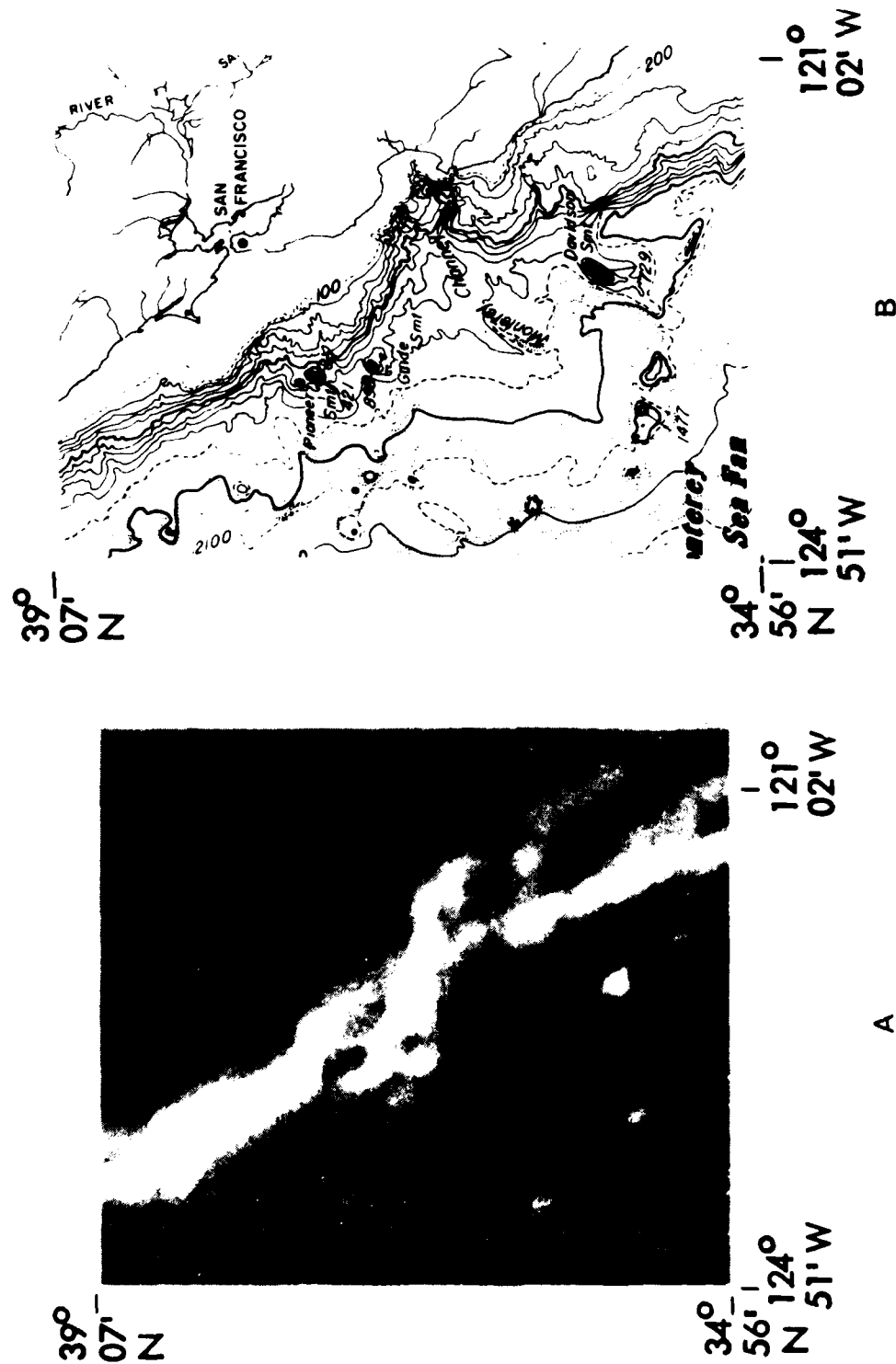


Figure 8. A shaded relief image was created by computing a directional gradient for each pixel in figure 7a. This image portrays the seafloor as a surface rather than a schematic representation as is the case with conventional contour charts (b) (after Paluzzi and Malin, 1981).

be possible to see slope changes that may go unnoticed in a contour map (figures 8a and 8b). In short, the use of shaded relief images to display bathymetric data is an elegant conceptual link between the data and the mind's eye.

One disadvantage to bathymetric imaging is that the display does not show quantitative data as does the contour map. The shading shows the shape of the terrain but does not directly yield elevations or depths. Yet, it is still possible to overlay the shaded relief image with contours generated from the gridded digital terrain model. If contours superposed upon the shaded relief image prove to be too confusing, the gray tones can be digitally painted different colors depending upon the depths. Also, because the shaded relief image was created from a digital terrain model, the data can be further processed to provide other displays.

#### V. PROSPECTS AND PROBLEMS FOR PATTERN ANALYSIS

Since bottom photographs are mostly monochromatic, the possibility of pattern analysis by multispectral classification is nil. On the other hand, spatial patterns appear repeatedly in these images. These patterns are mostly that of isolated objects, sedimentary bedforms, rock outcrops, bioturbation markings, benthic animals and miscellaneous articles lost or discarded by man. If one were to use automated pattern analysis to identify these features in bottom photographs, one should use algorithms that account for any distortion in the image as well as for changing shadows, illumination gradients and degraded contrast. Rather than considering all these factors in the pattern analysis scheme, it is better to correct the image shortcomings with a preprocessing step using the previously mentioned techniques.

Side-scan sonar images frequently contain patches or areas of nearly uniform gray tone. These areas are often irregular and are a result of differences in acoustic scattering of some material with the surrounding terrain (Clay and Medwin, 1977). Some images show long linear objects or lineaments which may be, in some cases, exposed pipelines or cables. Like bottom photographs, side-scan sonar images contain point like patterns which correspond to isolated targets such as rocks or man-made articles. Depending upon the local sedimentary environment, bedforms can be visible in side-scan sonar images. Some of the bedforms are large such as mega-dunes and current ripples (Belderson and others, 1971). Bedforms too small to be resolved by most side-scan sonars (typically <1m) can act as a diffuse scatterers and appear as the contrasting irregular patches previously described. The strength of this scattering depends upon the micro relief of the bedform as compared to the wavelength of the acoustic pulse (Urick, Clay and Medwin). Like the smaller bedforms, the workings of benthic animals are also small and scatter acoustic energy; yet, they may not be resolved in the side-scan sonar image. Areas of heavy biologic activity can also appear as contrasting irregular patches in the image.

Since the strength of the echoes recorded in side-scan sonar images has a wavelength dependence, at least with respect to surface roughness, it may be possible to employ multispectral pattern analysis to identify certain bottom types. Also, because some objects have characteristic spatial patterns associated with them, they may be identifiable using spatial pattern analysis techniques. However, some traits of the side-scan sonar imaging process itself present potential problems for using automated pattern analysis. Distortions introduced by the slant-range geometry and the motions of the towfish create ambiguities for spatially identifying known objects and features. Since many items of interest (bedforms, ships, etc.) are visible in the images by virtue of the shadows they cast, any change in tow depth or look direction may change their appearance. This is particularly true for

the irregular patches which have sonar signatures related to their scattering fields. The literature for radar imaging contains many references to the fact that rough surface scattering is not only affected by wavelength but also by the grazing and azimuth angles (Beckmann and Spizzicino, 1963; Shaber and others, 1976; Peake and Oliver). Urlick (1975) and Clay and Medwin (1977) have similarly described acoustic scattering to study this problem in the sonar context.

Uncertainties in the patterns recorded in the images also arise from inhomogeneities and stratification in the water column (Cole, 1968). The spatial aspect of a pattern can be altered if the speed of sound changes in the water column since the side-scan sonar echoes are recorded versus their time of flight. For short ranges, 100 m or less, this may not be a significant problem; however, ray bending and changes in acoustic transmission loss could affect the pattern's appearance in the image. Furthermore, the rapid loss of signal intensity with increasing range creates difficulties for unambiguously identifying patterns in the far range portions of the image.

Again, preprocessing of the side-scan sonar images can alleviate some of these problems associated with recognizing important patterns. Yet, the uncertainties introduced by the interaction of sound with targets require careful consideration for reliable automated pattern analysis. Most interpreters of side-scan sonar images agree that it is very tricky to reliably identify many scene features visually. Indeed, the same terrain will look differently when surveyed with changes in look direction or towdepth. In some cases, a highly trained interpreter who is familiar with the survey area is required to properly identify features in a side-scan sonar image. In the final analysis, the pattern analysis algorithm may have to be as equally as capable as this interpreter to perform equally as well.

## VI. SUMMARY

Although images returned from underwater surveys may not always be suitable for advanced image processing techniques such as automated pattern analysis, the quality of interpretation using these images can still be improved using other image processing techniques. DC notch convolutional filtering can suppress illumination gradients in bottom photographs and side-scan sonar images. In some cases, the convolutional filter can be combined with other methods such as rectangular to polar coordinate transformations to expand the overall power and usefulness. Geometric distortion in bottom photographs and side-scan sonar images can be corrected by digital resampling if the nature of the distortions is sufficiently understood. When the images are geometrically corrected, in particular side-scan sonar images, it is then possible to do direct comparisons to other map based data such as bathymetry. The bathymetric data can also be recast as an image to aid this type of comparison and display topographic details which may go unnoticed on the contour charts.

Pattern analysis in the form of multispectral classification as applied to underwater images holds greater promise for success when used with side-scan sonar images rather than bottom photographs. However, automated spatial pattern recognition may be equally suitable for both image types. In any event, setbacks for automated pattern analysis arising from image degradation or geometric warping can be minimized by employing the image processing techniques cited in this report. In fact, the image processing techniques by themselves are powerful tools for improving the effectiveness of those who must interpret images from underwater surveys.

## References

- Beckmann, P. and A. Spizzichino, 1963, The scattering of electromagnetic waves from rough surfaces: MacMillan Co., New York, 303 p.
- Belderson, R. H., N. H. Kenyon, A. H. Stride and A. R. Stubbs, 1972, Sonographs of the seafloor: a picture atlas: Elsevier, New York, 182 p.
- Berkson, J. M. and C. S. Clay, 1973, Transformation of side-scan sonar records to a linear display: International Hydrographic Review, v. L, n. 2, July, p. 55 to 60.
- Castleman, K. R., 1979, Digital image processing: Prentice-Hall, Inc. Englewood Cliffs, N. J., 429 p.
- Chesterman, W. D., P. R. Clynick and A. H. Stride, 1958, An acoustic aid to sea-bed survey: Acustica, v. 8, p 280 to 290.
- Clay, C. S. and H. Medwin, 1977, Acoustical oceanography: John Wiley and Sons, New York, 544 p.
- Cole, F. W., 1968, A familiarization with lateral or side-scanning sonars: Technical Report 159 prepared for The Office of Naval Research, CU-187-68-ONR-266-Phys., Hudson Laboratories, Columbia University, Dobbs Ferry, N. Y., 43 p.
- Heezen, B. C. and C. Hollister, 1971, The face of the deep: Oxford University Press, New York, 659 p.
- Paluzzi, P. R., W. R. Normark, G. R. Hess, H. D. Hess and M. J. Cruickshank, 1976, Computer image processing in marine resource exploration: Oceans '76 joint meeting of the Marine Technical Society and the Institute of Electrical and Electronics Engineers Conference Record, Washington, D. C., p. 4D-1 to 4D-10.
- Paluzzi, P. R., 1976, Analysis of images for marine resource exploration: JPL/Cal Tech conference on Image Processing Techniques, Data Sources and Applications Proceedings, Pasadena, p. 12-1 to 12-8.
- Paluzzi, P. R. and M. C. Malin, 1981, Bathymetric Imaging: Proceedings of the joint American Society of Photogrammetry-American Congress of Surveying and Mapping Annual Meeting, Washington, D. C., p. 249 to 258.
- Paluzzi, P. R., R. D. Toaz, D. G. Roberts, R. C. Searle and M. L. Somers, 1981, Computer rectification and mosaicking of side-looking sonar images: Proceedings of the Offshore Technology Conference, Houston, paper no. 4018, p. 103 to 114.

Peake, W. H. and T. L. Oliver, 1971, The response of terrestrial surfaces at microwave frequencies: U. S. Air Force Avionics Lab. Rept. AFAL-TR-70-301, 255 p.

Shaber, G. G., G. L. Berlin and W. E. Brown, Jr., 1976, Variations in surface roughness within Death Valley, California: Geologic evaluation of 25-cm-wavelength radar images: Geol. Soc. America Bull., v. 87, p. 29-41, January.

Urlick, R. J., 1975, Principles of underwater sound: McGraw-Hill, Inc., New York, 384 p.

# The Identification and Inversion of Acoustic Multipath Data at Long Range in the Ocean

Michael G. Brown

Institute of Geophysics & Planetary Physics  
Scripps Institution of Oceanography  
University of California, San Diego  
La Jolla, California 92093

ADP003123

Due to the presence of the ocean sound channel, in general many ray paths (multipaths) connect a given acoustic source-receiver pair in the ocean. The number and structure of the multipaths depend on the details of the sound channel and the positions of the source and receiver. As each multipath samples the ocean differently each contains unique information about the sound speed structure of the ocean. In order to exploit this information one must first identify each of the measured multipath arrivals. Here we address the related problems of identifying multipath arrivals and the subsequent inversion of this data for the ocean structure.

## I. INTRODUCTION

Sound speed profiles in most of the world's deep oceans are characterized by a well defined minimum at a depth of about one km. An acoustic source located within the ocean sound channel and a separate similarly placed receiver are connected by a number of ray paths (multipaths). This situation is depicted in Figure 1. The arrival pattern measured at the receiver contains a number of peaks (if the source bandwidth is sufficiently broad); each of these peaks corresponds to one or more of the multipaths. The exact number and structure of multipaths depend on the details of the sound channel and the positions of the source and receiver. As each multipath samples the ocean differently each contains unique information about the sound speed structure of the ocean.

Recently Munk and Wunsch<sup>1</sup> proposed a scheme to exploit this information. The purpose of the scheme, which they called ocean acoustic tomography, was to monitor the ocean's mesoscale variability (with a time scale of a few weeks and a spatial scale of about 100km). They proposed setting out an array of acoustic sources and receivers around the perimeter of some ocean volume (see Figure 2). Each source transmits to each receiver. The multipaths between each source-receiver pair contain information about the vertical ocean structure. The different source-receiver pairs contain information about the horizontal structure of the ocean. The combined information gives a three-dimensional picture of the ocean.

The present study deals with two related problems, both of which loosely fit under the heading, "Pattern Analysis in the Marine Environment."

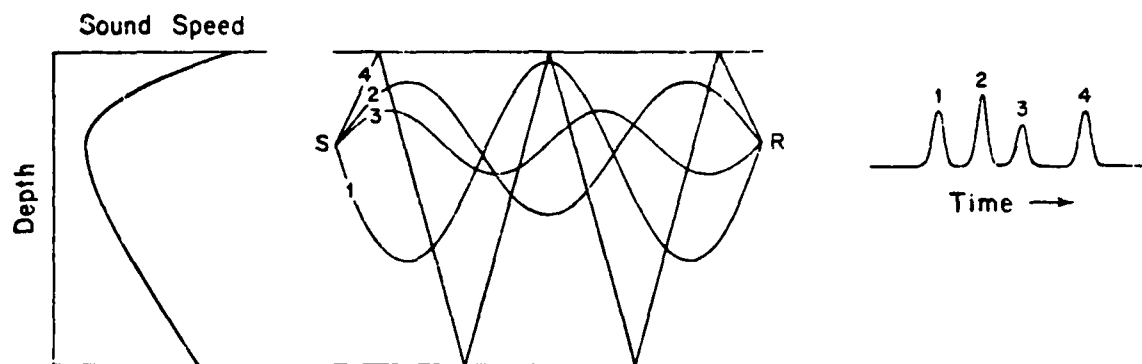


Figure 1. A schematic diagram showing: (left) a typical deep ocean sound speed profile; (center) selected acoustic ray paths connecting source and receiver; (right) an arrival pattern measured at the receiver. Numbers identifying arrival pattern peaks correspond to those identifying ray paths. The forward problem (discussed in the text) proceeds from left to right. The inverse problem proceeds from right to left.

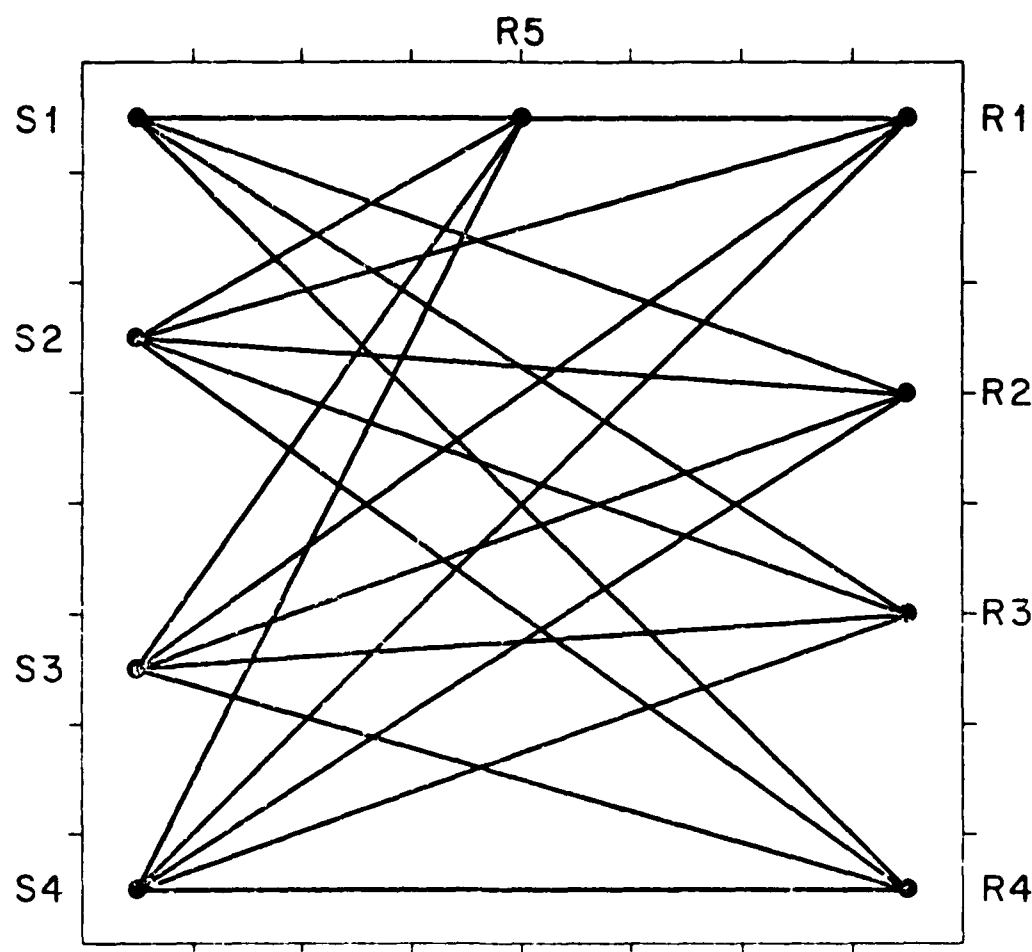


Figure 2. The acoustic source-receiver array used in the 1981 acoustic tomography experiment. The center of the 300 km x 300 km grid was located at 70°W, 26°N.

The first problem is the forward problem of identifying peaks in a measured arrival pattern with ray paths in the ocean. The second problem is that of inverting a measured arrival pattern for the ocean structure.

## II. THE IDENTIFICATION OF ACOUSTIC MULTIPATHS (THE FORWARD PROBLEM)

An essential preliminary step to using acoustics to monitor the ocean is identifying arrival pattern peaks with rays in the ocean. The information which might be used to make such an identification is listed below (note that the problem is discussed from a ray viewpoint - as opposed to an expansion in modes):

### A. TRAVEL TIMES

Here predicted travel times are compared to peak times in a measured arrival pattern. The comparison can be made using either relative or absolute travel times. In order to use absolute times, however, one must know the source and receiver positions extremely accurately and source and receiver must contain accurate synchronized clocks. These requirements are extremely difficult to meet in the ocean environment.

### B. AMPLITUDES

Predicted amplitudes can be compared to those measured. Again the comparison can be made using either relative or absolute values. Because of the extreme difficulty of modelling the physical processes involved, however, it is generally not practical to attempt to compare absolute amplitudes.

### C. ARRIVAL ANGLE

If one has an array of receivers, the ray inclination can be measured and compared to the predicted value. This information has been exploited by Worcester.<sup>2</sup>

### D. PHASE

Each time a ray touches a caustic it undergoes a phase delay of  $\pi/2$ . If a broad-band signal is transmitted this phase shift of each spectral component is equivalent to a Hilbert transform. As before predicted and measured phases (pulse shape) can be compared.

We shall concentrate on exploiting travel time information. The method we have used to compute the predicted travel times has been described previously.<sup>3,4</sup> The technique involves computing the WKBJ Green's function, an approximate solution to the full wave equation for an impulsive point source. As the technique is based on the WKB approximation it is not uniformly valid. It does represent a significant improvement over geometric ray theory, however; it is valid at caustics, for instance. The technique is applied here to model oceans in which sound speed is a function of depth only. As the technique is fundamentally a broad-band approximation (one



computes the acoustic impulse response of the ocean), it is particularly well suited to the exploitation of travel time information.

We show now two examples of successful identification made using the WKBJ Green's function. The procedure we follow is extremely simple: 1) Using all of the available information on the sound speed structure between source and receiver (measurements made during source-receiver deployment, historical data, etc.) we construct a sound speed profile; 2) Using this sound speed profile we compute the impulse response (WKBJ Green's function) and compare it to the measured data. If there is a one-to-one correspondence between measured and computed arrival pattern travel times (and to a lesser extent, amplitudes) we feel confident that the identification has been made. Examples of successful identification for a 215 km 224 + 8 Hz transmission in the North Pacific<sup>2</sup> and a 315 km 224 + 8 Hz transmission in the North Atlantic<sup>5</sup> are shown in Figures 3 and 4 respectively. Other examples of successful identification have been reported elsewhere.<sup>5,6</sup>

### III. THE INVERSION OF ACOUSTIC MULTIPATH DATA

The inverse problem is concerned with the problem of using a measured acoustic arrival pattern to infer something about the ocean's sound speed structure. The approach we take is a perturbation method: perturbations to an initial arrival pattern are used to compute perturbations to the corresponding initial ocean model. The initial model might be the initial state from which we wish to infer the oceans time evolution, or an initial guess at the correct model.

The first step in the inversion is to parameterize the model with a finite number of parameters (these might be the sound speeds at fixed depths or a set of modes, for example). Next, the data (to be specific we consider travel times) is expanded in a Taylor series expansion in the model parameters:

$$T_i^0 = T_i^I + \frac{\partial T_i^I}{\partial m_j} (m_j^0 - m_j^I) + \dots$$

i = travel time index  
j = model parameter index

The superscripts 0 and I refer to the ocean and initial model, respectively. Terms higher than first order in  $\delta m$  are neglected and the equation is written

$$\delta T_i = \frac{\partial T_i}{\partial m_j} \delta m_j.$$

This system of equations is then solved for the model parameter corrections,  $\delta m_j$ . The linearization is an approximation so in general it is necessary to iterate. Using this procedure the initial model is replaced by the corrected model  $m_j = m_j^I + \delta m_j$ . The entire procedure is then repeated as many times as necessary.

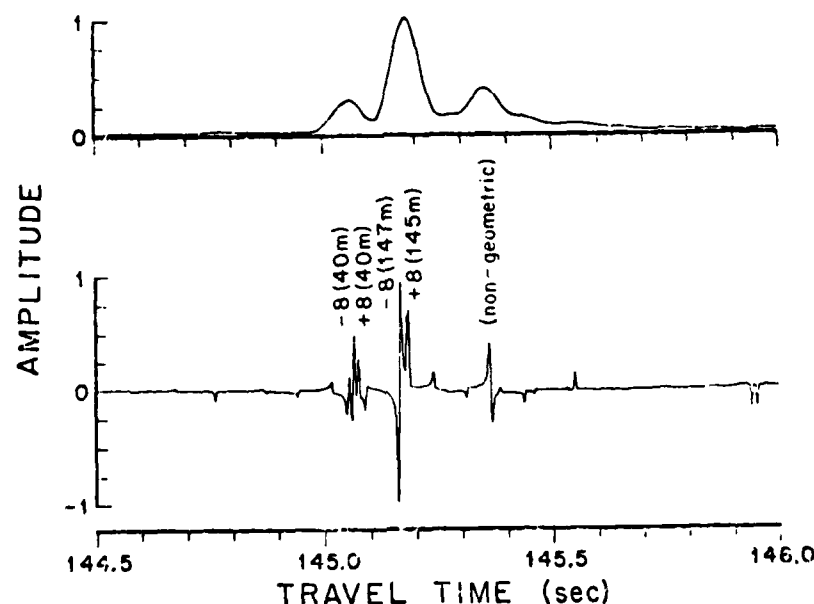


Figure 3. (top) Measured arrival pattern for a 215 km  $224 \pm 8$  Hz transmission in the North Pacific. (bottom) WKBJ impulse response calculation made using the sound speed profile measured during deployment of source and receiver. Selected arrivals are identified;  $+8(40m)$  refers to an upward launch angle with 8 ray turning points, the upper turning depth being at 40m. Note that the third prominent peak in the data is predicted by the WKBJ impulse response calculation but not by geometric ray theory. The time origin of the measured arrival pattern was adjusted to give the best fit to the calculated ones.

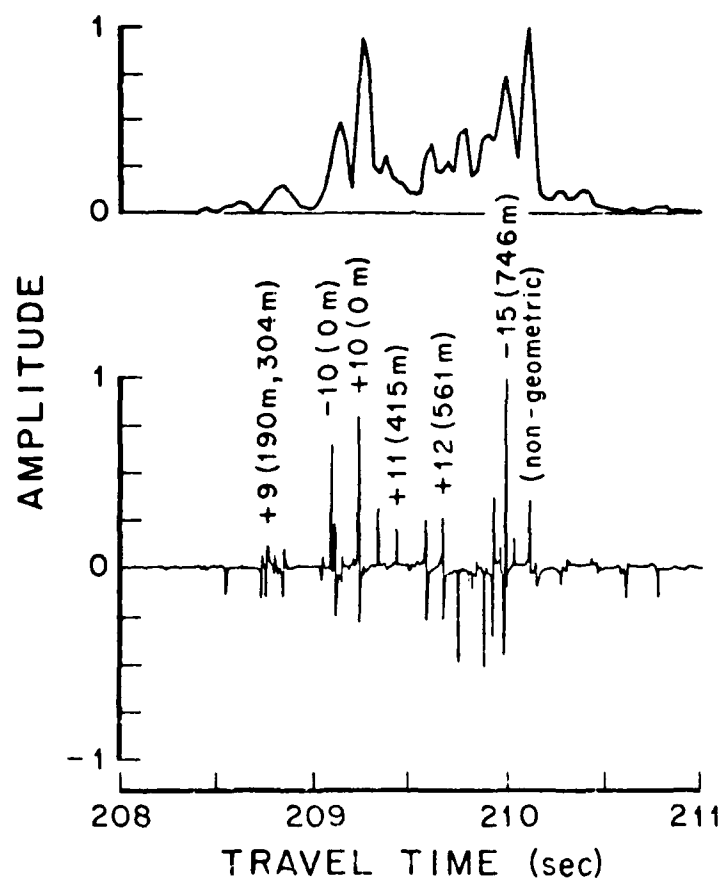


Figure 4. (top) Measured arrival pattern for a 315 km  $224 \pm 8$  Hz transmission in the North Atlantic. (bottom) WPBJ impulse response calculation made using sound speed profile measured at the time the transmission was made. Selected arrivals are identified. The time origin of the predicted arrival pattern was adjusted to give the best fit to the measured pattern.

All the foregoing remarks apply if data other than travel times (arrival pattern peaks) are being inverted. Brown<sup>7</sup> discusses the problem of inverting the entire arrival pattern. In this case  $T_i$  is replaced by  $p_i$ , the  $i^{\text{th}}$  point in the discrete time series recorded at the receiver. Munk and Wunsch<sup>8</sup> discuss the problem of inverting frequency shifts in modal dispersion curves.

As an example of an inversion, Figure 5 shows one horizontal slice of a preliminary three-dimensional inversion of travel time data collected during a 1981 acoustic tomography experiment.<sup>5</sup> The inversion was done by separating the three-dimensional inverse problem into vertical and horizontal slices (details are given in Brown<sup>9</sup>) as suggested by Munk and Wunsch.<sup>1</sup> This is a simplifying assumption which significantly reduces the computational burden of doing the inversion at the expense of introducing some error. Preliminary inversions of the same data set done without making the separability assumption are shown in reference 5. While the inversion results shown in Figure 4 are not perfect the main features of the measured field have been reproduced. We conclude that inverse methods combined with remote acoustic measurements may be used to monitor mesoscale ocean structure.

#### ACKNOWLEDGMENTS.

The work outlined here was carried out as a small part of a joint effort by the acoustic tomography group. Other members of the groups are: Walter Munk, Peter Worcester, Robert Knox, John Spiesberger (SIO); Carl Wunsch, Bruce Cornuelle, Bob Heinmiller (MIT); Robert Spindel; Doug Webb (WHOI); Ted Birdsall, Kurt Metzger (U. Michigan); David Behringer (NOAA, Miami). Peter Worcester provided the data shown in Figure 3. Diane Sumner prepared the text. Don Betts did the illustrations. This work was supported by the Office of Naval Research and The National Science Foundation.

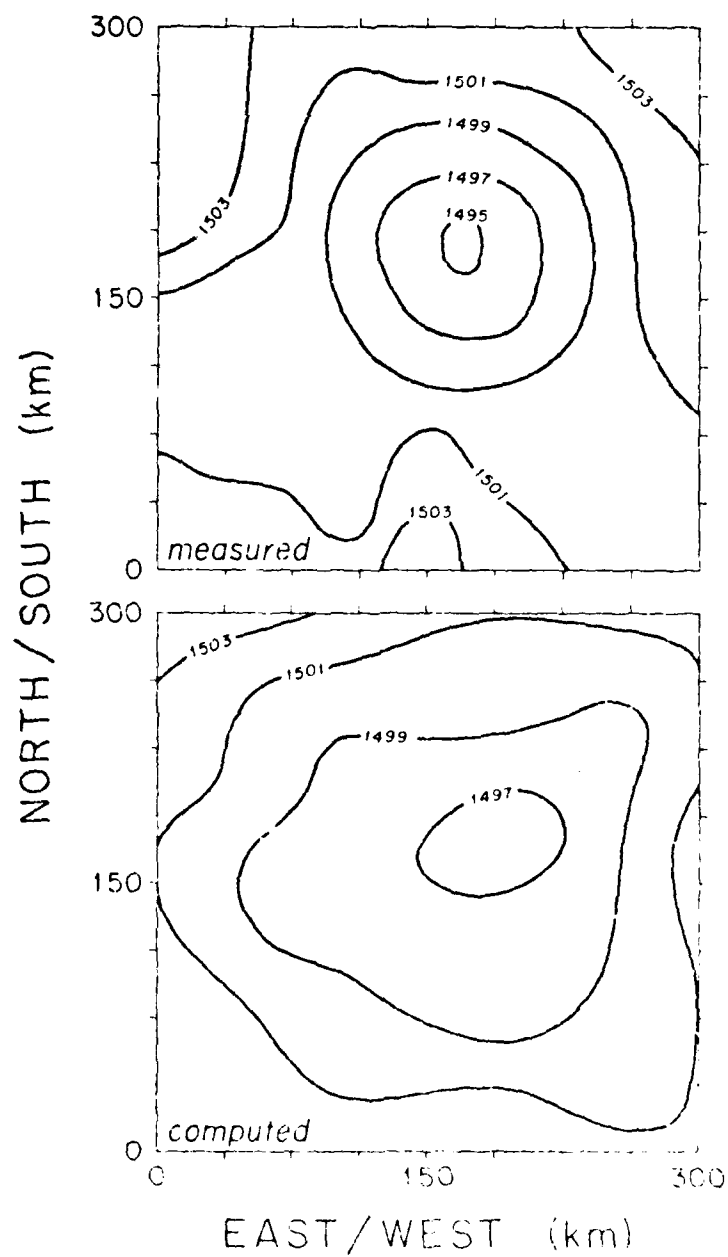


Figure 5. Contours of measured (above) and computed (below) sound speed at 800m depth during the 1991 acoustic tomography experiment. The contour interval is 2 m/sec. The source and receiver locations during the experiment are shown in Figure 1.

## REFERENCES

- 1 Munk, W.H. and C. Wunsch (1979) "Ocean acoustic tomography: a scheme for large scale monitoring," Deep-Sea Res. 26, 123-161.
- 2 Worcester, P.F. (1981) "An example of ocean acoustic multipath identification using both travel time and vertical arrival angle," J. Acoust. Soc. Am. 70, 1743-1747.
- 3 Brown, M.G. (1982) "Application of the WKBJ Green's function to acoustic propagation in horizontally stratified oceans," J. Acoust. Soc. Am. 71, 1427-1432.
- 4 Chapman, C.H. (1978) "A new method for computing synthetic seismograms," Geophys. J. Roy. Astron. Soc. 54, 481-518.
- 5 Ocean Tomography Group, The (1982) "Ocean acoustic tomography: a demonstration," submitted to Nature.
- 6 Brown, M.G., W.H. Munk, J.L. Spiesberger and P.F. Worcester (1980) "Long-range acoustic transmission in the Northwest Atlantic," J. Geophys. Res. 85, 2699-2703.
- 7 Brown, M.G. (1982) "Linearized travel time, intensity and waveform inversions - a comparison," submitted to J. Acoust. Soc. Am.
- 8 Munk, W.H. and C. Wunsch (1982) "Ocean acoustic tomography: rays and modes," submitted to Reviews Geophys. Space Physics.
- 9 Brown, M.G. (1982) "Inverting for the ocean sound speed structure," University of California, San Diego, Ph.D. Thesis.

ADP003124

# Principal Components as a Method for Atmospherically Correcting Coastal Zone Color Scanner Data

Ronald J. Holyer

Naval Ocean Research and Development Activity

NSTL, Ms. 39529

## ABSTRACT

The Coastal Zone Color Scanner (CZCS) images the earth's oceans in five visible/near-IR spectral bands. In the visible portion of the electromagnetic spectrum, satellite observed radiance typically consists of approximately 90% of atmospheric backscatter and 10% of ocean-scattered radiance. Subtle color signatures associated with oceanic features are frequently masked by this atmospheric path radiance. Accurate atmospheric correction of CZCS data is, therefore, a prerequisite to optimum information extraction from this imagery. The most widely accepted atmospheric correction scheme for CZCS data, based on a single scattering model of the atmosphere plus certain assumed optical properties of the ocean, has several inherent drawbacks that limit its effectiveness. Principal Components Analysis, a common pattern recognition tool, is offered as an alternate atmospheric correction scheme based upon a statistical rather than a modeling approach. The Principal Components method is applied to a representative CZCS data set and a comparison is made with corrections derived by the modeling method.

## I. INTRODUCTION

The Coastal Zone Color Scanner (CZCS) is a six-channel scanning radiometer in NIMBUS-7. The CZCS channels measure the earth's radiance in spectral bands centered at 443 nm, 520 nm, 550 nm, 670 nm, 750 nm, and 11,500 nm (Hovis, 1980). The first four channels are in the visible, the fifth is in the near (reflective) IR, and the sixth is in the thermal (emissive) IR portions of the electromagnetic spectrum. The radiance of the ocean viewed from space by channels one through five of the CZCS is a combination of radiance backscattered out of the ocean plus radiance backscattered by the atmosphere and radiance reflected by the sea surface. For most geographic applications of CZCS data, it is only the upwelled radiance from

within the water volume that is of interest. In the visible part of the spectrum the unwanted radiance (i.e., atmospheric backscatter and surface reflectance) typically accounts for more than 90% of the observed radiance. Therefore, very accurate removal of the unwanted radiance is necessary to achieve reasonably accurate estimates of upwelling subsurface ocean radiance from CZCS data.

The most widely accepted method of applying atmospheric corrections to CZCS data utilizes a mathematical model of the atmosphere based on single-scattering theory (Gordon, 1978). The single-scattering model, which will be discussed briefly in the following sections, requires several assumptions about the scattering or absorption properties of the atmosphere and ocean. These assumptions are valid in many cases, but can lead to significant uncertainties in the corrected data in other cases. This paper will demonstrate some of the uncertainties encountered in application of the Gordon (1978) method.

As an alternative to modeling the physics of the ocean-atmosphere system, this paper suggests that atmospheric correction can possibly be approached as a statistical problem. Principal Components Analysis (PCA), a statistical tool widely used in the field of pattern recognition, is offered as the basis for a new atmospheric correction method that avoids many of the problems associated with the modeling approach. However, it should be noted that at the present stage of development, the PCA method does not result in radiance values for each spectral band, but rather generates an atmospherically corrected image in an abstract mathematical measurement space. For this reason the PCA method is presently not of interest in applications where absolute spectral radiance values are required. Thus, it is not presented as a replacement for the modeling methodology. Rather, principal components are useful in applications where the desired analysis consists of descriptive interpretation of ocean features seen in the CZCS imagery.

## II. BACKGROUND

A brief and necessarily incomplete overview of the CZCS atmospheric correction problem is given here to identify some of the sources of uncertainty in the single-scattering model methodology, and to establish the desirability of introducing new techniques that do not encounter some of these problems.



## A. THE SINGLE-SCATTERING APPROXIMATION

Single-scattering theory, as the name implies, ignores multiple scattering. In other words, a photon is assumed to travel the atmospheric path from space to the earth's surface unperturbed or experiencing, at most, one interaction with atmospheric constituents. This theory is reasonable for optically thin atmospheres, but begins to break down for more optically dense cases. The advantage of single-scattering theory is that the Rayleigh (molecular) and aerosol (particulate) contributions to the backscattered radiance of the ocean are additive. Thus, the observed radiance of the ocean viewed from space is given by

$$L(\lambda) = L_r(\lambda) + L_a(\lambda) + t(\lambda) L_w(\lambda) \quad (1)$$

where  $L(\lambda)$ ,  $L_r(\lambda)$ ,  $L_a(\lambda)$ , and  $L_w(\lambda)$  are the observed, Rayleigh, aerosol, and ocean radiances, respectively, at wavelength  $\lambda$ , and  $t(\lambda)$  is the transmittance of the atmosphere. In Eq. (1)  $L(\lambda)$  is observed by the CZCS radiometer and  $L_r(\lambda)$  can be calculated with reasonable accuracy (Frohlich and Shaw, 1980). However  $L_w(\lambda)$  and  $L_a(\lambda)$  cannot be separated in Eq. (1), so a direct determination of  $L_w(\lambda)$  is not possible.

To solve for  $L_w(\lambda)$  Gordon (1978) has used two wavelengths simultaneously. Taking two equations like Eq. (1), one at  $\lambda_1$ , and the other at  $\lambda_2$ , the solution of the simultaneous equations yields

$$t(\lambda_1) L_w(\lambda_1) = [L(\lambda_1) - L_r(\lambda_1) - S(\lambda_1, \lambda_2) (L(\lambda_2) - L_r(\lambda_2) - t(\lambda_2) L_w(\lambda_2))] \quad (2)$$

$$\text{where } S(\lambda_1, \lambda_2) = L_a(\lambda_1)/L_a(\lambda_2) \quad (3)$$

Gordon (1981) gives the following expression for  $S(\lambda_1, \lambda_2)$ :

$$S(\lambda_1, \lambda_2) = e(\lambda_1, \lambda_2) [F_0(\lambda_1)/F_0(\lambda_2)] \exp \left\{ -[T_0(\lambda_1) - T_0(\lambda_2)] [1/\mu_0 + 1/\mu_s] \right\} \quad (4)$$

where  $T_0$  is the ozone optical thickness,  $F_0$  is the extraterrestrial solar irradiance,  $\mu_v$  and  $\mu_s$  are the cosines of the viewing angle and solar zenith angle, respectively, and  $e(\lambda_1, \lambda_2)$  is related to the aerosol optical thickness  $T_a$  and the single-scattering albedo  $w_0$  through

$$e(\lambda_1, \lambda_2) = w_0(\lambda_1) T_a(\lambda_1) / w_0(\lambda_2) T_a(\lambda_2) \quad (5)$$

To solve Eq. (2) for  $t(\lambda_1) L_w(\lambda_1)$ , one must make assumptions concerning  $L_w(\lambda_2)$  and  $e(\lambda_1, \lambda_2)$ .

#### B. ASSUMPTIONS ABOUT OCEANIC SPECTRAL RADIANCE

The term in Eq. (2) for water radiance at  $\lambda_2$ ,  $L_w(\lambda_2)$  is handled by selecting  $\lambda_2$  such that  $L_w(\lambda_2) = 0$ : thus, this term can be ignored. For CZCS the red channel at 670 nm is used at  $\lambda_2$ . This band is chosen because the absorption coefficient of sea water is higher here than for other parts of the visible spectrum so a relatively small backscattered return from the ocean can be expected. Figure 1 shows upwelling spectral radiance data measured just above the ocean surface at several stations in the Gulf of Mexico in December 1978. This figure shows that radiance does fall off drastically at red wavelengths. Actually, much of the observed radiance at 670 nm in Figure 1 is surface-reflected skylight rather than backscatter. Thus, the assumption of negligible ocean radiance in CZCS channel 4 seems to be reasonable for the deep ocean (low turbidity) cases. However, this assumption will not be valid for turbid coastal waters where significant backscatter occurs at 670 nm. Neville et al. (1980), reporting on CZCS work done in Lake Ontario, cite appreciable 670 nm reflectance as the reason for the poor performance of the Gordon (1978) method in that case. An iterative algorithm which reduces the 670 nm water radiance problem has been developed by Smith and Wilson (1980).

#### C. ASSUMPTIONS ABOUT THE UNCERTAINTY IN SPECTRAL DISTRIBUTION OF AEROSOL BACKSCATTER

The factor  $e(\lambda_1, \lambda_2)$  in Eq. (5) represents the spectral variability in the aerosol phase function. Information on atmospheric aerosol phase functions is sparse. For simplicity it can be assumed that the aerosol optical thickness at  $\lambda$ ,  $T_a(\lambda)$ , varies with wavelength according to the power law

$$T_a(\lambda) = T_a(\lambda_0) (\lambda_0/\lambda)^n \quad (6)$$

where  $n$  is referred to as the Angstrom exponent (Angstrom, 1961). To make an atmospheric correction to CZCS data one must either measure  $n$  at the time of satellite overpass or assume some  $n$  value. Gordon (1978) assumes that the aerosol

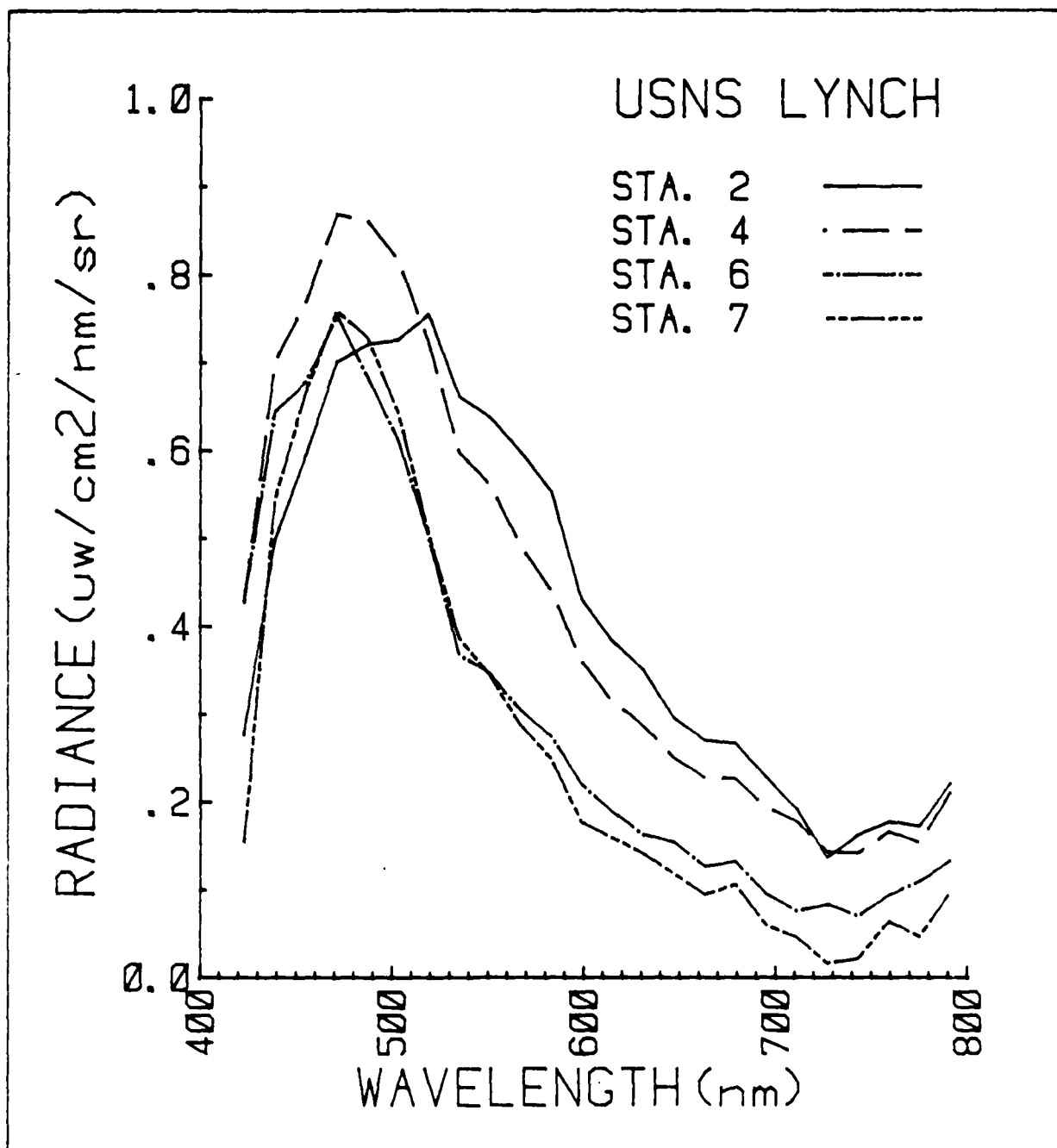


Figure 1. Spectral radiance of the ocean measured from just above the sea surface at several locations in the Gulf of Mexico during November and December 1978.

phase function depends weakly on wavelength over the visible part of the spectrum, i.e.,  $n$  is approximately zero. However, it is not a simple matter to assume  $n$  since the Angstrom exponent can range between 0 and 2 (Robinson, 1966). Tomasi and Prodi (1982) measured atmospheric turbidity in the Red Sea, Indian Ocean, and Somalian Coast and found  $n$  values generally ranging between 0.2 and 0.9.

Measurements of aerosol optical depth of the atmosphere were made by the author in November and December 1978 in the Gulf of Mexico. Figure 2 shows representative measurements along with power law fits to the measured values. It is seen in Figure 2 that the power law fit to aerosol optical depth is only approximate and that the Angstrom exponent varies from day to day. For the Gulf of Mexico data (the three shown in Figure 2 plus four others) the Angstrom exponents from the power law fits ranged from 0 to 1.9 with a mean value of 1.2. This range agrees well with the range previously cited and the mean is close to the 1.3 value often used for continental regions (Robinson, 1966). Because of this type of aerosol variability, large errors in correction terms can result when 670 nm values are extrapolated into the green and blue regions based on some assumed value for  $n$ .

Gordon (1981) has proposed the use of clear water spectral radiance values within a scene to derive values for the Angstrom exponent from the CZCS data itself. Good results are claimed to be possible with the clear water radiance method if water area with less than  $0.25 \text{ mg/m}^3$  of chlorophyll-a is available within the scene.

The modeling approach to atmospheric correction can then be summarized as follows. Each of the CZCS channels 1 through 4 are corrected for the Rayleigh backscatter of the atmosphere. Then, since the ocean is "black" at 670 nm, any radiance remaining in channel 4 after Rayleigh correction can be attributed to atmospheric aerosols. The Rayleigh corrected red (670 nm) channel is, therefore, used as the aerosol correction term to be applied to channels 1 through 3. The red channel aerosol correction is weighted differently before subtraction from each of the channels 1 through 3. The weighting factors require knowledge of the solar spectral irradiance, the ozone optical depth and the Angstrom Exponent for the atmospheric aerosols. The resulting corrected imagery may differ significantly in some cases from the true ocean spectral radiance for three major reasons; a) the single-scattering approximation is poor because the atmosphere is optically thick, b) the ocean is not really "black" at 670 nm; or c) an incorrect value has been used for the Angstrom exponent.

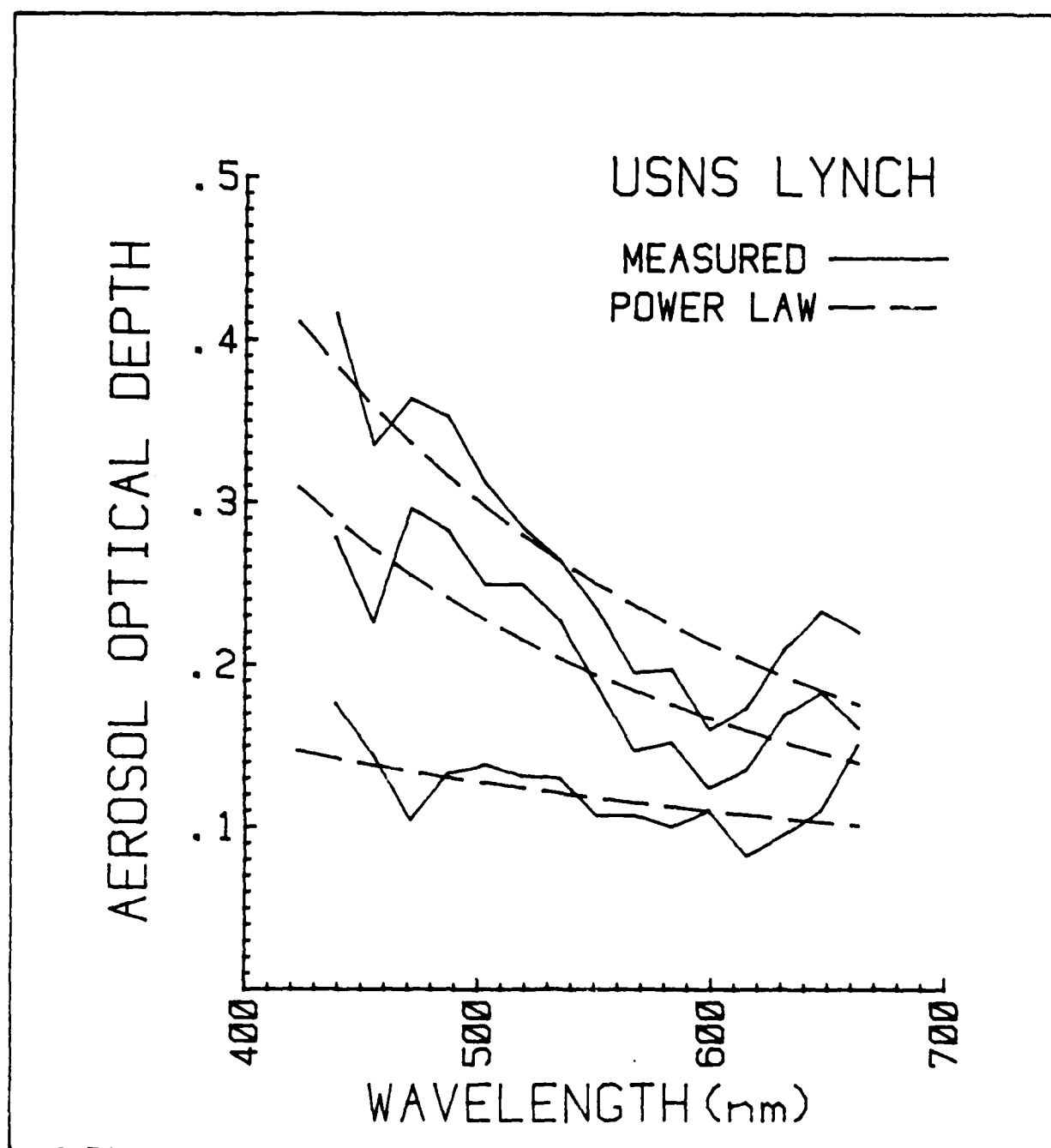


Figure 2. Aerosol optical depth of a vertical atmospheric path measured in the Gulf of Mexico onboard the USNS LYNCH on three different days in December 1978. Dotted lines are power law fits to the measured data.

### III. SINGLE-SCATTERING MODEL APPLIED TO A TEST CASE

A simplified form of the single-scattering model has been applied to a test data set to a) illustrate the essential elements of this established methodology; and b) serve as a reference for evaluating the performance of the statistical method. The test set is from the Grand Banks area of the North Atlantic. Figure 3 is a color composite of the CZCS channels 1, 2, and 3 of the test data. Figure 4 is the coincident CZCS channel 6 infrared image. The test data is from CZCS orbit 2811 on 15 May 1979 at 1456 Z. The area shown is oceanographically very dynamic because it covers the confluence of the three major current systems; the Gulf Stream, the Labrador Current, and the North Atlantic Gyre. Note that although the surface patterns created by the currents are well delineated in the IR imagery (Fig. 4), the visible color image (Fig. 3) does not exhibit similar patterns. Either there is no color signature associated with these divergent ocean systems or else the relatively small ocean surface upwelling radiance is obscured by a much stronger atmospheric backscatter. This is, therefore, an ideal case for demonstration of atmospheric correction procedures.

The conventional single-scattering model atmospheric correction was performed on this test data following the general methodology previously described. Clear water radiances (Gordon, 1981) were used to derive an Angstrom exponent of 2.8 for this case. Solar irradiance values,  $F_0(\lambda)$ , were assumed to be 184.63, 185.57, 185.01 and 153.13 in CZCS channels 1, 2, 3, and 4, respectively (Austin, 1981). The values for ozone transmittance of the atmosphere,  $T_o(\lambda)$ , were taken to be 0.0009, 0.0146, 0.0266 and 0.0138 from LOWTRAN-5A (Kneizys et al., 1980) code for mid-latitude summer atmosphere. Solar and satellite zenith angles were held constant at their values in the box drawn on Figure 3. Solar and satellite zenith angles at that location are  $23.5^\circ$  and  $25^\circ$ . Not permitting these angles to vary spatially results in Rayleigh correction errors of 15% at the left edge and 25% at the right edge of the image shown in Figure 3. The limb effects seen in the corrected data result from ignoring angular dependency in the Rayleigh correction. These limb effects should largely disappear if angular dependency was included in Rayleigh processing.

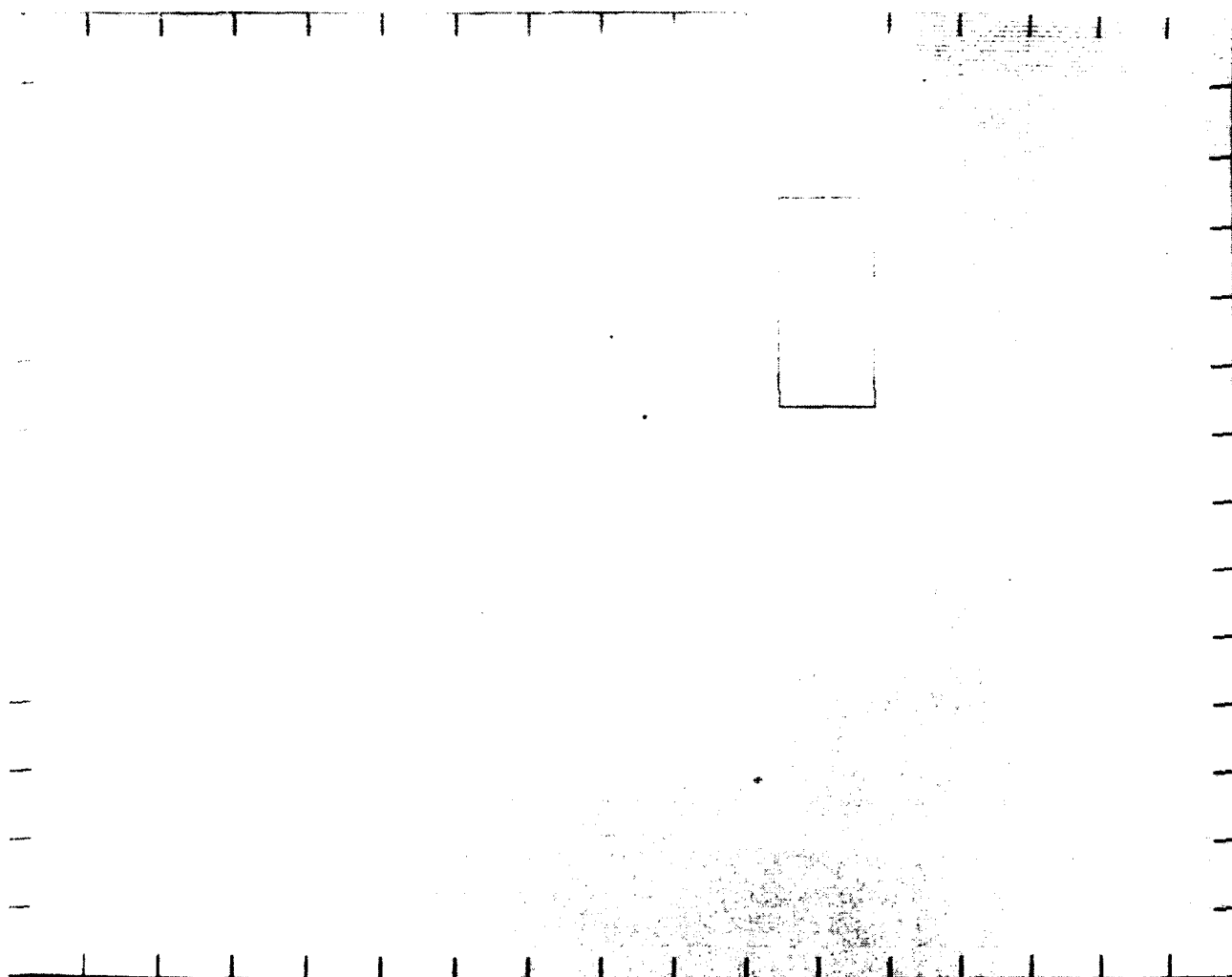


Figure 3. Color image formed from CZCS channels 1, 2, and 3 of orbit 2811 on 15 May 1979 at 1456 Z. Image is from raw data with no enhancements applied. Box outlines area used for PCA.



Figure 4. Image of CZCS channel 6 (infrared) data coincident with Figure 3. Labels on image identify major oceanographic regimes.



When the single-scattering correction was applied, the resulting corrected radiance values in channel 1 (443 nm) were negative. This, of course, is a physical impossibility implying that the correction method or parameters input to the method were erroneous. Negative corrected radiances could result from several sources including uncertainties in solar spectral irradiance or uncertainties in sensor calibration. In this case the Angstrom exponent value of 2.8 derived from clear water radiances is suspected. Since the Angstrom exponent is generally considered to range from 0 to 2, the 2.8 value seems suspiciously large. It is not obvious why the clear water radiance gave such a large value since we have no ground truth or other collaborating data for this case. The clear water radiance approach was, therefore, abandoned and a mid-range Angstrom exponent of 1 was assumed. Under this assumption, the following values of  $S(\lambda_1, \lambda_2)$  resulted.

$$\begin{aligned} S(443, 670) &= 1.80 \\ S(520, 670) &= 1.56 \\ S(550, 670) &= 1.44 \end{aligned}$$

Correction was repeated using these values. The channel 1 radiances came out positive when  $n=1$  was used. A subjective visual examination of the corrected imagery indicated that a reasonable correction had been achieved.

Figure 5 is a color composite formed from atmospherically corrected channel 1, 2, and 3 data. The correction has effectively stripped away the atmospheric path radiance revealing color patterns in the ocean below that show the same general features seen in the IR image in Figure 4.

#### IV. A STATISTICAL APPROACH

To overcome some of the problems just described, atmospheric correction of CZCS imagery can be approached as a statistics problem. Assumptions about physical properties, such as the ocean is black at 670 nm or aerosol phase functions vary only weakly with wavelength, are replaced with assumptions about the statistical properties of the data. Specifically, one begins by assuming that an area of the image can be chosen for analysis where the majority of the variance in the multi-spectral measurement space is attributable to aerosol variability. This implies two criteria for selection of the analysis area. First, it should be an

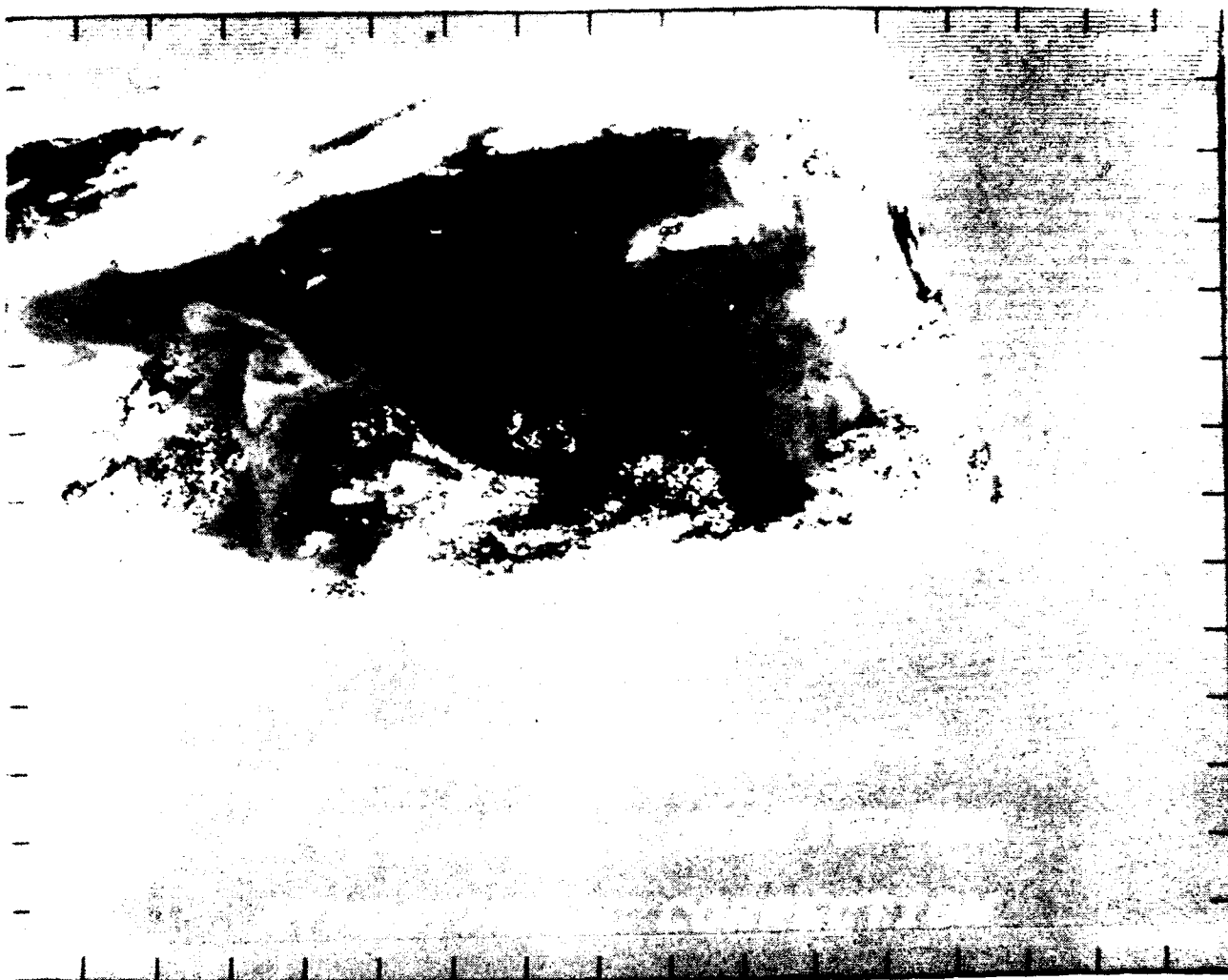


Figure 5. Color image formed from atmospherically corrected CZCS channels 1, 2, and 3. Atmospheric correction was by means of a simplified single-scattering atmospheric model.

area of high variability in aerosol concentration, and second, the ocean in the selected area should be as nearly uniform in color as possible. Thus, coastal areas with their typically high water color variability are to be avoided. Likewise, clouds are to be avoided because their brightness saturates the eight-bit dynamic range of the CZCS. Saturation introduces a non-linearity into the problem that degrades the results of the subsequent PCA, which is a linear transformation technique.

#### A. PRINCIPAL COMPONENTS ANALYSIS

Principal Components Analysis is most frequently used in pattern recognition problems to reduce the dimensionality of a measurement space. For example, it may be possible to transform ten-channel multispectral imagery into only three channels and yet preserve 95% or more of the "information" present in the original ten-channel data. PCA would be one possible method of defining the optimum ten-dimensional to three-dimensional transformation so as to minimize "information" loss. In PCA "information" is synonymous with variance, i.e., PCA as a dimensionality reduction tool preserves maximum possible variance. In some situations, of course, variance corresponds to noise rather than to information, so the analyst should know the statistical properties of his data before choosing PCA. In the present case the image subarea selected for PCA has been deliberately chosen to have prescribed statistical properties. If the desired properties do exist in the data, then the same characteristics of PCA that make it useful for dimensionality reduction can also be utilized to achieve atmospheric correction.

A non-rigorous mathematical definition of PCA is as follows. PCA is the transformation (linear) of the original variables into a set of new variables (called principal components) which are considered in a sequence such that each succeeding component is that linear combination of the original variables which has the maximum variance of all possible combinations, under the constraints that each component be uncorrelated with an orthogonal to all preceding components. For more details see references such as Anderson (1958) or Cooley and Lohnes (1971). It can be shown mathematically that the principal components defined in this manner are in fact the eigenvectors of the covariance matrix. Further, it can be shown that the  $i$ -th principal component is identically equal to the  $i$ -th eigenvalue of the covariance matrix.

The variance ordering properties of the sequence of principal components combined with the fact that most of the variance in the selected image subarea results from aerosol variability, permits removal of aerosol effects. If the first principal component maximizes variance, then this component captures the aerosol contribution to total variance. In other words, the first principal component is oriented in the original measurement space parallel to the aerosol variability. Component one can then simply be discarded to make the aerosol correction. In the CZCS image shown here to illustrate the technique, the original measurement space is four-dimensional (spectral channels 1 through 4). PCA results in a transformation to a new four-dimensional space. One of these new dimensions (specifically, the first one) is removed (projected onto the other three in mathematical terms), resulting in a three- rather than four-channel image; but in the course of reduction in dimensionality, the obscuring effect of atmospheric aerosols is removed. The resulting three-channel image will more clearly show the oceanic portion of the variance that was in the original imagery.

#### B. STATISTICS OF THE TEST CASE DATA

Figure 3, showing the Grand Banks test data set, has a box overlaid on the image that indicates the area selected in this case for PCA. Statistics for the boxed subarea are given below along with the principal components and the eigenvalues of the covariance matrix. As was previously mentioned, the principal components are formed from linear combinations of the original spectral bands. If  $x_{ij}$  is the  $i$ -th subarea pixel from channel  $j$ , then the  $k$ -th principal component,  $P_{ik}$ , can be written

$$P_{ik} = \sum_j a_{kj} x_{ij} . \quad (6)$$

The coefficients  $a_{kj}$ , therefore, define the transformation from spectral measurement space to principal component space. Statistics below are given in vector form where the vector components represent each of the four spectral bands.

### Grand Banks PCA box statistics

mean = 162, 149, 151, 148  
 std dev = 6.57, 8.64, 10.13, 17.08  
 eigenvalues = 0.966, 0.028, 0.004, 0.000

	0.265	0.381	0.451	0.761
$a_{kj}$ =	-0.731	-0.382	-0.159	0.541
	-0.529	0.199	0.743	-0.356
	0.337	-0.817	0.466	0.015

Note from the eigenvalues that the first principal component (the atmospheric aerosol component) in this case accounts for 96.6% of the total variance within the box. This means that only 3.4% of the variance is of oceanic origin, which shows why one could not see oceanic features in the raw data in Figure 3.

It is also of interest to note the  $a_{kj}$  values. In particular, the weights for the third principal component are interesting. The coefficients -0.529, 0.199, and 0.743 for channels 1, 2, and 3, respectively (row three of the  $a_{kj}$  matrix), indicate that the third component has captured the variability associated with changes in chlorophyll concentration. The association of this component with chlorophyll is based on the fact that it will be composed of contributions from channels 1 and 3 that are large but of opposite sign plus a relatively small contribution from channel 2. This weighting exhibits the "hinge point" behavior that is well known for chlorophyll-a (Duntley et al., 1974). It can, therefore, be predicted that the third principal component will probably show the most oceanic structure for this deep ocean location where chlorophyll-a is most likely the primary contributor to ocean color.

### C. CORRECTED IMAGERY

The  $a_{kj}$  coefficients derived from PCA within the box can now be used as a transformation matrix to be applied to the entire image according to Eq. (6). The first principal component, which contains 96.6% of the total variance in the original image, can be associated with atmospheric aerosol backscatter if the initial assumptions about statistical properties of the data were valid. Figure 6 shows the first component alongside the original channel 4 image with the Rayleigh contribution removed. Channel 4 minus the Rayleigh radiance of the atmosphere is

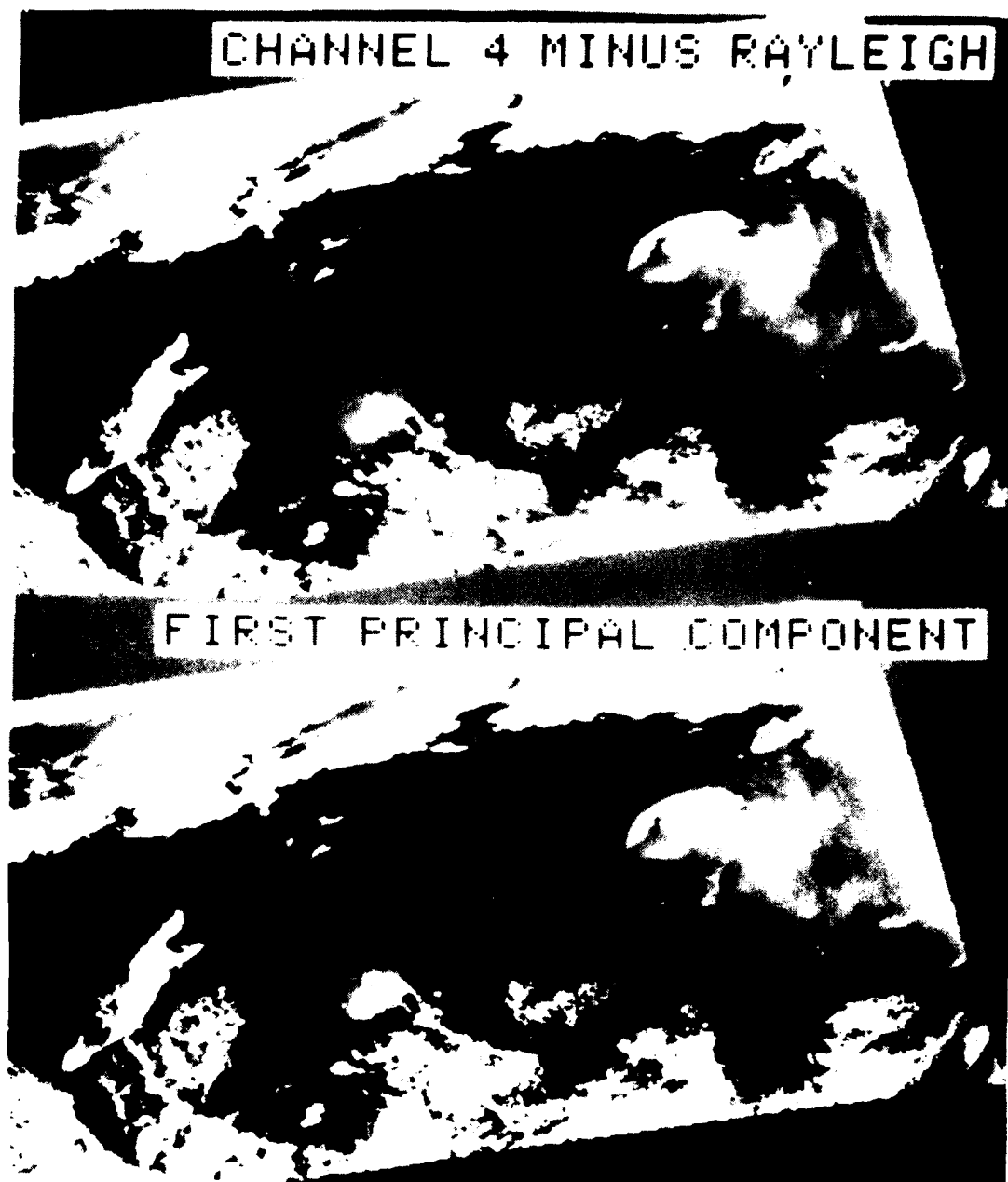


Figure 6. Comparison of the aerosol corrections for the two methods. Channel 4 minus Rayleigh is the aerosol correction from single-scattering theory while the first principal component is the aerosol correction from the PCA method.

the aerosol correction factor utilized in the single-scattering method. Visual comparison of the first principal component with the channel 4 minus Rayleigh image confirms that the first principal component is essentially the aerosol contribution to the CZCS data.

As expected, based upon the previous cursory examination of the  $a_{kj}$  coefficients, the third principal component did show the most features of apparent oceanographic origin. Figure 7 is an image of the third principal component which accounted for 0.4% of the total variance. Comparison of Figure 7 with the IR data (Fig. 4) and the corrected color image (Fig. 5) reveals that the oceanographic features of the earlier figures are also evident in the third principal component. Thus, the third component is, in effect, an atmospherically corrected image showing ocean color variability patterns. It should be noted that the third component will not always be the one to give maximum definition of oceanic patterns. In other cases where PCA was applied to a small subsection of an image so that angular variation of path radiance was small, the second component seemed to contain the chlorophyll-a variance and, hence, the best oceanic patterns. In general, one cannot say which component will show the ocean patterns the best, nor can one even assume that any single component will yield optimal results. It may be in some cases that several of the components can be combined to give a corrected image that is superior to any of the individual components.

The second and fourth components contain some oceanographic information but are predominated by other influences. The second component, with 2.8% of the total variance, seems to represent the angular dependency of the atmospheric path radiance, while the fourth, with <0.1% of the total variance, contains mainly random noise. For sake of completeness, components two and four are shown in Figure 8.

## V. CONCLUSIONS

This paper has shown how one can begin from a statistical frame of reference and develop CZCS aerosol atmospheric correction terms that are basically equivalent to those derived from single-scattering theory. Further, the statistical approach, based upon Principal Components Analysis, has resulted in an aerosol corrected image that shows essentially all of the ocean features evident in IR imagery. The

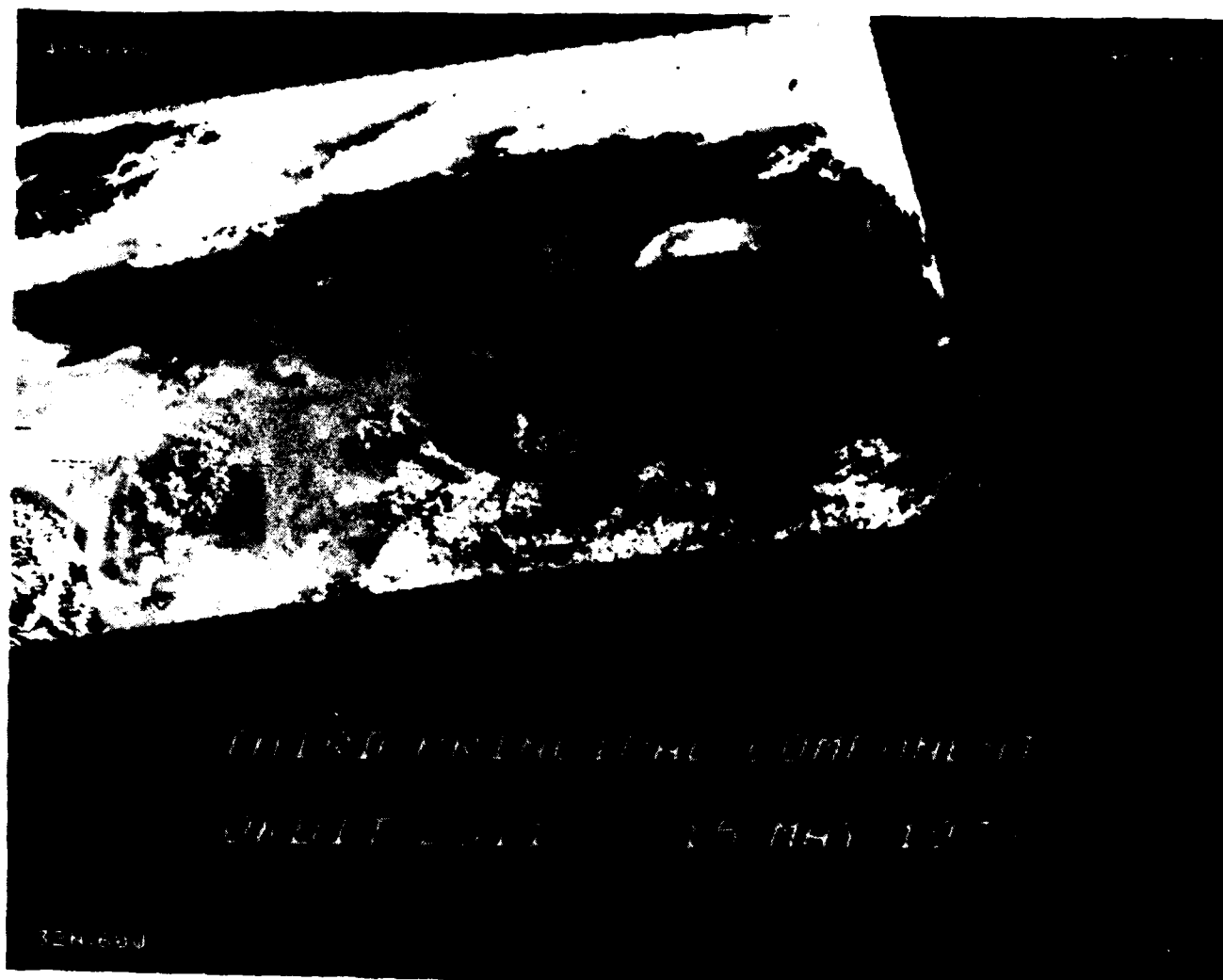


Figure 7. The third principal component of the CZCS image shown in Figure 3.





Figure 8. The second and fourth principal components of the image shown in Figure 3.

statistical analysis was accomplished without having to consider such problems as determination of an Angstrom exponent, the validity of the "ocean blackness at 670 nm" assumption, sensor calibration, or many of the other problems confronting those using the modeling approach. It is, therefore, concluded that the statistical approach may be an attractive alternative to single-scatter modeling of the atmosphere for those applications of CZCS data where image pattern interpretation rather than ocean spectral radiance measurement, is the objective. Certainly the statistical treatment of the CZCS atmospheric correction problem is worthy of further investigation. Perhaps pattern recognition tools and concepts other than PCA can also be brought to bear upon the atmospheric correction problem.

## VI. REFERENCES

Hovis, W.A., D.K. Clark, F. Anderson, R.W. Austin, W.H. Wilson, E.T. Baker, D. Ball, H.R. Gordon, J.L. Mueller, S.Z. El-Sayed, B. Sturm, R.C. Wrigley, C.S. Yentsch, "NIMBUS-7 coastal zone color scanner: system description and initial imagery," *Science*, Vol. 210, pp. 60-63, 1980.

Gordon, H.R., "Reduction of error introduced in the processing of coastal zone color scanner-type imagery resulting from sensor calibration and solar irradiance uncertainty," *Applied Optics*, Vol. 20, No. 2, pp. 207-210, 1981.

Gordon, H.R., "Removal of atmospheric effects from satellite imagery of the oceans," *Applied Optics*, Vol. 17, No. 10, pp. 1631-1636, 1978.

Angstrom, A., *Tellus* 16, 64, 1964.

Robinson, N., editor, *Solar Radiation*, Elsevier Publ. Co., New York, 1966.

Smith, R.C. and W.H. Wilson, "Ship and satellite bio-optical research in the California Bight," *Oceanography from Space Symposium*, Venice, 1980.

Neville, R.A., "Comparison of suspended solids and chlorophyll estimates from aircraft and CZCS with in-situ measurements," *IAMAP Meeting "Radiation transfer in the oceans and remote sensing of ocean properties"*, Hamburg, 1980.

Anderson, T.W., "An introduction to multivariate statistical analysis," John Wiley and Sons, 1958.

Cooley, W.W. and P.R. Lohnes, "Multivariate data analysis," John Wiley and Sons, 1971.

Tomasi, C. and F. Prodi, "Measurements of atmospheric turbidity and vertical mass loading of particulate matter in marine environments (Red Sea, Indian Ocean, and Somalian Coast)," JGR, Vol. 87 No. C2, pp 1279-1286, 1982.

Frohlich, C. and G.E. Shaw, "New determination of Rayleigh scattering in the terrestrial atmosphere," Applied Optics, Vol. 19, No. 11, pp 1773-1775, 1980.

#### Acknowledgments

This work was funded by ONR program element 61153N, "Satellite Measurement of Ocean Optical Properties." The image processing performed for this project was accomplished on the NORDA Code 335 Interactive Digital Satellite Image Processing System (IDSIPS).

# Water Mass Classification in the North Atlantic Using IR Digital Data and Bayesian Decision Theory

Robert E. Coulter

Naval Oceanographic Office  
NSTL Station  
Bay St. Louis, MS 39522

## ADP003125 ABSTRACT

A method is described which utilizes Bayesian decision theory and historical statistics of sea surface temperature to classify surface water masses and ocean fronts from satellite-derived infrared data. Probabilities that certain features occur are determined from the normal distributions of specific statistical characteristics, known a priori, and the same characteristics computed from satellite data. The better the match between the a priori information associated with a feature and the computed statistics, the higher the probability that the feature exists. The maximum probability determined by Bayes' theory is subjected to two tests, based on absolute and relative threshold values, to reduce the chance of incorrect classification. The method was used for classifying satellite IR data to locate the major water masses in the Gulf Stream region. Results were compared to frontal positions obtained by conventional, subjective means.

## I. INTRODUCTION

An ocean front is a zone of rapid transition between two water masses of different physical characteristics. In the northwestern Atlantic, the important fronts can be recognized at the surface from a significant difference in mean temperature.

Generally, the identification of surface fronts from satellite infrared (IR) imagery is a manual, subjective procedure. For a timely environmental product, this procedure must be automated. The fully automated sea surface temperature (SST) analysis techniques that are presently operational are of limited value when applied to the detection of fronts. For example, the SST analyses from Fleet Numerical Oceanography Center (FLENUMOCEANCEN) and the National Oceanic Atmospheric Administration (NOAA) tend to smooth out fronts and are not real-time products.

Gerson and Gaborski (1977) and Gerson et al. (1982) experimented with a sequential decision rule scheme for the automatic location of ocean fronts from GOES satellite data. This report presents the preliminary results after applying another decision rule to a satellite image containing the Gulf Stream. This rule, described in Horton and Coulter (1981), is based on Bayes' decision theory. With it, all the decisions are combined in one step as opposed to the above sequential scheme.

This decision rule technique is preferred for automatic pattern discrimination because one knows precisely what is searched for in the data.

The computer can be used to determine whether or not a data point (or pixel) belongs to a certain front or water mass by comparing the data to some parameter that is characteristic of the front or water mass. In short, we combine Bayes' Decision Rule with our oceanographic experience.

## II. BAYES DECISION THEORY

Bayes decision theory is a fundamental statistical approach to the problem of pattern classification. It is based on the assumption that the problem is posed in probabilistic terms and that all the relevant probabilities associated with the states of nature to be detected are known "a priori".

It is necessary first to determine the probability that the statistical parameter  $x_i$ , computed from the input data, represents the state of nature,  $m_j$  by equation (1):

$$P(x_i/m_j) = \frac{1}{\sqrt{2\pi} \sigma(x_i, m_j)} \exp \left( -\frac{1}{2} \left( \frac{x_i - \mu(x_i, m_j)}{\sigma(x_i, m_j)} \right)^2 \right) \quad (1)$$

where  $\mu$  and  $\sigma^2$  are the mean and variance of the normal distribution of the same statistical parameter  $x_i$  that is associated, a priori, with  $m_j$ . This is called the state-conditional probability.

If  $n$  statistical parameters are utilized to identify  $m_j$ , the probabilities that they represent  $m_j$  can be combined in this manner:

$$P(x_1, \dots, x_n/m_j) = P(x_1/m_j) \cdot P(x_2/m_j) \dots P(x_{n-1}/m_j) \cdot P(x_n/m_j) \quad (2)$$

assuming that each probability is independent of the others.

This, together with the a priori probability that  $m_j$  occurs ( $P(m_j)$ ), leads to the "a posteriori" probability that  $m_j$  occurs given  $x_i$ . The normalized a posteriori probability is:

$$P(m_j/\vec{x}) = \frac{P(x_1, \dots, x_n/m_j) P(m_j)}{p(x_1, \dots, x_n)} \quad (3)$$

where  $p(x_1, \dots, x_n)$  is the numerator summed over all  $j$ 's.

If there are two possible states of nature,  $m_a$  and  $m_b$ ,  $m_b$  is selected as the most likely to occur if  $P(m_b/x) > P(m_a/x)$ .

A more rigorous description of Bayes' Decision Rule is described in Duda and Hart (1973).

## III. DATA

GOES satellite images covering the North Atlantic Ocean were surveyed to locate a cloud-free area that included the Gulf Stream. The northwestern

Atlantic south of Cape Hatteras was mostly cloud-free on 10-11 April 1980 and a set of four high resolution images from the NOAA-6 polar orbiting satellite covering this period were obtained from NOAA.

The images received did not measure up to expectations, primarily due to an abundance of low level cloud cover that was not evident in the GOES images. Only one image was deemed suitable for analysis. The data consisted of one visible channel and three IR channels. To roughly simulate APT low resolution (4 km) data, the pixels were averaged into consecutive 4 by 4 windows and only the visible and far IR (10.5-11.5  $\mu$ m) channels were utilized. Temperatures (in Celsius) were computed from the IR data and were not corrected for water vapor contamination. Two degrees were added to account for CO<sub>2</sub> attenuation and reflectivity.

#### IV. COMPUTATIONAL PROCEDURE

##### A. CLOUD AND LAND DETECTION

In the visible image, the water was clearly less bright than the land and clouds. This was important because the land-water boundary was barely discernible in the infrared image. Therefore, the combination of the visible and the IR data was necessary to prevent the misclassification of land and clouds for water and vice versa.

This compositing of the two images was accomplished by first selecting a threshold visible value with the visible data identifiable as land and cloud cover on one side of the threshold and that indicative of water on the other side. Next, the visible data identified as water were set equal to 1 and the land and cloud pixels were arbitrarily assigned the value of 10 to exaggerate their separation from the water pixels. Finally, these numbers were multiplied by the IR-derived temperatures which left the water surface temperatures unchanged (when multiplied by 1) while making them quite distinct from the cloud and land temperatures (which increased tenfold).

##### B. COMPUTATION OF STATISTICAL PARAMETERS FROM THE DATA

Four statistical parameters were selected to identify the surface ocean fronts and water masses (figure 1 from Khedouri *et al.*, 1976) from the temperature data. They were mean temperature, standard deviation of temperature, total temperature gradient, and east-west temperature gradient. The equations used are shown in Horton and Coulter (1981).

The statistics were computed by marching across each row of temperatures in overlapping square windows as diagrammed in figure 2. A 5 by 5 window is illustrated and was initially used but was abandoned in favor of a 3 by 3 frame.

##### C. APPLYING THE BAYES THEOREM

With the 3 by 3 window, 3 rows by 128 columns of temperatures were initially entered into the algorithms for computing the statistics. This resulted in one row of 126 values for each of the four statistical parameters. In equation (1), these statistics were matched to the same a priori statistics associated with the fronts and water masses (designated in

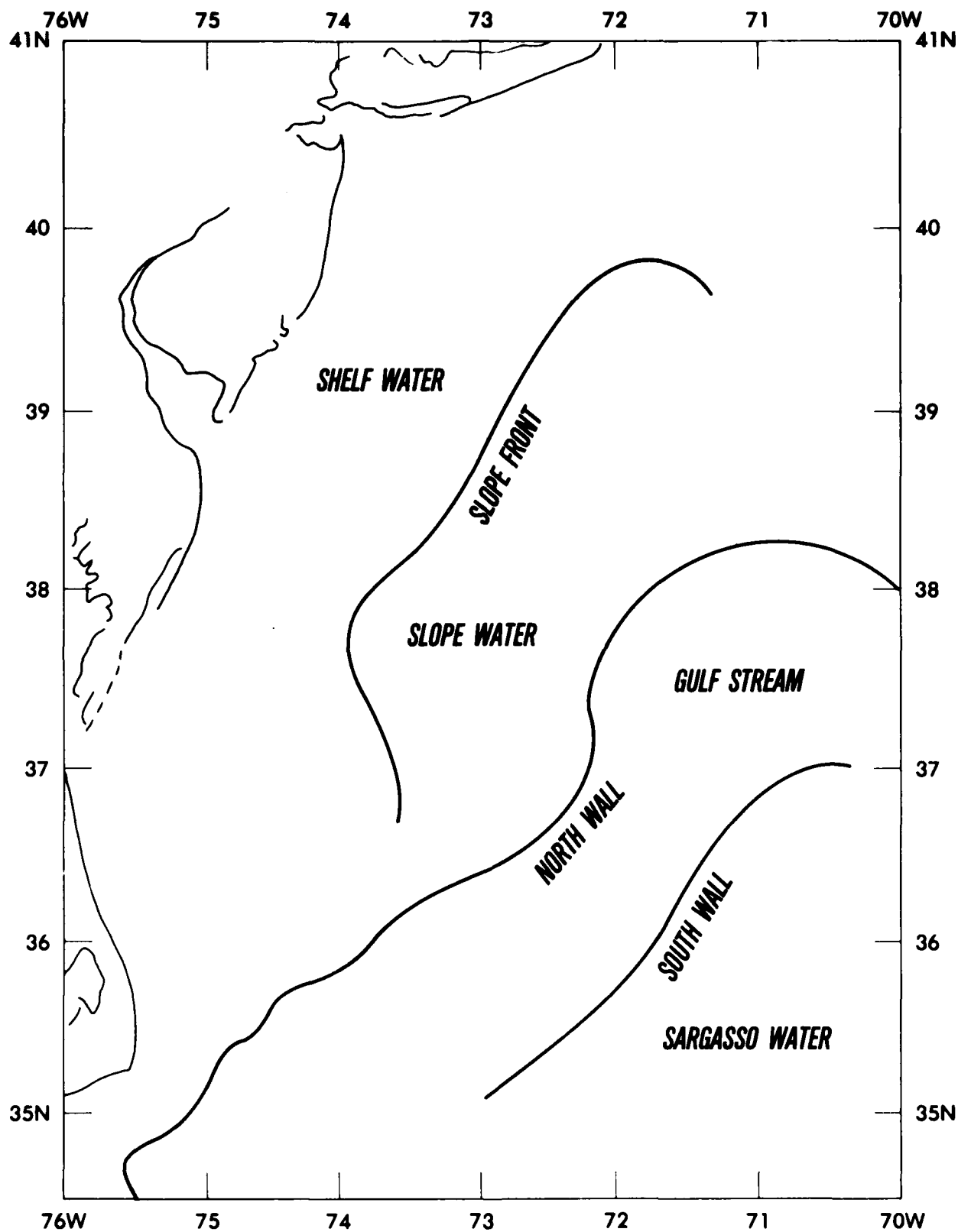
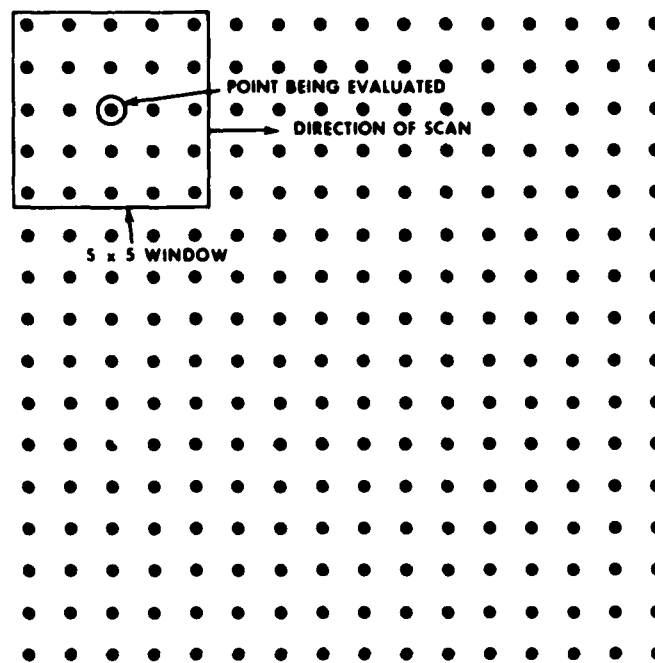
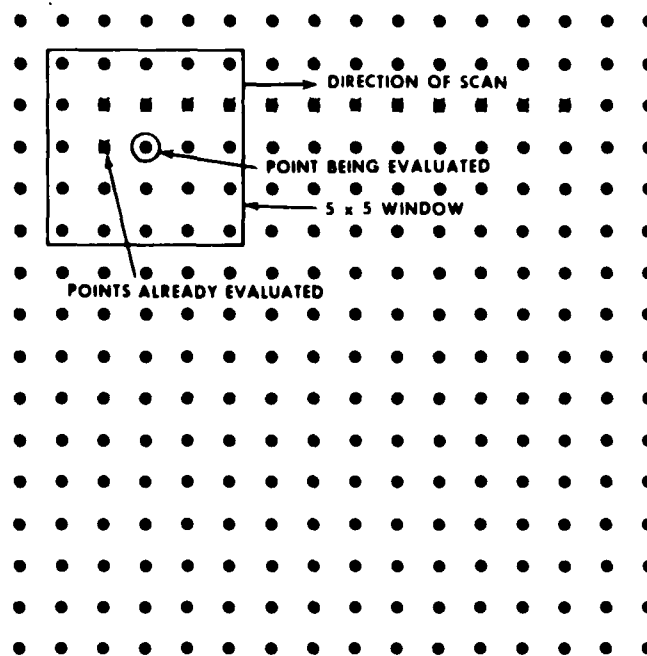


Figure 1. Fronts and water masses in the western North Atlantic.



FIRST POINT EVALUATED



SECOND POINT ON SECOND LINE TO BE EVALUATED

Figure 2. Procedure for computing statistics about pixels in 5 x 5 overlapping windows.



figure 1) to produce the state-conditional probabilities. For example, the probability that a mean temperature, computed from a 3 by 3 array of IR-derived temperatures, represented Slope Water was obtained by comparing it to the climatological mean temperature of Slope Water at the location of the array. The a priori statistics, especially mean temperature, do, of course, vary with geographical position; however, for the first test of the Bayes classifier, they were held constant per state of nature. The only exception was to assign two mean temperatures to Shelf Water because of the considerable variability in temperature of this water mass with location relative to the others.

The state-conditional probabilities were combined by equation (2) and the results were left as the final a posteriori probabilities without proceeding to equation (3). This happened because of two simplifications. First, the a priori probabilities were set to 1 implying that all the states of nature had an equally likely chance of occurring and second, the probabilities were left unnormalized. This conserved mass storage and reduced computational time.

Finally, the states of nature associated with the maximum a posteriori probabilities were output as a row of symbols defined in the key in figure 4. This entire procedure of computing statistics and probabilities was repeated each time a new row of 128 temperatures was input and combined with the previous second and third rows. This limited the storage of temperatures to three rows at a time.

#### D. AUTOMATED TESTING OF RESULTS

After each cycle, the maximum probabilities were subjected to two tests to reduce the chance of incorrect classification. To start with, the maximum probabilities had to exceed a minimum value (arbitrarily set at 0.01).

Next, a relative threshold technique was employed. This required that the maximum probability or the probability of the most likely state of nature divided by the probability of the next most likely state of nature equal an amount greater than the relative threshold. If a maximum probability failed either of the tests, a default symbol was inserted in place of the feature symbol.

#### V. RESULTS

The same data were analyzed subjectively to provide a comparison to the automated classification. This manual analysis depicted in figure 3 is not definitive due to a lack of ground truth and likely errors in interpretation.

The fronts are represented by the lines separating the water masses identified in figure 3. The Slope Front separates the Shelf Water and Slope Water. The North Wall is the shoreward boundary of the Gulf Stream and the South Wall is the seaward boundary. Dotted lines indicate weak and partially indeterminate fronts. The dotted line at the bottom of the figure represents a front that could be related to the merging of the Antilles Current with the Florida Current further south or to a discontinuity in the amount of water vapor in the atmospheric column (i.e., a false front).

35°00'N  
82°54'W

33°24'N  
75°24'W

- SH — SHELF WATER
- SL — SLOPE WATER
- ST — GULF STREAM
- SA — SARGASSO WATER

30°00'N  
84°30'W

28°30'N  
77°18'W

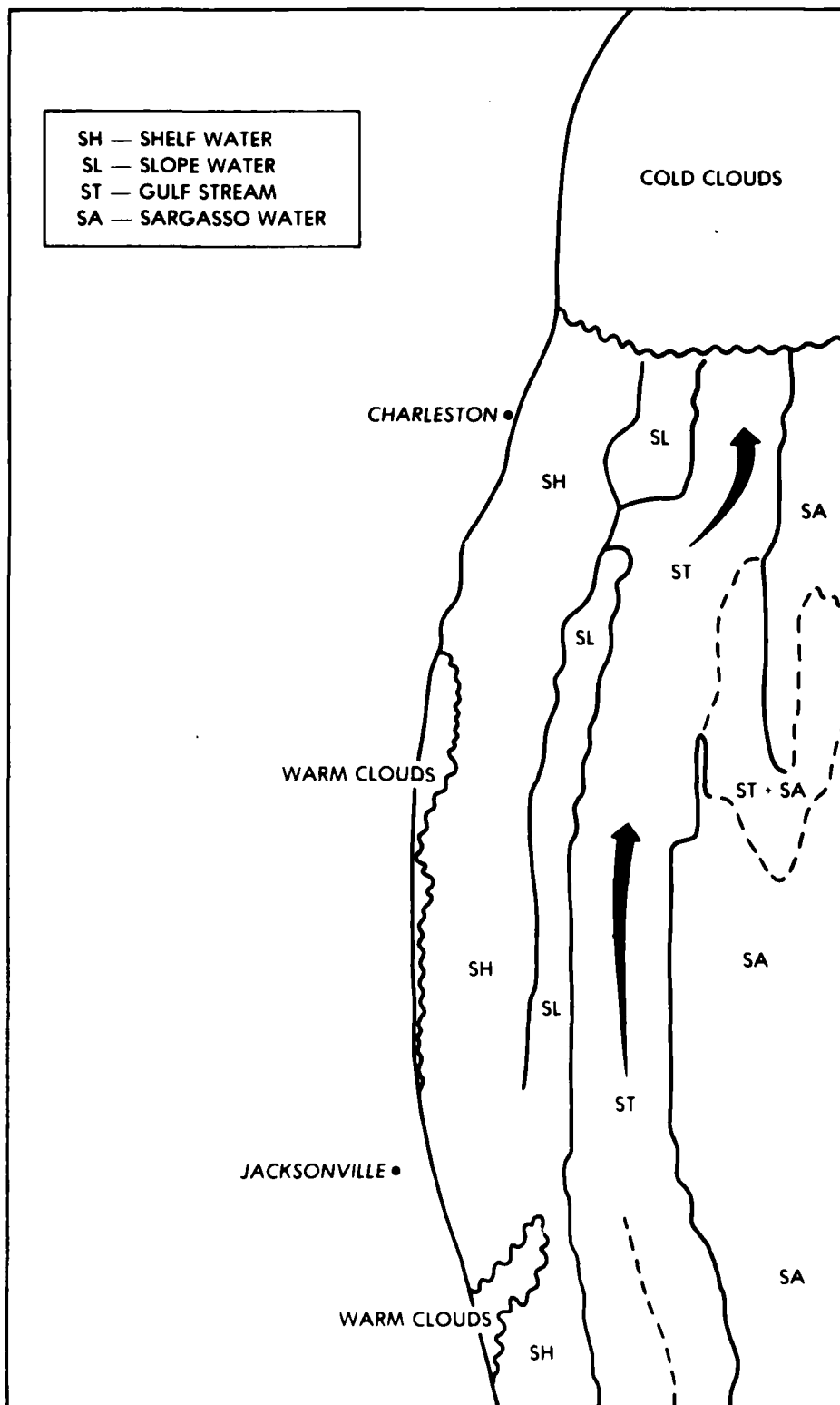


Figure 3. Manual analysis of the satellite image, 11 April 1980, 1400Z.

35°00'N  
82°54'W

33°24'N  
75°24'W

NO REL. THRESHOLD

- > SHELF WATER
- M SLOPE FRONT
- = SLOPE WATER
- \* NORTH WALL
- 1 GULF STREAM
- & SOUTH WALL
- / SARGASSO WATER
- DEFAULT
- LAND AND CLOUD

30°00'N  
84°30'W

28°30'N  
77°18'W

Figure 4. Automatic ocean surface classification without the application of a relative threshold, 11 April 1980, 1400Z.

The warm clouds are clouds (or haze) indicated by the visible data but not evident in the IR temperatures. Conversely, cold clouds were evident in the IR but not necessarily in the visible. The area of cold clouds was also extended to cover the area where the surface structure could not be resolved. This confusion was probably due to very thin cloud cover (not obvious in the visible and IR) surrounding the cold clouds.

Figures 4 and 5 are the computer analyses, enhanced for display, with the boundaries in the manual analysis overlaid. Both figures show confusing structure where the manual analysis was labeled cold clouds. Algorithms for improved cloud removal, water vapor correction, and compositing with previous classified images should have been applied to prevent this clutter but were unavailable at the time the analysis was made.

In figure 4, with no relative threshold applied, the comparison with the manual analysis is good below the cold cloud line (shown in figure 3). However, some pixels were classified Shelf Water or Slope Water where the manual analysis indicates Sargasso Water and vice versa. Figure 5 shows the results after a relative threshold of 5.0 was applied to the classifications in figure 4. The classifications that failed the threshold test, indicating uncertain decisions, were eliminated. Those rejected generally were at odds with the states of nature expected according to the manual analysis.

The remaining classifications represent the tradeoff of less accuracy (by not altering the a priori information with location) for a considerable savings in mass storage. Subsequent experiments on the same image where the a priori probabilities and mean temperatures were permitted to vary with location led to a substantial improvement in classification.

## VI. CONCLUSIONS

1. The use of Bayesian decision theory appears quite promising for classifying ocean surface features assuming that there are good statistics available that describe the features.

2. The a priori statistics that are the most variable with location are the mean temperatures. Since this statistical parameter represents the only discriminator among the water masses, the simplest version of the classifier, in which the statistics do not vary with location, works better for identifying fronts. Other statistical parameters that might separate the water masses need to be tested. Otherwise, an increase in mass storage is necessary to store a latitude-longitude array of mean temperatures.

3. The accuracy of the classification of both fronts and water masses can be substantially improved by the use of location-dependent, a priori probabilities.

35°00'N  
82°54'W

33°24'N  
75°24'W

REL. THRESHOLD = 5

- ☐ > SHELF WATER
- ☐ M SLOPE FRONT
- ☐ = SLOPE WATER
- ☐ \* NORTH WALL
- ☐ 1 GULF STREAM
- ☐ & SOUTH WALL
- ☐ SARGASSO WATER
- ☐ DEFAULT
- ☐ LAND AND CLOUD

30°00'N  
84°30'W

28°30'N  
77°18'W

Figure 5. Automatic ocean surface classification tested with a relative threshold of 5.0, 11 April 1980, 1400Z.

## REFERENCES

- Duda, R.O. and P.E. Hart, Pattern Classification and Scene Analysis, J. Wiley & Sons, New York, 1973.
- Gerson, D.J. and P. Gaborski, Pattern analysis for automatic location of oceanic fronts in digital satellite imagery, Technical Note 3700-65-77, Naval Oceanographic Office, NSTL Station, Bay St. Louis, MS, 1977.
- Gerson, D. J., E. Khedouri, and P. Gaborski, Detecting the Gulf Stream from digital data pattern recognition, The Belle W. Baruch Library in Marine Science: No. 12, Processes in Marine Remote Sensing, University of South Carolina Press, Columbia, SC, 19-39, 1982.
- Horton, C.W. and R.E. Coulter, Proposed plan for automatic mapping of surface and subsurface ocean features using satellite imagery, Technical Note 9100-2-81, Naval Oceanographic Office, NSTL Station, Bay St. Louis, MS, 1981.
- Khedouri, E., W. Gemmill, and M. Shank, Statistical summary of oceanic fronts and water masses in the western North Atlantic, Reference Publication 9, Naval Oceanographic Office, Washington, DC, 1976.

# Spatial Image Processing Masks from Frequency Domain Specifications\*

E. R. Meyer and R. C. Gonzalez  
Electrical Engineering Department  
University of Tennessee  
Knoxville, TN 37996

## Abstract

A method for obtaining a spatial convolution mask from a frequency-domain specification is discussed. This technique is motivated by the need in many applications to achieve processing speeds that cannot be met via Fourier transform formulations. The method is illustrated with synthetic and forward-looking infrared (FLIR) images.

## I. INTRODUCTION

The two-dimensional Fourier transform is one of the techniques most often used for image enhancement and restoration. Image sharpening and smoothing, noise reduction, contrast enhancement, and image de-blurring have been done with filters in the Fourier frequency domain [1]. These filters tend to be simple, intuitively understood, and mathematically tractable, making them easy to design and implement. Properties of the Fourier transform are well known and help in the filter design process. Various FFT algorithms have made the transform process for digital images practical in speed and size for many applications [1].

Unfortunately, FFT algorithms are not fast enough for on-line, real time rates (T.V. video frame rates for instance). Real time rates typically require several images to be processed per second [2] while the fastest FFT algorithms require seconds for an image with a reasonable resolution. It is possible to do small convolution processes at real or near-real time rates, with small (e.g.,  $3 \times 3$ ) convolution masks [3]. Since the Fourier filtering process is mathematically equivalent to a large convolution process, it is possible to approximate in some sense the Fourier filtering process with a convolution process involving small convolution masks. Schutten and Vermeij, for example, have proposed a method for finding a small convolution mask that approximates a filter given its frequency domain specification [4]. Schutten and Vermeij's approach is based on the infinite discrete Fourier transform. In the following discussion we show that it is possible to obtain the same results using the finite discrete transform and illustrate the technique with several test patterns and FLIR images.

## II. GENERATION OF SPATIAL CONVOLUTION MASKS

The process of Fourier filtering a discrete image is equivalent to the following convolution [1]:

\*Work partially supported by the Equipment Group, Texas Instruments, Inc., Lewisville, TX, through an image processing fellowship with the University of Tennessee.

$$g(x,y) = \sum_{\alpha=0}^{N-1} \sum_{\beta=0}^{N-1} h(x - \alpha, y - \beta) f(\alpha, \beta) \quad 0 \leq x, y < N \quad (1)$$

where:

$h(x,y)$  is a spatial representation of the filter,  
 $f(x,y)$  is the image to be filtered, and  
 $g(x,y)$  is the resulting image.

The Fourier domain representation of the convolution is

$$G(u,v) = H(u,v)F(u,v) \quad 0 \leq u, v < N \quad (2)$$

where

$G(u,v)$  is the Fourier transform of  $g(x,y)$ ,  
 $H(u,v)$  is the filter (the transform of  $h(x,y)$ ), and  
 $F(u,v)$  is the Fourier transform of  $f(x,y)$ .

The objective of the following discussion is to generate a small spatial convolution mask,  $h'$ , that approximates the filtering process of a given Fourier filter  $H(u,v)$ . The convolution mask would be used in the following convolution to produce a result image,  $g'$ , that somehow approximates the result image of the Fourier filtering process:

$$g'(x,y) = \sum_{\alpha=0}^{N-1} \sum_{\beta=0}^{N-1} h'(x - \alpha, y - \beta) f(\alpha, \beta) \quad 0 \leq x, y < N \quad (3)$$

The convolution mask,  $h'$ , should have the following properties:

1.  $h'$  should be a small convolution mask. This means that for some  $n \ll N$ ,  $h'(x,y) = 0$  for  $x$  or  $y > n$ . This gives an  $n \times n$  convolution mask.
2.  $h'$  should approximate  $h$  (the spatial domain representation of the desired Fourier filter  $H(u,v)$ ) in some way. The method developed here minimizes the criterion

$$e^2 = \sum_u \sum_v |H'(u,v) - H(u,v)|^2 \quad (4)$$

where  $H'(u,v)$  is the Fourier transform of  $h'(x,y)$  and  $|\cdot|$  designates the complex magnitude.

The Fourier transform of  $h'(x,y)$ ,  $H'(u,v)$ , is in general given by the following equation.

$$H'(u,v) = \frac{1}{N} \sum_{x=0}^{N-1} \sum_{y=0}^{N-1} h'(x,y) e^{-j2\pi(ux + vy)/N} \quad 0 \leq u, v < N \quad (5)$$

Using property 1,  $h'(x,y) = 0$  for  $x, y > n$ , the following is obtained:



$$H'(u,v) = \frac{1}{N} \sum_{x=0}^{n-1} \sum_{y=0}^{n-1} h'(x,y) e^{-j2\pi(ux + vy)/N} \quad 0 \leq u, v < N \quad (6)$$

This can be rewritten in matrix notation as

$$\underline{H}' = \underline{C} \underline{h}' \quad (7)$$

where:

$\underline{H}'$  is a column vector containing the terms  $H'(u,v)$  in some order,  
 $\underline{h}'$  is a column vector containing the terms  $h'(x,y)$  in some order,  
 $\underline{C}$  is a matrix containing the exponential terms in positions as determined by the orderings used in  $\underline{H}'$  and  $\underline{h}'$ . The elements of  $\underline{C}$  will be denoted by  $\underline{C}(i,k)$ .

Obviously  $\underline{H}'$  is an  $N^2$  vector and  $\underline{h}'$  is an  $n^2$  vector. Thus  $\underline{C}$  is an  $N^2 \times n^2$  matrix. A straightforward arrangement for  $\underline{H}'$  and  $\underline{h}'$  is row by row. Symbolically, if the vectors  $\underline{H}'$  and  $\underline{h}'$  are indexed with  $i = uN + v$  and  $k = xn + y$ , the elements are given by

$$\underline{H}'(i) = \underline{H}'(uN + v) = H'(u,v) \quad 0 \leq i < N^2, 0 \leq u, v < N \quad (8)$$

$$\underline{h}'(k) = \underline{h}'(xn + y) = h'(x,y) \quad 0 \leq k < n^2, 0 \leq x, y < n \quad (9)$$

This gives the following arrangement for the elements of  $\underline{C}$ ,

$$\underline{C}(i,k) = \underline{C}(uN + v, xn + y) = \exp(-j2\pi(ux + vy)/N) \quad (10)$$

Next, we satisfy property 2 by minimizing Eq. (4), which may be expressed as

$$e^2 = (\underline{H}' - \underline{H}) * (\underline{H}' - \underline{H}) = \|\underline{H}' - \underline{H}\|^2 = \|\underline{C}\underline{h}' - \underline{H}\|^2 \quad (11)$$

where  $\|\cdot\|$  indicates the complex Euclidean norm. A least-squares solution of the matrix equation  $\underline{H} = \underline{C} \underline{h}'$  will minimize  $e^2$ . This solution is given by

$$\underline{h}' = \underline{C}^\# \underline{H} \quad (12)$$

where  $\underline{C}^\#$  is the Moore-Penrose generalized inverse [5]. If  $\underline{C}$  has rank  $n^2$ ,  $\underline{C}^\#$  can be calculated by the equation

$$\underline{C}^\# = (\underline{C}^* \underline{C})^{-1} \underline{C}^* \quad (13)$$

where  $*$  indicates the conjugate transpose.

Since a full  $N^2 \times N^2$  Fourier matrix is guaranteed to have an inverse by the existence and uniqueness of the inverse Fourier transform, the matrix will have rank  $N^2$ .  $\underline{C}$  is composed of unique columns of this matrix, so  $\underline{C}$  must have rank  $n^2$ .

The foregoing procedure is valid for any arbitrary filter  $\underline{H}$ , and may be summarized by the following steps:

1. Input the desired frequency domain filter  $\underline{H}$ . For an  $N \times N$  filter this will involve storage of an  $N^2$  vector.
2. Generate the transform matrix  $\underline{C}$ . To generate an  $n \times n$  mask from an  $N \times N$  filter requires an  $N^2 \times n^2$  matrix.
3. Calculate the Moore-Penrose inverse using the equation  $\underline{C}^\# = (\underline{C}^* \underline{C})^{-1} \underline{C}^*$ . This requires taking the inverse of an  $n^2 \times n^2$  matrix.
4. Calculate the mask  $\underline{h'}$  using the equation  $\underline{h'} = \underline{C}^\# \underline{H}$ .

A drawback of the method, as given above, is that the small convolution mask generated may have complex terms. Since  $\underline{H}$  and  $\underline{C}$  both contain complex values,  $\underline{C}^\#$  and  $\underline{h'}$  may contain complex values. If  $\underline{h'}$  contains complex values, then the resulting image from the convolution may also contain complex values. From a more practical standpoint, the method, as stated, generates matrices too large for many computers. Typical values of  $n$  range between 3 and 9.  $N$  should be as large as possible to give maximum resolution to the Fourier filter. Values of 32 or greater are desirable. A straightforward implementation using  $n = 9$  and  $N = 32$  would require 1024 complex storage locations for  $\underline{H}$  and  $1024 \times 81 = 82944$  complex number storage locations for  $\underline{C}$ .  $N = 64$ , a more desirable value, requires 4096 and 331776 locations respectively. These requirements rapidly strain the resources of even a large main-frame computer. The addition of some constraints on the Fourier filter  $\underline{H}$  will eliminate complex values in the equations and reduce storage requirements to more manageable levels, as discussed in the following section.

### 111. SIMPLIFICATION OF THE METHOD USING FILTER CONSTRAINTS

The constraints used for simplification should reflect those properties found in most practical filters. Most practical filters exhibit conjugate symmetry because conjugate symmetry is necessary and sufficient to ensure the filtered result will not have any imaginary terms. Also, most filters have only real terms. Mathematically, these two constraints are expressed by the following two equations:

$$1. \quad H(u,v) = H^*(-u,-v) \quad (\text{Conjugate Symmetry}) \quad (14)$$

$$2. \quad H(u,v) = H^*(u,v) \quad (H \text{ is real}) \quad (15)$$

These constraints allow us to eliminate complex terms in the following manner. Assume  $h(x,y)$  and  $H(u,v)$  are transform pairs. They are related by

$$H(u,v) = \frac{1}{N} \sum_{x=0}^{N-1} \sum_{y=0}^{N-1} h(x,y) e^{-j2\pi(ux + vy)/N} \quad 0 \leq u, v < N \quad (16)$$

Constraint 1 implies  $h(x,y)$  is real or  $h(x,y) = h^*(x,y)$ . The second constraint implies conjugate symmetry on  $h$  or  $h(x,y) = h^*(-x,-y) = h(-x,-y)$ . This gives

$$\begin{aligned}
2H(u,v) &= H(u,v) + H^*(-u,-v) \\
&= \frac{1}{N} \sum_{x=0}^{N-1} \sum_{y=0}^{N-1} [h(x,y) e^{-j2\pi(ux + vy)/N} + h^*(x,y) e^{j2\pi(-ux - vy)/N}] \\
&= \frac{1}{N} \sum_{x=0}^{N-1} \sum_{y=0}^{N-1} [h(x,y) e^{-j2\pi(ux + vy)/N} + h^*(-x,-y) e^{j2\pi(ux + vy)/N}] \\
&= \frac{1}{N} \sum_{x=0}^{N-1} \sum_{y=0}^{N-1} h(x,y) [e^{-j2\pi(ux + vy)/N} + e^{j2\pi(ux + vy)/N}] \\
2H(u,v) &= \frac{1}{N} \sum_{x=0}^{N-1} \sum_{y=0}^{N-1} h(x,y) 2\cos[2\pi(ux + vy)/N] \\
H(u,v) &= \frac{1}{N} \sum_{x=0}^{N-1} \sum_{y=0}^{N-1} h(x,y) \cos[2\pi(ux + vy)/N] \quad 0 \leq u,v < N \quad (17)
\end{aligned}$$

Using this formulation of the Fourier transform causes all of the equations in the small convolution mask generation method to involve real terms only and causes the resulting masks to also have real terms.

Many filters are also symmetric about both the  $u$  and  $v$  axes [1]. Mathematically, this is expressed as  $H(u,v) = H(u,-v)$  and  $H(u,v) = H(-u,v)$ . These symmetries imply  $h(x,y) = h(x,-y)$  and  $h(x,y) = h(-x,y)$ , respectively. Making use of these symmetries and the periodicity of the finite discrete Fourier transform [1], the number of terms in the transform equation can be reduced by a factor of 4. The Fourier transform equation is then

$$\begin{aligned}
H(u,v) &= \frac{1}{N} \left[ h(0,0) + h\left(\frac{N}{2}, 0\right) \cos(\pi u) + h\left(0, \frac{N}{2}\right) \cos(\pi v) + h\left(\frac{N}{2}, \frac{N}{2}\right) \cos[\pi(u + v)] \right. \\
&\quad + 2 \sum_{y=1}^{\frac{N}{2}-1} [h(0,y) \cos(2\pi vy/N) + h\left(\frac{N}{2}, y\right) \cos[2\pi(\frac{uN}{2} + vy)/N]] \\
&\quad + 2 \sum_{x=1}^{\frac{N}{2}-1} [h(x,0) \cos(2\pi ux/N) + h\left(x, \frac{N}{2}\right) \cos[2\pi(ux + \frac{vN}{2})/N]] \\
&\quad \left. + 4 \sum_{y=1}^{\frac{N}{2}-1} \sum_{x=1}^{\frac{N}{2}-1} h(x,y) \cos[2\pi(ux + vy)/N] \right] \quad 0 \leq u,v < \frac{N}{2} \quad (18)
\end{aligned}$$

Using this final version of the transform equation in the matrix formulation of the convolution mask generation method, the filter  $\underline{H}$  can be stored in  $N^2/4$

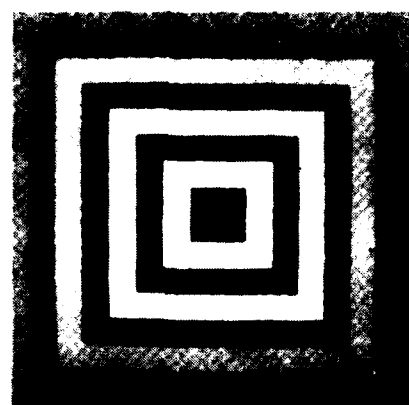
locations, the convolution mask  $h'$  in  $n^2/4$  locations, and the matrix  $C$  in  $N^2n^2/16$  locations (the matrix is now  $N^2/4 \times n^2/4$ ). For  $n = 9$  and  $N = 64$ , the matrix  $C$  now requires 20736 locations as compared to 331776 locations required previously, a substantial saving.

#### IV. EXPERIMENTAL RESULTS

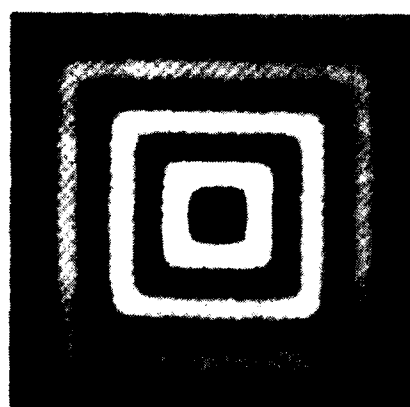
First-order lowpass and highpass Butterworth filters were selected to illustrate the technique discussed in the previous sections. This covers two complementary techniques that are commonly used for image enhancement; the lowpass filter reduces noise and blurs edges while the highpass filter enhances noise and sharpens edges. An inverse first order Butterworth lowpass filter was selected to give a good comparison of how the spatial and Fourier techniques do at reversing the effects of a previously applied filter (inverse filtering). A rectangular notch filter was also used to filter horizontal periodic striping in FLIR images. The resolution for all filters was  $64 \times 64$  ( $N = 64$ ).  $9 \times 9$  masks were generated ( $n = 9$ ). The matrix  $C$  is thus  $1024 \times 25$  elements.

Figure 1 compares a  $9 \times 9$  mask convolution to the equivalent Fourier filtered result of a lowpass filter. Figure 2 compares the two techniques for inverse filtering. Note how, in both figures, the mask convolution results tend to have less of an effect than the Fourier filtered results. This seems to be true regardless of the filter selected, and it is due to the fact that we are only approximating the filtering process.

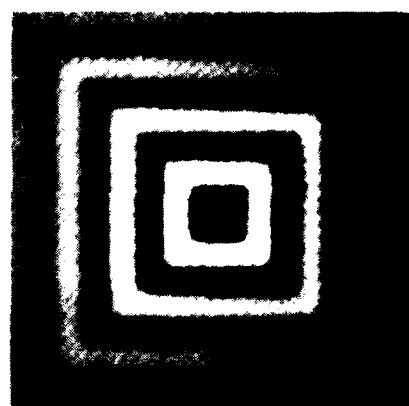
As a more practical illustration of the technique, Figure 3(a) shows a FLIR image corrupted by periodic interference, visible as horizontal stripes in the picture. This periodic interference manifests itself in the Fourier spectrum as energy bursts along the vertical axis, as shown in Fig. 4(a). The removal of these bursts can be achieved by the notch filter shown in Fig. 4(b). The inverse of the filtered Fourier transform is shown in Fig. 3(b). Note that, for all practical purposes, the degradation has been removed. The equivalent spatial process using a  $9 \times 9$  mask is shown in Fig. 3(c), which still has a mild degree of striping due to the fact that the mask was not large enough to properly approximate the frequency-domain filter. A second pass of the mask (Fig. 3(d)) accomplishes removal of the stripes at the expense of some smoothing of the image.



(a)



(b)



(c)

Figure 1. (a) Original test picture. (b) Fourier filtered result obtained with a first order Butterworth lowpass filter with a 3 dB point of 4 pixels. (c) 9 x 9 mask convolution of 1(a). The mask was generated from the filter used in 1(b).

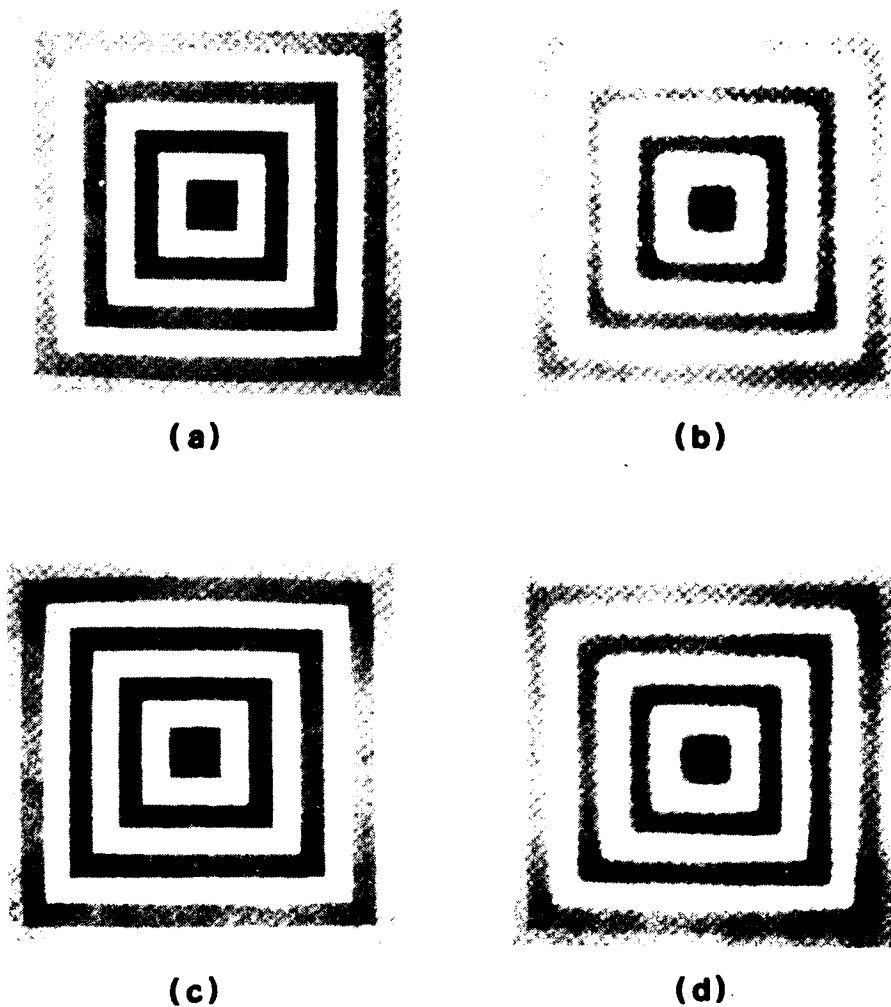


Figure 2. (a) Original test picture. (b) Fourier-filtered result obtained using a first order Butterworth lowpass filter with a 3 dB point of 8 pixels. (c) Fourier filtered result using the inverse of the filter used in 2(b). This gives back the original image plus a little spottiness due to round off error in the transform process. (d) 9 x 9 mask convolution result. The mask was generated from the filter used in 2(c).

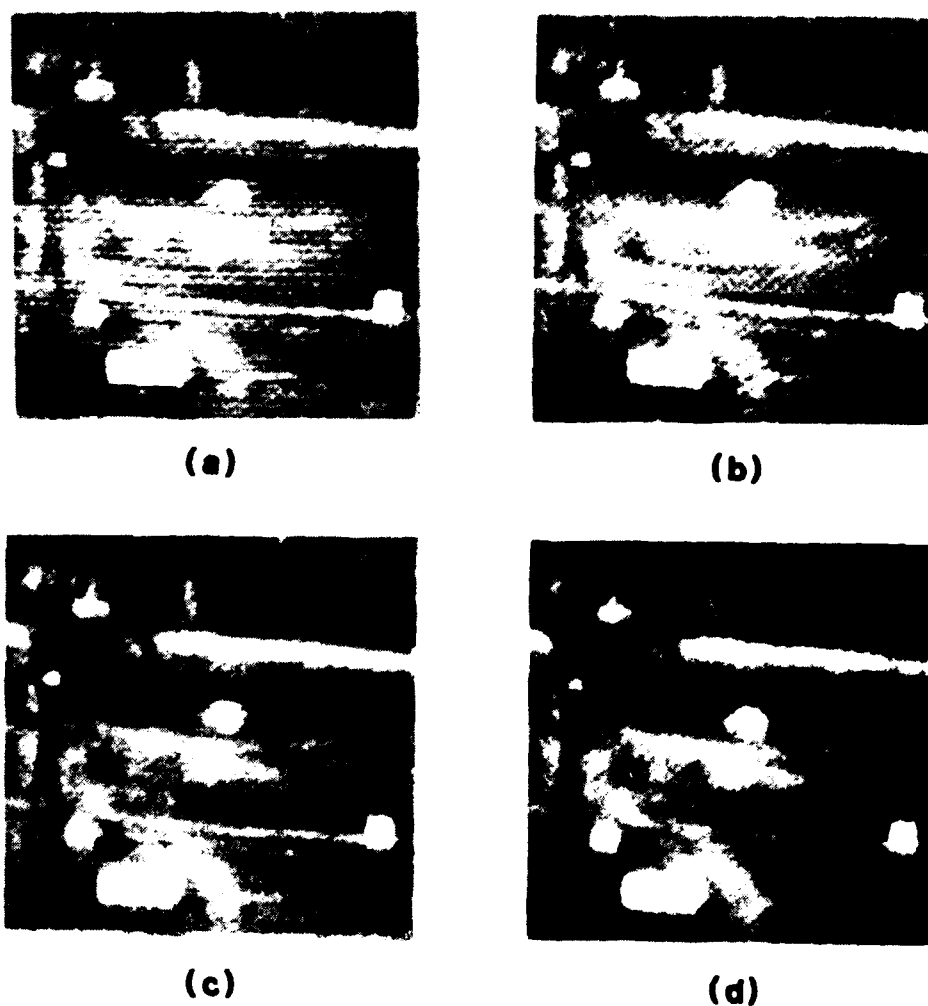
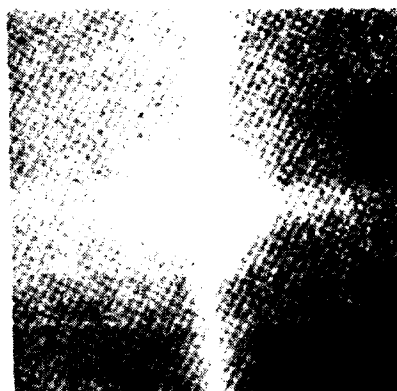
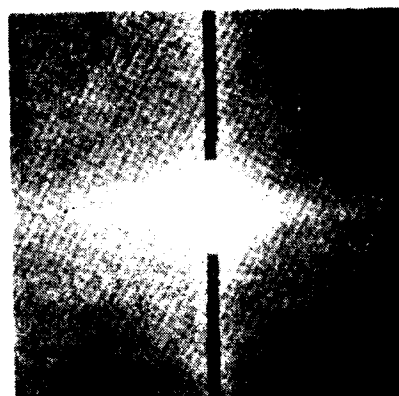


Figure 3. (a) Original FLIR scene of a field with tank and decoys. (b) Image 3(a) Fourier filtered with a rectangular notch filter that eliminates horizontal periodical components. (c) 9 x 9 mask convolution of 3(a) using a mask generated from the filter used in 3(b). (d) A second pass of the mask. [Original image courtesy of the Equipment Group, Texas Instruments, Inc., Lewisville, Texas.]



(a)



(b)

Figure 4. (a) Fourier spectrum of the image shown in Fig. 3(a). (b) Use of a notch filter to remove energy bursts associated with the horizontal periodic interference.



## REFERENCES

1. Gonzalez, R. C. and Wintz, P., Digital Image Processing, Addison-Wesley, Reading, MA, 1977.
2. Woods, R. E. and Gonzalez, R. C., "Real-Time Digital Image Enhancement," Proc. IEEE, vol. 69, no. 5, pp. 643-654, 1981.
3. Lee, J. S., "Digital Image Enhancement and Noise Filtering by Use of Local Statistics," IEEE Trans. Pattern Analysis and Machine Intelligence, vol. PAMI 2, no. 2, pp. 165-168, 1980.
4. Schutten, R. W. and Vermeij, G. F., "The Approximation of Image Blur Restoration Filters by Finite Impulse Responses," IEEE Trans. Pattern Analysis and Machine Intelligence, vol. PAMI-2, no. 2, pp. 176-180, 1980.
5. Davis, P. J., Circulant Matrices, John Wiley & Sons, New York, NY, 1979.
6. "Automated Image Enhancement Techniques for Second Generation FLIR," Contract No. DAAG53-76-C-0195, Final Report, Honeywell Systems and Research Center, Defense Documentation Center No. AD-A0-49564, December, 1977.

## **Appendix A: Agenda**

## AGENDA

### PATTERN ANALYSIS IN THE MARINE ENVIRONMENT

P A M E

March 24-26, 1982

Wednesday, March 24

0800 - 0830	Registration	Coffee and Danish
0830 - 0845	Welcome	James E. Andrews, Technical Director, NORDA
0845 - 1145	Session 1	Image Analysis Techniques 1 Chairman: Robert M. Brown, Pattern Analysis Laboratory, NORDA

RECENT TRENDS IN IMAGE ANALYSIS....Azriel Rosenfeld, University of Maryland

A CLUSTER ANALYSIS PROGRAM FOR IMAGE SEGMENTATION....Melvin F. Janowitz, University of Massachusetts

INFORMATION CONTENT OF OCEAN SURFACE WAVE PATTERNS....Robert C. Beal, Applied Physics Laboratory, Johns Hopkins University

SYNTACTIC APPROACH TO SIGNAL AND IMAGE ANALYSIS....K.S. Fu, Purdue University

1145 - 1330	Lunch under the trees - Cypress House Pavillion
1330 - 1630	Session 2      Pattern Analysis Techniques Chairman: Robert Ehrlich, University of South Carolina

GRAIN SHAPE ANALYSIS--A MULTILEVEL PATTERN RECOGNITION  
PROCEDURE FOR TRACKING DEEPWATER BOTTOM CURRENTS....Robert  
Ehrlich, University of South Carolina

FUZZY ALGORITHMS FOR PATTERN RECOGNITION....James C. Bezdek,  
Utah State University

THE EXTENDED CABFAC/QMODEL FAMILY OF ALGORITHMS - A MULTIVARIATE  
PATTERN CLASSIFICATION SCHEME....William E. Full, University of  
South Carolina

HIGH-SPEED PROCESSING OF ZOOPLANKTON SAMPLES....Arthur D.  
Poularikas, University of Rhode Island, Luther E. Bivins, Office  
of Ocean Technology and Engineering Services, NOAA, Mark Berman,  
University of Rhode Island

1800 - 1900	Social - Terrace Room, Diamondhead Country Club
1900 - 2100	Dinner and Address: THE OCEAN SCIENTIST'S VIEW OF PATTERN ANALYSIS . . . . James E. Andrews, Technical Director, NORDA

Thursday, March 25

0800 - 0830 Late Registration Coffee and Danish  
0830 - 1130 Session 3 Space Technology for Ocean Applications  
Chairman: James R. Edberg, Jet Propulsion  
Laboratory, California Institute of Technology

ON OBSERVING THE OCEANS AND SEA ICE WITH A SPACEBORNE IMAGING  
RADAR-THE SEASAT SYNTHETIC-APERTURE RADAR (SAR)....Lee-Lueng Fu,  
Jet Propulsion Laboratory, California Institute of Technology

THE USE OF SATELLITE OBSERVATIONS OF THE OCEAN SURFACE IN  
COMMERCIAL FISHING OPERATIONS....Donald R. Montgomery, Jet Propulsion  
Laboratory, California Institute of Technology

AN ENERGY THEOREM AND ITS RELATIONSHIP TO SIGNAL CHARACTERIZA-  
TION....Richard C. Heyser, Jet Propulsion Laboratory, California  
Institute of Technology

DIGITALLY CONTROLLED SONARS....George Hansen, Jet Propulsion Lab-  
oratory, California Institute of Technology

APPLICATION OF COMPUTER IMAGE PROCESSING TO UNDERWATER SURVEYS....  
Peter Paluzzi, McQuest Marine R & D Company Ltd., Burlington, Ontario,  
Canada

1130 - 1330 Lunch under the tree - Cypress House Pavillion  
1330 - 1630 Session 4 Ocean Patterns in Space-Time  
Chairman: Ramesh Jain, Wayne State University

OCEAN ACOUSTIC MULTI-PATH IDENTIFICATION AT LONG RANGE....  
Mike Brown, University of California at San Diego

SEA SURFACE TEMPERATURE ANALYSIS....William H. Gemmill, National  
Weather Service, NOAA

POTENTIALS FOR PATTERN RECOGNITION IN PHYSICAL OCEANOGRAPHY....  
Albert W. Green, Physical Oceanography Branch, NORDA

DYNAMIC SCENE ANALYSIS.... Ramesh Jain, Wayne State University

1630 Shrimp Boil Buffet - Cypress House Pavillion

Friday, March 26

0800 - 0830 Coffee and Danish  
0830 - 1130 Session 5

Image Analysis Techniques II  
Chairman: Rafael C. Gonzalez, University of  
Tennessee

IMAGING ROUGH SEAFLOOR; AN ANALOGY TO OPTICS....Clarence Clay,  
University of Wisconsin-Madison

PRELIMINARY RESULTS FROM SEAMARC II .... Joseph F. Gettrust,  
University of Hawaii

FLUCTUATION SPECTRUM OF OCEANIC STRUCTURE....Ronald J. Holyer,  
Remote Sensing Branch, NORDA

ATMOSPHERIC CORRECTION OF CZCS DATA BY THE METHOD OF PRINCIPAL  
COMPONENTS....Ronald J. Holyer, Remote Sensing Branch, NORDA

SPATIAL TECHNIQUES FOR ENHANCEMENT AND RESTORATION OF INFRARED  
IMAGES....Rafael C. Gonzalez, University of Tennessee

1130 Workshop Adjourns

## **Appendix B: Abstracts**

## A CLUSTER ANALYSIS PROGRAM FOR IMAGE SEGMENTATION

Melvin F. Janowitz, Ph.D.  
Department of Mathematics and Statistics  
University of Massachusetts  
Amherst, Massachusetts 01003

### Abstract

A description will be given of an unsupervised program for the detection of regions of uniform brightness in remote sensing data. The program is based in part upon histogram analysis, and in part upon the "scatter" of the various regions in the picture. There is a statistic built into the program that enables the computer to automatically determine the proper number of regions in the picture. The program is illustrated with some concrete examples, and an application presented for the rapid automatic detection of objects of interest in a remote sensing picture. The operation of the program with noisy data will also be examined by taking remote sensing data, and adding varying amounts of normal and uniform noise to it.

DR. MELVIN F. JANOWITZ earned a BA from the University of Minnesota in 1950, with a major in mathematics and a minor in physics. In 1963 he earned a Ph.D. in mathematics from Wayne State University.

Dr. Janowitz's professional experience includes: assistant professor, University of New Mexico, 1963-1968; Associate Professor, Western Michigan University, 1966-1967; Associate Professor, University of Massachusetts, 1967-1970; Professor, University of Massachusetts, 1970 to present; Assistant Dean, Faculty of Natural Sciences and Mathematics, University of Massachusetts, 1979 to present.

Having published over 30 papers in lattice theory, mathematical models for cluster analysis, Dr. Janowitz's research interests include: lattice theory, algebraic theory of semigroups, cluster analysis, image segmentation, classification of plants and animals by means of cluster analysis.

## INFORMATION CONTENT OF OCEAN SURFACE WAVE PATTERNS

Robert C. Beal  
Applied Physics Laboratory  
Johns Hopkins University  
Laurel, Maryland 20707

### Abstract

Gravity waves traveling on the ocean surface behave according to well established kinematic and dynamic laws of physics. During its typical life cycle, for example, a wave train grows from a small amplitude higher frequency ensemble into a large energy fully developed spectrum extending over several octaves in frequency. In time, dispersion causes a spatial separation of the longer wave components and, aided by loss mechanisms, the initially broad spectrum degenerates into a narrow band swell. The nearly monochromatic swell is subject to changes in wave number and direction according to the action of local currents or finite depth.

By examining the spatial evolution of ocean wave spectra measured by the Seasat synthetic aperture radar, information regarding

- (1) storm generation sources,
- (2) deep ocean and coast currents, and
- (3) coastal bathymetry may be extracted.

Pattern analysis methods applied in spectral domain may be useful in the optimal extraction of this information.



# SYNTACTIC APPROACH TO SIGNAL AND IMAGE ANALYSIS

K. S. Fu  
School of Electrical Engineering  
Purdue University  
West Lafayette, Indiana 479-7

## Abstract

Syntactic approach to pattern analysis is introduced. Primitive selection and structural (or syntax) analysis are described. Methods for recognizing noisy and distorted patterns are discussed. Applications of the syntactic approach to signal and image analysis are illustrated by examples.

GRAIN SHAPE ANALYSIS -- A MULTILEVEL PATTERN RECOGNITION  
PROCEDURE FOR TRACKING DEEPWATER BOTTOM CURRENTS

Robert Ehrlich  
Department of Geology  
University of South Carolina  
Columbia, SC 29208

Abstract

Strong deepwater bottom currents can move quartz sand and silt for hundreds or thousands of kilometers. Away from the boundaries of such currents, the sediments are dominantly of "local" derivation. Because the shape of a quartz grain reflects the grain's origin and transport history, this differential provenance of local and distal sources can be detected via quartz shape analysis. Such analysis involves optimization of all parts of an image analysis/pattern recognition data analytical scheme. --

Individual two-dimensional shapes are digitized from microscopic imagery and edges located on a microprocessor-based video analyzer of our own design. The 200-1000 edge points per grain are reduced to 48 points spaced equangularly about the grain centroid and 24 terms (harmonics) of a finite Fourier series in polar form are calculated. Each sample consists of 200 or more particles such that a distribution of the frequency-of-occurrence of amplitudes in various class intervals are generated for each harmonic. Class intervals are of variable width based on information theoretic concepts which result in frequency counts arrayed in a manner to produce maximum information. The amplitude array (frequencies per class interval) is evaluated at each harmonic in terms of normalized average entropy (NAE). Harmonics with low NAE display the most contrast between samples. Data at such harmonics are selected for further analysis (NAE serves as a feature extractor).

The subsequent data-analytic steps are relevant to any spectral/multichannel data set. Frequency counts from each class interval from a chosen harmonic constitute a multivariate data set for the final stage in the analysis. Using vector-analytic techniques the sample set can be examined in terms of its configuration in data space: whether the data from a series of discrete tight clusters or whether the data array is "smeared out". In the latter case each sample can be described as a mixture of a small number of end members. The algorithms EXTENDED CABFAC/FUZZY QMODEL are designed to determine mixing proportions and end member compositions. Successful unmixing of collections of grain shapes is verified by SEM imagery of grains from selected samples which shows that each end member consists of grains of distinctly different origin.

## FUZZY ALGORITHMS FOR PATTERN RECOGNITION

James C. Bezdek  
Mathematics Department  
Utah State University  
Logan, Utah 84322

### Abstract

This paper surveys some available techniques based on fuzzy sets for several problems of current interest in pattern recognition and image processing. In particular, we consider some fuzzy approaches for clustering, feature selection, classification, and shape analysis.

THE EXTENDED CABFAC/QMODEL FAMILY OF ALGORITHMS -  
MULTIVARIATE PATTERN CLASSIFICATION SCHEME

William E. Full  
Department of Geology  
University of South Carolina  
Columbia, SC 29208

Abstract

Many problems in pattern recognition involve multivariate data sets; for instance, a collection of amplitudes in the frequency domain, chemical analysis, Fourier transformations of shapes, and so forth. Generally the number of variables per data point are high (for example, 5-50+). Because each variable represents a reference axis, the data can be envisioned as being plotted in a data space of dimension equal to the number of variables. It has been shown that many classification problems can be reduced by deduction of the geometrical character of the multidimensional data array. Individual multivariate elements can be classified in terms of membership in one or more clusters, or relative position within a data cloud. However, only when the number of variables are three or less can we correctly visualize the nature of the data array. When the number of variables (dimensions) of the data are four or more, additional tools must be used to visualize the nature of the data. For instance, often times even though the data space has high dimensionality, the data themselves are analyzed in a configuration of much lower dimensionality (for example, all the data may be clustered at one point in a plane). Furthermore, the data themselves may be smeared out or grouped in several clusters in the data space. Determining the nature of the data in such terms is critical to any model we may have for our data. For instance, if the data does group, then a clustering model may be appropriate; if the data are smeared in a space of lower dimensionality than that of data space, a mixing model may be apropos.

The EXTENDED CABFAC-QMODEL family of algorithms [EXTENDED CABFAC (EC), QMODEL (QM), EXTENDED QMODEL (EQM), FUZZY QMODEL (FQM)] are algorithms which attempt to answer such questions. The EC algorithm, via vector analysis, determines the proper number of dimensions wherein the data array may truly lie (often much less than the number of variables) and provides a set of new reference axes for this "reduced" space. The determination of the proper number of dimensions for this reduced space is accomplished by the following three step procedure: 1) locate all of the original points in a series of reduced spaces from the original measurement space by projection using eigenvectors; 2) back calculate the corresponding real data in the original measurement space from the set of projected points in each of the reduced spaces; and 3) compare the back calculated data to the original data via the coefficient of determination and determine the proper reduced space to be used in any further analysis.

Within the reduced space, the QM family of algorithms determine the proper classification scheme (hard clustering, fuzzy clustering, or unmixing). The three QM algorithms (QM, EQM, FQM) are designed to analyze progressively more complex problems. If a mixing model is appropriate, QM is optimal if end members are present in the data set and there are few extraneous "outliers". EQM is appropriate for mixing if the end members may not have been captured in the data array and there are few extraneous "outliers".

FQM is appropriate for mixing if the end members may not have been captured in the data set and the data may be "dirty" (that is, contain extraneous outliers). If the clustering model is more appropriate, FQM is the appropriate algorithm. The data can be observed to be clustered by examining the fuzzy cluster memberships as produced by the FQM algorithm. If these memberships tend to be close to either zero or one, then the data are clustered. Points with intermediate memberships are indicative of shared components with at least one other group or end member. Data with intermediate memberships can be modeled as mixtures while data with extremes in membership should be modeled as clusters. In each of the above algorithms, the final linear relationships between all of the data (proportions in terms of unmixing, linear fuzzy memberships in terms of clustering) will be produced. In addition, FQM will provide non-linear fuzzy memberships for the data.

These algorithms have successfully classified sand grain shapes into families of different origin. In addition, scientifically successful analysis of grain size, gas chromatographic, and foraminifera imagery has been accomplished.

## HIGH-SPEED PROCESSING OF ZOOPLANKTON SAMPLES

Alexander D. Poularikas  
University of Rhode Island

Luther E. Bivins  
NOAA, Office of Ocean Technology and Engineering Services

Mark Berman  
University of Rhode Island

### Abstract

Research conducted by the University of Rhode Island (URI) and sponsored by the National Oceanic and Atmospheric Administration (NOAA) has demonstrated that pattern recognition techniques can be utilized to process samples of ichthyo and zooplankton. The objective is to size, count, and identify within five minutes the approximately 500 organisms aliquoted from a bongo net tow. The identification required is to classify each organism into one of the ten major taxonomic groups of zooplankton found in the North Atlantic. Recent tests using image processing equipment and algorithms based on simple morphometric features of the organisms of interest, enabled 240 preserved organisms to be separated into five of the ten major taxonomic groups of interest, with a recognition success of 95 percent. These tests have demonstrated the feasibility of using pattern recognition for automated processing of zooplankton. Thus, preparations are underway to demonstrate the entire automated process in October of 1983.

ON OBSERVING THE OCEANS AND SEA ICE WITH A SPACEBORNE  
IMAGING RADAR - THE SEASAT SYNTHETIC-APERTURE RADAR (SAR)

Lee-Lueng Fu  
Jet Propulsion Laboratory  
California Institute of Technology  
4800 Oak Grove Drive  
Pasadena, CA 91109

Abstract

The Seasat SAR was an L-band (23.5 cm wavelength) radar which imaged the ocean surface primarily through Bragg resonant scattering by short gravity waves. Voluminous imagery was produced of the North Atlantic, the eastern North Pacific and the Beaufort Sea area of the Arctic Ocean, revealing a wide spectrum of phenomena occurring on the ocean surface and sea ice: surface and internal waves, current boundaries, eddies, bathymetric features, storms, rainfalls, ice motions and morphology, etc. Images of each phenomenon category will be presented. Aspects of the utility of a spaceborne SAR for monitoring ocean and ice variabilities will be discussed.

# THE USE OF SATELLITE OBSERVATIONS OF THE OCEAN SURFACE IN COMMERCIAL FISHING OPERATIONS

D.R. Montgomery  
Jet Propulsion Laboratory  
California Institute of Technology  
4800 Oak Grove Drive  
Pasadena, CA 91109

## Abstract

Commercial fishermen are interested in the safety of their crews, boats and gear, and in making the best catch for their time and money. Rising fuel costs, increased competition from foreign fisheries, improved knowledge about fish habits and the new 200-mile economic zone have all had an impact on the U.S. fishing industry. As a consequence, the modern fisherman, more than ever, requires reliable and timely information about the marine environment.

This paper described an experimental program to utilize satellite observation of the ocean surface, in conjunction with conventional observations and products, to prepare special "Fisheries-Aids" charts for daily radio-facsimile broadcasts to commercial fishermen. These special fisheries products aggregate a broad set of ocean observations, including ocean color structure, to depict oceanographic conditions of importance to commercial fishing tactics.

Results to date have shown that improved safety at sea and decreased fuel costs can be achieved through the applied use of these special fisheries charts.



## AN ENERGY THEOREM AND ITS RELATIONSHIP TO SIGNAL CHARACTERIZATION

Richard C. Heyser  
Jet Propulsion Laboratory  
California Institute of Technology  
4800 Oak Grove Drive  
Pasadena, CA 91109

### Abstract

Sound and seismic signals are elastic waves passing through a physical medium. These waves are initiated through a local departure of energy state from its equilibrium value. Restoration of equilibrium results in the transmittal of energy density away from the place of initial disturbance. Interception of this energy density constitutes a signal describing not only the original source but also the physical elastic properties of the intervening medium. By invoking conservation of energy, it is shown that a necessary and sufficient condition exists for such observations of energy density in spaces of description which are Lebesgue square integrable. Since time domain analysis and frequency domain analysis conform to this condition, some new insights into signal characterization can be gained. Examples are presented of real-world applications of this theory.

MR. RICHARD C. HEYSER received an M.S. degree in Electrical Engineering from California Institute of Technology in 1954. He is currently a member of the Technical Staff of the Information Systems Division of JPS. His professional interests include (a) underwater sonic signal processing utilizing advanced communication techniques, (b) successful development of a system for ultrasonic soft tissue visualization, and (c) development of a medical ultrasonic tomographic reconstruction system. This work involved application of the new concept of Time Delay Spectrometry to improve sonic and ultrasonic measurement techniques beyond that possible with conventional technology. His experience in imaging technology includes participation in the conceptual design, or mission performance of 14 Lunar Imaging (VIDEO) Missions and all Planetary Imaging (VIDEO) Missions since 1958 to the present. His current work involves ultrasonic imaging of deep arteries, underwater sound measurements, imaging of heart valves, ultrasonic sensing of levitated spheres at high temperatures.

## DIGITALLY CONTROLLED SONARS

George Hansen  
Jet Propulsion Laboratory  
California Institute of Technology  
4800 Oak Grove Drive  
Pasadena, CA 91109

### Abstract

Operational and side scan sonars have been developed at the Jet Propulsion Laboratory as part of the Advanced Ocean Development Test Platform. The AOTDP is a deep ocean survey submersible using digital command, control, and data retrieval. The sonars are all controlled by digital commands entered from a CRT terminal keyboard. All echos received by each sonar are digitized and processed within the submersible or transmitted to the surface as part of the telemetry data stream.

Quantitative recordings of the operating parameters of the sonars are made along with the amplitude and phase of the echos received by the side scans. The parameters of the other sonars are also recorded by the surface system.

The sonar functions that are digitally controlled and parameters recorded are the carrier frequency, time varying gain curve, constant gain, pulse power, risetime, duration and envelope. Six envelopes or pulse shapes are presently available for use.

The system software presents the available options for the different sonars in menu form on the CRT. The operator can select the parameters to be changed and transmitted to the sonar at the next pulse time and these parameters will remain in force until altered. The designed operation of the sonars has been verified in several sea trials.

## THE IDENTIFICATION OF ACOUSTIC MULTIPATHS AT LONG RANGE IN THE OCEAN

Michael G. Brown  
Institute of Geophysics & Planetary Physics, A-025  
University of California, San Diego  
La Jolla, California 92093

### Abstract

Due to the presence of the ocean sound channel, in general many ray paths (multipaths) connect a fixed acoustic source and a separate fixed receiver in the ocean. The number and structure of the multipaths depend on the details of the sound channel and the positions of the source and the receiver. As each multipath samples the ocean differently, each contains unique information about the (sound speed) structure of the ocean. In order to exploit this information one must first identify each of the measured multipath arrivals. This is the problem addressed here. Several examples of successful identification are shown; these are based primarily on travel time information. The utility of other information is also discussed.

MICHAEL G. BROWN received a Ph. D. in Oceanography from the University of California, San Diego in 1982. He is currently with the Institute of Geophysics and Planetary Physics at that university. His research interests are in acoustic wave propagation in the ocean and geophysical inverse problems.

## APPLICATION OF COMPUTER IMAGE PROCESSING TO UNDERWATER SURVEYS

Peter R. Paluzzi  
Image Processing Laboratory  
California Institute of Technology  
Pasadena, California 91109

Unlike exploration involving spacecraft images, seafloor exploration has not extensively employed computer image processing. The images created by bottom cameras and side scan sonars have not been previously acquired digitally. Today, the number of digital data collection systems has grown and existing capabilities to analyze the data have not kept pace with that growth. To this end, image processing techniques have been applied to three types of images used in marine geology: bottom photographs, side scan sonar records, and bathymetric data recast as an image.

Photographs of the sea floor are often beset by strong illumination gradients. Because of these gradients, it is troublesome to print the photographs and still preserve detail in all portions of the scene. The computer can suppress illumination gradients using a digital filter that passes only the finer details of a scene and not the broad changes in illumination. This is particularly important when joining adjacent images to make mosaics. Bottom photographs computer processed in this way can sustain stronger contrast enhancements in order to adequately display important features.

Side scan sonar records also have illumination gradients; however, these gradients arise from the attenuation of echos at increasing ranges. The same digital filtering technique used with photographs effectively suppresses this illumination gradient in the sonar images. In addition, side scan sonar images possess distortions owing to the slant-range geometry and the ship's speed. Techniques used to geometrically rectify spacecraft images for camera and perspective distortion have immediate application for correcting side scan sonar images. Navigation data has been used to further correct side scan sonar images for trackline distortion. Once trackline is corrected and registered to a cartographic reference system, adjacent sonar images can be mosaicked and further rectified into a standard map projection.

Although not traditionally displayed as an image, bathymetric data can be processed using computer image processing techniques. Individual soundings and profiles can be rendered into an image by interpolating and regridding the data. The resulting surface is displayed using digital surface shading techniques. Topographic data sets that are available in a gridded format (e.g. the Global Topographic Dataset) can be shaded without interpolation. These digital terrain models are images of a sort and, being so, can also be rectified into a standard map projection.

Using computer graphics techniques, the bathymetric surfaces can be displayed in perspective view as if seen from the window of an airplane or a spacecraft. This capability allows the interpreter to move above and about the terrain to see a representation of the sea floor without the necessity of diving in a submersible or draining away the oceans.

PETER R. PALUZZI

Mr. Paluzzi currently supervises all image and data processing activities for McQuest Marine Research & Development Company Limited. He received an M.S. in remote sensing geology from the University of Southern California in 1979 and a B.S. in geology from the State University of New York at Albany in 1973. For the past eight years, he has been a senior computer image processing analyst at the Jet Propulsion Laboratory (JPL) of the California Institute of Technology. While at JPL, he planned and implemented image and data processing activities for the JPL undersea technology program. From 1979 to 1981 he was science and image processing advisor for the JPL Advanced Ocean Technology Development Platform Project (AOTDP). In addition, he has computer processed side scan sonar images collected on surveys of the sunken U.S.S. Hamilton on Lake Ontario. Prior to his work dealing with the computer processing of side scan sonar images, he was involved in image processing for JPL terrestrial remote sensing projects. These projects employed digital images from the Landsat Multispectral scanner, NOAA Very High Resolution Radiometer, and the Skylab S-192 scanner.

## SEA SURFACE TEMPERATURE ANALYSIS

William H. Gemmill  
National Meteorological Center  
National Weather Service, NOAA  
Camp Springs, MD 20232

### Abstract

The Ocean Services Group at the National Meteorological Center has been developing and improving oceanographic products with emphasis on coastal and off-shore ocean regions adjacent to the U.S. These products serve as "real-time" guidance to Ocean Service Units of the National Weather Service as well as members of the maritime community.

Over the past several years, a concentrated effort has been devoted to sea surface temperature (SST) and ocean feature analyses. Four types of analyses are now being prepared on a routine basis; 1) objectively prepared global SST analyses, 2) objectively prepared regional SST analyses, 3) subjectively prepared regional ocean feature analyses, and 4) subjectively prepared coastal SST analyses.

The objective analyses are a "blend" of in-situ SST observations obtained from ships, fixed buoys, drifting buoys and XBT's, and satellite derived measurements. The subjective analyses require the interpretation of high-resolution satellite imagery along with in-situ measurements.

Each of the products has its own scale and pattern that is being displayed.

MR. WILLIAM H. GEMMILL received a M.S. degree in Meteorology from Pennsylvania State University in 1963.

Between 1963-1975, he was employed by NAVOCEANO in Suitland, Maryland. There he worked as a physical oceanographer dealing with ASW problems. Much of the work was carried out using large-scale computer systems.

Since 1975, he has been working at the National Meteorological Center in the Ocean Services Group, involved in improving and developing ocean services, especially, for the Coastal and Off-shore areas adjacent to the U.S. coastline.

## POTENTIALS FOR PATTERN RECOGNITION IN PHYSICAL OCEANOGRAPHY

A.W. Green

Naval Ocean Research and Development Activity  
Ocean Science and Technology Laboratory  
NSTL Station, MS 39529

### Abstract

Types of data collected by physical oceanographers are described in terms of space-time variability. Some examples of possible applications of pattern recognition to detect and describe physical hydrodynamic events in the oceans are given. The examples include: recurrent structures in oceanic variables caused by internal gravity waves; surface wave patterns resulting from nonlinear wave interactions; thermal patterns associated with oceanic eddies; interleaving of water types in ocean fronts. Ocean dynamics dictate that the "patterns" of events constantly change, so that the algorithms for pattern recognition in the oceans must usually be "adaptive" in order that the spatial and temporal changes of the pattern occurring during sampling can be tracked.

DR. ALBERT W. GREEN received his Ph.D. in Physical Oceanography at Massachusetts Institute of Technology in 1969. He is currently the head of the Physical Oceanography Branch, Naval Ocean Research and Development Activity. Before coming to NORDA he was an assistant professor of Atmospheric and Oceanic Science, University of Michigan. His research interests are in the development of methods for measurement of high frequency-high wave number internal gravity waves, experimental analysis of strongly nonlinear surface waves, processes governing generation of mesoscale eddies and waves in the ocean.

## DYNAMIC SCENE ANALYSIS

Ramesh Jain  
Intelligent Systems Laboratory  
Department of Computer Science  
Wayne State University  
Detroit, Michigan 48202

### Abstract

Understanding of a complex dynamic scene requires integration of diverse knowledge sources at different levels. In a dynamic scene analysis system the peripheral processes may be used to extract information useful in constraining combinatorial explosion at subsequent levels. A partial segmentation of the scene may be obtained using domain independent knowledge sources. This segmentation step partitions the scene based only on intrinsic characteristics of surfaces appearing in the scene. A complete segmentation and then analysis of the scene can be performed by a cooperative effort of domain specific and domain independent knowledge sources. This paper presents an overview of a system called Vili, based on the above approach. Some experimental results will also be presented.

DR. RAMESH JAIN is an associate professor of Computer Science at Wayne State University. His current research is in the area of computer vision with emphasis on dynamic scene analysis, shape from shading, the use of Knowledge in vision, and the application of artificial intelligence to industrial engineering and computer graphics. He was formerly employed by the Indian Institute of Technology, Kharagpur, India, the University of Hamburg, Germany, and the University of Texas at Austin.

Jain received his Ph.D. in Electronics and Electrical Communication Engineering from IIT, Kharagpur, in 1975.



## FLUCTUATION SPECTRUM OF OCEANIC STRUCTURE

Ronald J. Holyer  
Remote Sensing Branch  
Naval Ocean Research &  
Development Activity  
NSTL Station, MS 39529

### Abstract

Present day satellite infrared and visible sensors permit investigation of meso-scale ocean features such as fronts, eddies and plumes. In addition to these visually apparent features, a part of the temperature/color field must be considered as random and containing some other information which can only be retrieved by statistical analysis - e.g., the spectral density of variance. The measured spectral density of variance,  $E(k)=k \cdot \text{Exp}(-n)$ , or alternatively the structure function, results in an  $n$  value which can be compared with turbulence theories which predict  $n$  values ranging from one to five. Spectral analysis of LANDSAT data south of Iceland is presented to suggest that pattern recognition techniques could possibly be more fully merged with physical oceanography to gain new insight into turbulent flow in the mixed layer.

The Coastal Zone Color Scanner (CZCS) images the earth's oceans in five visible/near-IR spectral bands. In the visible portion of the electromagnetic spectrum, satellite observed radiance typically consists approximately 90% of atmospheric backscatter and 10% of ocean scattered radiance. Subtle color signatures associated with oceanic features are frequently masked by this atmospheric path radiance. Accurate atmospheric correction of CZCS data is, therefore, a prerequisite to optimum information extraction from this imagery. The most widely accepted atmospheric correction scheme for CZCS data, based on a single scattering model of the atmosphere plus certain assumed optical properties of the ocean, has several inherent drawbacks that limit its effectiveness. Principal Components Analysis (the KL transformation) is offered as an alternate atmospheric correction scheme based upon a statistical rather than a modeling approach. The Principal Components Method is applied to two CZCS data sets and a comparison is made with corrections derived by the modelling method.

MR. RONALD J. HOLYER received his M.S. in Physics from South Dakota School of Mines and Technology. He is presently employed in the Remote Sensing Branch, Naval Ocean Research and Development Activity. Mr. Holyer's professional interests are in digital image processing and the application of remote sensing to oceanographic problems.

# SPATIAL TECHNIQUES FOR ENHANCEMENT AND RESTORATION OF INFRARED IMAGES

R.C. Gonzalez  
University of Tennessee

## Abstract

Two methods for image enhancement and restoration in the spatial domain are presented. The first is a noise filtering algorithm based on a least-squares predictive filter. The second technique generates a small convolution mask that approximates the effects of a given frequency-domain filter. Both methods are suitable for real-time implementation.

DR. RAFAEL C. GONZALEZ received the B.S.E.E. degree from the University of Miami in 1965 and the M.E. and Ph.D. degrees in Electrical Engineering from the University of Florida, Gainesville, in 1967 and 1970, respectively.

He has been affiliated with the GT&E Corp., the Center for Information Research at the University of Florida, NASA, and is presently IBM Professor of Electrical Engineering and Computer Science at the University of Tennessee, Knoxville.

Dr. Gonzalez is co-author of the books Pattern Recognition Principles, Digital Image Processing, and Syntactic Pattern Recognition: An Introduction, all published by Addison-Wesley. He is an associate editor for the IEEE Trans. on Systems, Man and Cybernetics and the International Journal of Computer and Information Sciences.

The following abstracts are for papers invited by the PAME Workshop Chairman and presented at the Pattern Recognition Session of the Third biennial Society of Exploration Geophysicists/U.S. Navy Symposium, March 23, 1982, just preceeding this workshop.

ACTIVITIES AT THE UNIVERSITY OF HOUSTON'S ALLIED GEOPHYSICAL LABORATORIES  
WITH A SUMMARY OF NEW DEVELOPMENTS IN 3D DISPLAY DEVICES

H. Roice Nelson, Jr.  
General Manager  
Allied Geophysical Laboratories

Abstract

This presentation will briefly review the history and plans of the Allied Geophysical Laboratories (AGL) at the University of Houston. The AGL consists of 5 independent industry supported research laboratories. Research at the AGL is evaluating the full spectrum of reflection seismology, with emphasis on 3D seismic techniques. These laboratories presently include the Field Research Laboratory (FRL), the Seismic Acoustics Laboratory (SAL), the Keck Research Computation Laboratory (RCL), the Cullen Image Processing Laboratory (IPL), and the Well Logging Laboratory (WLL).

There is a good equipment base valued at over \$2.0 million. The main processor is a VAX 11/780 that is directly tied to Cybernet and specifically to a CDC-205 vector processor in Minneapolis. Other significant equipment includes the SAL physical modeling tank and controlling ComMand computer, a Tektronix 4081 intelligent terminal, an Adage 4145 vector refresh graphics system with a raster segment generator, and a SpaceGraph vibrating mirror 3D display device. Each laboratory is responsible for their own funding and there is a total annual budget for 1982 of about \$1.5 million.

A brief summary of the research activities of each of these 5 laboratories will be presented. There will also be examples of how research under way at the AGL ties into the themes of the SEG/USN symposium on Shear Waves and the workshop on Pattern Recognition.

Because the primary emphasis at the AGL is in studying 3D seismic techniques, there has been a careful evaluation of display techniques that can be used to evaluate three-dimensional volumes of data. A summary of the results of this evaluation will be presented as an introduction to new research tools for pattern recognition. The techniques used to display 3D data volumes that will be described include: a toy made with a pair of parabolic mirrors; projection imaging techniques; auto-stereoscopic and synthalyzer film display devices; beam splitting techniques; a device based on rotating LED's; and varifocal or vibrating mirror devices. Although scientists in many different fields are interested in developing a useable 3D display there has not been a completely satisfactory answer developed. The problems with holographic displays are an example of how 3D display techniques can be oversold, before an acceptable solution is developed.

WATER MASS CLASSIFICATION IN THE NORTH ATLANTIC USING  
IR DIGITAL DATA AND BAYESIAN DECISION THEORY

Robert Coulter  
Naval Oceanographic Office  
NSTL Station, MS 39529

Abstract

A method is described which utilizes Bayesian (maximum likelihood) decision theory and historical statistics of sea surface temperature to classify surface water masses and detect ocean surface fronts from satellite-derived infrared data. Probabilities that certain features occur are determined from the probability distributions of specific statistical characteristics, known a priori, and the same characteristics, computed from the data. The better the match between the a priori information associated with a feature and the computed statistics, the higher the probability will be that the feature exists. The maximum probability, as determined by Bayes' theory, is subject to two tests, based on absolute and relative threshold values, to reduce the chance of incorrect classification. The method was used for classifying both airborne and satellite IR data to locate the Gulf Stream surface front. The results are compared to frontal positions obtained by conventional means.

MR. ROBERT E. COULTER received his B.S. degree in Engineering at Florida State University. He obtained his M.S. degree in Physical Oceanography at Texas A & M University. He is presently employed at the Fleet Applications Department of the Naval Oceanographic Office. Prior to this, he held positions with the firm of A.H. Glenn and Associates and with the Mississippi State University Research Center in conjunction with the NOAA Data Buoy Office. Mr. Coulter's professional interests include automated, sea surface wave measurement, environmental data quality control, and the automatic interpretation of infrared satellite data for oceanographic applications.

## UTILIZATION OF SIDE SCAN SONAR FOR SEA FLOOR CLASSIFICATION

Carey Ingram  
Naval Oceanographic Office  
NSTL Station, MS 39529

Joseph N. Suhayda  
Department of Civil Engineering  
Louisiana State University  
Baton Rouge, LA 70802

### Abstract

Side scan sonar imagery of the sea floor may be likened to the subaerial imagery produced by side-looking airborne radar, typically providing swath coverage of up to half a kilometer to each side of a survey vessel's transit path. At the present time, interpretation of sonar imagery is a laborious process culminating in qualitative classification of bottom sediment types and morphological features. The application of pattern recognition technology currently used in radar image interpretation could significantly automate the processing of sonar data. Examples of the state of the art in sonar imagery and interpretation will be presented.

MR. CAREY INGRAM received his B.S. in Geology from the George Washington University and holds a Master's degree in Marine Science from the Virginia Institute of Marine Science at The College of William and Mary. He currently manages the Marine Geological Laboratory of the Naval Oceanographic Office. His current professional interests include automation of analytical procedures in the laboratory, the development of more efficient instrumentation for real-time sea floor classification, and in-situ measurement of physical and acoustical properties in marine sediments.

DR. JOSEPH SUHAYDA received his B.S. in Physics from California State University at Northridge and holds the Ph.D. in Physical Oceanography from the University of California at San Diego. He is currently an Associate Professor in the Department of Civil Engineering at Louisiana State University. His current professional interest is in the geotechnical properties of sea floor sediments, with a subsidiary interest in attendant geoaoustic properties.

## **Appendix C: List of Attendees**

Dr. Robert Brown  
NORDA, NSTL, MS 39529  
Chairman

ANDREWS, Jim  
NORDA

BEAL, Robert  
Applied Physics Lab  
Johns Hopkins University  
Johns Hopkins Road  
Laurel, MD 20707

BERKOWITZ, Sidney  
David Taylor Naval Sys  
Washington, DC

BERMAN, Mark  
Graduate School of  
Oceanography  
U. of Rhode Island  
Kingston, RI 02881

BEZDEK, James  
Dept. of Mathematics  
Utah State Univ.  
UMC 41  
Logan, UT 87322

BROWN, Mike  
U. of California at  
San Diego  
Mail Code A025  
La Jolla, CA 92093

BUTLER, Dwaine  
U. S. Army Corps of  
Engineers  
Vicksburg, MS 39180

CARRON, Mike  
NAVOCEANO  
NSTL Station, MS 39529

CHANG, B. B.  
O'Connor Research  
730 17th St.,  
Suite 300  
Denver, CO 80202

CHANG, C. Y.  
Cities Service Co.  
Box 3908  
Tulsa, OK 74102

CLAY, Clarence  
U. of Wisconsin  
at Madison  
5033 St. Cyr Rd.  
Middleton, WI 53562

CLOUTIER, Jim  
NAVOCEANO  
Bay St. Louis, MS 39522

COULTER, Robert  
NAVOCEANO  
Bay St. Louis, MS 39522

EDBERG, James R.  
Undersea Tech. Dev.  
Jet Propulsion Lab  
California Institute  
of Technology  
4800 Oak Grove Drive  
Pasadena, CA 91109

EHRlich, Robert  
Geology/USC  
Columbia, SC 29208

FARR, John  
Western Geophysical  
Box 2469  
Houston, TX

FRAZER, Neil  
Hawaii Institute of  
Geophysics  
2525 Correa Rd.  
Honolulu, HI 96822

FU, K. S.  
Electrical Engin. Dept.  
Purdue University  
West Lafayette, IN 47907

FU, L. L.  
Jet Propulsion Lab  
Mail Stop 183-701  
4800 Oak Grove Drive  
Pasadena, CA 91109

FULL, Bill  
Geology/USC  
Columbia, SC 29208

GEMMILL, Bill  
NOAA  
Camp Springs, MD

GETTRUST, Joe  
University of Hawaii  
Honolulu, HI 96822

GONZALEZ, Ralph  
Electrical Engin. Dept.  
U. of Tennessee  
Knoxville, TN 37916

GREEN, Albert  
NORDA

GULIZIA, William  
Jet Propulsion Lab  
California Institute  
of Technology  
4800 Oak Grove Drive  
Pasadena, CA 91109

HANSEN, George  
Jet Propulsion Lab  
Mail Stop 510-110  
4800 Oak Grove Drive  
Pasadena, CA 91109

HEYSER, Richard  
Jet Propulsion Lab  
Mail Stop 183-901  
4800 Oak Grove Dr.  
Pasadena, CA 91109

HOLYER, Ronald  
NORDA

HORVATH, Peter  
Arco Oil & Gas co.  
P. O. Box 2819  
Dallas, TX 75221

INGRAM, Carey  
NAVOCEANO  
NSTL, MS 39529



JAIN, Ramesh  
Dept. of Computer Science  
Wayne State University  
Detroit, MI 48202

JANOWITZ, Melvin  
Mathematics & Statistics  
Dept.  
U. of Massachusetts  
Amherst, MA 01003

KALDEN, A. B.  
Shell International  
Holland  
The Netherlands

KHEDOURI, Edward  
NAVOCEANO  
Bay St. Louis, MS 39522

LOWRY, Robert  
Naval Ocean Sys Center  
Panama City, FL

MARSHALL, William  
NAVOCEANO  
Bay St. Louis, MS 39522

MAZEL, Charles  
Klein Assoc.  
Salem, NH

McKENDRICK, John  
NORDA

MONTGOMERY, Donald  
Jet Propulsion Lab  
Mail Stop 180-701  
4800 Oak Grove Drive  
Pasadena, CA 91109

NELSON, Roice  
Allied Geophysical Lab  
U. of Houston  
Houston, Tx 77004

NEW, Ronald  
NOAA  
Rockville, MD 20852

PALUZZI, Peter  
McQuest Marine  
R&D Co., LTD.  
489 Infield Rd.  
Burlington, Ontario  
CANADA L7T2X5

POULARIKAS, Alexander D.  
Graduate School of  
Oceanography  
U. of Rhode Island  
Kingston, RI 02881

RANKIN, Bill  
NAVOCEANO  
Bay St. Louis, MS 39522

ROSENFELD, Azriel  
Computer Science Center  
Computer Vision Lab  
U. of Maryland  
College Park, MD 20742

SUHAYDA, Joe  
Dept. of Civil Engin.  
Louisiana State Univ.  
Baton Rouge, LA 70803

TYCHSEN, John  
Danish Geotechnical Inst.  
DENMARK

UNCLASSIFIED

SECURITY CLASSIFICATION OF THIS PAGE (When Data Entered)

REPORT DOCUMENTATION PAGE		READ INSTRUCTIONS BEFORE COMPLETING FORM
1. REPORT NUMBER NORDA Technical Note 176	2. GOVT ACCESSION NO. <b>AD-A240 295</b>	3. RECIPIENT'S CATALOG NUMBER
4. TITLE (and Subtitle) PAME Proceedings		5. TYPE OF REPORT & PERIOD COVERED Final
		6. PERFORMING ORG. REPORT NUMBER
7. AUTHOR(s) Robert M. Brown, editor		8. CONTRACT OR GRANT NUMBER(s)
9. PERFORMING ORGANIZATION NAME AND ADDRESS Naval Ocean Research and Development Activity Ocean Science and Technology Laboratory NSTL, Mississippi 39529		10. PROGRAM ELEMENT, PROJECT, TASK AREA & WORK UNIT NUMBERS PE61153N
11. CONTROLLING OFFICE NAME AND ADDRESS same		12. REPORT DATE October 1983
		13. NUMBER OF PAGES 290
14. MONITORING AGENCY NAME & ADDRESS (if different from Controlling Office)		15. SECURITY CLASS. (of this report) Unclassified
		15a. DECLASSIFICATION/DOWNGRADING SCHEDULE
16. DISTRIBUTION STATEMENT (of this Report) Approved for public release. Distribution unlimited.		
17. DISTRIBUTION STATEMENT (of the abstract entered in Block 20, if different from Report)		
18. SUPPLEMENTARY NOTES		
19. KEY WORDS (Continue on reverse side if necessary and identify by block number) Pattern analysis                      Ocean science                      Marine environment Artificial intelligence              Pattern recognition              Image enhancement		
20. ABSTRACT (Continue on reverse side if necessary and identify by block number) The Pattern Analysis in the Marine Environment (PAME) Workshop Proceedings contains ten of the papers presented at an Ocean Science and Technology Workshop sponsored by the Chief of Naval Research and hosted by the Naval Ocean Research and Development Activity, NSTL, Mississippi, 24-26 March 1982. PAME Workshop topics ranged from computer science, pattern analysis, and artificial intelligence to specific problem areas, applications, and requirements in ocean science. The workshop was organized in the following five sessions:		

DD FORM 1473  
1 JAN 73EDITION OF 1 NOV 65 IS OBSOLETE  
S/N 0102-LF-014-6601

UNCLASSIFIED

SECURITY CLASSIFICATION OF THIS PAGE (When Data Entered)

**UNCLASSIFIED**

SECURITY CLASSIFICATION OF THIS PAGE (When Data Entered)

- Image Analysis Techniques I;
- Image Analysis Techniques II;
- Pattern Analysis Techniques;
- Space Technology for Ocean Applications;
- Ocean Patterns in Space-Time.

A number of presentations were informal and tutorial in nature. An abstract of all presentations is included, along with a complete list of attendees.

**UNCLASSIFIED**

SECURITY CLASSIFICATION OF THIS PAGE(When Data Entered)